

# **$^{19}\text{F}$ -MRI of Inhaled Perfluoropropane for Quantitative Imaging of Pulmonary Ventilation**

**Mary Neal**

Thesis submitted for the degree of Doctor of Philosophy

Newcastle Magnetic Resonance Centre

Institute of Cellular Medicine

Newcastle University

September 2017



## **Abstract**

MRI of exogenous imaging agents offers a safely repeatable modality to assess regional pulmonary ventilation. A small number of studies have validated the safety and potential utility of  $^{19}\text{F}$  imaging of inhaled thermally polarised perfluoropropane. However, the relative scarcity of signal in restrictive breath hold length acquisition times inhibits translation of this technique to clinical application. This work presents methods used to maximise the attainable image quality of inhaled perfluoropropane. Novel quantitative measures of ventilation and perfusion have been investigated and discussed.

A preliminary healthy volunteer study was conducted to verify the efficacy of the imaging technique and to assess perfluoropropane wash-in and wash-out rates. Quantitative assessment of the suitability of four RF coil designs was performed, comparing power efficiency with loading and signal homogeneity within the sensitive volume of each coil. The 3D spoiled gradient echo sequence was simulated, accounting for the power performance of the chosen birdcage coil design, for calculation of acquisition parameter values required to achieve the highest SNR in a fixed acquisition period for  $^{19}\text{F}$ -MRI of inhaled perfluoropropane. Studies on resolution phantoms and healthy volunteers assessed the performance of the optimised imaging protocol, in combination with a compressed sensing technique that permitted up to three-fold acceleration.

Two novel lung-representative phantoms were fabricated and used to investigate the behaviour of the MR properties of inhaled perfluoropropane with changing structural and magnetic environments. Finally, a method for lengthening the  $T_2^*$  of inhaled perfluoropropane by susceptibility matching the alveolar tissue to the inhaled gas by intravenous injection of a highly paramagnetic contrast agent is presented. Initial development work was conducted in phantoms and rodents before translation to healthy volunteers. This technique offers the potential to concurrently acquire images reflecting both pulmonary ventilation and perfusion.

## **Acknowledgements**

First, I would like to express my gratitude to my supervisor Dr Pete Thelwall for his guidance, enthusiasm and patience over the past three years, and for being such a supportive mentor. I would also like to thank my second supervisor, Professor Andrew Blamire, for freely sharing his time and invaluable expertise.

I am indebted to all of my colleagues at the Newcastle Magnetic Resonance Centre for their continued support. I'd like to offer a special thanks to Dr Ben Pippard for ensuring the smooth running of the many healthy volunteer studies over the past year, and for readily sharing his clinical expertise. Equally, I wish to thank Dr Kieren Hollingsworth for his invaluable assistance in applying his compressed sensing technique to some of the acquisition sequences used in this thesis. Thanks also to Dr Eric Hughes for sharing his microfluidics experience and apparatus. I would also like to thank Dr Ross Maxwell and Professor John Simpson for overseeing my annual progress reviews, and for the valuable discussions that stemmed from them. Thanks also to Dr Prosenjit Dutta for offering invaluable clinical support for the first human study, and to the NMRC Radiographers for patiently overseeing every one of the countless number of human scan sessions.

I would like to extend my gratitude to the staff at the Royal Children's Hospital in Melbourne who readily supported this work by providing their expertise and generous access to their scanner hardware during my visit.

On a personal note, I would like to thank my family: my father, Simon, for his immeasurable love and support, and for encouraging me to pursue my interest in science; my siblings, Grace, Francis, and Madeline, for their camaraderie; and finally, my partner Christopher, for his endless love and encouragement through all the ups and downs of this research.



# Table of Contents

ABSTRACT.....	I
ACKNOWLEDGEMENTS.....	II
TABLE OF CONTENTS.....	IV
LIST OF FIGURES.....	IX
LIST OF TABLES.....	XV
LIST OF ABBREVIATIONS.....	XVII
<b>CHAPTER 1: MRI OF PULMONARY VENTILATION: THEORETICAL BACKGROUND AND LITERATURE REVIEW.....</b>	<b>1</b>
1.1 RESPIRATORY PHYSIOLOGY AND PATHOPHYSIOLOGY .....	1
1.1.1 Pulmonary anatomy.....	1
1.1.2 Respiratory mechanics.....	1
1.1.3 Pulmonary volumes.....	2
1.1.4 Ventilation homogeneity in healthy subjects.....	3
1.1.5 Respiratory pathophysiology.....	3
1.2 MAGNETIC RESONANCE THEORY .....	6
1.2.1 Nuclear spin angular momentum and polarisation .....	6
1.2.2 Nuclear excitation.....	9
1.2.3 Nuclear relaxation and the Bloch equations.....	10
1.2.4 Free induction decay.....	12
1.2.5 NMR to MRI: image formation in k-space .....	13
1.2.6 The spoiled gradient echo pulse sequence.....	14
1.2.7 RF pulse shapes .....	16
1.2.8 Producing a radio frequency pulse: basic RF coil theory.....	17
1.2.9 The birdcage coil.....	18
1.3 MODALITIES FOR THE ASSESSMENT OF PULMONARY VENTILATION.....	23
1.3.1 Pulmonary ventilation imaging techniques utilising ionising radiation.....	23
1.3.2 <sup>1</sup> H MRI of pulmonary ventilation.....	24

1.3.3	<i>Hyperpolarised noble gas MRI of pulmonary ventilation</i> .....	25
1.3.4	<i>MRI of pulmonary ventilation using perfluorinated gases</i> .....	28
1.4	OUTLINE OF CHAPTERS .....	33
<b>CHAPTER 2: HEALTHY VOLUNTEER PROOF OF CONCEPT STUDY</b> .....		<b>34</b>
2.1	OVERVIEW .....	34
2.2	METHODS.....	35
2.2.1	<i>Volunteers</i> .....	35
2.2.2	<i><sup>19</sup>F MRI hardware set-up</i> .....	35
2.2.3	<i>Testing intra-volunteer reproducibility</i> .....	37
2.2.4	<i>Assessment of gas wash-in and wash-out rate</i> .....	39
2.2.5	<i>In vivo measurement of T<sub>2</sub>*</i> .....	40
2.3	RESULTS.....	41
2.3.1	<i>Testing intra-volunteer reproducibility</i> .....	41
2.3.2	<i>Assessment of gas wash-in and wash-out rate</i> .....	42
2.3.3	<i>In vivo measurement of T<sub>2</sub>*</i> .....	44
2.4	DISCUSSION .....	46
2.5	CONCLUSIONS.....	48
<b>CHAPTER 3: <sup>19</sup>F COIL CONSTRUCTION AND ASSESSMENT OF FOUR <sup>19</sup>F COIL DESIGNS FOR SUITABILITY FOR PULMONARY IMAGING</b> .....		<b>49</b>
3.1	OVERVIEW .....	49
3.2	METHODS.....	50
3.2.1	<i>Birdcage coil construction</i> .....	50
3.2.2	<i>Assessment of RF coil power performance</i> .....	53
3.2.3	<i>Measurement of achievable SNR in four coils</i> .....	54
3.2.4	<i>Assessment of signal homogeneity in four coils</i> .....	55
3.3	RESULTS.....	57
3.3.1	<i>Assessment of RF coil power performance</i> .....	57
3.3.2	<i>Measurement of achievable SNR in four coils</i> .....	59
3.3.3	<i>Assessment of signal homogeneity in four coils</i> .....	59

3.4	DISCUSSION .....	62
3.5	CONCLUSIONS.....	64
<b>CHAPTER 4: DEVELOPMENT OF AN OPTIMISED ACQUISITION SEQUENCE FOR IMAGING</b>		
<b>INHALED PERFLUOROPROPANE .....</b>		
<b>65</b>		
4.1	OVERVIEW .....	65
4.2	DERIVATION OF THE RELATIVE SNR ACHIEVED IN A 3D SPGR PULSE SEQUENCE .....	66
4.2.1	<i>Sequence optimisation.....</i>	67
4.2.2	<i>Defining input variables for the simulation.....</i>	69
4.3	METHODS.....	71
4.3.1	<i>Simulation and optimisation of a 3D SPGR sequence.....</i>	71
4.3.2	<i>Verification of optimised parameters in vitro .....</i>	71
4.3.3	<i>Application of compressed sensing techniques to the optimised imaging sequence: phantom based assessment of resultant image quality.....</i>	72
4.3.4	<i>Application of the optimised protocol to imaging healthy volunteers .....</i>	74
4.4	RESULTS.....	75
4.4.1	<i>Simulation and optimisation of a 3D SPGR sequence.....</i>	75
4.4.2	<i>Verification of optimised parameters in vitro .....</i>	77
4.4.3	<i>Phantom based assessment of scan resolution.....</i>	79
4.4.4	<i>Application of the optimised protocol to imaging healthy volunteers .....</i>	81
4.5	DISCUSSION .....	83
4.6	CONCLUSIONS.....	85
<b>CHAPTER 5: THE EFFECT OF SUSCEPTIBILITY GRADIENTS ON THE T<sub>2</sub>* OF</b>		
<b>PERFLUOROPROPANE: STUDIES IN LUNG-REPRESENTATIVE PHANTOMS .....</b>		
<b>86</b>		
5.1	OVERVIEW.....	86
5.2	THEORETICAL OVERVIEW OF MAGNETIC SUSCEPTIBILITY IN PULMONARY ALVEOLI.....	87
5.3	METHODS .....	91
5.3.1	<i>Construction of a lung representative phantom: monodisperse foam.....</i>	91
5.3.2	<i>In vitro measurements: monodisperse foam .....</i>	92
5.3.3	<i>Construction of a lung representative phantom: polydisperse foam.....</i>	94

5.3.4 <i>In vitro</i> measurements: polydisperse foam .....	95
5.4 RESULTS.....	96
5.4.1 <i>In vitro</i> measurements: monodisperse foam .....	96
5.4.2 <i>In vitro</i> measurements: polydisperse foam .....	99
5.4.3 Altering magnetic susceptibility of the foam liquid component.....	100
5.5 DISCUSSION .....	103
5.5.1 Assessment of the efficacy of the lung representative phantoms .....	103
5.5.2 Determinants of PFP –CF <sub>3</sub> T <sub>2</sub> * .....	104
5.5.3 Translation of findings to <i>in vivo</i> measurements .....	105
5.5.4 Potential clinical applications .....	105
5.6 CONCLUSIONS .....	107
<b>CHAPTER 6: DYNAMIC CONTRAST-ENHANCED <sup>19</sup>F MRI OF INHALED PERFLUOROPROPANE IN RODENTS AND HEALTHY VOLUNTEERS .....</b>	<b>108</b>
6.1 OVERVIEW .....	108
6.2 SUSCEPTIBILITY MATCHING IN THE LUNG FOR MAPPING PULMONARY PERFUSION: BACKGROUND .....	110
6.2.1 Existing modalities for imaging pulmonary perfusion .....	110
6.2.2 Susceptibility matching in the mouse lung.....	111
6.2.3 Safety review of gadolinium based contrast agents.....	111
6.2.4 Susceptibility matching in healthy volunteers.....	112
6.3 METHODS .....	114
6.3.1 Mouse study: <sup>19</sup> F MRI preparation .....	114
6.3.2 Mouse study: acquisition protocol.....	115
6.3.3 Healthy volunteer study: effect of intravenous gadolinium-based contrast agent on PFP T <sub>2</sub> * and signal magnitude .....	116
6.4 RESULTS.....	119
6.4.1 Mouse study: effect of intravenous Gadobutrol on T <sub>2</sub> * and signal amplitude.....	119
6.4.2 Healthy volunteer study: effect of intravenous gadolinium on average T <sub>2</sub> * .....	121
6.4.3 Healthy volunteer study: effect of intravenous GBCA on <sup>19</sup> F-MRI signal amplitude .....	122
6.5 DISCUSSION .....	124

6.5.1 Mouse study.....	124
6.5.2 Healthy volunteer study.....	125
6.5.3 Application to clinical practice.....	125
6.6 CONCLUSIONS .....	127
<b>CHAPTER 7: CONCLUSIONS AND FUTURE WORK.....</b>	<b>128</b>
REFERENCES .....	131

## List of Figures

- Figure 1-1:** Typical lung volumes and capacities for a healthy subject depicted on a spirometric trace. Only a small fraction of the total lung volume is exchanged in tidal breathing. Deep respiratory manoeuvres that engage the accessory muscles of the respiratory system are required to exchange a volume of air close the vital capacity..... 2
- Figure 1-2:** Relative lung volumes in healthy subjects and patients with obstructive lung disease. Notably, an increase in total lung capacity (TLC) and residual volume (RV) is present. Tidal volume (TV), and vital capacity (VC) remain approximately constant..... 5
- Figure 1-3: a.** Illustration of the precession of the spin magnetic moment,  $\mu$ , around an external static magnetic field,  $B_0$ , pointing along the z-axis.  $\mu$  precesses around  $B_0$  at the Larmor frequency,  $\omega_0$ . **b.** The net magnetisation,  $M$ , from many nuclei experiencing the same external  $B_0$  field is along the positive z-axis, as the spins precess out of phase, and a small excess (not to scale) inhabit the lower energy parallel spin state..... 9
- Figure 1-4:** Free induction decay after a RF pulse. The envelope of the FID (marked in blue) describes the  $T_2^*$  signal decay of the subject nuclei..... 12
- Figure 1-5:** A 3D spoiled gradient echo pulse sequence. The slice selection, phase encoding, and frequency encoding gradients are used to encode spatial information into the MR signal..... 15
- Figure 1-6: a.** A sinc pulse, and its corresponding sharp slice profile. Ringing is present due to it not being an infinite example. **b.** A heavily truncated sinc pulse, and its corresponding imperfect slice profile with notable ringing..... 16
- Figure 1-7: a.** A simple LC circuit in a surface coil. **b.** A transverse view of a surface coil, with  $B_1$  field lines depicted..... 18
- Figure 1-8: a.** Capacitor location on a high-pass birdcage coil. **b.** Capacitor location on a low-pass birdcage coil..... 19
- Figure 1-9:** Simulated  $B_1$  field maps for a birdcage coil with 4, 8, and 16 legs respectively. These were simulated by applying the Biot-Savart law to each leg, then summing the B-field values experienced at each point in the image. .... 19
- Figure 1-10:** A small segment of the circuit in a N-rung birdcage coil..... 20

<b>Figure 1-11:</b> An example tune and match circuit. The tuning capacitor is joined in parallel to the coil circuit, and the matching capacitors are connected in series. ....	22
<b>Figure 2-1:</b> Diagrammatic layout of the inhalation rig components. The pneumotachometer and pulse oximeter are passed through the waveguide and monitored from the control room. The 100% O <sub>2</sub> supply was only made available if the subject's oxygen saturation dropped below 90% whilst in the scanner bore. ....	36
<b>Figure 2-2:</b> Positioning of <sup>19</sup> F surface coil on the volunteers back. The coil was positioned to cover the apex of both lungs. ....	37
<b>Figure 2-3:</b> Diagram of the breathing and breath hold pattern followed by each volunteer. Three deep inhalations of PFP/O <sub>2</sub> are followed by three deep inhalations of room air. The dynamic acquisition sequence runs throughout, permitting dynamics from the breath holds following each inhalation to be compared. ....	39
<b>Figure 2-4:</b> Rows one and two: Slices in the coronal plane proximal to the coil from six <sup>19</sup> F 3D SPGR acquisitions in three healthy volunteers. All were acquired within a 15 s breath hold duration after wash-in of PFP/O <sub>2</sub> . Row three: Masked <sup>19</sup> F signal overlaid on an anatomical proton image.....	41
<b>Figure 2-5:</b> <b>a.</b> SNR over distance from coil surface. High SNR seen posteriorly, proximal to the coil surface, with exponential loss of signal over the following 10 cm. <b>b.</b> Image of slice at 30 mm distance from coil surface. <b>c.</b> Image of slice at 50 mm. <b>d.</b> Image of slice at 70 mm. ....	42
<b>Figure 2-6:</b> SNR change over three deep inhalations of PFP/O <sub>2</sub> gas, also displayed as percentage change. With increased wash-in an increase in SNR and a reduction in range is noted. The box plots display the mean SNR (horizontal line) and interquartile range. The error bars denote the minimum and maximum SNR values measured. ....	43
<b>Figure 2-7:</b> SNR change over three deep inhalations of room air after three wash-in inhalations of PFP/O <sub>2</sub> , also displayed as percentage change. The box plots display the mean SNR (horizontal line) and interquartile range. The error bars denote the minimum and maximum SNR values measured. ....	44
<b>Figure 2-8:</b> FID decay curves at full inspiration and expiration, with solid lines denoting monoexponential fits. The poor fit is due to the unlocalised FID signals representing	

poly-exponential  $T_2^*$  decay averaged over all regions in the sensitive volume of the coil. .... 45

**Figure 2-9:** Change in PFP  $T_2^*$  over the respiratory cycle. The relative signal amplitude (upper curve) is indicative of the position in the respiratory cycle when inhaling PFP/O<sub>2</sub>. The  $T_2^*$  follows the same pattern. Notably, in the final 10 s, a wash-out inspiration of room air is performed causing the signal amplitude to stay at the level at expiration, whereas the  $T_2^*$  increases. .... 45

**Figure 3-1:** Structure of the completed coil frame. The coil is 400 mm long, and designed to be elliptical to maximise its sensitive volume. The 16 capacitor points are labelled. .... 50

**Figure 3-2: a.** The dimensions and required resonant frequency of the birdcage coil specified in the Birdcage Builder interface. **b.** The fixed capacitance distribution output from the Birdcage Builder interface. .... 51

**Figure 3-3:** Spectra showing all eight resonant peaks. The target resonant peak (red arrow) is tuned to 109 MHz on the lab bench. This resonance shifted to 120.24 MHz when the coil was placed in the scanner bore or bore simulator. .... 52

**Figure 3-4:** The tune and match circuit. The tuning capacitor is joined in parallel to the birdcage coil circuit, and the matching capacitors are connected in series. .... 52

**Figure 3-5:** For successful quadrature use, the coil must be driven by two points with 90° separation that have approximately equal resonant frequencies. It was decided that points 7 and 11 most closely match these requirements. .... 53

**Figure 3-6:** The four transmit-receive coils assessed. **a.** 20 cm diameter surface coil (PulseTeq Ltd.). **b.** 50 cm long linear birdcage coil in situ at the Royal Children’s Hospital, Melbourne (Rapid Biomedical). **c.** 40 cm long birdcage coil (constructed in-house). **d.** 50 cm long quadrature birdcage coil (Rapid Biomedical). .... 53

**Figure 3-7:** Spectra from a flip angle array of the unloaded in-house built birdcage coil. The peak (90°) signal is seen when a ~90° flip angle is requested. This maximal signal intensity shifts to the right (i.e. the achieved 90° occurs at a requested flip >90°) when the coil is loaded. .... 57

**Figure 3-8:** Comparison of coil efficiency when loaded with large volumes of loading solution in the in-house built and commercially built quadrature birdcage coils. A data

point for human loading in the commercially built coil is also shown.....	57
<b>Figure 3-9: a.</b> Signal homogeneity in the anterior-posterior direction. <b>b.</b> Signal homogeneity in the head-foot direction. <b>c.</b> Signal homogeneity in the left-right direction. Only limited data was collected for the linear birdcage coil based at the RCH.....	60
<b>Figure 4-1:</b> A 3D SPGR pulse sequence. This figure depicts a single repetition time, and the process must be repeated for multiple phase encode steps, and signal averages.....	66
<b>Figure 4-2:</b> Schematic of the resolution phantom with 5 cylindrical obstructions of diameters: 5 mm, 10 mm, 15 mm, 22 mm, and 40 mm.....	73
<b>Figure 4-3:</b> Relative SNR achievable (colour scale) in a fixed acquisition time over a range of flip angles and receiver bandwidths, using PFP $T_1$ and $T_2^*$ values measured in vivo. Isolines mark SAR values where 2, 4 and 10 W/kg are reached. ....	75
<b>Figure 4-4:</b> Relative SNR achievable in a fixed acquisition time over a range of flip angles and bandwidths, using $T_1$ and $T_2^*$ values representative of the human lung. ....	76
<b>Figure 4-5:</b> Relative SNR (colour scale) achievable over a range of maximum $B_1$ values for SAR = 2, 4 and 10 W/kg, with the point at which maximum SNR is reached (circles) for each SAR level.....	77
<b>Figure 4-6:</b> Measured SNR over a range of <b>a.</b> $\theta$ , and <b>b.</b> BW. The predicted SNR (scaled to the SNR amplitude with least-squares fitting) is displayed as a grey line on both plots. Although plot b confirms the most suitable bandwidth in the 500-2000 Hz/pixel range, the simulated curve describes a different gradient to the collected data points.....	78
<b>Figure 4-7:</b> Images from four acquisitions with different compressed sensing regimes applied. <b>a.</b> 18 s fully sampled image. <b>b.</b> 10.2 s image (1.8 $\times$ acceleration). <b>c.</b> 7.5 s image (2.4 $\times$ acceleration). <b>d.</b> 6 s image (3.0 $\times$ acceleration). ....	79
<b>Figure 4-8:</b> Visibility of obstructions plotted as a percentage decrease in signal measured within the ROI compared to the mean signal in the unobstructed regions of the phantom. ....	80
<b>Figure 4-9:</b> Signal intensity plot across the (left-right) 22 mm, 40 mm, and 15 mm diameter obstructions. The loss of edge definition is apparent.....	81

<b>Figure 4-10:</b> Slices through the two acquisition protocols: <b>a.</b> Fully sampled data, and <b>b.</b> 3×acceleration. ....	81
<b>Figure 4-11:</b> Lung images with a binary mask applied for <b>a.</b> The fully sampled acquisition, and <b>b.</b> The 3× accelerated acquisition. ....	82
<b>Figure 5-1:</b> <b>a.</b> The apparatus used to produce monodisperse PFP/O <sub>2</sub> -filled foam, using an aqueous detergent and agarose solution. <b>b.</b> The microfluidic chip used. The liquid and gas entered the chip via the top two tubes on the left, and the foam exited via the upper right tube. ....	92
<b>Figure 5-2:</b> RF coil with 6 ml vial of foam. ....	93
<b>Figure 5-3:</b> Schematic depicting the method for frothing the egg white based foam. A sample of the foam was decanted into a 6 ml vial for MR acquisitions. ....	95
<b>Figure 5-4:</b> Microscopy images of: <b>a.</b> bubbles produced using a liquid flow rate of 25 ml/hour, and <b>b.</b> bubbles produced using a liquid flow rate of 45 ml/hour. The scale bar in both images defines a length of 250 μm. <b>c.</b> Microbubbles leaving the T-junction during foam formation, where PFP/O <sub>2</sub> was fed from the left into the stream of liquid. ....	96
<b>Figure 5-5:</b> Relative signal amplitude over varying TE for two foam samples. ....	96
<b>Figure 5-6:</b> T <sub>2</sub> * maps of: <b>a.</b> ~140 μm diameter bubble foam and <b>b.</b> ~250 μm diameter bubble foam. ....	97
<b>Figure 5-7:</b> Percentage liquid measured in the surfactant and agarose phantoms plotted against the T <sub>2</sub> * measured from a spectroscopic FID. The markers differentiate the two distinct bubble sizes. ....	98
<b>Figure 5-8:</b> Relative signal amplitude over varying TE for foam samples with and without Gadodiamide. ....	98
<b>Figure 5-9:</b> T <sub>2</sub> * maps of: <b>a.</b> ~250 μm diameter bubble foam, and <b>b.</b> ~250 μm diameter bubble foam with 30 mM Gadodiamide. ....	99
<b>Figure 5-10:</b> <b>a.</b> A microscope image from a sample of PFP/O <sub>2</sub> bubbles in an egg white solution. The scale bar represents a length of 250 μm. <b>b.</b> An image of the bulk foam. <b>c.</b> A histogram depicting the spread of bubble sizes in the polydisperse bubble sample. ....	99

<b>Figure 5-11:</b> $T_2^*$ maps of the polydisperse foam containing Gadobutrol concentrations of 0 mM to 60 mM. ....	101
<b>Figure 5-12:</b> The effect of gadolinium based contrast agent concentration on the $T_2^*$ of PFP in polydisperse foam phantoms. The crosses represent measurements from foam containing Gadobutrol, with the error bars displaying the standard deviation of three samples made at each concentration. ....	101
<b>Figure 5-13:</b> $T_1$ and $T_2$ measurements for the polydisperse foam at a range of Gadobutrol concentrations. The error bars represent the SD from three samples. ....	102
<b>Figure 6-1:</b> Schematic of the hardware configuration for imaging inhaled PFP/ $O_2$ after Gadobutrol injections in a 7.0 T preclinical MR system. ....	114
<b>Figure 6-2:</b> Relative signal intensity over a range of echo times from <b>a.</b> inhaled PFP/ $O_2$ before injection of Gadobutrol, and <b>b.</b> inhaled PFP/ $O_2$ after injection of a total volume of 400 $\mu$ L of Gadobutrol. ....	119
<b>Figure 6-3:</b> Relative signal change over a range of injected Gadobutrol volumes in a representative mouse. ....	120
<b>Figure 6-4:</b> Average $T_2^*$ ( $\pm$ SD) after cumulative intravenous injections of 200 $\mu$ L volumes of 1.0 mmol/ml Gadobutrol for four mice. ....	120
<b>Figure 6-5:</b> Unlocalised spectroscopy data displayed as average $T_2^*$ , and signal amplitude. The arrow denotes the time-point at which Gadobutrol was injected, coinciding with the commencement of a 30 s breath hold. It is seen to transiently alter the $T_2^*$ of inhaled PFP shortly after. ....	121
<b>Figure 6-6:</b> Unlocalised spectroscopy data displayed as average $T_2^*$ and signal amplitude. This acquisition was performed without administration of intravenous Gadobutrol. ...	122
<b>Figure 6-7:</b> Relative signal change over the breath hold period. Peak signal is seen at 12-15s. ....	122
<b>Figure 6-8:</b> Relative signal amplitude across the 25 second breath hold. Gadobutrol is injected at $t = 0$ s. ....	123

## List of Tables

<b>Table 1.1:</b> NMR properties of $^1\text{H}$ and $^{19}\text{F}$ . The biological abundance is described as being the atomic percentage of one type of atom in the human body from Emsley (1998). All other values were taken from Bruno and Svoronos (2010).....	7
<b>Table 1.2:</b> MR properties of hyperpolarised $^3\text{He}$ and $^{129}\text{Xe}$ . a. (Kramer, 2011), all other values from Mugler et al., (2013).....	26
<b>Table 1.3:</b> MR properties of $^1\text{H}$ and $^{19}\text{F}$ . The high gyromagnetic ratio of $^{19}\text{F}$ produces good imaging sensitivity relative to that of $^1\text{H}$ (Ruiz-Cabello <i>et al.</i> , 2011). ....	28
<b>Table 1.4:</b> A summary of the chemical and MR properties of perfluorinated gasses used in previous lung MR studies. a: Exact $T_2$ values aren't described in the literature but are described as approximately equal to $T_1$ . No value for cyclo- $\text{C}_4\text{F}_8$ $T_2$ could be found in the literature. ....	29
<b>Table 2.1:</b> The acquisition parameters for a dynamic 3D spoiled gradient echo sequence. The field of view was designed to be larger than the sensitive volume of the coil. ....	38
<b>Table 2.2:</b> The acquisition parameters for dynamic measurement of average $T_2^*$ in vivo.....	40
<b>Table 3.1:</b> The resonant frequency achieved on the lab bench when driven via each of the 16 port locations. Here, 109 MHz equates to achieving the $^{19}\text{F}$ resonant frequency (120.24 MHz) in the magnet bore. ....	53
<b>Table 3.2:</b> Acquisition parameters used to measure SNR in breath hold length scan times. Values were chosen to be as similar as feasible whilst selecting close to the optimal achievable parameter values for each hardware set-up.....	55
<b>Table 3.3:</b> Acquisition parameters used to test relative signal homogeneity within the coil volume.....	56
<b>Table 3.4:</b> The power efficiency measured in four coils with zero loading and heavy loading. The maximum achievable $B_1$ with low loading and human loading is also displayed....	58
<b>Table 3.5:</b> SNR measured in the four coil designs using similar acquisition parameters, all achieved in a 10-15 s acquisition time. ....	59
<b>Table 3.6:</b> Percentage signal drop-off measured along each dimension. The surface coil has	

notably poor signal homogeneity. The 50 cm quadrature birdcage coil offers the most homogeneous coverage along the length of the lungs. ....	61
<b>Table 4.1:</b> Parameters used to test the optimum bandwidth and flip angle. Minimum TE and TR were used in all acquisitions. ....	72
<b>Table 4.2:</b> Acquisition parameters for a 3D spoiled gradient echo sequence to assess the relative image quality in scans with compressed sensing applied. ....	73
<b>Table 5.1:</b> $D_0$ , apparent diffusion coefficient and $T_2^*$ in the healthy human lung. Each has been measured at dilutions typically used in vivo. ....	90
<b>Table 5.2:</b> The acquisition parameters for measurement of the average $T_2^*$ in the foam phantoms. ....	93
<b>Table 5.3:</b> The acquisition parameters for an echo time array of a 3D spoiled gradient echo sequence, allowing mapping of $T_2^*$ in the sample. ....	93
<b>Table 5.4:</b> The acquisition parameters for an inversion recovery sequence with an inversion time array, allowing measurement of average $T_1$ in each of the foam samples. ....	94
<b>Table 5.5:</b> The acquisition parameters for a spin echo sequence, allowing measurement of the average $T_2$ in the foam samples. ....	94
<b>Table 5.6:</b> Average ( $\pm$ SD) relaxation properties of the foam samples with two bubble diameters. ....	97
<b>Table 5.7:</b> Average ( $\pm$ SD) relaxation properties for the polydisperse foam. ....	100
<b>Table 5.8:</b> Magnetic susceptibility of the polydisperse foam components. ....	100
<b>Table 6.1:</b> Acquisition parameters for a 2D spoiled gradient echo sequence with an TE array. This acquisition protocol was repeated after intravenous administration of five cumulative 0.2 mmol doses of Gadobutrol. ....	115
<b>Table 6.2:</b> Acquisition parameters for a dynamic unlocalised FID sequence. The Gadobutrol bolus was injected 20 s into the acquisition. ....	117
<b>Table 6.3:</b> Acquisition parameters for a 2D spoiled gradient echo sequence to dynamically detect PFP - $CF_3$ signal. ....	118

## List of Abbreviations

ADC	Apparent diffusion coefficient
BW	Bandwidth
COPD	Chronic obstructive pulmonary disease
CT	Computed tomography
$D_0$	Free diffusion coefficient
DCE-MRI	Dynamic contrast enhanced MRI
DSC-MRI	Dynamic susceptibility weighted MRI
FEV <sub>1</sub>	Forced expiratory volume in one second
FOV	Field of view
FVC	Forced vital capacity
GBCA	Gadolinium based contrast agent
HP	Hyperpolarised
NMR	Nuclear magnetic resonance
PCB	Printed circuit board
PEG-40s	Polyethyleneglycol-40 stearate
PET	Positron emission tomography
PFP	Perfluoropropane
pO <sub>2</sub>	Oxygen partial pressure
RF	Radio frequency
RV	Residual volume
SNR	Signal to noise ratio
SPECT	Single photon emission computed tomography
SPGR	Spoiled gradient echo
T/R	Transmit/receive
T <sub>1</sub>	Longitudinal relaxation time
T <sub>2</sub>	Transverse relaxation time
T <sub>2</sub> <sup>*</sup>	Reduced transverse relaxation time
TE	Echo time
TLC	Total lung capacity
TR	Repetition time
TV	Tidal volume
UTE	Ultrashort echo time
V/Q	Ventilation/perfusion ratio
VC	Vital capacity



# **Chapter 1:**

## **MRI of Pulmonary Ventilation: Theoretical Background and Literature Review**

### **1.1 Respiratory physiology and pathophysiology**

Clinical understanding of obstructive lung disease has been refined in parallel with our knowledge of lung function. Despite this, it has a steadily increasing incidence of morbidity and mortality globally, with early identification a principle step to improved treatment outcome (Vestbo *et al.*, 2013; Vogelmeier *et al.*, 2017). This section presents a very brief overview of pulmonary physiology and the impact of obstructive lung disease upon ventilation to guide direction in the development of a <sup>19</sup>F-MRI based modality for imaging pulmonary ventilation. The following background, unless referenced otherwise, is based upon the reference texts Respiratory Physiology (West, 2012) and Pulmonary Pathophysiology (West, 2008).

#### **1.1.1 Pulmonary anatomy**

There are a total of typically 23 bifurcations along the respiratory tract beginning at the trachea, with a gradual narrowing and shortening at each generation. The terminal bronchioles at generation 16 mark the end of the conducting region of the lungs. These divide into the respiratory bronchioles, and finally pulmonary acini, made up of alveolar ducts, and alveolar sacs, which together form the respiratory zone. The dichotomous nature of these bifurcations over many generations produce good ventilation homogeneity over the full lung volume in healthy individuals, with the structure generating 480 million alveoli in an average adult human lung (Ochs *et al.*, 2004). This creates a large lung surface area to gas volume ratio, resulting in an efficient interchange boundary for gases.

#### **1.1.2 Respiratory mechanics**

Ventilation is the exchange of air between the lung and the atmosphere, and is the process by which oxygenated air is transported into the lungs for gas exchange (perfusion) between the alveoli and capillaries. In this process, carbon dioxide along with deoxygenated air is removed from the lungs. During relaxed inhalation, the diaphragm contracts, and the external intercostal muscles widen and lift the ribcage. These actions increase the volume of the

thoracic cavity. The process of ventilation then occurs by the decreased pressure formed in the thoracic cavity causing the lungs to expand. Exhalation at rest is a passive process, whereby the diaphragm and external intercostal muscles relax. This increases the relative pressure of the thoracic cavity to larger than that of the external environment, forcing the lungs to compress, and air to be exhaled.

Forced breathing utilises additional accessory muscles in the torso. By engaging more muscles, deeper inhalations can be achieved. Active exhalations can also be performed by forcing the thoracic cavity to decrease further in volume than what can be achieved passively.

### 1.1.3 Pulmonary volumes

There are several key terms used to quantify pulmonary volumes at specific points in both tidal breathing and forced breathing respiratory cycles (Lutfi, 2017). These are summarised in Figure 1-1.

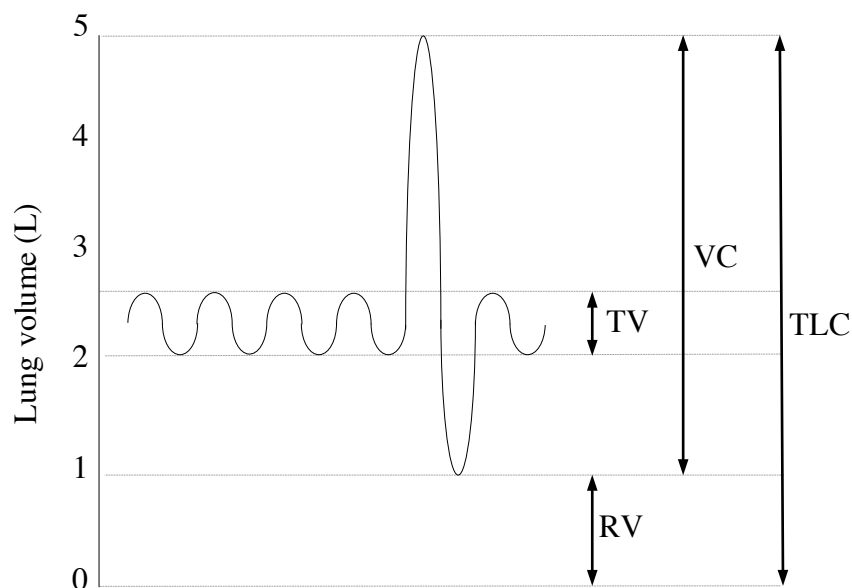


**Figure 1-1:** Typical lung volumes and capacities for a healthy subject depicted on a spirometric trace. Only a small fraction of the total lung volume is exchanged in tidal breathing. Deep respiratory manoeuvres that engage the accessory muscles of the respiratory system are required to exchange a volume of air close the vital capacity.

The tidal volume (TV) is the volume of air displaced during relaxed ventilation. In a healthy adult, this volume is typically approximately 500 ml. The vital capacity (VC) is the volume of air displaced during forced breathing between maximum inhalation and maximum exhalation. In healthy adults, this volume is typically around 3 – 5 L, varying with gender (Thurlbeck,

1982) and height (Bhatti *et al.*, 2014). After maximal exhalation, the volume of gas remaining in the lungs is known as the residual volume (RV), approximately 1 L in healthy adults. The total volume of air in the lungs is known as the total lung capacity (TLC), and ranges from 4 – 6 L in healthy adults.

Spirometric tests are regularly used to assess pulmonary volumes in the clinical environment; in this case lung function is often described by FEV<sub>1</sub>, defined as the volume exhaled in the first one second of forced expiration after maximal inhalation, and FVC the total volume exhaled following maximal inhalation.

#### ***1.1.4 Ventilation homogeneity in healthy subjects***

Studies as early as the 1960s have shown that ventilation in the healthy human lung is not entirely homogeneous and is greater in the dependent (lowermost) part of the lung (Bryan *et al.*, 1964). This natural level of ventilation heterogeneity is primarily due to the mechanics of the lung under the effect of gravity; the gravitational force causes an intrapleural pressure gradient between the apex and base of the lungs (Milic-Emili *et al.*, 1966). This intrapleural pressure gradient results in higher relative ventilation at the lung base. In the upright position, there is a ventilation inhomogeneity between the apex and base of the lungs of 1:1.6 (Bryan *et al.*, 1964). There also remains a detectable ventilation gradient in the supine position both in the cranial to caudal direction as well as from superior to inferior (Amis *et al.*, 1984; Orphanidou *et al.*, 1986; Musch *et al.*, 2002). Pulmonary ventilation is also known to be age dependent (Holland *et al.*, 1968), as well as dependent upon the speed and volume of gas inspired (Frerichs *et al.*, 2001). This demonstrates that there is a small but measureable and variable level of ventilation inhomogeneity in healthy subjects. As MR studies are almost always restricted to only measuring the ventilation in the supine or prone positions, it is salient to recognise that the ventilation homogeneity measured differs from that of an upright subject breathing spontaneously.

#### ***1.1.5 Respiratory pathophysiology***

Lung disease can be broadly classified as either restrictive or obstructive, representing the mechanism by which the efficiency of ventilation is reduced. Restrictive lung disease limits expansion of the lung. This could be caused by weakened musculature, or a build-up of fibrotic tissue in the lung parenchyma. Obstructive lung disease is characterised by increased regional airway resistance, resulting in significantly increased ventilation heterogeneity compared to that found in healthy lungs (Galvin *et al.*, 2007). Obstructive lung disease,

specifically asthma and chronic obstructive pulmonary disease (COPD) is the primary focus of the work presented here.

Asthma is characterised by a reversible obstruction of the bronchial airways caused by increased responsiveness to external allergenic stimuli. Bronchoconstriction and inflammation occurs, along with production of excess mucus, all of which results in an increase in airway resistance, causing dyspnoea (Kudo *et al.*, 2013). This can lead to increased ventilation heterogeneity, caused by unmatched airflow resistance along equivalent branches after each bifurcation. During acute asthmatic episodes, the lungs are typically hyperinflated, and the accessory muscles are utilised. Expiratory flow rates (FEV<sub>1</sub>, FVC) are reduced, whereas static volumes (TLC, RV) are increased. Less pronounced but measurable changes in flow rates and volumes are seen between exacerbations. Asthma is associated with considerable morbidity; the lifetime prevalence of clinically diagnosed asthma in the UK is 15.6%, with 93,000 people receiving of in-patient treatment annually (Mukherjee *et al.*, 2016).

The pathophysiology of COPD is complex and can vary considerably between patients, with early disease often being asymptomatic. Key characteristics include permanent destructive enlargement of the lung parenchyma (known as emphysema), and narrowing of the airways due to inflammation and scarring. These factors combined can result in reduced compliance caused by the loss of elastic recoil of the alveolar walls. Dynamic compression, often resulting in air trapping behind the collapsed airway, and therefore difficulty fully exhaling is also commonly seen. Trapped air in emphysematous areas produces spatially localised ventilation inhomogeneities (Celli *et al.*, 2004). In COPD patients, similarly to asthmatic patients, reduced flow rates and increased lung volumes are seen, causing an increased expiratory time. However, in COPD this is minimally reversed after treatment. COPD is the second most common lung disease in the UK, affecting 2% of the UK population, and accounting for 140,000 hospital admissions annually. It is also associated with high mortality rates, accounting for 5% of all deaths annually in the UK in recent years (Snell *et al.*, 2016).

Figure 1-2 illustrates the typical change in pulmonary volumes that is seen in obstructive lung disease patients relative to healthy subjects.

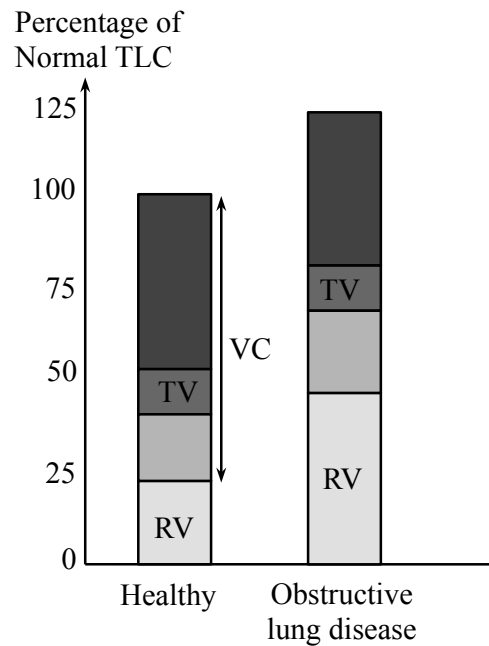


**Figure 1-2:** Relative lung volumes in healthy subjects and patients with obstructive lung disease. Notably, an increase in total lung capacity (TLC) and residual volume (RV) is present. Tidal volume (TV), and vital capacity (VC) remain approximately constant.

Airway resistance is often present in both COPD and asthma. The change in airway resistance with radius can be approximated by the Hagen-Poiseuille equation, which expresses that airway resistance is proportional to the reciprocal of the radius to the power of four (Ogrady *et al.*, 1997). Consequently, it only takes a small change in radius to greatly affect the resistance of the airways. Although the individual small bronchioles have the highest resistance, the large quantity of them offsets their increased resistance. This is true even for peripheral airways in COPD patients where their resistance can double. In the human lung, it is the bronchi in the 4<sup>th</sup> to 8<sup>th</sup> generations that impart the highest resistance on inhaled air (Irvin, 2011).

Spatial disparity in ventilation due to increased airway resistance, enlarged alveoli, and areas of air trapping are therefore key characteristics associated with obstructive lung disease. Detection of each of these pathological features is considered in the development of the pulmonary imaging modality detailed in the following chapters.

## 1.2 Magnetic resonance theory

Nuclear spin angular momentum is a fundamental property of atomic nuclei that was first postulated by Wolfgang Pauli in the early 1920s (Pauli, 1924). In 1946, Felix Bloch and Edward Mills Purcell simultaneously published their independent discoveries of nuclear magnetic resonance (NMR) (Bloch *et al.*, 1946; Purcell *et al.*, 1946) – a process that uses an external magnetic field to detect and quantify nuclear spin angular momentum. They were jointly awarded the 1952 Nobel Prize in Physics for their discovery.

Herman Carr is credited for introducing the use of magnetic field gradients, and from this producing the first one-dimensional NMR spectra, described in this PhD thesis in 1952 and published shortly after (Carr and Purcell, 1954). This formed the foundation for developing NMR into an imaging technique, MRI, thus allowing the first 2D and 3D images to be acquired by Lauterbur and Mansfield (Lauterbur, 1973; Mansfield and Grannell, 1975). The first in vivo human image was published in 1977 (Damadian *et al.*, 1977), and the first diagnostic image was published shortly after in Aberdeen (Smith *et al.*, 1981). It was in this same period that fluorine-19 ( $^{19}\text{F}$ ) MRI was first proposed (Holland *et al.*, 1977), and the first application of  $^{19}\text{F}$  MRI to lung imaging was reported in the following decade (Rinck *et al.*, 1984).

The following section outlines the basic theoretical foundation of nuclear magnetic resonance spectroscopy and imaging. Further explanation of select MR concepts relevant to the methodological developments that follow in this thesis are also given.

### 1.2.1 Nuclear spin angular momentum and polarisation

All nuclei have a fundamental intrinsic nuclear property, like mass and charge, called nuclear angular momentum, or spin. Spin,  $\mathbf{I}$ , is characterised by its angular momentum quantum number,  $I$ , which can take a fixed half-integer or integer value, dependent on the pairing of protons and neutrons (nucleons) in the nucleus.  $\mathbf{I}$  is also characterised by its spin angular momentum projection quantum number,  $m$ , which describes the direction of the spin along an arbitrary axis, known as a spin state.  $m$  can take the values:

$$m = -I, -I + 1, -I + 2, \dots, I \quad 1.1$$

Each nucleus therefore has  $2I + 1$  allowed spin states.

All nuclei with non-zero nuclear spins (ie. one unpaired nucleon) exhibit NMR. They are analogous to charged particles moving in a perpetual loop, which generates an associated magnetic dipole moment,  $\mu$ . The magnetic dipole moment produced is related to nuclear spin by the gyromagnetic ratio,  $\gamma$ , a constant specific to each nucleus type, such that:

$$\mu = \gamma I \quad 1.2$$

The bulk magnetisation,  $\mathbf{M}$ , is the sum of all the individual magnetic moments in the material of interest. Normally,  $\mathbf{M}$  is zero because the magnetic moments are randomly orientated. However, application of an external static magnetic field,  $\mathbf{B}_0$ , imparts a torque on each of the magnetic moments, causing them to align with the field. This produces a non-zero net magnetisation. This principle forms the basis of NMR.

The majority of NMR techniques applied in vivo utilise  $^1\text{H}$  nuclei as the signal source, due to their large natural abundance within water and fat molecules.  $^{19}\text{F}$  is one of many other MR-sensitive nuclei, and analogously to  $^1\text{H}$ , has  $I = \frac{1}{2}$ . A comparison of the magnetic properties of  $^1\text{H}$  and  $^{19}\text{F}$  is shown in Table 1.1.

Nucleus	Number of unpaired protons	Number of unpaired neutrons	Natural abundance (%)	Biological abundance (%)	Gyro-magnetic ratio, $\gamma$ (MHz/T)	Spin quantum number, $I$
$^1_1\text{H}$	1	0	99.99	63	42.58	$\frac{1}{2}$
$^{19}_9\text{F}$	1	0	100	0	40.05	$\frac{1}{2}$

**Table 1.1:** NMR properties of  $^1\text{H}$  and  $^{19}\text{F}$ . The biological abundance is described as being the atomic percentage of one type of atom in the human body from Emsley (1998). All other values were taken from Bruno and Svoronos (2010).

Therefore, for  $I = \frac{1}{2}$ , in the case of both  $^1\text{H}$  and  $^{19}\text{F}$ , there are two spin states:  $m = \pm \frac{1}{2}$ , in accordance with Equation 1.1. These are degenerate until an external magnetic field is applied, in which case Zeeman splitting occurs and the two spin states can be measured (Brown *et al.*, 2014). The nuclear spins orientate either parallel or anti-parallel to the magnitude of the magnetic field in the nominal z-direction,  $B_0$ . The energy difference between the parallel ground state and the anti-parallel excited state is given by (Brown *et al.*, 2014):

$$\Delta E = \gamma B_0 \hbar \quad 1.3$$

Where  $\hbar$  is the reduced Planck constant,  $\hbar = \frac{h}{2\pi} = 1.05 \times 10^{-34}$  J s.

The parallel position is favoured due to it being a lower energy state. The proportion of nuclei in the parallel,  $N_p$ , to the antiparallel state,  $N_{ap}$ , is determined by the Boltzmann distribution (McDowell, 1999):

$$\frac{N_{ap}}{N_p} = e^{-\Delta E/kT} \quad 1.4$$

Where  $k$  is the Boltzmann constant,  $k = 1.38 \times 10^{-23}$  kg s<sup>-2</sup> K<sup>-1</sup>, and  $T$  is the absolute temperature (body temperature is approximately 310 K). It can therefore be seen that the ratio of nuclei in each state increases with magnetic field and gyromagnetic ratio, and decreases with temperature.

For <sup>19</sup>F ( $\omega_0 = 120.15$  MHz at  $B_0 = 3.0$  T), at body temperature,  $\frac{N_{ap}}{N_p} = 0.999997$ . That is, for 1,000,000 nuclei in the higher energy anti-parallel position, there is expected to be 1,000,003 nuclei in the lower energy parallel position. This  $\sim 10^{-6}$  excess of nuclei in the parallel position is the source of the net magnetisation,  $\mathbf{M}$ , pointing in the direction of the external  $B_0$  field. This excess is detected by NMR.

This small polarisation necessitates a high spin density, which for protons in tissues is of the order of  $10^{22}$  cm<sup>-3</sup> (Kauczor *et al.*, 1998). In contrast, the biological abundance of <sup>19</sup>F is effectively zero. Where the physiological concentration of <sup>19</sup>F is above the detection limit ( $\sim 10^{-3}$   $\mu$ mol g<sup>-1</sup> wet tissue weight) such as in the teeth and bone matrix, it is immobilised, and therefore undetectable (Ruiz-Cabello *et al.*, 2011). Therefore, any <sup>19</sup>F signal must come from an imaging agent administered to the subject. This has the useful effect of avoiding endogenous background signal.

Substitution of the Bohr condition, Equation 1.5, where  $\nu$  is frequency in hertz, into Equation 1.3 yields the angular Larmor frequency,  $\omega_0$  (rad s<sup>-1</sup>), of the nucleus:

$$\Delta E = h\nu = \hbar\omega_0 \quad 1.5$$

$$\omega_0 = \gamma B_0$$

1.6

The nuclear magnetic moments therefore precess around  $B_0$  at frequency  $\omega_0$ , rather than aligning exactly with  $B_0$ , illustrated in Figure 1-3.

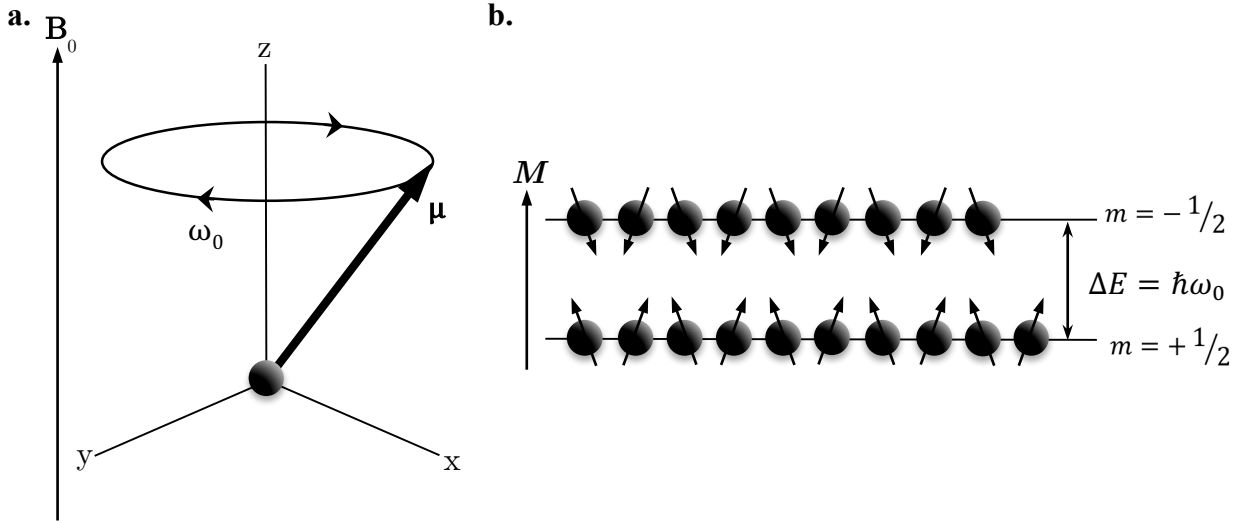


**Figure 1-3:** **a.** Illustration of the precession of the spin magnetic moment,  $\mu$ , around an external static magnetic field,  $B_0$ , pointing along the z-axis.  $\mu$  precesses around  $B_0$  at the Larmor frequency,  $\omega_0$ . **b.** The net magnetisation,  $M$ , from many nuclei experiencing the same external  $B_0$  field is along the positive z-axis, as the spins precess out of phase, and a small excess (not to scale) inhabit the lower energy parallel spin state.

### 1.2.2 Nuclear excitation

It is possible for nuclei to transition between the two spin states by absorbing an amount of energy that is equal to the  $\Delta E$  between the two states. The energy required falls in the radio frequency (RF) range. The geometry of RF pulse producing hardware is designed such that when an RF pulse at the Larmor frequency of the nucleus is applied, a small magnetic field,  $B_1$ , is generated perpendicular to the static  $B_0$  field. The torque produced ( $M \times B_1$ ) tips the magnetisation vector towards the transverse plane by a flip angle,  $\theta$ , described by (Bloch, 1946):

$$\theta = \int_0^t \gamma B_1(t) dt \quad 1.7$$

The angle subtended is therefore proportional to the length of the RF pulse. There is an equal

probability of any nucleus switching between the two energy states, however as there are more nuclei in the lower energy state, the transition to the higher energy state is most likely until there are equal populations in each (saturation). On a macroscopic level, the RF pulse will cause the net magnetisation to tip towards the x-y plane, so a 90° flip angle is representative of saturation occurring on the nuclear level.

### 1.2.3 Nuclear relaxation and the Bloch equations

Immediately following a RF pulse, several relaxation processes occur that are dependent on the material being imaged and its environment which cause the nuclear signal to decay. Felix Bloch (1946) developed phenomenological equations that formally describe this macroscopic nuclear magnetisation, and the relaxation mechanisms that follow.

#### *Longitudinal relaxation*

Nuclei return to their equilibrium state along the z-axis by stimulated emission, and the energy that was absorbed from the RF pulse is transferred from the nuclei to the surrounding lattice as heat. This process, also known as spin-lattice relaxation, is defined by the empirical Bloch equation:

$$\frac{dM_z(t)}{dt} = \gamma(\mathbf{M}(t) \times \mathbf{B}(t))_z + \frac{1}{T_1}(M_0 - M_z(t)) \quad 1.8$$

Where the cross product describes the initial flip without any relaxation, seen in Equation 1.7.  $T_1$  is the time required for the system to reach 63% of the equilibrium value, and is known as the longitudinal relaxation time (Nitz and Reimer, 1999).  $M_z(t)$  is the proportion of the equilibrium value,  $M_0$ , remaining after time,  $t$ .

By integration, the amount of net nuclear magnetisation lost over the time of the relaxation process after saturation can therefore be written as the exponential:

$$M_z(t) = M_0 + (M_z(0) - M_0)e^{-t/T_1} \quad 1.9$$

$T_1$  is dependent on the external magnetic field strength and the rotation speed of the molecule (Bloembergen *et al.*, 1948).

### ***Transverse relaxation***

There is a loss of phase coherence in the x-y plane after excitation. This is known as transverse, or  $T_2$  relaxation. Transverse relaxation is caused by the nuclei experiencing a slightly different magnetic field to  $B_0$  due to interference from magnetic moments of neighbouring nuclei (Nitz and Reimer, 1999). As the nuclei come into contact with many other magnetic moments, their precessional frequencies vary, and their transverse magnetisations dephase from each other. The Bloch equations that describe this are:

$$\frac{dM_x(t)}{dt} = \gamma(\mathbf{M}(t) \times \mathbf{B}(t))_x - \frac{M_x(t)}{T_2} \quad 1.10$$

$$\frac{dM_y(t)}{dt} = \gamma(\mathbf{M}(t) \times \mathbf{B}(t))_y - \frac{M_y(t)}{T_2} \quad 1.11$$

Where  $T_2$  is the time after which net the magnetisation,  $M_{x,y}$ , decays to 37% of its original value. Again, by analysis this occurs according to:

$$M_{x,y}(t) = M_{x,y}(0) e^{-t/T_2} \quad 1.12$$

This process produces an exponential decay of the magnitude of coherent transverse magnetisation. Unlike  $T_1$  relaxation, no energy is lost during this process, but energy is transferred between nuclei. It is therefore referred to as spin-spin relaxation.

The three Bloch equations can be combined to present the total evolution of magnetisation in a system interacting with an external magnetic field:

$$\frac{d\mathbf{M}(t)}{dt} = \gamma(\mathbf{M}(t) \times \mathbf{B}(t)) - \frac{M_x(t)}{T_2} \hat{\mathbf{x}} - \frac{M_y(t)}{T_2} \hat{\mathbf{y}} - \frac{M_z(t)}{T_1} \hat{\mathbf{z}} \quad 1.13$$

Where  $\hat{\mathbf{x}}$ ,  $\hat{\mathbf{y}}$  and  $\hat{\mathbf{z}}$  are the unit vectors in the x, y, and z directions respectively.

In practice, the transverse relaxation time is further shortened by regional magnetic field inhomogeneities. This can be caused by an imperfectly shimmed  $B_0$  field, or inhomogeneities in the local environment caused by differences in magnetic susceptibility at the boundaries of two tissues. This therefore changes the resonant frequency of the nuclei, which is dependent on the strength of the magnetic field they experience. An extreme case of this is seen in the

human lung where many air-tissue boundaries are present. This reduces the  $T_2$  to  $T_2^*$ , described by (Chavhan *et al.*, 2009):

$$\frac{1}{T_2^*} = \frac{1}{T_2} + \frac{1}{T_2'} \quad 1.14$$

$$T_2' = \frac{1}{\Delta B_0 \cdot \gamma} \quad 1.15$$

Where  $\Delta B_0$  is the change in magnetic field experienced by the nuclei from the original  $B_0$ .

#### 1.2.4 Free induction decay

As previously discussed, a single RF pulse at the Larmor frequency of the subject nuclei that produced a  $B_1$  field perpendicular to  $B_0$  will produce a magnetisation whose subsequent decay can be measured (Hahn, 1953). This is a free induction decay (FID), and is illustrated in Figure 1-4.

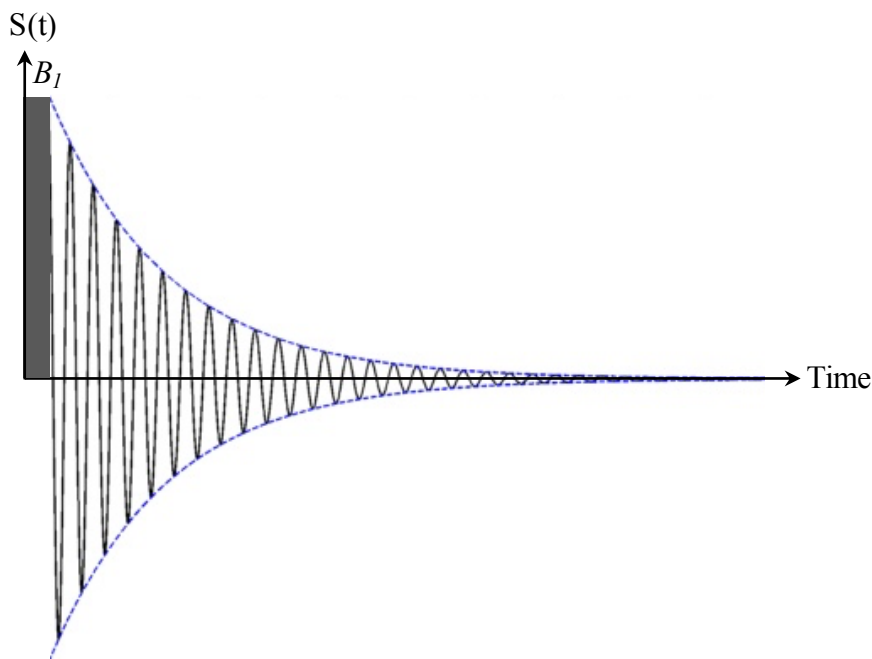


**Figure 1-4:** Free induction decay after a RF pulse. The envelope of the FID (marked in blue) describes the  $T_2^*$  signal decay of the subject nuclei.

The envelope of the FID measures the rate of  $T_2^*$  relaxation as the total signal in the sample decays over time, regardless of its spatial location in the magnetic field.

### 1.2.5 NMR to MRI: image formation in k-space

Moving from a 1-dimensional signal peak observed in a simple FID to a spatially localised image is achieved by recording the signal amplitude, the phase and the frequency of the spins, and their variation as magnetic field gradients are applied across the sample. This information is mapped as complex values in the spatial-frequency domain, known as k-space, with each dimension ( $k_x$ ,  $k_y$ ,  $k_z$ ) being defined by the frequency encoding gradient, phase encoding gradient, or slice selection gradient. It is converted into the Cartesian ( $x$ ,  $y$ ,  $z$ ) image by Fourier transformation. K-space maps the spatial frequency distribution of each 2D image slice. Multiple k-spaces form a 3D image, with the low frequencies (at the centre of k-space) representing the coarse signal to noise distribution of the image, and the high frequencies representing the fine detail and resolution (Lai and Lauterbur, 1981; Hinshaw and H, 1983; Brown *et al.*, 2014). The principles of this technique, which allows signal localisation using phase, frequency, and slice encoding gradients is discussed below.

#### **Frequency encoding**

There are three sets of gradient coils in the MR system:  $G_x$ ,  $G_y$ , and  $G_z$ . These serve to linearly alter the  $B_0$  field strength along their respective dimensions. Within a 2D slice, altering the  $B_0$  field in the nominal x-direction by several  $\text{mT m}^{-1}$  around the magnet isocentre will change the Larmor frequency of the spins precession dependent on where along this dimension the nucleus is in. This is described by Equation 1.16, which is simply modified from Equation 1.6.

$$\omega_x = \gamma(B_0 + x \cdot G_x) \quad 1.16$$

Presence of this gradient during signal acquisition causes precession at a range of frequencies dependent upon the sample position in the gradient (Bernstein *et al.*, 2004). A dephasing gradient is applied immediately before to counteract any spin dephasing it causes, a Fourier transform presents a plot of signal amplitude against position. This gradient allows the signal to be localised to single column within a slice.

#### **Phase encoding**

The phase encoding gradient is applied perpendicularly to the frequency encoding gradient in order to change the phase of spins within a column. When the gradient is switched off, the spins return to precessing at the same speed, but remain phase shifted from each other. This

can be measured by the net signal seen as the magnitude of the phase shift caused by this gradient is determined by position along the gradient. By arraying many phase shift values, the difference in signal produced from each phase encoding step is used to accurately define which voxel in a column the signal originated from (Felmlee *et al.*, 1989).

### ***Slice selection***

The method of slice selection is dependent upon the imaging protocol used. For 3D acquisitions, phase encoding is applied in two orthogonal directions, allowing spatial encoding in the third direction. In a 2D acquisition, slice selection works analogously to the frequency encoding gradient, by simply applying the gradient along the z-direction during the RF pulse. The RF pulse therefore excites a single slab of the sample. In this case, the thickness of the slab is dependent on the transmit bandwidth of the RF pulse used, and the applied gradient strength:

$$\text{slab width} = \frac{2\pi BW}{\gamma G_z} \quad 1.17$$

#### ***1.2.6 The spoiled gradient echo pulse sequence***

The process of filling k-space varies upon the pulse sequence used, as it is variations in the way in which phase and frequency encoding gradients are activated that defines the filling order. A widely used imaging technique is the spoiled gradient echo (SPGR) pulse sequence. The SPGR sequence samples k-space linearly, the most common sampling form. A schematic of the 3D SPGR sequence is shown in Figure 1-5 (Haase *et al.*, 1986; Elster, 1993).

A spatially non-selective RF pulse is applied, producing a defined flip angle (typically between 0° - 90°). The phase encoding gradients are then applied immediately after the pulse. Simultaneously, a dephasing frequency encoding gradient equal to half the length of the sampling period is applied. This has the effect of causing the spins to be in phase at the centre of the acquisition period. The direction of the frequency encoding gradient is then switched, and an echo is produced as it rephases the previously dephased spins. It is during this period that the signal is sampled, with the spatial resolution determined by the number of points collected and the amplitude of the frequency encoding gradient. Gradient spoiling may then be applied at the end of the sequence to dephase any magnetisation before the next repetition. A more effective form of spoiling which is more commonly used however is RF spoiling, where the phase of each successive RF excitation pulse is incremented by a specific angle

such that coherence of transverse magnetisation is destroyed.

Also shown in Figure 1-5 are the echo time (TE, the time between the centre point of the RF pulse to the centre of the data acquisition) and the repetition time (TR, defined as the time of a single repetition, measured from the centre of the first RF pulse, to the centre of the next).

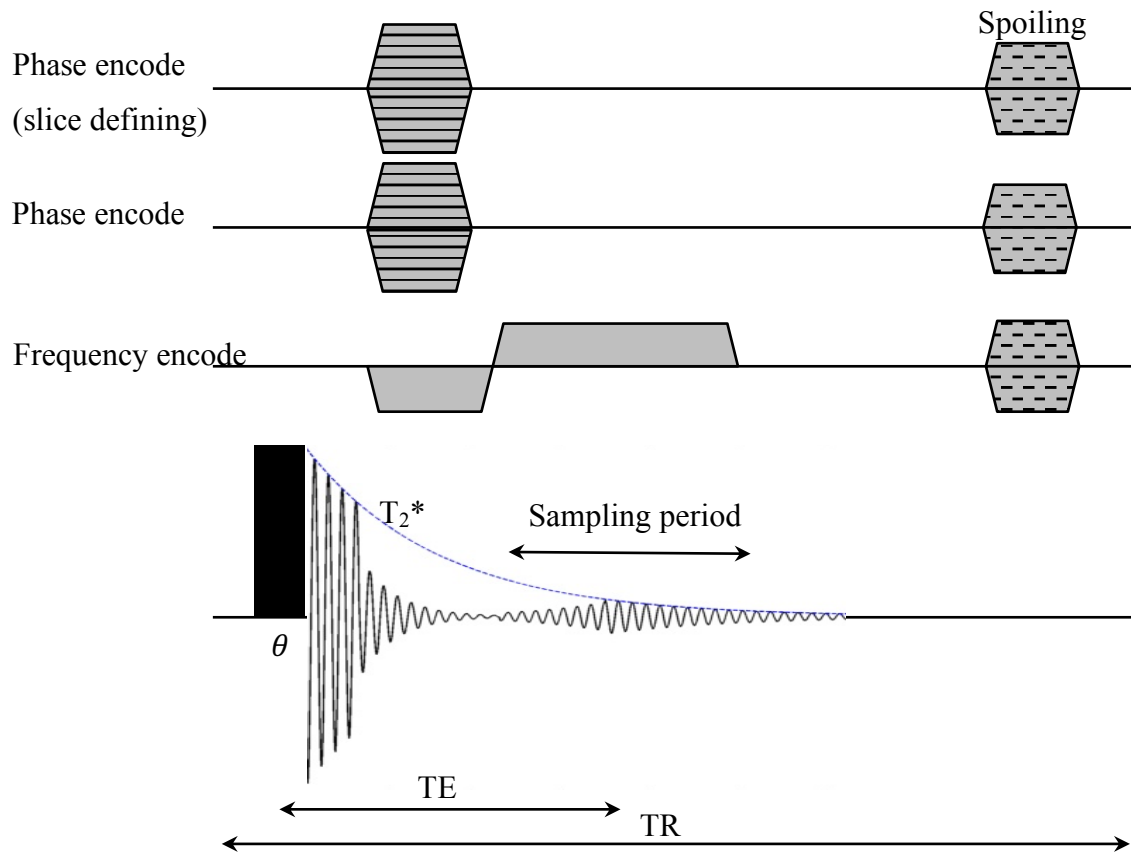


**Figure 1-5:** A 3D spoiled gradient echo pulse sequence. The slice selection, phase encoding, and frequency encoding gradients are used to encode spatial information into the MR signal. The echo time (TE) is labelled. This figure depicts a single repetition time (TR), and the process must be repeated for multiple phase encode steps and signal averages.

Figure 1-5 represents a single phase encode step, and the sequence fills k-space linearly, filling one line per excitation. Therefore, to produce a two-dimensional  $N \times N$  matrix,  $N$  phase encoding steps,  $N_p$ , are required, each with a different phase encoding gradient, and this will have to be repeated for the number of slices,  $N_{slices}$ , and the number of signal averages,  $NSA$ , required. The time for a 3D gradient echo scan,  $t_{3D-GRE}$ , is therefore defined by (Bernstein *et al.*, 2004):

$$t_{3D-GRE} = TR \cdot N_p \cdot NSA \cdot N_{slices} \quad 1.18$$

### 1.2.7 RF pulse shapes

A wide variety of RF pulse shapes are used to aid spatial localisation, as well as excitation. The choice of the pulse shape depends on the aims of the acquisition. Two common pulse shapes used in this work, the sinc pulse and the rectangular pulse, are discussed below (Dale *et al.*, 2015; Brown, 2016).

#### The sinc pulse

The sinc pulse, defined as  $\sin(x)/x$ , and depicted in Figure 1-6a, is a widely used RF pulse shape due to it allowing accurate slice selective excitation for 2D acquisitions. This is due to its Fourier transform (the shape of the sample excited) having a sharp rectangular profile. The profile of a Fourier transform is representative of the frequency profile that is excited, thus, if the slice-selection gradient makes a slice a specific range of frequencies, a sinc RF pulse can be applied to excite that very same range of frequencies.

Practically, a perfect rectangular profile is unachievable, due to the sinc function (which would have infinite duration) having to be heavily truncated to the first few pairs of lobes. This has a detrimental effect on the slice profile, as depicted in Figure 1-6b. The slice profile is often improved by Gaussian modulation of the sinc pulse envelope, giving greater weighting to the central lobes.

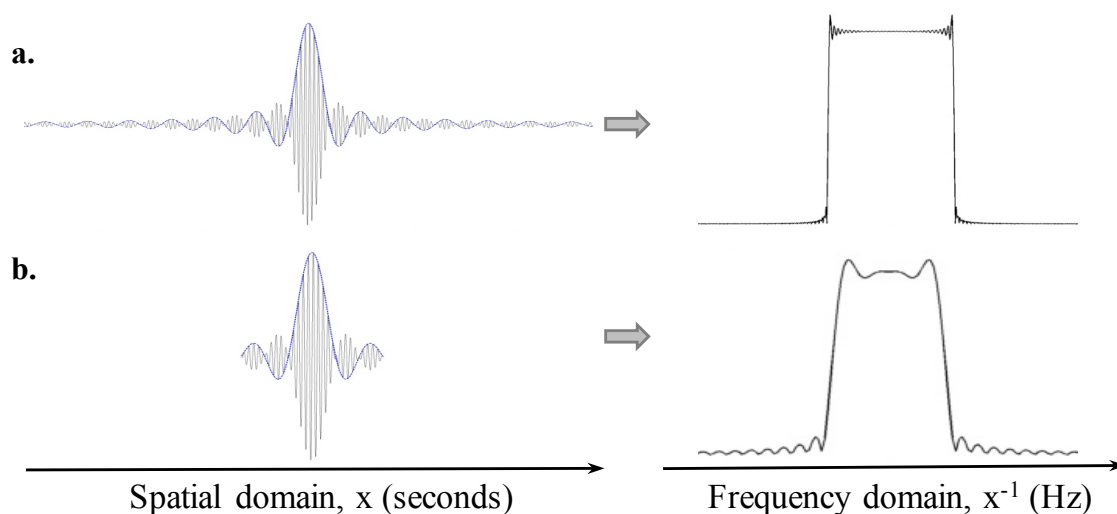


**Figure 1-6:** **a.** A sinc pulse, and its corresponding sharp slice profile. Ringing is present due to it not being an infinite example. **b.** A heavily truncated sinc pulse, and its corresponding imperfect slice profile with notable ringing.

A heavily truncated sinc pulse still suffers from being a relatively long duration to achieve a specified  $B_1$  pulse, necessitating a long TE.

### ***The rectangular pulse***

The rectangular RF pulse is known as a hard pulse, as its shape is not variant with time. It requires a much shorter time to impart the same flip angle, thus a broad bandwidth to excite spins with a wider range of frequencies than a sinc pulse as its Fourier transform is a sinc curve. This non-selective excitation therefore does not offer the ability to excite a sharp slice profile like the sinc pulse, but it is well suited for 3D imaging, where whole-volume excitation is acceptable and phase encoding is used to encode spatial information in two dimensions. The flip angle produced with a hard pulse is the simplest form of Equation 1.7:  $\theta = \gamma B_1 t$ , where  $t$  is the pulse length.

### ***1.2.8 Producing a radio frequency pulse: basic RF coil theory***

Radio frequency coils are named due to them resonating in the RF electromagnetic frequency range, typically tens to hundreds of MHz at 3.0 T. They serve two purposes; the first is to flip the net magnetisation by generating an oscillating magnetic field ( $B_1$ ) at the Larmor frequency of the target nuclei, the second is to receive the signal subsequently emitted as the nuclei decay to the lower energy alignment with the  $B_0$  field. This ‘transmit’ and ‘receive’ functionality can be carried out by individual coils, named respectively, or a single coil, referred to as a T/R coil. Coils can take a variety of geometries, with their design suited to imaging different anatomical geometries, but they can be broadly broken down into either surface coils, or volume coils.

The surface coil is the simplest type of RF coil, made up of single or multiple loops in an LC circuit (Figure 1-7a). The coil wire can be considered an electrical inductor with inductance,  $L$ . With this fixed, the coil can be tuned to produce a  $B_1$  field that resonates at the Larmor frequency of the target nuclei,  $\omega_o$ , by varying the capacitance,  $C$ , following the equation:

$$\omega_o = \frac{1}{\sqrt{LC}} \quad 1.19$$

Surface coils are widely used in MRI as their design produces high SNR and enhanced sensitivity in superficial imaging regions proximal to the coils surface. However, the sensitivity of the surface coil falls off rapidly with distance (Hayes and Axel, 1985). The  $B_1$  field it transmits (Figure 1-7b), and therefore also the flip angle, decreases with distance from

the coil (Hernández - Flores *et al.*, 2002).

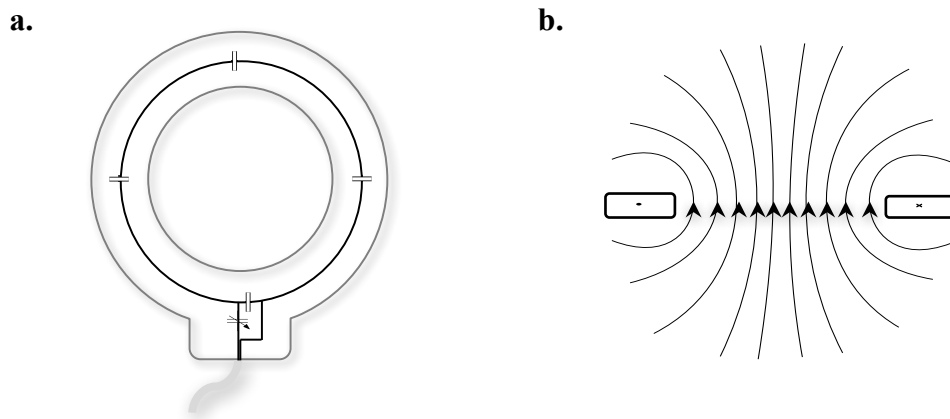


**Figure 1-7:** **a.** A simple LC circuit in a surface coil. **b.** A transverse view of a surface coil, with  $B_1$  field lines depicted.

Volume coils offer the ability to image a large field of view with a more homogeneous  $B_1$  than surface coils, making them distinctly more suitable for imaging a large volume such as the human lung. The birdcage coil is a commonly used volume coil design in MRI, first designed by Hayes *et al.* (1985). It is often used as a T/R coil as it offers good  $B_1$  transmit homogeneity, and high receive uniformity. However, use as a transmit coil in conjunction with a surface coil offers higher receive sensitivity (Giovannetti, 2014). This work will focus on utilisation of birdcage coil in T/R mode.

### 1.2.9 The birdcage coil

#### *Structure of the birdcage coil*

The birdcage coil is fabricated from a number of equally spaced conductive rungs, referred to as legs, connected between two conductive circular or elliptical loops, called end rings. Capacitors are placed at different locations on the coil to produce the desired resonant frequency (Hayes *et al.*, 1985).

A high-pass coil has the capacitors placed on the end rings, between each leg, as depicted in Figure 1-8a. This is in contrast to a low-pass coil, in which the capacitors are placed on each of the rungs, as shown in Figure 1-8b. A band-pass coil has capacitors in both locations.

In a high-pass coil, the high frequency signals will pass through the capacitors in the end rings, as they offer low impedance compared to the legs (inductors). Low frequency signals will be blocked by the capacitors that will offer high impedance, and shorted by the inductors (Vullo *et al.*, 1992). The same is true for low-pass coils. A band-pass coil allows tuning to two nuclei at a high and low frequency respectively (Rath, 1990). Therefore, for high-field  $^{19}\text{F}$  MRI, a high-pass coil is considered optimal.

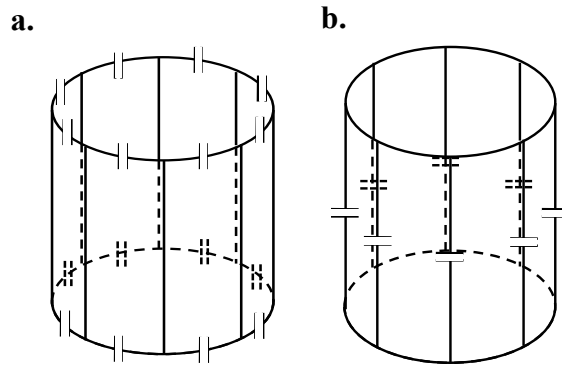


**Figure 1-8:** **a.** Capacitor location on a high-pass birdcage coil. **b.** Capacitor location on a low-pass birdcage coil.

### ***Production of a homogeneous $B_1$ field***

A homogeneous transverse  $B_1$  field can be produced in a cylinder whose axis is aligned with  $B_0$ , by applying a current along the length of the cylinders surface with an amplitude that varies proportionally to the sine of the cylinders azimuthal angle,  $\phi$ . The birdcage coil approximates this with sinusoidally varying current amplitude in each leg. It is for this reason that a greater number of legs on a birdcage coil results in a more homogeneous  $B_1$  field, as displayed in Figure 1-9. However, this is a compromise as fabricating many legs can become impractical and uneconomical.

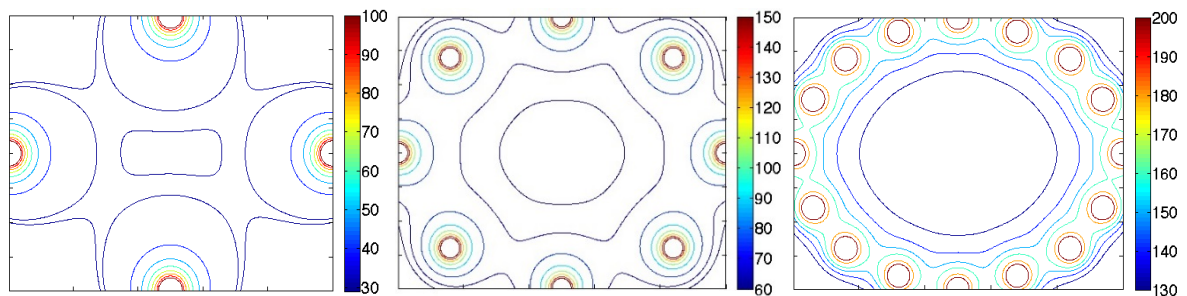


**Figure 1-9:** Simulated  $B_1$  field maps for a birdcage coil with 4, 8, and 16 legs respectively. These were simulated by applying the Biot-Savart law to each leg, then summing the B-field values experienced at each point in the image.

The equivalent circuit of a small section of an N-rung birdcage coil is shown in Figure 1-10.

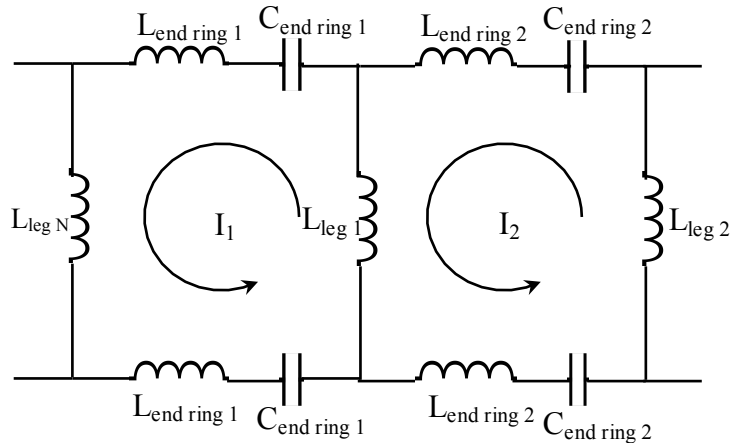


**Figure 1-10:** A small segment of the circuit in a N-rung birdcage coil.

The total phase shift around the cylinder must be an integer multiple ( $M$ ) of  $360^\circ$  to produce a resonant standing wave in the circuit. The phase shift of the current for the  $n^{\text{th}}$  rung of a coil with  $N$  rungs must therefore satisfy the equation  $\phi_n = M(360^\circ/N)n$ .  $M$  can take  $N/2$  values, each representing distinct resonant modes. The  $M = 1$  resonant frequency is known as the dominant mode. It is this mode that must be tuned to the resonant frequency of the nucleus in question, as the other modes produce inhomogeneous  $B_1$  fields from larger phase rotation increments around the coil. For this reason they are unsuitable for traditional MR-studies (Hayes *et al.*, 1985).

The coil can be tuned to the required resonant frequency by adjusting the capacitance of the circuit. Theoretical models have been published to predict the capacitance required (Chin *et al.*, 2002; Boissoles and Caloz, 2006; Gurler and Ider, 2012). However, due to the extent of the RF interactions, combined with an imperfect coil structure, these predictions provide only a starting point, and iterative adjustments are required. Further to this, the  $B_1$  field is sensitive to the coils external environment; RF coupling resulting from the birdcage coil interacting with structures in scanner when placed in the scanner bore causes a reduction in the achieved  $B_1$  amplitude. Loading the coil lowers the  $B_1$  homogeneity due to standing wave and attenuation effects. For these reasons, birdcage coils are sometimes also fitted with variable capacitors, allowing fine-tuning when loaded.

### *Linear and quadrature mode*

The birdcage coil can be driven in either linear or quadrature mode. In linear mode, the coil is excited from one port and produces a linearly polarised field of the form:

$$\mathbf{B}_1 = B_1 \cos \phi \hat{\mathbf{x}} \quad 1.20$$

In quadrature mode, it is driven from two orthogonal ports with a 90° phase shift, producing a circularly polarised field of the form:

$$\mathbf{B}_1 = B_1 (\cos \phi \hat{\mathbf{x}} + \sin \phi \hat{\mathbf{y}}) \quad 1.21$$

It is possible to compare the transmit power efficiency of the linear and quadrature coils, as power is proportional to the square of the  $B_1$  field created. As a linearly polarised field can be described as the sum two opposing circularly polarised fields,  $\mathbf{B}_{1,\text{linear}} = \mathbf{B}_1^+ + \mathbf{B}_1^-$ , such that:

$$\mathbf{B}_{1,\text{linear}} = \frac{B_1}{2} (\cos \phi \hat{\mathbf{x}} + \sin \phi \hat{\mathbf{y}}) + \frac{B_1}{2} (\cos \phi \hat{\mathbf{x}} - \sin \phi \hat{\mathbf{y}}) \quad 1.22$$

Squaring this results in:

$$P_{\text{linear}} \propto 2 \times \left( \frac{B_1}{2} (\cos \phi \hat{\mathbf{x}} \pm \sin \phi \hat{\mathbf{y}}) \right)^2 \quad 1.23$$

Where  $P$  is power, measured in Watts.  $P_{\text{quadrature}}$  is proportional the square of Equation 1.21. By inspection, it is therefore clear that:

$$P_{\text{quadrature}} = 2 \times P_{\text{linear}} \quad 1.24$$

Hence by using a circularly polarised field, the transmit capabilities of the coil are twice as efficient at tipping the nuclei, with half as much power required to produce the same  $B_1$  field. This can be visualised by noting that a circularly polarised field never has zero magnitude, and is therefore always imparting  $B_1$  on the nuclei. This is in contrast with a linearly polarised  $B_1$  field, which oscillates in magnitude.

Additionally, as the signal produced is complexly summed from the two separate receive

channels, the correlated signal detected is doubled, whereas the noise detected, due to them being uncorrelated, increases by only a factor of  $\sqrt{2}$ . Therefore, for a quadrature design, along with a 50% reduction in power requirements, there is also a  $\sqrt{2}$  improvement in SNR (Chen *et al.*, 1983; Redpath, 1998).

### ***Tuning and impedance matching***

At the interface between the coil and the coaxial cable from the RF amplifier, a tune and match circuit is used to allow crucial capacitance adjustments to maximise coil performance. An example simple tune and match circuit diagram is shown in Figure 1-11.

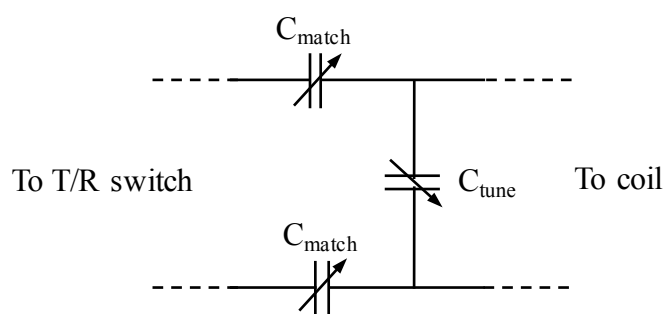


**Figure 1-11:** An example tune and match circuit. The tuning capacitor is joined in parallel to the coil circuit, and the matching capacitors are connected in series.

All coils behave as variations of LC circuits, where Equation 1.19 describes a simple case of how the resonant frequency of the oscillating field can be change by varying L or C. As inductance is determined by the geometry of the coil, tuning is most easily accomplished by varying the capacitors on the end rings using feedback from a network analyser, until resonance at the Larmor frequency is achieved.

Once this has been determined, the variable matching capacitor is adjusted to match the 50  $\Omega$  impedance of the RF amplifier to that of the coil in order to minimise power loss and achieve maximum signal (Hoult and Richards, 1976; Maclaughlin, 1989).

The coil construction theory covered in this section in addition to the pulse sequence design theory discussed earlier, is applied to the technical development conducted in the following chapters.

### **1.3 Modalities for the assessment of pulmonary ventilation**

Pulmonary function tests including spirometry, plethysmography, multiple breath nitrogen wash-out and helium dilution are regularly used to assess the pulmonary function of patients with obstructive lung disease. However, they only provide a global measurement of function in diseases that are well known to be spatially heterogeneous (Nakawah *et al.*, 2013). To address this, a number of imaging modalities have been utilised for pulmonary ventilation assessment. These include single-photon emission computed tomography (SPECT), positron emission tomography (PET), x-ray computed tomography (CT), and magnetic resonance imaging (MRI). The remainder of this section comprises a brief overview of each of these imaging modalities with a review of pertinent publications. MR imaging techniques are then discussed in further detail with an emphasis on imaging inhaled perfluorinated gases.

#### ***1.3.1 Pulmonary ventilation imaging techniques utilising ionising radiation***

Radioactive tracer gases have been utilised for the assessment of regional ventilation for several decades. Early xenon-133 ( $^{133}\text{Xe}$ ) scintigraphy, using six scintillation cameras fixed vertically to the torso, was able to detect the gravity dependent ventilation distribution between the apex, middle and base of each lung (Ball *et al.*, 1962). However, this relatively primitive study offered minimal spatial localisation of the detected gamma radiation, with an inability to distinguish ventilation differences within horizontal planes. SPECT extended this planar scintigraphic technique into a modality that is capable of producing a three-dimensional image of radioactivity distribution by iterative reconstruction or filtered back projection techniques. Ventilation SPECT commonly utilises a technetium-99m ( $^{99\text{m}}\text{Tc}$ ) labeled aerosol or  $^{133}\text{Xe}$  as tracers (Petersson *et al.*, 2007; Roach *et al.*, 2013). Both static ventilation distribution and dynamic wash-out images can be acquired (Suga, 2002; Yokoe *et al.*, 2006). Studies have shown SPECT to be able to detect a difference in signal distribution between healthy volunteers and emphysematous patients at varying disease severity (Nagao *et al.*, 2000; Xu *et al.*, 2001; Yokoe *et al.*, 2006). SPECT is a readily available technique, which uses relatively inexpensive tracers, making it an easily accessible lung imaging option. Its primary limitation is the low resolution; pulmonary imaging SPECT can produce a spatial resolution of typically 10 mm – 20 mm, coarser than comparable imaging methods. A secondary limitation is that exposure to typically 2 – 3 mSv of ionising radiation is required (Petersson *et al.*, 2007). It is half the dose of a typical comparable CT scan, however this factor still dissuades repeated use of this technique in cases calling for longitudinal disease monitoring.

Positron emission tomography utilises decaying radionuclides as the tracer source, typically nitrogen-13 ( $^{13}\text{N}_2$ ), fluorine-18 ( $^{18}\text{F}$ ) or neon-19 ( $^{19}\text{Ne}$ ) for ventilation imaging (Rhodes and Hughes, 1995; de Prost *et al.*, 2015; Chen *et al.*, 2017). The positrons emitted in the decay annihilate with an electron, producing two gamma rays travelling in opposite directions. The paths between each of the detected gamma-ray pairs are reconstructed, and the information used to form an image. Ventilation has been assessed by quantification of wash-in and wash-out rates of the radioactive tracer gas (Senda *et al.*, 1986; Venegas *et al.*, 2013). PET is a more expensive option than SPECT, but better diagnostic accuracy can be achieved with the higher (typically 5 mm) resolution (Conway, 2012).

CT is considered the gold standard for chest imaging in current clinical practice, primarily thanks to its ability to achieve high spatial resolution, typically less than 0.5 mm (Kakinuma *et al.*, 2015). The technique utilises an x-ray generator and detector mounted on a rotating gantry. The x-ray attenuation from multiple angles around the patient is collected to produce a 3D map of tissue density. This has been used to detect both airway narrowing (Kirby *et al.*, 2016), and alveolar enlargement (emphysema) (Lynch *et al.*, 2015). CT can measure the regional distribution of ventilation with the use of a radiopaque xenon gas contrast agent. The signal output is directly proportional to the concentration of the xenon gas (Murphy *et al.*, 1989), which therefore provides a direct measure of ventilation homogeneity. Dual-energy CT utilises two x-ray sources, and allows dynamic ventilation imaging as well as simultaneous anatomical and ventilation acquisitions (Chae *et al.*, 2008). It has been shown to be reliable at quantifying COPD (Park *et al.*, 2010; Bodduluri *et al.*, 2017). As CT is a technique that relies on ionising radiation, the associated carcinogenic risk of particular concern in the case of longitudinal pulmonary disease monitoring and paediatric imaging.

### **1.3.2 $^1\text{H}$ MRI of pulmonary ventilation**

Conventional MRI exploits the high gyromagnetic ratio of hydrogen-1 ( $^1\text{H}$ ) nuclei to produce a signal that can be imaged. The primary problem with successful pulmonary MRI is the lack of  $^1\text{H}$  nuclei available in the lungs to produce satisfactory images. The proton density of the parenchyma is one fifth of that of most body tissues (Theilmann *et al.*, 2009), resulting in reduced signal. Furthermore, the air-tissue boundaries produces a 9 ppm magnetic susceptibility gradient between the two media (Wild, 2009). This produces magnetic field inhomogeneities at these interfaces, resulting in the nuclei losing phase coherence at a much faster rate; the transverse relaxation time of the lung parenchyma is greatly reduced from  $T_2 \approx 100$  ms for water in body tissues to about  $T_2^* \approx 1$  ms for water in the lungs at full inspiration

(Hatabu *et al.*, 1999a; Hatabu *et al.*, 1999b). Respiratory gating or breath-hold duration scans are also typically required, reducing the capacity for signal averaging. Due to these challenging MR properties, MRI of pulmonary ventilation benefits from a departure from standard MR techniques.

Ultra-short echo time (UTE) imaging is adept at imaging short- $T_2^*$  tissues, such as the lung parenchyma, by use of non-linear sampling of k-space to permit use of short (typically <1 ms) echo times (Tyler *et al.*, 2007). As this MR technique does not image the airspace it is therefore only capable of identifying biomarkers of ventilation defects through indirect methods such as measuring lung tissue density (Lederlin and Cremillieux, 2014; Sheikh *et al.*, 2017) or parenchymal  $T_2^*$  measurements (Ohno *et al.*, 2011).

The measurement of ventilation requires the ability to distinguish between freshly inspired gas and the pre-existing gas in the lungs, allowing wash-in rates to be mapped. This necessity has encouraged the use of contrast enhancement for ventilation imaging. Oxygen-enhanced pulmonary MRI uses 100%  $O_2$  as the contrast agent. It exploits the paramagnetic effects of dissolved molecular oxygen along with the large surface area of the lung tissue to map a change in signal from the parenchyma (Chen *et al.*, 1998; Mai *et al.*, 2002; Zhang *et al.*, 2015). A decrease in the longitudinal relaxation time ( $T_1$ ) of the tissues by 7% – 14% has been reported (Webb, 1988; Loffler *et al.*, 2000; Jakob *et al.*, 2001; Nakagawa *et al.*, 2001; Mai *et al.*, 2002).

Ventilation and perfusion rate along with molecular oxygen diffusion speed all contribute to the change in oxygen levels, and consequently the change in  $T_1$ , therefore this lung imaging technique can only give combined information about lung function. Despite being an indirect measure of pulmonary ventilation, and challenging to quantitate reproducibly (Triphan *et al.*, 2017), oxygen enhanced MRI has been shown to be significantly more precise at classifying the clinical stage of COPD than quantitative CT (Ohno *et al.*, 2008).

### ***1.3.3 Hyperpolarised noble gas MRI of pulmonary ventilation***

Inhalable hyperpolarised (HP) noble gases, namely helium-3 ( $^3\text{He}$ ) and xenon-129 ( $^{129}\text{Xe}$ ) have been the subjects of a large body of research over the last two decades which has demonstrated their utility for lung ventilation imaging using hyperpolarised imaging agents. Their MR properties are summarised in Table 1.2.

Isotope	Spin, I	Gyromagnetic ratio, $\gamma$ (MHz/T)	Natural abundance	Cost per litre
$^3\text{He}$	$\frac{1}{2}$	32.4	0.0001%	>US\$600 <sup>a</sup>
$^{129}\text{Xe}$	$\frac{1}{2}$	11.8	26%	Enriched: US\$100 Natural: US\$10

**Table 1.2:** MR properties of hyperpolarised  $^3\text{He}$  and  $^{129}\text{Xe}$ . a. (Kramer, 2011), all other values from Mugler et al., (2013).

$^3\text{He}$  is a stable isotope of helium with a high gyromagnetic ratio making it very sensitive to MRI. It is also inert and non-toxic. However, the  $^3\text{He}$  isotope has a negligible natural abundance, so is most commonly sourced from tritium decay of nuclear warheads. This finite supply makes it particularly uneconomical (Walkup and Woods, 2014).

$^{129}\text{Xe}$  benefits from being more readily available, with an adequately high natural abundance to not require the enriched isotope (Lilburn *et al.*, 2013). However, its gyromagnetic ratio is one third of that of  $^3\text{He}$ , consequently comparable polarisation would result in poorer image quality than  $^3\text{He}$ . Unlike  $^3\text{He}$ ,  $^{129}\text{Xe}$  is soluble in tissue, thus can readily diffuse into the blood stream once inhaled and has anaesthetic properties at alveolar concentrations above 70%, and is therefore regulated as such (Goto *et al.*, 2000).

$^3\text{He}$  and  $^{129}\text{Xe}$  have low spin density in the gaseous phase and long longitudinal relaxation times ( $T_1$ ), which limits signal averaging. They are therefore unsuitable for MRI without the use of a mechanism to modify the Boltzmann thermal polarisation. Hyperpolarisation results in an increase in polarisation of nuclei by a factor of up to 100,000 times beyond thermal equilibrium to produce a polarisation of up to 50% (Mugler and Altes, 2013). Once the gas has been hyperpolarised, it has a  $T_1$  of several days if stored under controlled conditions; it must not be exposed to magnetic field gradients, radio frequency irradiation or come into contact with paramagnetic gases such as oxygen. Molecular oxygen can reduce the  $T_1$  of HP  $^3\text{He}$  and  $^{129}\text{Xe}$  to 10 – 20 s (Albert *et al.*, 1994); this enforces a limit on the scan length, as  $T_1$  relaxation accelerates the moment it is inhaled and mixed with oxygen.

$^3\text{He}$  had been the prime focus of HP gas lung imaging studies due to  $^{129}\text{Xe}$  historically being challenging to polarise above ~25% (Albert *et al.*, 1994). Technological advances mean this is no longer a limitation (Hersman *et al.*, 2008), and recent studies have shown that  $^{129}\text{Xe}$  can be more sensitive to visualising ventilation defects than  $^3\text{He}$ , and more accurate at diffusion weighted imaging (Kirby *et al.*, 2013; Kołodziej *et al.*, 2017). This could be due to  $^{129}\text{Xe}$

being a much larger, higher density and slower-diffusing gas, with higher resistance in narrow obstructed airways.

Ventilation is most commonly imaged by spin density weighted imaging sequences, in which the signal achieved is proportional to the volume of gas in each voxel. Spin density imaging of hyperpolarised gas was first demonstrated with  $^{129}\text{Xe}$  MR images of mouse lungs by Albert *et al.* (1994). It has since been researched extensively in humans by exploiting the characteristic inhomogeneous distribution of air that these diseases cause to visualise a range of obstructive pulmonary diseases including asthma (Lange *et al.*, 2009; Hahn *et al.*, 2016; Ebner *et al.*, 2017), COPD (Woodhouse *et al.*, 2009; Hamedani *et al.*, 2016; Kirby *et al.*, 2017), and emphysema (Sun *et al.*, 2011). In all cases, spin density weighted imaging exploits the characteristic inhomogeneous distribution of gas seen in these obstructive diseases, resulting in areas that are devoid of signal. A comparison of the effectiveness of hyperpolarised  $^3\text{He}$  spin density imaging to CT for detecting ventilation defects in lung transplant patients showed that  $^3\text{He}$  offers a significant improvement in the ability to detect defects (Gast *et al.*, 2002). This is due to CT offering only lung structural information rather than visualisation of a gas.

Alongside spin density imaging, HP gases can be used to indirectly measure pulmonary function status: free diffusion of gas occurs in the trachea, but the bronchiolar and alveolar walls restrict the movement of gases, reducing their diffusivity to that of the apparent diffusion coefficient (ADC), which is determined by compartment size. Diffusion weighted imaging allows the ADC to be mapped. This application has been valuable in studies of emphysema, as it allows the location and severity of tissue destruction to be visualised (Saam *et al.*, 2000; Salerno *et al.*, 2002; Kirby *et al.*, 2014; Wang *et al.*, 2014; Weatherley *et al.*, 2016).

The  $T_1$  of hyperpolarised gas is inversely proportional to oxygen concentration; therefore  $T_1$ -weighted images can also produce information about pulmonary ventilation. Oxygen-sensitive HP  $^3\text{He}$  MRI is used to detect differences in oxygen partial pressures ( $p\text{O}_2$ ). In diseases where ventilation is reduced, alveolar partial pressure in the diseased regions will be reduced (Saam *et al.*, 1995). The  $T_1$  shortening effect of molecular oxygen on hyperpolarised  $^3\text{He}$  has been used to calculate the in vivo  $p\text{O}_2$  distribution with 3% accuracy (Deninger *et al.*, 1999).

The high sensitivity of HP noble gas MRI to airway structure due to its high SNR has made it an attractive pulmonary ventilation imaging technique to research. However, the requirement

for expensive hyperpolarisation hardware, gas, and expertise has slowed its translation to clinical practice with the first diagnostic images only published within the past couple of years (Wild *et al.*, 2015). An imaging modality that utilises thermally polarised gas could therefore present improved opportunities for widespread clinical use.

### 1.3.4 MRI of pulmonary ventilation using perfluorinated gases

Fluorine-19 ( $^{19}\text{F}$ ) is the only stable isotope of fluorine. Its MR properties in comparison to  $^1\text{H}$  are summarised in Table 1.3.

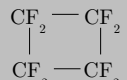
Isotope	Spin, $I$	Gyromagnetic ratio, $\gamma$ (MHz/T)	Relative sensitivity (%)
$^1\text{H}$	$\frac{1}{2}$	42.58	100
$^{19}\text{F}$	$\frac{1}{2}$	40.05	83

**Table 1.3:** MR properties of  $^1\text{H}$  and  $^{19}\text{F}$ . The high gyromagnetic ratio of  $^{19}\text{F}$  produces good imaging sensitivity relative to that of  $^1\text{H}$  (Ruiz-Cabello *et al.*, 2011).

The  $^{19}\text{F}$  isotope has a 100% natural abundance, and is the second most receptive nucleus for MRI, giving a relative sensitivity of 83% to that of  $^1\text{H}$ . With no detectable natural background signal in vivo, endogenous background signal is also minimised. The MR relaxation times of thermally polarised  $^{19}\text{F}$  molecules aren't highly affected by exposure to oxygen, allowing more permissive breathing protocols than hyperpolarised gas MRI, such as gas wash-in measurements and acquisitions during steady-state breathing (Chang and Conradi, 2006). However, pulmonary imaging challenges arise from its low spin density and thermal polarisation. Careful selection of an appropriate perfluorinated molecule for MR studies is therefore necessary to attain adequate signal.

Candidates that have previously been investigated for  $^{19}\text{F}$ -MRI of pulmonary ventilation include  $\text{SF}_6$  (sulfurhexafluoride),  $\text{C}_2\text{F}_6$  (perfluoroethane),  $\text{CF}_4$  (tetrafluoromethane), cyclo- $\text{C}_4\text{F}_8$  (cyclo-octafluorobutane) and  $\text{C}_3\text{F}_8$  (perfluoropropane). A summary of their chemical properties is displayed in Table 1.4 (Mohanty and Bernstein, 1970; Chang and Conradi, 2006; Wild, 2009).

Cyclo- $\text{C}_4\text{F}_8$  has been shown to cause severe convulsions in rats thus is considered unsuitable for further in vivo use (Miller *et al.*, 1972). However, the other gases listed are all chemically and physiologically inert, non-toxic, and insoluble (Mosbah *et al.*, 2008).

Molecule	Molecular weight (g/mol)	Chemical structure	T <sub>1</sub> in vitro at 1.5 T (ms)	T <sub>2</sub> in vitro at 1.5 T (ms)
CF <sub>4</sub>	88.01		1.9	~T <sub>1</sub> <sup>a</sup>
C <sub>2</sub> F <sub>6</sub>	138.02	CF <sub>3</sub> — CF <sub>3</sub>	7.9	6.6
Cyclo-C <sub>4</sub> F <sub>8</sub>	200.04		47	-
SF <sub>6</sub>	146.06		1.7	~T <sub>1</sub> <sup>a</sup>
C <sub>3</sub> F <sub>8</sub>	188.02	CF <sub>3</sub> — CF <sub>2</sub> — CF <sub>3</sub>	20	13.8

**Table 1.4:** A summary of the chemical and MR properties of perfluorinated gasses used in previous lung MR studies. a: Exact T<sub>2</sub> values aren't described in the literature but are described as approximately equal to T<sub>1</sub>. No value for cyclo-C<sub>4</sub>F<sub>8</sub> T<sub>2</sub> could be found in the literature.

The quality of the images produced is dependent upon the T<sub>1</sub> and T<sub>2</sub>\* relaxation times of the nuclei, as well as the spin density of chemically equivalent <sup>19</sup>F atoms within a molecule. A shorter T<sub>1</sub> permits a higher degree of signal averaging within a fixed acquisition time improving the SNR by the square root of the number of averages. A very short T<sub>2</sub>\* however necessitates a short TE, resulting in a wide receiver bandwidth. A high bandwidth has a larger frequency range and therefore picks up a larger range of noise frequencies, reducing the SNR (Wild, 2009).

CF<sub>4</sub> and SF<sub>6</sub> both exhibit particularly short T<sub>2</sub> relaxation times in vivo due to their smaller molecular size and shorter correlation times, analogous to their short T<sub>1</sub> (Mohanty and Bernstein, 1970; Wild, 2009), requiring high receiver bandwidths and fast gradient switching rates to image successfully. However, they both differ in utility primarily due to <sup>19</sup>F density; with just four <sup>19</sup>F nuclei per molecule CF<sub>4</sub> is considered an unfavourable gaseous imaging agent for MRI. SF<sub>6</sub> however, with a 50% higher signal density than CF<sub>4</sub>, has been widely researched in small and large animals and excised human lungs imaging studies (Jacob *et al.*, 2005; Perez-Sanchez *et al.*, 2005; Scholz *et al.*, 2009). It is well established as a safe gas due to its chemical and biological inertness and is the first fluorinated gas to be approved for human use in studies in a 78%/22% mixture with oxygen (Wolf *et al.*, 2008). The study participants tolerated the gas mix well for the 3 – 5 breaths required for the study with no adverse events reported. For clinical use, it is preferable that the inhaled gas can be imaged

within a single breath hold, noting that a patient with lung disease may be less able to hold their breath than a healthy individual. Previous work on SF<sub>6</sub> (Schreiber *et al.*, 2001) has shown that 3D images with adequate signal to noise ratios were obtained with a 49 second temporal resolution. Any considerable improvement on this acquisition time whilst maintaining image quality necessitates using a more suitable fluorine gas with a longer T<sub>2</sub>\*. This obstacle to further development is reflected in the observation that SF<sub>6</sub> hasn't been utilised in any human studies in this field since 2008.

The MR relaxation times of C<sub>2</sub>F<sub>6</sub> are longer than those of SF<sub>6</sub>, which would make it a potentially suitable candidate for MR applications. It has been used as the imaging agent in a number of in vivo mouse and excised human lung studies of both spin density and diffusion weighted imaging (Jacob *et al.*, 2005; Wolf *et al.*, 2006; Carrero-Gonzalez *et al.*, 2013). However, it has no precedent for use as an inhalable imaging agent in human subjects; seeking regulatory approvals and verifying safety would therefore be a primary concern before beginning human in vivo investigations that utilise this gas.

Recent publications have focussed on utilising C<sub>3</sub>F<sub>8</sub> as an inhalable agent for pulmonary imaging in human subjects (Couch *et al.*, 2013; Halaweish *et al.*, 2013; Halaweish and Charles, 2014). C<sub>3</sub>F<sub>8</sub> is composed of <sup>19</sup>F groups in two distinct chemical environments, -CF<sub>3</sub> and -CF<sub>2</sub>, whose resonant frequencies are separated by 48 ppm. Therefore, maximal MR signal is detected from the -CF<sub>3</sub> group, providing a relatively high spin density of six <sup>19</sup>F nuclei per molecule. C<sub>3</sub>F<sub>8</sub> mixed with 21% O<sub>2</sub> has been measured to have an in vivo T<sub>1</sub> of 12.4 ms at 3.0 T (Couch *et al.*, 2013) and a T<sub>2</sub>\* of 2.2 ms (Couch *et al.*, 2013) in the human lung. Its comparably long relaxation times make it more suitable than SF<sub>6</sub> and CF<sub>4</sub> for lung imaging, and it has a precedent for safe inhalation in human subjects. C<sub>3</sub>F<sub>8</sub> is therefore considered the most suitable MR-sensitive inhalable imaging agent for this study, and will be used throughout the subsequent chapters.

As with hyperpolarised noble gas imaging, perfluorocarbons have an ADC dependent on alveolar size. Diffusion weighted images could therefore approximate the severity of ventilation defects such as emphysema. Diffusion weighted <sup>19</sup>F MRI has been demonstrated (Perez-Sanchez *et al.*, 2005; Ruiz-Cabello *et al.*, 2005). In anatomically healthy excised human lungs, the ADC of perfluorocarbon gases is approximately 50% of the free diffusivity D<sub>0</sub>. In comparison, emphysematous lung models have produced a perfluorocarbon diffusivity approximately 90% of D<sub>0</sub> (Jacob *et al.*, 2005). Diffusion weighted imaging has been carried out in vivo using C<sub>2</sub>F<sub>6</sub> gas to compare ADC measurements in a preclinical model of

emphysematous and healthy rat lungs (Carrero-Gonzalez *et al.*, 2013), with the former resulting in an increased ADC, in agreement with diagnostic theory.

Literature investigating  $^{19}\text{F}$ -MRI of pulmonary ventilation is limited. The majority of publications reporting application of perfluorinated gas MRI of pulmonary imaging focus on spin density imaging, which will be the primary focus of this thesis. Early papers have concentrated on acquiring spin density images, typically with a 3D gradient echo acquisition sequence, in rodents (Kuethe *et al.*, 1998; Kuethe *et al.*, 2002), pigs (Schreiber *et al.*, 2000; Wolf *et al.*, 2006), and excised human lungs (Jacob *et al.*, 2005) with the latter achieving an SNR of 9:1 in 13 s using  $5.5 \times 5.5 \times 32 \text{ mm}^3$  voxels. These studies validated the efficacy of the imaging technique to provide information about the distribution of gas in the lung.

Mapping fractional ventilation over wash-in and wash-out breathing cycles provides a tool with clinical utility that hyperpolarised gas MRI has a limited capacity to measure due to the loss of longitudinal polarisation within tens of seconds. Application of spin density weighted  $^{19}\text{F}$ -MRI of inhaled perfluorinated gases to mapping wash-in and wash-out kinetics has been reported in a small number of studies. Its feasibility was first tested in mechanically ventilated porcine lungs (Schreiber *et al.*, 2001), recording fractional ventilation during deep and shallow breathing protocols; 2 and 5 inspirations respectively were required for near complete wash-in. Since,  $^{19}\text{F}$  wash-out rate has been reported in rat lungs (Ouriadov *et al.*, 2015) and mouse models of obstructive lung disease (Couch *et al.*, 2016), where a slower wash-out rate was observed in mice with inflamed lung tissue than in comparable healthy controls.

Spin density imaging is the only MR technique imaging inhaled perfluoropropane that has been studied in human subjects. The first demonstration of which used an 3D SPGR acquisition taken during a 15 s breath hold after inhalation of perfluoropropane in a 79%/21% mixture with oxygen (PFP/ $\text{O}_2$ ) achieving acceptable image quality with an SNR of 15:1 in a single healthy volunteer (Soher *et al.*, 2010). Halaweish *et al.* (2013) built on this preliminary result to image 11 healthy volunteers and 17 subjects who had been diagnosed with obstructive lung disease following a similar acquisition protocol. The images produced had SNRs that ranged between 5 and 30 using  $6.25 \times 6.25 \times 15 \text{ mm}^3$  voxel sizes, and depicted defects typical of each of the lung diseases. The extent of ventilation defects visible  $^{19}\text{F}$ -MRI images of COPD patients was seen to qualitatively increase with previously diagnosed disease severity. In parallel to this, Couch *et al.* (2013) achieved a SNR of  $18 \pm 6$  in healthy volunteers, again applying a similar acquisition protocol. In all cases acquisition times of  $\sim 15$  s were used. Application to the measurement of wash-out rates in humans has been carried out

under tidal breathing conditions (Charles *et al.*, 2014). Assessment of 35 subjects recorded greatly reduced wash-out rates in COPD patients and smokers in comparison to non-smokers. These studies have demonstrated the feasibility of MR imaging of pulmonary ventilation in human subjects using inhaled PFP/O<sub>2</sub>.

Although there has been no literature to-date, further development of ventilation imaging *in vivo* is likely to utilise the MR effect of the physiological environment on the gas; the transverse relaxation times of perfluorinated gases are known to be reduced when confined to small pores (Lizak *et al.*, 1991), as is found in the lung. Therefore, the signal from T<sub>2</sub>\* maps of an inhaled perfluorinated gas is expected to vary across regions of the lung, and with lung pathology.

Unlike other pulmonary ventilation imaging techniques, the use of ionising radiation is negated with MRI, making it favourable particularly for repeat acquisitions for long-term patient monitoring. <sup>19</sup>F MRI is demonstrably more economical than hyperpolarised noble gas imaging due to reduced hyperpolarisation equipment and expertise requirements, and the MR relaxation times are minimally affected by the presence of oxygen, unlike HP noble gases, permitting longer imaging studies. There have only been a handful of published human <sup>19</sup>F pulmonary ventilation studies, but they have shown promising results with adequate SNR values being achieved, providing a solid foundation for further development of the technique. The larger body of *in vitro* studies and *in vivo* animal research has demonstrated the potential for several future avenues of development and application.

## 1.4 Outline of chapters

The body of work described in this thesis has aimed to develop methods for quantitative measurement of pulmonary function using inhaled perfluoropropane as an MR sensitive imaging agent. It has achieved this through both optimisation of pre-existing methods in human subjects, as well as the development of novel techniques which have built a foundation for future methodologies. This work is outlined below.

Chapter 2 describes a preliminary  $^{19}\text{F}$ -MRI study imaging inhaled perfluoropropane in twelve healthy volunteers. This was conducted to verify the efficacy of the technique and to identify key limitations which were addressed in subsequent chapters. Perfluoropropane wash-in and wash-out rates with a deep-breathing protocol were also assessed.

In Chapter 3 a quadrature birdcage coil was designed and constructed for use with  $^{19}\text{F}$ -MR development work in phantoms. A larger commercial quadrature transmit/receive birdcage coil was then assessed for suitability for imaging inhaled perfluoropropane, and compared with three alternative RF coils by assessment of signal homogeneity within their sensitive volumes as well as their power handling efficiency.

In Chapter 4 the 3D spoiled gradient echo pulse sequence was simulated to determine the dependence of  $^{19}\text{F}$  signal to noise ratio achievable in a fixed acquisition time on acquisition parameters, followed by application of a compressed sensing acceleration technique. The optimised sequence was validated in both phantom models and healthy volunteers.

Chapter 5 focusses on the application of susceptibility matching of gas and aqueous compartments to increase the  $T_2^*$  of perfluoropropane. Two stable lung-representative phantoms that mimic the magnetic properties of alveolar tissue were developed. Gadolinium based contrast agents were added to the lung-representative phantoms to verify the amount of paramagnetic contrast agent required to achieve full susceptibility matching between the parenchymal representative media and the perfluoropropane gas suspension.

Chapter 6 translated this novel technique to in vivo applications. Gadobutrol was used to modify the susceptibility gradient in mouse alveoli, and  $T_2^*$  mapping of perfluoropropane –  $\text{CF}_3$  was performed to verify this change. Finally, healthy volunteers were imaged following perfluoropropane inhalation with a concurrent intravenous injection of Gadobutrol. Dynamic acquisition sequences were used to detect the change in  $T_2^*$  on the first pass through the pulmonary vasculature.

## Chapter 2: Healthy Volunteer Proof of Concept Study

### 2.1 Overview

Imaging inhaled perfluoropropane to assess lung function is a relatively novel but promising concept, with just three human studies published to-date (Couch *et al.*, 2013; Halaweish *et al.*, 2013; Couch *et al.*, 2014). In this chapter, a small-scale healthy volunteer study is conducted in order to test and verify the potential of this technique, and to identify possible obstacles to future clinical application. This work was conducted with the aim of assessing magnetic properties and signal behaviour of the inhaled PFP/O<sub>2</sub> as detailed below in order to guide further development of this imaging technique.

<sup>19</sup>F images are acquired during a single breath hold after inhalation of perfluoropropane. Intra-volunteer reproducibility is assessed from these images, and the benefits and limitations of the RF coil utilised for the study is determined and discussed.

Satisfactory image detail requires adequate signal. The number of wash-in breaths should be minimised such that when utilised on patient groups, adequate contrast between areas of differing ventilation is achieved. It is therefore valuable to understand the wash-in rate of perfluoropropane. A fast dynamic imaging acquisition is thus utilised to allow assessment of perfluoropropane wash-in and wash-out rates after one, two, and three deep respiratory cycles.

Finally, in vivo measurements of perfluoropropane –CF<sub>3</sub> T<sub>2</sub>\* are made over the full breathing cycle to corroborate and expand upon values published in the literature. The implications of these results are discussed.

## 2.2 Methods

### 2.2.1 Volunteers

This study utilised in vivo  $^{19}\text{F}$  MRI of healthy volunteers. Full ethical approval was in place (assessed by the Newcastle and North Tyneside 1 Ethics Committee. REC reference number: 14/NE/0135, IRAS project ID: 69343), and the volunteers gave informed consent to participate. A respiratory clinician and MR radiographers were present throughout all human perfluoropropane inhalation scans.

Twelve healthy volunteers (six male, six female) attended two MRI sessions each between November 2014 and June 2015. The men had a mean age of 34 with a range of 23 – 40 years. The women had a mean age of 24, with a range of 21 – 31 years. All volunteers were assessed by a clinical fellow and were confirmed to be in good health with no history of respiratory, cardiac, or cerebrovascular disease. Volunteers were also required to be non-smokers with a smoking history of less than 10 pack-years (where 20 cigarettes a day for one year is one pack year), and to have ceased smoking more than two years prior to the study. A spirometric test was carried out on each participant to confirm normal lung function.

### 2.2.2 $^{19}\text{F}$ MRI hardware set-up

Perfluoropropane ( $\text{C}_3\text{F}_8$ , PFP) was selected as the perfluorinated imaging agent, in a 79:21 mixture with oxygen (referred to from this point forward as PFP/ $\text{O}_2$ ). This was due to it having been used successfully in previous human inhalation studies (Couch *et al.*, 2013; Halaweish *et al.*, 2013), it being available in ‘patient consumption’ grade, and it having a useful  $T_2^*$  in vivo of 2.2 ms (Couch *et al.*, 2013). The two  $\text{CF}_3$  groups in PFP have chemically equivalent environments, and constitute the majority of the fluorine signal. The chemical environments of the  $\text{CF}_3$  and  $\text{CF}_2$  groups are separated by 48 ppm, meaning that  $\text{CF}_2$  resonances were not visible in acquisitions at  $\text{CF}_3$  frequencies.

An inhalation rig was designed and built to control the supply of gas to the volunteer. A diagram illustrating the layout of its primary components is displayed in Figure 2-1.

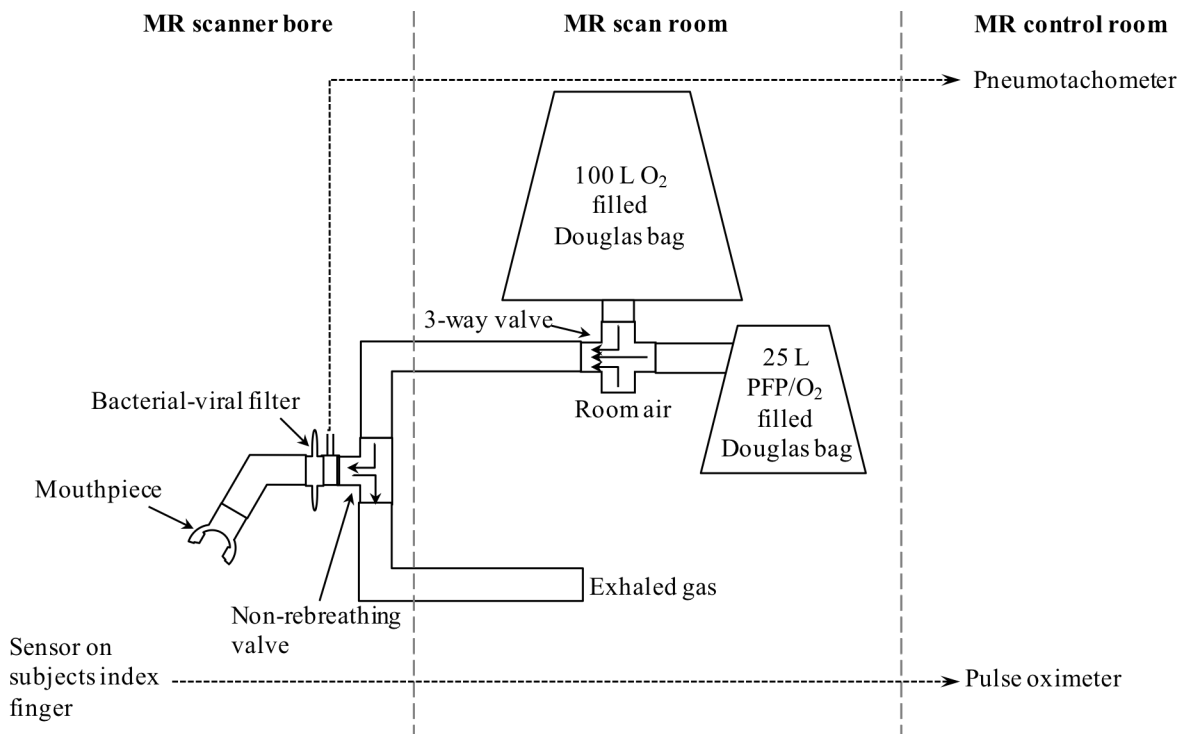


**Figure 2-1:** Diagrammatic layout of the inhalation rig components. The pneumotachometer and pulse oximeter are passed through the waveguide and monitored from the control room. The 100% O<sub>2</sub> supply was only made available if the subject's oxygen saturation dropped below 90% whilst in the scanner bore.

Two Douglas bags (100 L and 25 L) were filled with 100% O<sub>2</sub> and 79:21 PFP/O<sub>2</sub> respectively from non-MR safe gas cylinders (both supplied by BOC) prior to each scan. The Douglas bags were hung on an MR-safe PVC-U frame.

Smooth bore, 35 mm internal diameter (ID) low resistance tubing was used to connect the gas supplies to a manually controlled 3-way valve (2500 series, Hans Rudolph). 22 mm ID tubing was used to connect all components forward of this in order to minimise dead space. A 2-way non-rebreathing valve (1410 series, Hans Rudolph) and tubing allowed the exhaled gas to be deposited away from the magnet bore and the volunteer. An antibacterial filter was fitted to a disposable mouthpiece. All volunteers wore nose clips during the scans to aid adherence to the respiration protocol.

A pneumotach sensor (TSD127, Biopac Systems) was used for both assessing the volunteers breathing rate and volume compliance, as well as providing live feedback of this information to the volunteer.

Oxygen saturation and heart rate values were acquired throughout each scan using a MR-safe pulse oximetry sensor on the volunteer's finger (Model 7500FO, Nonin Medical). The pulse

oximeter and pneumotachometer cables were passed through a waveguide in the scanners Faraday cage, allowing the live feedback displays to be monitored by the clinician during the experiment. The live pneumotachometer airflow data could optionally be viewed by the volunteer through projection onto a display in the scanner room and a small mirror inside the scanner bore.

This study was performed on a Philips Achieva 3.0 T system in conjunction with a circular transmit/receive 20 cm diameter surface coil tuned to the fluorine resonant frequency, manufactured by PulseTeq Ltd (Model MN20A2).

During the scan, the subject was positioned supine on top of the RF coil. The coil was positioned beneath the lungs as shown in Figure 2-2, with the top of the coil aligned centrally with the volunteer's clavicle; this ensured repeatable positioning, whilst fully covering the apex of both lungs.

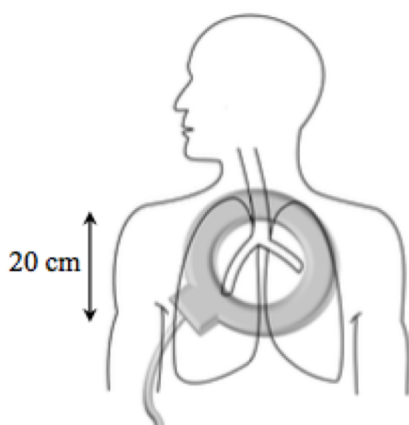


**Figure 2-2:** Positioning of  $^{19}\text{F}$  surface coil on the volunteers back. The coil was positioned to cover the apex of both lungs.

### **2.2.3 Testing intra-volunteer reproducibility**

The feasibility of this imaging technique is dependent on an adequate image quality being achieved, and this image quality being reproducible. Due to the strong dependence of  $^{19}\text{F}$  SNR with distance from the coil, arising from the surface coils  $B_1$  field and receive geometry, inter-volunteer reproducibility of SNR was deemed an unsuitable measurement, as the distance between the coil and the lungs varied between individuals. Intra-volunteer reproducibility of SNR was therefore tested instead.

Twelve healthy volunteers performed three deep wash-in inhalations of PFP/ $\text{O}_2$ . This was

followed by a 15 second long breath-hold during which a coronal 3D spoiled gradient echo (SPGR) image was acquired, using the imaging parameters described in Table 2-1.

Acquisition sequence	3D SPGR
Flip angle	50°
TE (ms)	1.55
TR (ms)	4.95
Bandwidth (Hz/pixel)	500
FOV: H-F × L-R × A-P (mm <sup>3</sup> )	400 × 400 × 160
Voxel size (mm <sup>3</sup> )	10 × 10 × 10
Dynamic duration (s)	1.8

**Table 2.1:** The acquisition parameters for a dynamic 3D spoiled gradient echo sequence. The field of view was designed to be larger than the sensitive volume of the coil.

Due to the poor  $B_1$  homogeneity associated with the surface coil design, any requested flip angle would not be achievable over the entire field of view. For this study, the coil was calibrated to achieve an average flip angle of 50° at the centre of the field of view. This was achieved by performing a spectroscopic free induction decay and arraying the requested flip angle between 0° and 180° at 10° intervals during a breath hold of PFP/O<sub>2</sub>, then calibrating the power delivered to the coil to achieve peak signal at 90°.

The 1.8 s dynamics were averaged 8 times, producing a 14.4 s long acquisition. This was done in order to improve the SNR by a factor of  $\sqrt{N}$ , where N is the number of averages, whilst maintaining a breath hold length scan time. A default slice oversampling factor of 1.28 was used. Both the echo time and repetition time were the minimum allowed values, and the flip angle was chosen to be close to the Ernst angle for the gas, in order to maximise the signal with averaging. Each volunteer underwent this protocol twice to allow reproducibility testing.

The signal-to-noise ratio ( $\mu_{signal}/\sigma_{noise}$ ) was calculated from the 14.4 s acquisition. The mean signal was assessed using a 50 × 50 mm region of interest (ROI) in the upper right section of each volunteer's lung. The noise measurement was taken from a 50 × 50 mm ROI outside the lung volume in the same image slice as the signal measurement. In each case, a slice proximal to the coil was chosen. The reproducibility between acquisitions from each volunteer was tested using a two-way fixed intra-class correlation (ICC).

### 2.2.4 Assessment of gas wash-in and wash-out rate

Understanding the wash-in rate of the PFP/O<sub>2</sub> gas mixture in healthy volunteers is necessary for further development of the <sup>19</sup>F lung imaging. The benefits are two-fold: achieving images with maximum SNR by imaging after an adequate number of respiration cycles, and eventually comparing wash-in rates to those with obstructive lung disease, as it may prove a useful quantitative marker for assessment of lung function severity. 3D SPGR acquisitions were carried out to measure signal increase over time during respiration of the PFP/O<sub>2</sub> gas mixture in 12 scan sessions. The same acquisition parameters as listed in Table 2.1 were used, with 70 dynamics, allowing collection of images over several breathing cycles.

The volunteers followed visual timed breathing instructions. A deep-breathing protocol was used that required all volunteers to inhale and exhale maximally at near vital capacity. This was chosen as it was deemed easy for volunteers to adhere to reproducibly, and would allow the volume of PFP/O<sub>2</sub> inhaled to scale with participant lung volume. Inhalation and exhalation times of 4 seconds were chosen as they were long enough to ensure the volunteer had time to inhale and exhale fully. After each inspiration, the volunteers were required to hold their breath for 5 seconds in order to measure the signal intensity. This breath hold duration was chosen to ensure that at least two 1.8 s dynamics fell within that time period. Each volunteer performed three ‘inhale, breath hold, exhale’ breathing manoeuvres of the PFP/O<sub>2</sub> gas, before being switched to breathing room air, and repeating the same respiration procedure three more times. This allowed collection of images over three wash-in and wash-out respiration cycles.

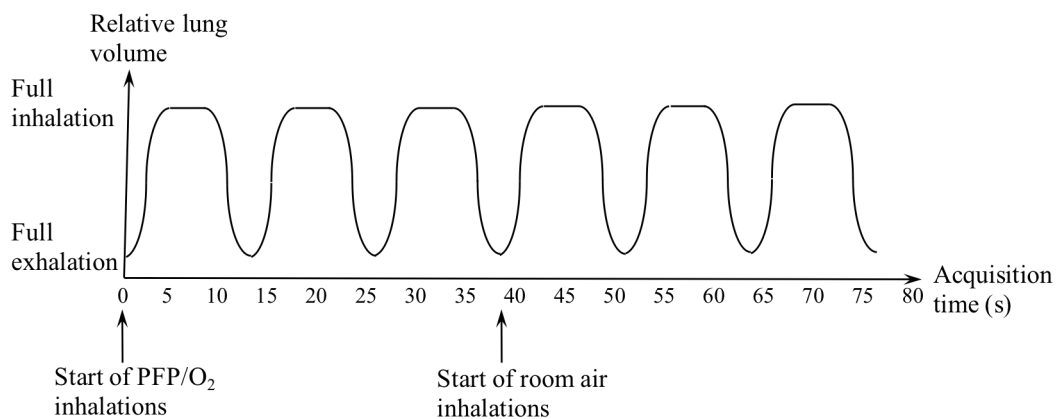


**Figure 2-3:** Diagram of the breathing and breath hold pattern followed by each volunteer. Three deep inhalations of PFP/O<sub>2</sub> are followed by three deep inhalations of room air. The dynamic acquisition sequence runs throughout, permitting dynamics from the breath holds following each inhalation to be compared.

Figure 2-3 displays a spirometric trace of the breathing and breath hold pattern followed over the acquisition.

The SNR achieved during each breath hold was measured using signal from a  $50 \times 50$  mm ROI positioned near the apex of the right lung, and noise from an equal sized ROI outside the lung volume.

### 2.2.5 *In vivo measurement of $T_2^*$*

Average in vivo  $T_2^*$  of the inhaled PFP -CF<sub>3</sub> resonance was measured using a dynamic free induction decay (FID) sequence, summarised in Table 2-2.

Acquisition sequence	Unlocalised FID
Flip angle / shape	90° hard pulse
Number of FID samples	256
Sample frequency (Hz)	8000
Acquisition length (ms)	42
Number of dynamics	2500

**Table 2.2:** The acquisition parameters for dynamic measurement of average  $T_2^*$  in vivo.

The sequence was acquired while the volunteer followed a deep breathing protocol. This regime allowed average  $T_2^*$  values to be collected at both full inspiration and expiration. The protocol was repeated on four volunteers.  $T_2^*$  was calculated by fitting FID signal decay from each dynamic to an exponential decay curve for the form  $S = S_0 e^{-TE/T_2^*}$ , taken from Equation 1.12. Where  $S$  is the signal measured in the FID at time point TE, and  $S_0$  is the signal before any decay, ie. at TE = 0 ms.

## 2.3 Results

### 2.3.1 Testing intra-volunteer reproducibility

3D SPGR lung images with a mean SNR of  $40.3 \pm 5.3$  were achieved in 14.4 s acquisitions after three vital capacity wash-in inhalations in twelve healthy volunteers. The intra-volunteer reproducibility of SNR measurements was calculated to be  $ICC(3,1) = 0.961$  with a 95% confidence interval of 0.863 to 0.989.

Data from three representative volunteers of the total twelve are displayed in Figure 2-4. The first and second rows show a single slice from the first and second acquisition respectively. The third row depicts the  $^{19}\text{F}$  signal in a slice, threshold-masked and overlaid on a proton image to demonstrate anatomical positioning of the signal.

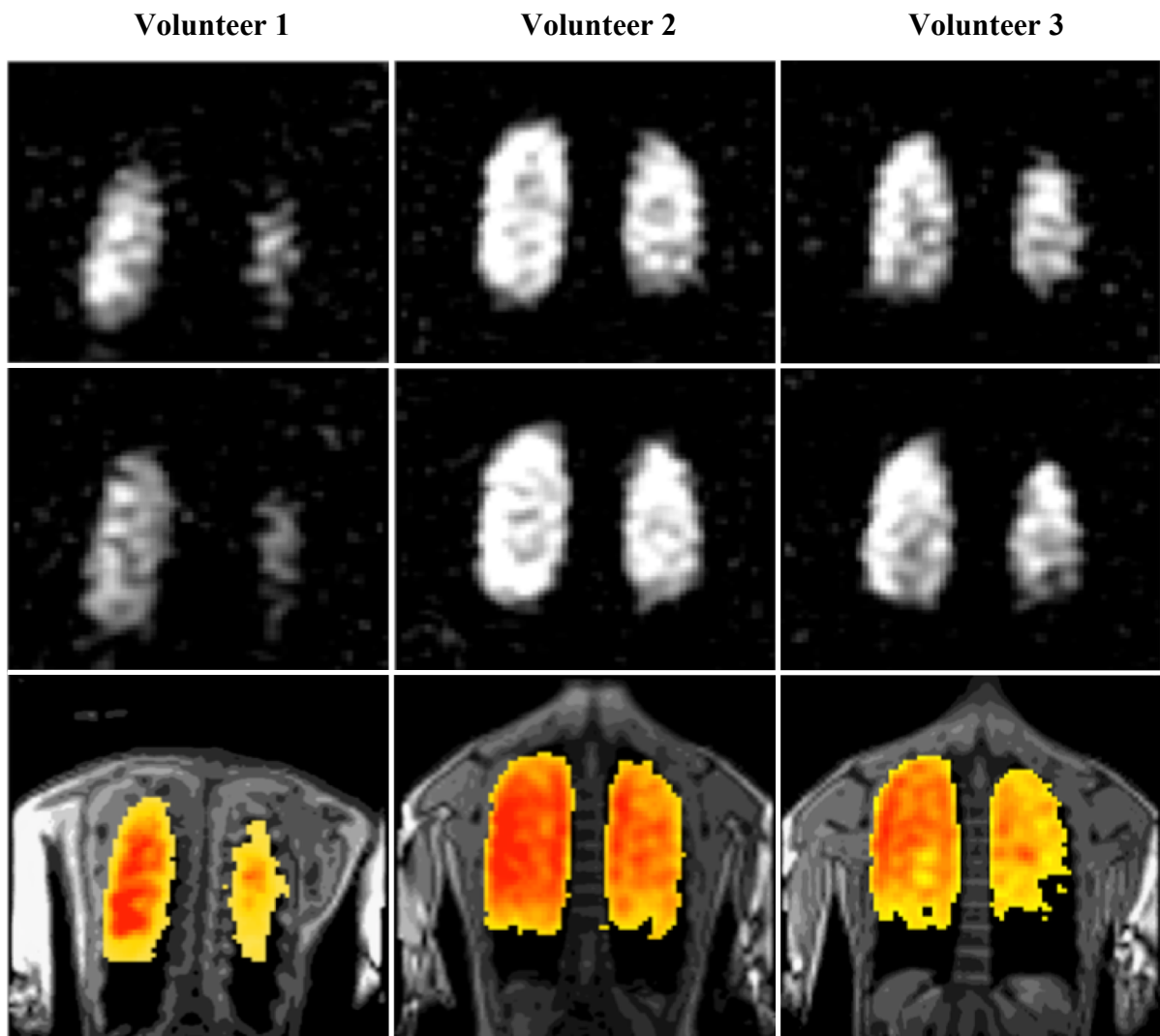


**Figure 2-4:** Rows one and two: Slices in the coronal plane proximal to the coil from six  $^{19}\text{F}$  3D SPGR acquisitions in three healthy volunteers. All were acquired within a 15 s breath hold duration after wash-in of PFP/ $\text{O}_2$ . Row three: Masked  $^{19}\text{F}$  signal overlaid on an anatomical proton image.

Figure 2-4 illustrates the good intra-volunteer reproducibility of the technique, and the variable signal distribution between volunteers. The absence of signal in the base of the lungs represents the small sensitive volume of the surface coil. Notably, analysis only of slices proximal to the coil (in the same coronal plane as the subjects' spines) was performed due to exponential signal decay with distance. This is illustrated in Figure 2-5a, which plots the average SNR loss ( $\pm$ SD) in the A-P direction from three measurements in a representative subject. Example images at three A-P distances is also shown.

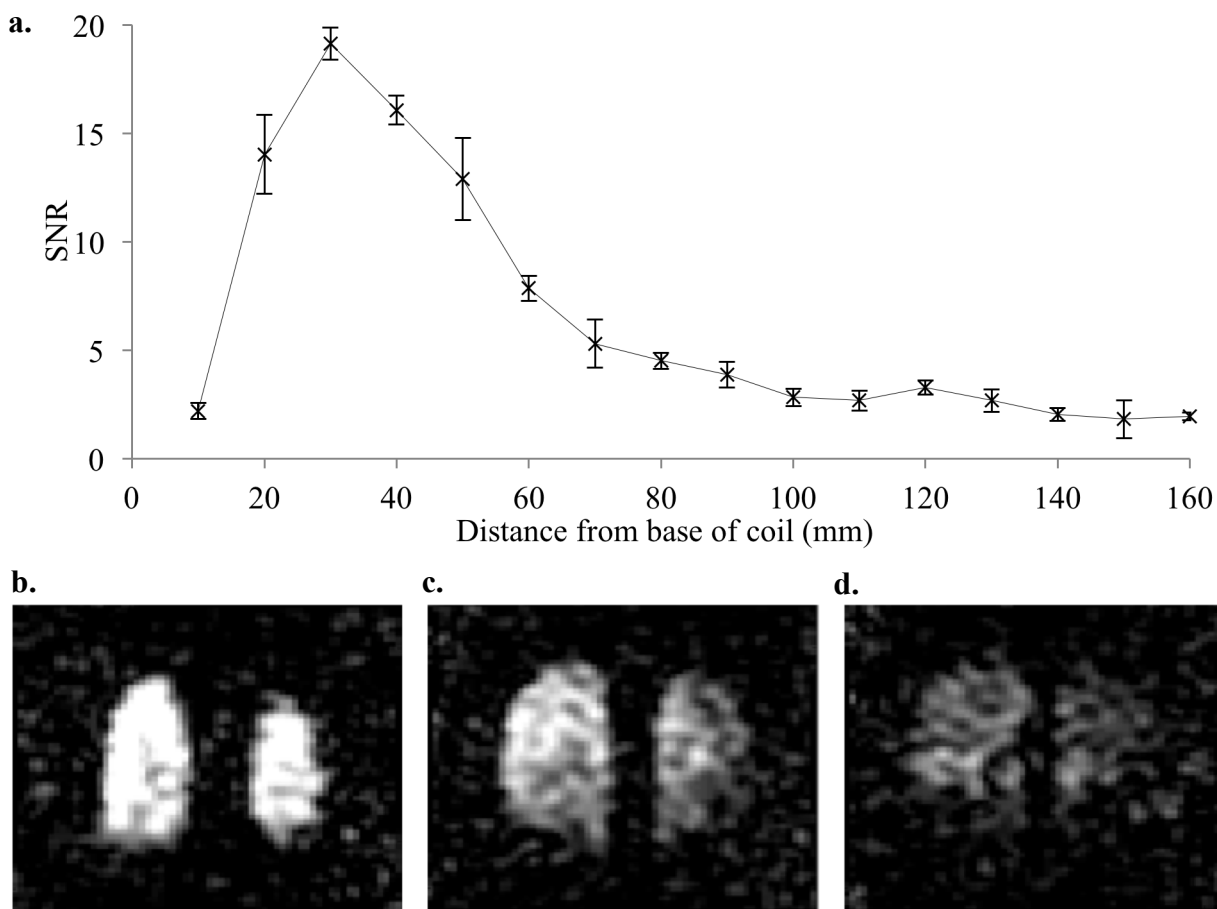


**Figure 2-5:** **a.** SNR over distance from coil surface. High SNR seen posteriorly, proximal to the coil surface, with exponential loss of signal over the following 10 cm. **b.** Image of slice at 30 mm distance from coil surface. **c.** Image of slice at 50 mm. **d.** Image of slice at 70 mm.

### 2.3.2 Assessment of gas wash-in and wash-out rate

The resulting SNR after one, two, and three deep wash-in inhalations of PFP/O<sub>2</sub> was calculated from twelve scan sessions (one per subject). An increase in mean SNR and decrease in its standard deviation was seen as the wash-in progressed, from SNR =  $9.7 \pm 2.9$

after the first inhalation, to  $12.8 \pm 2.3$  after the second inhalation, and  $14.3 \pm 1.9$  after the final inspiration. The results are displayed in Figure 2-6, alongside the same results displayed as a percentage of their final SNR.

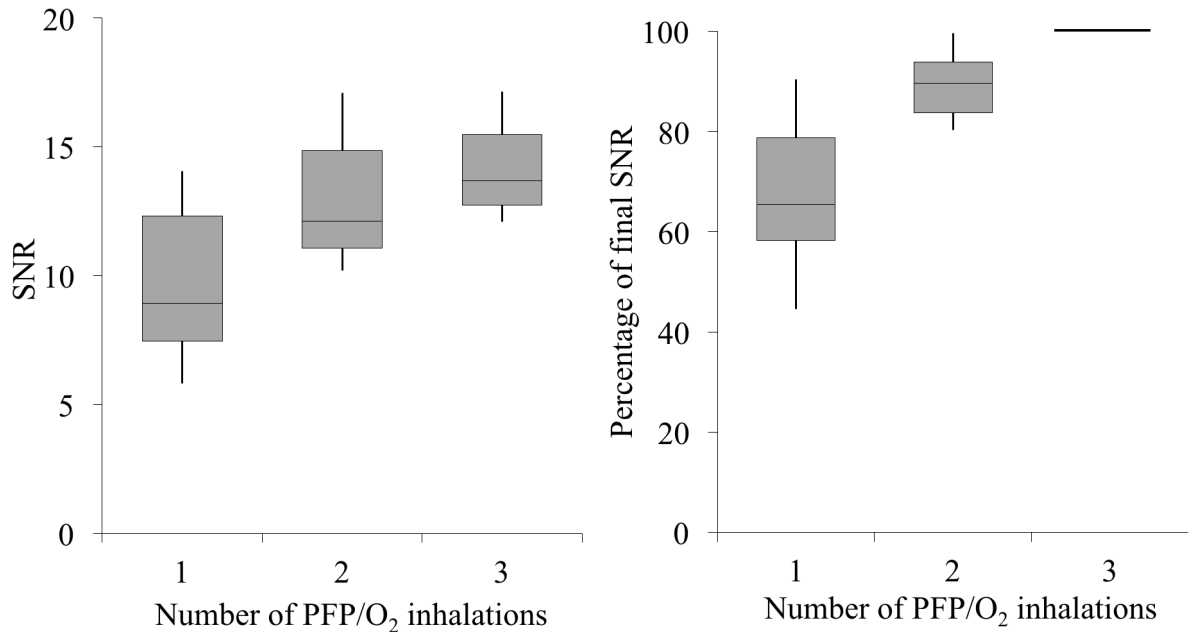


**Figure 2-6:** SNR change over three deep inhalations of PFP/O<sub>2</sub> gas, also displayed as percentage change. With increased wash-in an increase in SNR and a reduction in range is noted. The box plots display the mean SNR (horizontal line) and interquartile range. The error bars denote the minimum and maximum SNR values measured.

It was found that the SNR range decreases with the number of inhalations despite poor inter-volunteer reproducibility. The average increase in SNR between inhalations one and two was 32%. This decreased to 12% between inhalation two and three, suggesting that near maximal wash-in is being achieved in this region of the lung after three inhalations. Fitting the mean SNR values to a recovering exponential curve suggests that a maximum mean SNR is 14.7, which is achieved in upwards of 5 inhalations. This confirms the adequacy and efficiency of performing a three-inhalation wash-in after which an only slightly smaller mean SNR of 14.3 is achieved.

Three wash-out respiratory cycles following the above wash-in protocol reduced the mean SNR from  $14.3 \pm 1.9$  to  $2.5 \pm 1.2$ . The results are summarised in Figure 2-7. Fitting to a decaying exponential determines that approximate complete wash-out (in this case where mean SNR is equal to the minimum value to 1-decimal place) occurs after five deep wash-out respiratory cycles.

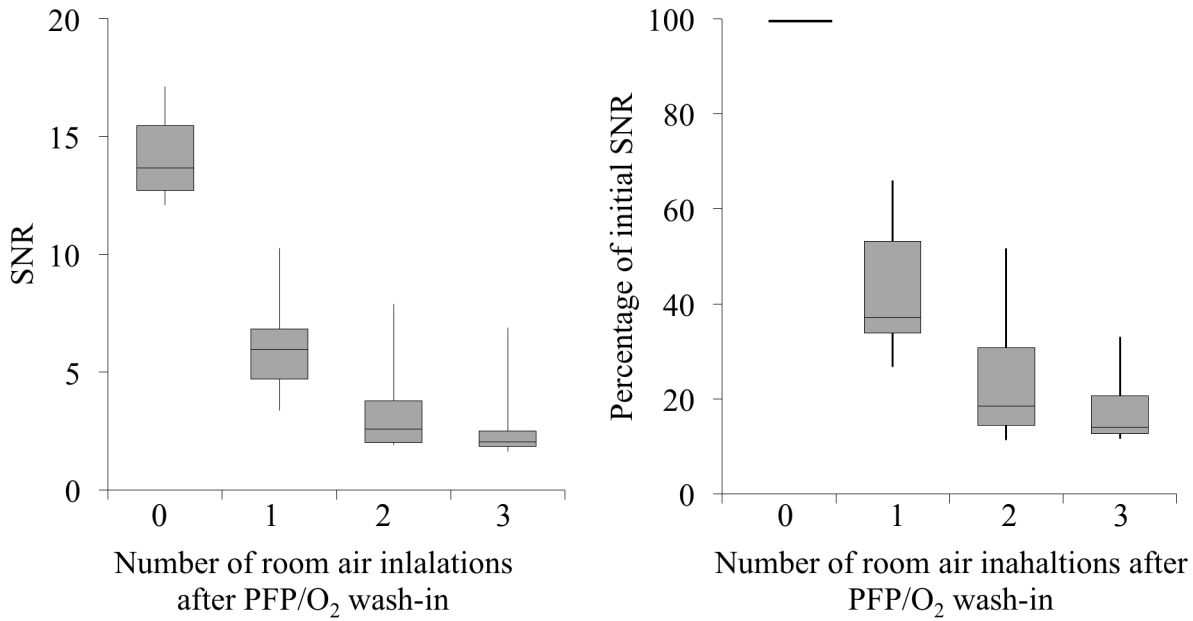


**Figure 2-7:** SNR change over three deep inhalations of room air after three wash-in inhalations of PFP/O<sub>2</sub>, also displayed as percentage change. The box plots display the mean SNR (horizontal line) and interquartile range. The error bars denote the minimum and maximum SNR values measured.

### 2.3.3 *In vivo measurement of T<sub>2</sub>\**

Figure 2-8 plots representative FIDs measured at full expiration and full inspiration. This shows the average signal drop-off from multiple T<sub>2</sub>\* values in the lung volume. For the purposes of this preliminary experiment, a simple monoexponential line of best fit was utilised and displayed on this plot to approximate the average T<sub>2</sub>\* values. This was calculated by direct fitting of  $S = S_0 e^{-TE/T_2^*}$  in Matlab (R2014a, USA) with no noise flooring constant due to negligible noise levels being present. Multiple initial approximations of S<sub>0</sub> and T<sub>2</sub>\* were used to verify the robustness of the calculated fit.

The average T<sub>2</sub>\* measured at full inspiration after three deep wash-in inhalations of PFP/O<sub>2</sub> was 1.7 ± 0.26 ms. At full expiration, the T<sub>2</sub>\* was seen to reduce to 1.3 ± 0.3 ms.

A key observation made was that T<sub>2</sub>\* varied as a function of place in the respiratory cycle. The fluctuation of T<sub>2</sub>\* over the respiratory cycle is shown for a representative volunteer in Figure 2-9. PFP/O<sub>2</sub> inhalations occurred at zero and twelve seconds. An inhalation of room air occurred at 28 seconds. The horizontal sections represent periods where the volunteer held their breath.

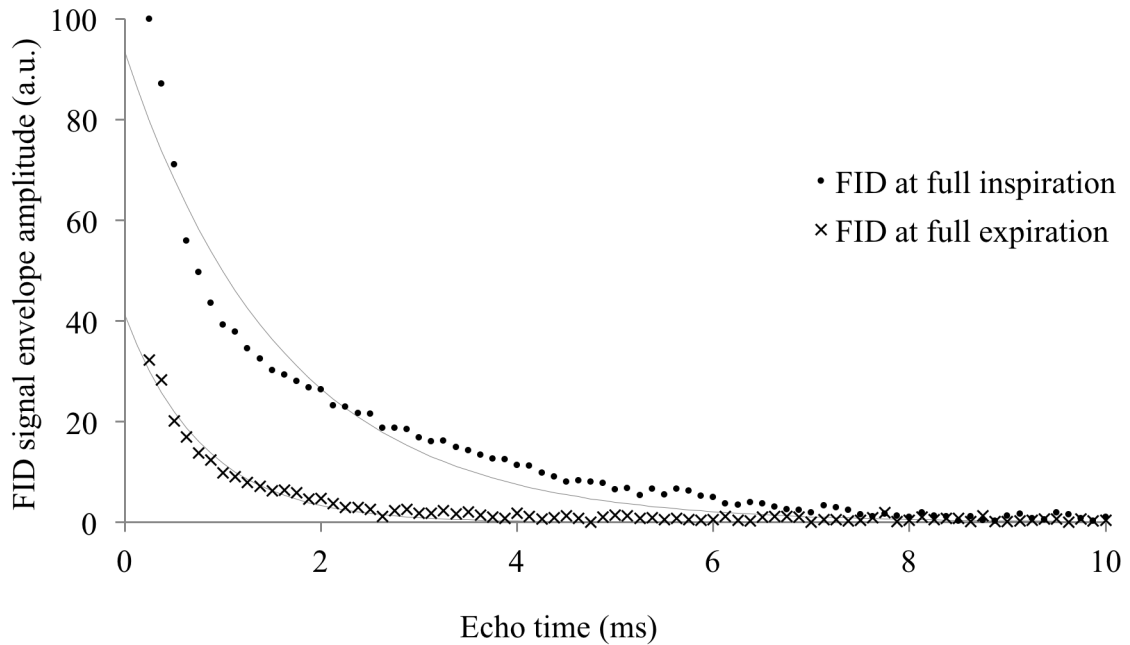


**Figure 2-8:** FID decay curves at full inspiration and expiration, with solid lines denoting monoexponential fits. The poor fit is due to the unlocalised FID signals representing poly-exponential  $T_2^*$  decay averaged over all regions in the sensitive volume of the coil.

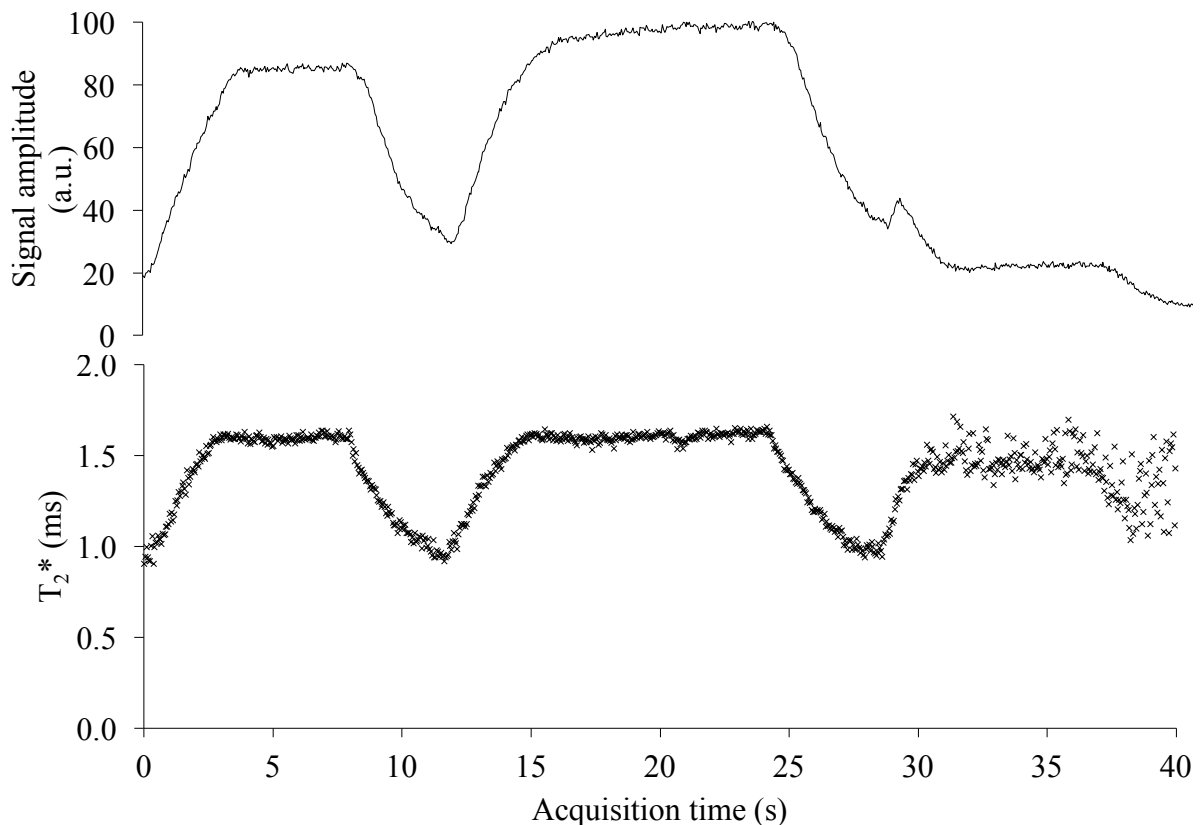


**Figure 2-9:** Change in PFP  $T_2^*$  over the respiratory cycle. The relative signal amplitude (upper curve) is indicative of the position in the respiratory cycle when inhaling PFP/ $O_2$ . The  $T_2^*$  follows the same pattern. Notably, in the final 10 s, a wash-out inspiration of room air is performed causing the signal amplitude to stay at the level at expiration, whereas the  $T_2^*$  increases.

## 2.4 Discussion

The rate of PFP wash-in over three respiration cycles resembles an approximate exponential curve. In this case, further inhalations would continue to increase the SNR, but by a considerably reduced amount that is likely to be of minimal benefit for vital capacity scans, which has been the primary focus of this study to date. Therefore, for future healthy volunteer scans, a minimum of two vital capacity inhalations is recommended, with three inhalations nearing maximal wash-in. This fast PFP/O<sub>2</sub> wash-in seen consistently in healthy volunteers offers a clear baseline to contrast with wash-in data from patients with COPD or asthma. The application of this information to imaging patients with lung disease will require a compromise between achieving an adequate SNR to produce clear images with good coverage in healthy areas of the lungs, and aiming to avoid wash-in to areas with airway obstruction, to allow clinically useful contrast in the image. The extent of PFP wash-in and gas diffusion this requires may vary between subjects, and cannot be decided without completing similar measurements on relevant patient groups.

To date insufficient wash-in data has been collected in our tidal breathing studies to draw any conclusions on wash-in rate. It is known that vital capacity breathing produces different lung expansion homogeneity than the more natural tidal breathing, but it is apparent that tidal breathing wash-in is particularly uneconomical and impractical as volunteer compliance and repeatability of respiration volumes is considerably harder to regulate, and a larger number of inhalations would be required to achieve satisfactory wash-in. For this reason, only deep inhalation protocols will be used in this work.

Also of note is that a previous study has measured an in vivo  $T_2^*$  of PFP –CF<sub>3</sub> in the lungs of 2.2 ms (Couch *et al.*, 2013), however preliminary unlocalised measurements in this work found that the value typically decreased to 1.3 ms upon exhalation, reaching values near 2 ms after deep inhalation. This change in  $T_2^*$  is postulated to be explained by the varying magnetic susceptibility gradients in the alveoli between inhalation and exhalation. The exact physiological cause of this is unknown, but could be the increased parenchymal surface area to alveolar volume ratio, or the increased ratio of parenchyma to gas seen at exhalation. These potential determinants of  $T_2^*$  in the human lung will be investigated in later chapters. This fluctuation in  $T_2^*$  may be more extreme in patients with alveolar damage. If this occurred, acquiring maps of PFP  $T_2^*$  in vivo could offer a useful measure of emphysematous areas of the lung. This would require a fast imaging protocol due to the high SNR required to calculate an accurate  $T_2^*$  map with adequate resolution within a breath hold. Optimisation of the

current imaging sequence is therefore necessary to achieve this, and is the focus of Chapter 4.

The very restricted sensitive volume of the surface coil compared to lung volume, both in the anterior to posterior direction as well as head to foot, compromised signal homogeneity in return for good SNR proximal to the coil. It would be expected that the necessary move to a coil with improved signal homogeneity and a larger sensitive volume would be at the cost of a lower SNR to that achieved in this study, the extent of which is investigated in the following chapter. In this case, the use of an optimised imaging sequence to maximise SNR for a volume coil will again be valuable.

## 2.5 Conclusions

This preliminary work has verified the utility of MRI as a pulmonary ventilation imaging technique at 3.0 T. Images with a SNR of 40 have been produced within a 15 s scan time at 1.0 cm<sup>3</sup> resolution.

The work has laid a solid foundation for future <sup>19</sup>F MRI studies, and identified several areas for improvement. These consist of: identification of a more suitable RF coil that provides full lung coverage, optimisation of the imaging protocol to maximise the SNR achieved in a breath-hold length scan time (with the understanding that using a different coil type will likely reduce the SNR), and development of new measures with which to assess lung function by further investigating the observed changes in T<sub>2</sub>\* with alveolar volume. These subjects are investigated in the following three chapters.

## **Chapter 3:**

### **<sup>19</sup>F Coil Construction and Assessment of Four <sup>19</sup>F Coil Designs for Suitability for Pulmonary Imaging**

#### **3.1 Overview**

The ideal RF coil design is highly dependent upon its application, as discussed in Section 1.2.8. Lung imaging necessitates use of a coil that offers a large homogeneous field of view in order to cover the entire thoracic cavity, whilst maintaining good power efficiency in order to maximise SNR and temporal resolution and comply with SAR constraints. The 20 cm diameter surface coil utilised in the previous chapter demonstrated adequately high SNR proximal to the coil, but offered a very restrictive sensitive volume. It is evident from the resulting images (eg. Figures 2-4 and 2-5) that a more suitable coil design is required to attain clinically useful images of pulmonary ventilation.

This chapter tests the hypothesis that <sup>19</sup>F MRI of perfluoropropane using a larger RF coil design produces images of satisfactory quality despite reduced power efficiency. To investigate this, a 40 cm long quadrature birdcage torso coil was designed and constructed. This allowed verification of the coil performance and method development work to be carried out before purchase of a commercial coil with similar geometry. Initial tuning was performed on the lab bench, before undergoing validation checks and assessment of the coils performance in a Philips Achieva 3.0 T system. This aimed to test the practicalities of using a coil geometry that provides a more suitable FOV but lower power efficiency.

The utility of four <sup>19</sup>F RF coils built to differing geometric specifications was then evaluated and compared with the aim of defining the most suitable of the four coil designs for this application. The coils were: a 20 cm diameter surface coil (PulseTeq, used in the previous chapter), a 50 cm long linear birdcage torso coil (Rapid Biomedical – installed at the Royal Children’s Hospital, Melbourne), a 50 cm long quadrature birdcage torso coil (Rapid Biomedical), and the 40 cm long in-house built quadrature birdcage torso coil. In each case, the achievable SNR, power efficiency, and image homogeneity were assessed.

## 3.2 Methods

### 3.2.1 Birdcage coil construction

A 16-rung birdcage coil was designed to be elliptical, fitting body morphology, with a height and width of 400 mm × 500 mm respectively. The coil was constructed on a shell fabricated out of 6 mm thick acrylic sheets, laser cut to shape using a template produced in CAD software (Inventor Professional 2015). Sixteen 400 mm long rungs were cut from 8 mm diameter hollow copper pipe. End rings were then constructed from single sided FR-4 copper-clad printed circuit board (PCB), sliced into thirty-two 16 mm wide strips using an industrial metal guillotine. The ends of each strip were cut to a taper, leaving thirty-two 3 mm spaces for capacitors to form two elliptical end rings (Figure 3-1). The copper legs were affixed between the two end rings by soldering strips of copper braid into the ends of the copper pipes, and onto the PCB strips through 8 mm diameter holes drilled centrally in each of the strips. The assembled coil structure is displayed in Figure 3-1.

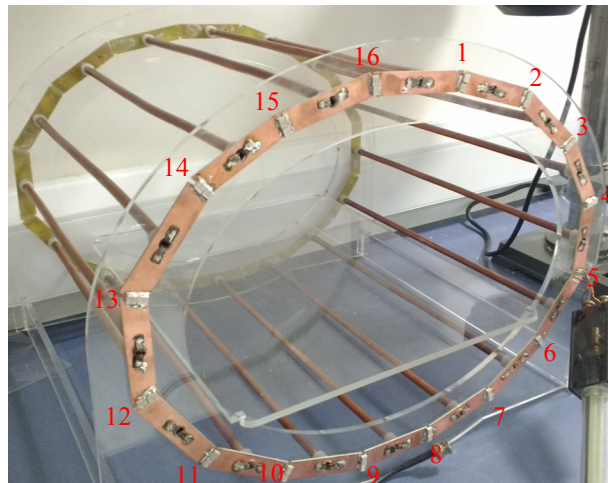


**Figure 3-1:** Structure of the completed coil frame. The coil is 400 mm long, and designed to be elliptical to maximise its sensitive volume. The 16 capacitor points are labelled.

Ceramic chip capacitors (Temex Ceramics, Fr.) were soldered between end ring PCB sections. Capacitance values were chosen using Birdcage Builder software developed by Penn State Hershey College of Medicine (Chin *et al.*, 2002). This software calculates the approximate capacitance distribution required around a birdcage coil of given dimensions. Figures 3-2a and 3-2b depict the input and output values of the software respectively.

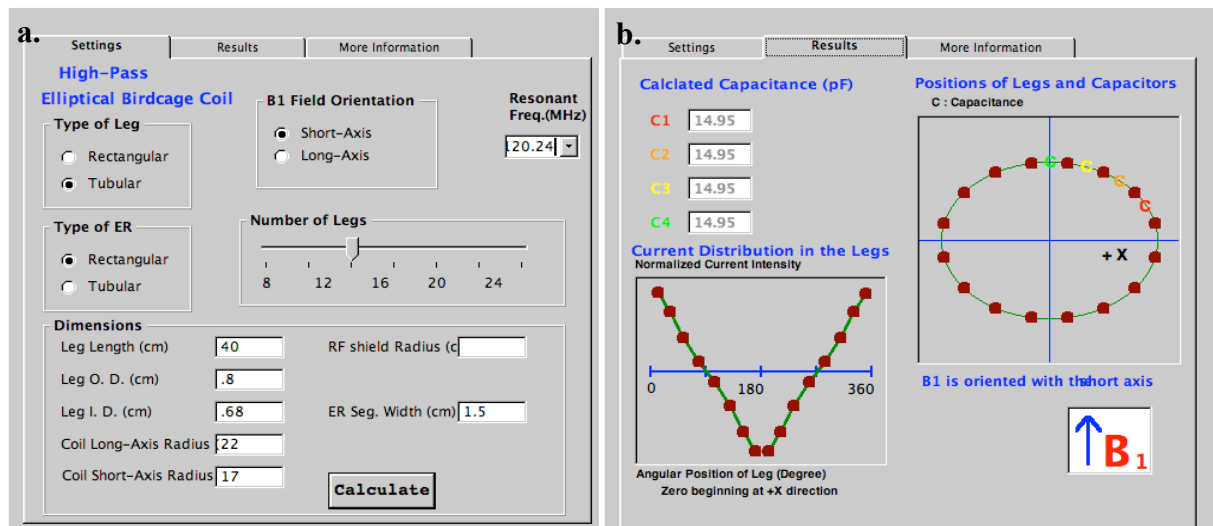


**Figure 3-2: a.** The dimensions and required resonant frequency of the birdcage coil specified in the Birdcage Builder interface. **b.** The fixed capacitance distribution output from the Birdcage Builder interface.

The estimated capacitance required at each point to tune the coil to the resonant frequency of  $^{19}\text{F}$  (120.24 MHz) was 14.95 pF. The calculated value was used as a starting point for tuning. The coil was tuned whilst driven in linear mode from the fourth capacitor junction clockwise from the top of the coil (at the right of the image displayed in Figure 3-1). Iterative adjustments of capacitance values at each point on the birdcage coil made until the resonant peak was tuned to 120.24 MHz using a network analyser.

The effective shielding produced around the birdcage coil when placed in the scanner bore resulted in a different tuning to that achieved on the lab bench. To overcome this, the scanner bore was simulated in the lab using an aluminium-lined cylinder of equal dimensions to the bore. A resonance at 120.24 MHz in the scanner bore and simulator was found to be equivalent to 109 MHz when measured on the lab bench. A capacitance of 16.8 pF at each capacitor point achieved resonant tuning. The tuned resonant peak is displayed in Figure 3-3.

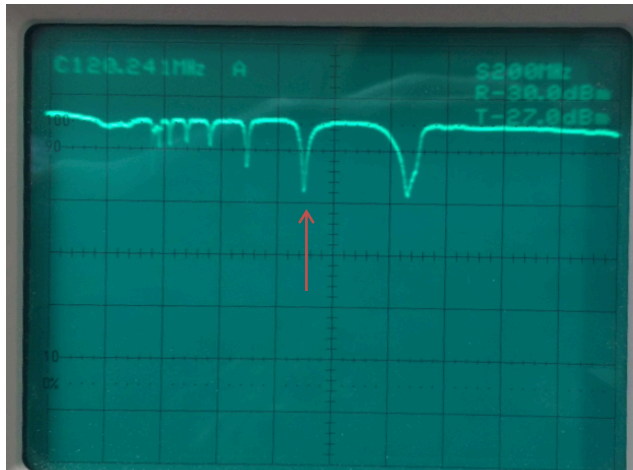


**Figure 3-3:** Spectra showing all eight resonant peaks. The target resonant peak (red arrow) is tuned to 109 MHz on the lab bench. This resonance shifted to 120.24 MHz when the coil was placed in the scanner bore or bore simulator.

The coil was constructed to be connected to the scanner via a set of variable capacitors, arranged as shown in Figure 3-4, to allow coil fine-tuning to  $^{19}\text{F}$  resonant frequency, and matching to  $50\ \Omega$ .

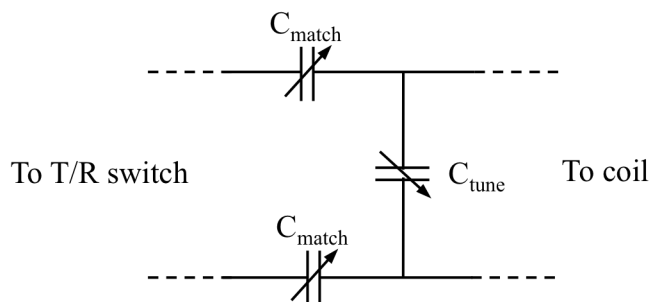


**Figure 3-4:** The tune and match circuit. The tuning capacitor is joined in parallel to the birdcage coil circuit, and the matching capacitors are connected in series.

After validation of acceptable tuning of the coil in linear mode, the coil was then modified to be driven in quadrature. This required driving the coil from two points that produce an equivalent resonant peak on the network analyser. These should appear at any two points that are  $90^\circ$  apart. However, our test measurements showed that this did not hold true in practice due to the elliptical shape of the coil. The resonant frequency at each of the 16 potential input points was measured by interchanging the capacitor at each point for the cable/tune/match circuit. The values achieved are depicted in Figure 3-5. Using these values, the two driving ports chosen were points 7 and 11 (labelled in Figure 3-1), which both recorded peaks of 109.0 MHz on the lab bench.

Location number	Resonant frequency on bench (MHz)
1	109.0
2	109.0
3	110.4
4	110.5
5	113.0
6	109.7
7	109.0
8	108.0
9	108.0
10	109.0
11	109.0
12	109.5
13	110.0
14	110.5
15	109.3
16	109.0

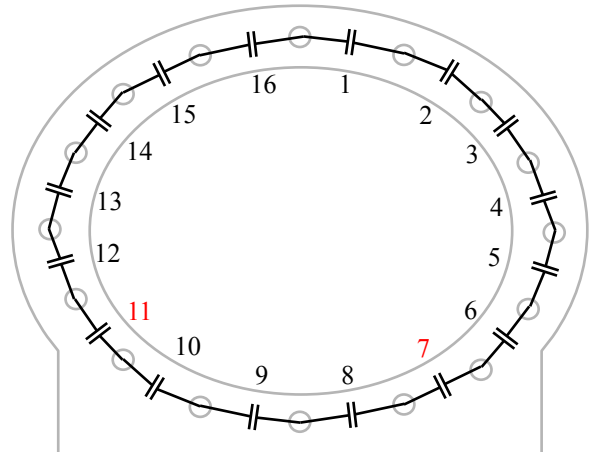


**Table 3.1:** The resonant frequency achieved on the lab bench when driven via each of the 16 port locations. Here, 109 MHz equates to achieving the  $^{19}\text{F}$  resonant frequency (120.24 MHz) in the magnet bore.

**Figure 3-5:** For successful quadrature use, the coil must be driven by two points with  $90^\circ$  separation that have approximately equal resonant frequencies. It was decided that points 7 and 11 most closely match these requirements.

### 3.2.2 Assessment of RF coil power performance

The four coils assessed in the following subchapters are displayed in Figure 3-6.

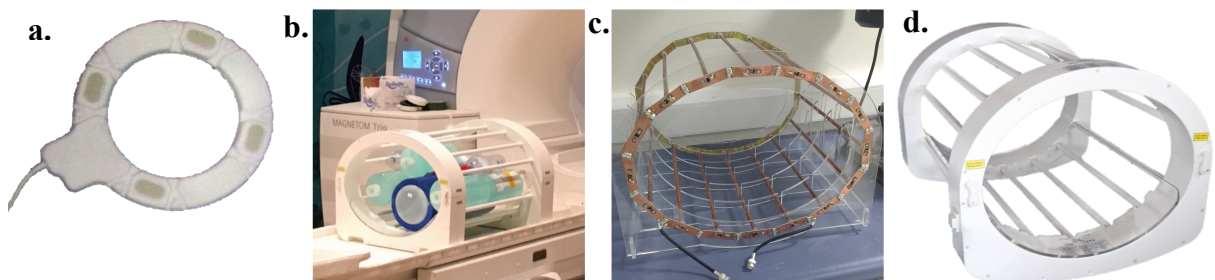


**Figure 3-6:** The four transmit-receive coils assessed. **a.** 20 cm diameter surface coil (PulseTeq Ltd.). **b.** 50 cm long linear birdcage coil in situ at the Royal Children’s Hospital, Melbourne (Rapid Biomedical). **c.** 40 cm long birdcage coil (constructed in-house). **d.** 50 cm long quadrature birdcage coil (Rapid Biomedical).

The quadrature in-house birdcage coil was calibrated to produce an  $180^\circ$  flip when  $180^\circ$  was requested on the scanner interface using a phantom composed of a 2 L bottle filled with 79%  $\text{C}_3\text{F}_8$  and 21%  $\text{O}_2$  (PFP/ $\text{O}_2$ ), positioned centrally in the coil. Once calibrated, the power handling performance under larger loading volumes could be tested. A pulse-acquire sequence was used with requested flip angles arrayed from  $10^\circ$  to  $300^\circ$  in  $10^\circ$  increments. The

flip angle analysis was carried out with the coil loaded with 4 L, 8 L, and 18 L volumes of loading solution (Rapid Biomedical standard phantom solution containing 5.0 g NaCl and 3.8 g NiSO<sub>4</sub>·6H<sub>2</sub>O in 1.0 L distilled water), in order to quantify the effect of loading on the flip angle produced. The above protocol was repeated on the commercially built quadrature birdcage coil in order to compare power performance. From these power measurements, the loading factor, defined as the factor the requested flip angle had to be changed by to achieve the desired flip angle, for each volume of loading was determined.

The achievable B<sub>1</sub> amplitude is proportional to the square of the peak power. Coil performance can therefore be quantified and compared by calculating  $B_1/\sqrt{P}$ , where  $P$  is the amount of power deposited in a coil to achieve a specified B<sub>1</sub>. This measure describes the power efficiency of the coil. This value was assessed for each of the four coils with no loading, and when heavily loaded with 18 L of loading solution.

### **3.2.3 Measurement of achievable SNR in four coils**

The signal-to-noise ratio achievable with each of the coils was determined. Acquisitions were carried out on a 2 L PFP/O<sub>2</sub> phantom, positioned centrally in the coil. The acquisition using the 50 cm linear birdcage coil was conducted on a Siemens MAGNETOM Trio 3.0 T at the Royal Children's Hospital, Melbourne. All other images were acquired on a Philips Achieva 3.0 T system at the Newcastle Magnetic Resonance Centre.

A 3D spoiled gradient echo (SPGR) acquisition sequence was implemented on each of the scanner and hardware configurations, and were designed to be as similar to each other as practically feasible. Table 3.2 shows SPGR acquisition parameters, each imaging sequence was considered the best achievable for the hardware set-up with the minimum achievable TE and TR used in each case. The most notable difference was seen in the repetition time, which stemmed from differing limitations on the maximum average RF power allowed in each configuration. This reflects the fact that the power restrictions for the birdcage coils are limited by a combination of several factors, namely component heating, scanner software limits, SAR restrictions, and the maximum allowed power from the amplifier, whereas the surface coil power restrictions were much more permissive due to its more efficient power handling. Therefore, component heating primarily restricted surface coil RF power limits. The minimum achievable echo times were restricted by RF pulse duration, determined by the maximum permitted peak power of the pulse. Opportunity for quantitative comparison is therefore limited, however an insight into the general practical performance of coils in a

breath hold length scan time was obtained.

	<b>40 cm quadrature birdcage coil, built in-house</b>	<b>20 cm surface coil, PulseTeq</b>	<b>50 cm linear birdcage coil, Rapid</b>	<b>50 cm quadrature birdcage coil, Rapid</b>
<b>Acquisition sequence</b>	3D SPGR	3D SPGR	3D SPGR	3D SPGR
<b>Field of view (mm<sup>3</sup>) H-F × L-R × A-P</b>	400 × 400 × 300	400 × 400 × 160	400 × 400 × 160	400 × 400 × 150
<b>Voxel size (mm<sup>3</sup>)</b>	10 × 10 × 10	10 × 10 × 10	10 × 10 × 10	10 × 10 × 10
<b>Flip angle</b>	50°	50°	45°	50°
<b>Bandwidth (Hz/pixel)</b>	500	500	500	500
<b>Echo time (ms)</b>	0.70	1.50	1.64	1.72
<b>Repetition time (ms)</b>	10.0	4.1	7.5	15.1
<b>k-space under sampling pattern</b>	Half-scan	Elliptical filter	None	Half-scan
<b>Number of averages × length</b>	3 × 4.38 s = 13.4 s	7 × 2.06 s = 14.4 s	3 × 4.80 s = 14.4 s	2 × 5.80 s = 11.6 s

**Table 3.2:** Acquisition parameters used to measure SNR in breath hold length scan times. Values were chosen to be as similar as feasible whilst selecting close to the optimal achievable parameter values for each hardware set-up. The number of averages was selected to provide an acquisition length representative of a breath hold length scan (10 - 15 s) to compare practical performance. In all cases, the acquisitions had an elliptical k-space filter applied.

### 3.2.4 Assessment of signal homogeneity in four coils

Signal homogeneity was assessed in all coils using a 3D SPGR imaging sequence with acquisition parameters as shown in Table 3.3. The images were acquired over a minimum FOV of 400 mm in the head-foot (H-F) and left-right (L-R) dimensions, and a minimum of 300 mm in the anterior-posterior (A-P) dimension. As only relative signal homogeneity was compared with these acquisitions, the acquisition parameters used were not required to be comparable. A PFP/O<sub>2</sub> phantom that filled the full sensitive volume of each coil was used to detect the signal over the volume. The signal intensity was then measured along the central axis in each dimension.

	<b>40 cm quadrature birdcage coil, built in-house</b>	<b>20 cm surface coil, PulseTeq</b>	<b>50 cm linear birdcage coil, Rapid</b>	<b>50 cm quadrature birdcage coil, Rapid</b>
<b>Acquisition sequence</b>	3D SPGR	3D SPGR	3D SPGR	3D SPGR
<b>Field of view (mm<sup>3</sup>) H-F × L-R × A-P</b>	400 × 400 × 300	400 × 400 × 300	500 × 500 × 320	530 × 530 × 400
<b>Voxel size (mm<sup>3</sup>)</b>	10 × 10 × 10	10 × 10 × 10	10 × 10 × 10	10 × 10 × 10
<b>Flip angle</b>	50°	50°	45°	90°
<b>Bandwidth (Hz/pixel)</b>	500	500	500	500
<b>Echo time (ms)</b>	0.70	1.50	1.56	1.68
<b>Repetition time (ms)</b>	10.0	4.1	30.0	100.0

**Table 3.3:** Acquisition parameters used to test relative signal homogeneity within the coil volume.

### 3.3 Results

#### 3.3.1 Assessment of RF coil power performance

The flip angle analysis confirmed that an 180° flip was achieved at a requested 180° flip angle for the unloaded in-house built birdcage coil in the chosen configuration. The flip angle array spectra are shown in Figure 3-7.

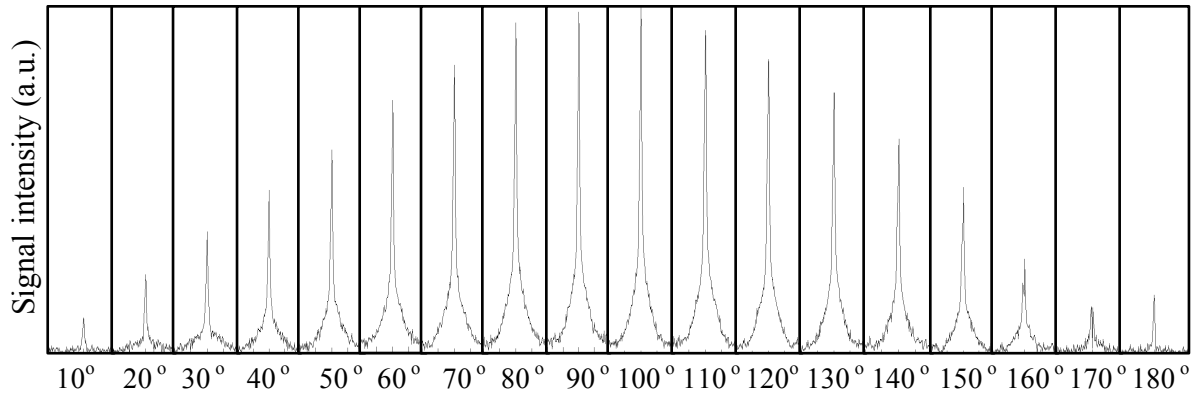


**Figure 3-7:** Spectra from a flip angle array of the unloaded in-house built birdcage coil. The peak (90°) signal is seen when a ~90° flip angle is requested. This maximal signal intensity shifts to the right (i.e. the achieved 90° occurs at a requested flip >90°) when the coil is loaded.

Figure 3-8 displays how the actual flip angle varied with requested flip angle when the loading in both the in-house and commercially built coils were increased from 0 L to 18 L of loading solution.

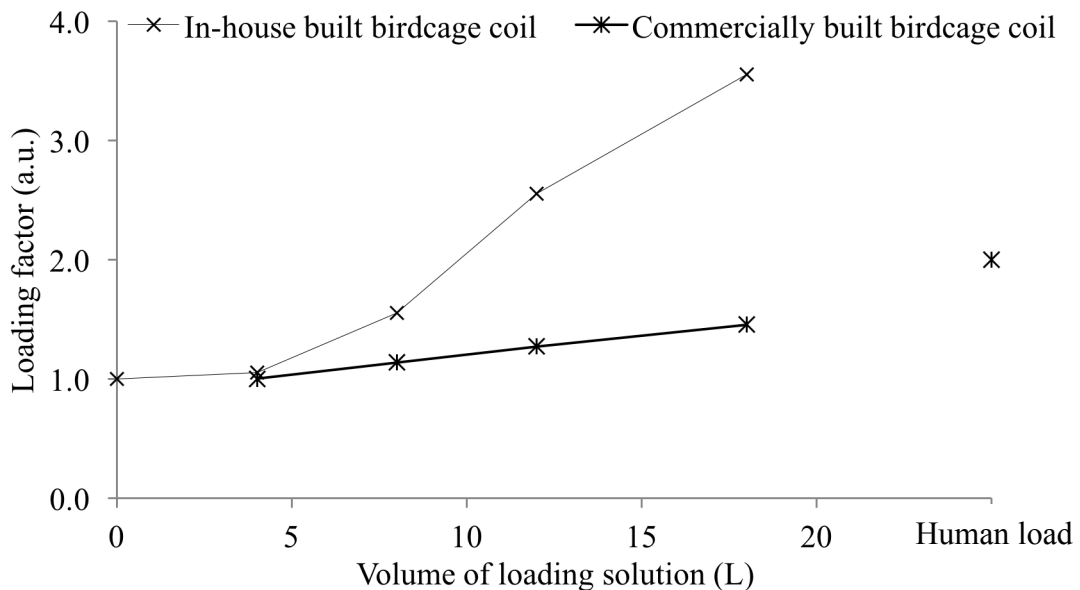


**Figure 3-8:** Comparison of coil efficiency when loaded with large volumes of loading solution in the in-house built and commercially built quadrature birdcage coils. A data point for human loading in the commercially built coil is also shown.

This demonstrates that the in-house built coil's performance is greatly affected by relatively small amounts of loading. In order to calibrate the coil when loaded with 18 L of solution, a 12.6-fold increase in RF power would be needed. This is less problematic for phantom experiments, for which this coil was designed, where loading can be minimised.

With human loading, the commercially built birdcage coil achieves only half the flip angle achieved with no loading. Also of note is the poor approximation to human loading that even a large volume of commercially used phantom solution provides. Higher conductivity phantoms (constructed from sodium chloride solutions of varying concentrations) were also found to be poorly representative of a human load.

The  $B_1/\sqrt{P}$  values for the unloaded coils and heavily loaded coils respectively are displayed in Table 3.4

	<b>40 cm quadrature birdcage coil, built in-house</b>	<b>20 cm surface coil, PulseTeq</b>	<b>50 cm linear birdcage coil, Rapid</b>	<b>50 cm quadrature birdcage coil, Rapid</b>
$B_1/\sqrt{P}$ ( $\mu\text{T W}^{-\frac{1}{2}}$ ) <b>0 L loading</b>	0.28	0.25	0.25	0.21
$B_1/\sqrt{P}$ ( $\mu\text{T W}^{-\frac{1}{2}}$ ) <b>18 L loading</b>	0.11	0.25	0.17	0.14
<b>Maximum achievable <math>B_1</math>, low-load phantom (<math>\mu\text{T}</math>)</b>	8	8	10	8
<b>Maximum achievable <math>B_1</math>, human load (<math>\mu\text{T}</math>)</b>	-	8	-	4

**Table 3.4:** The power efficiency measured in four coils with zero loading and heavy loading. The maximum achievable  $B_1$  with low loading and human loading is also displayed. No human studies were carried out on the 40 cm birdcage or 50 cm linear birdcage, so respective loading data is not available. The difference in  $B_1/\sqrt{P}$  values in the first two rows describes the power efficiency of the coil under loading. This change is reflected in the achievable  $B_1$  values.

Comparison of the power efficiency of the surface coil and the commercially built quadrature birdcage coil with human loads was made.

During the preliminary healthy volunteer study (Chapter 2), the surface coil achieved an 8  $\mu\text{T}$   $B_1$  when receiving a peak power of 1 kW from the scanners RF amplifier. This is in contrast to the birdcage coil, which achieved a maximum  $B_1$  of 4  $\mu\text{T}$  when receiving a peak power of 1.5 kW from the RF amplifier (Figure 3-8). In order to achieve an 8  $\mu\text{T}$   $B_1$  on the birdcage

coil with a human load, 6 kW of power would be needed.

Although the Philips Achieva multi-nuclear RF amplifier outputs a peak power of 4 kW, 1.5 kW was the maximum amount of power available to this birdcage coil due to power being attenuated in the transmission chain elements, namely the cable, T/R switch, and the coil connector socket.

### 3.3.2 *Measurement of achievable SNR in four coils*

The SNR achieved in comparable scans using each of the four coils is listed in Table 3.5.

	<b>40 cm quadrature birdcage coil, built in-house</b>	<b>20 cm surface coil, PulseTeq</b>	<b>50 cm linear birdcage coil, Rapid</b>	<b>50 cm quadrature birdcage coil, Rapid</b>
<b>SNR achieved in breath hold length scan</b>	21.8	64.4	18.7	27.7
<b>SNR achieved in a single dynamic</b>	12.6	24.3	10.8	19.6

**Table 3.5:** SNR measured in the four coil designs using similar acquisition parameters, all achieved in a 10-15 s acquisition time.

Notably, the 50 cm quadrature coil offered the highest SNR of the birdcage coil designs, despite acquisition with the longest TE and TR, and shortest scan time. There are likely several contributory factors that cause this including its comparably good power handling efficiency with loading to the in-house built birdcage coil, and the Philips 3.0 T magnet operating at a slightly higher field strength in practice than the Siemens system utilised for the linear birdcage coil.

### 3.3.3 *Assessment of signal homogeneity in four coils*

The signal homogeneity (normalised to percentage of each coil's maximum value) for the four coils is displayed in Figure 3-9. The three graphs depict the change in SNR in the anterior-posterior direction, head-foot directions, and left-right directions respectively.

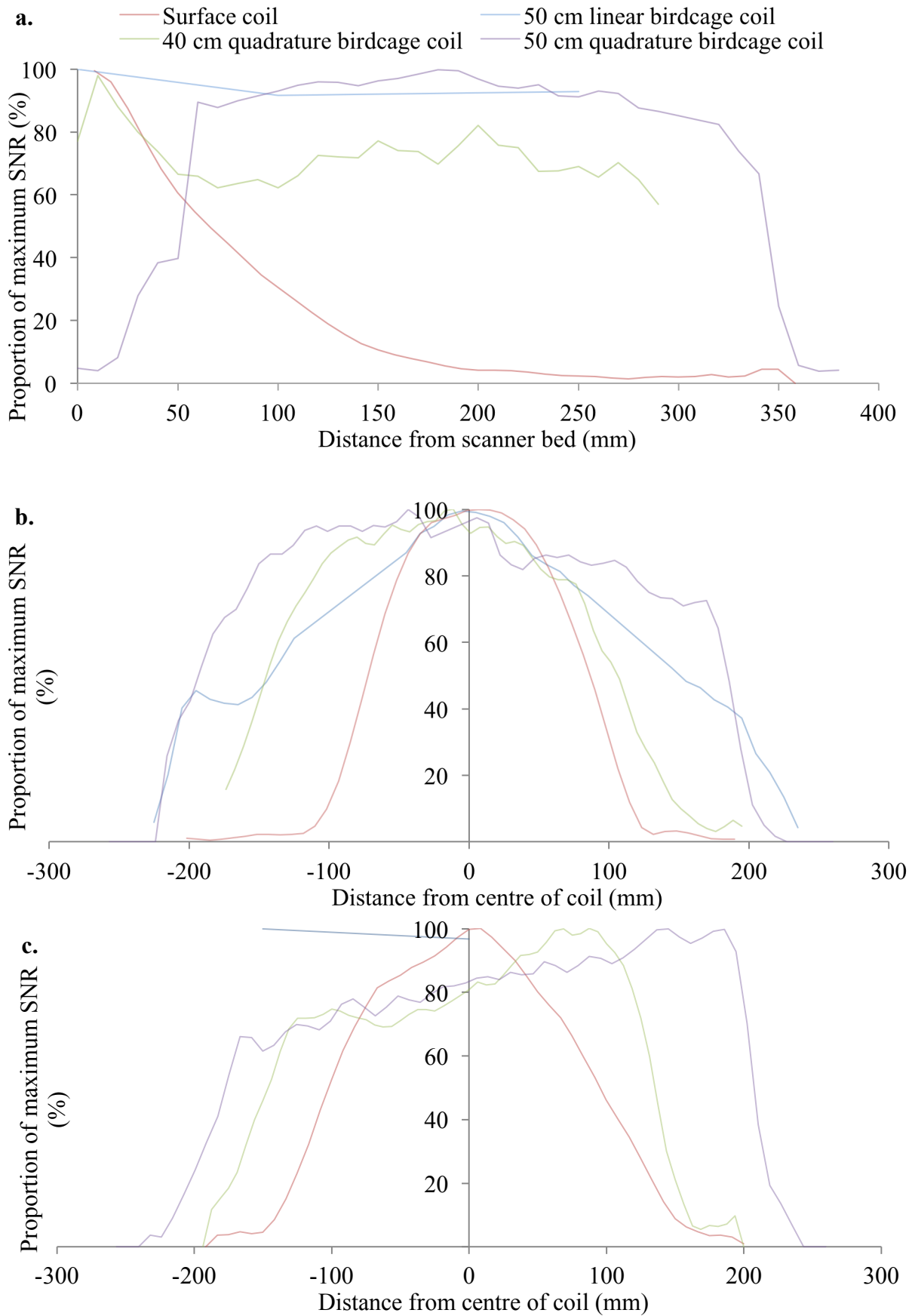


**Figure 3-9:** **a.** Signal homogeneity in the anterior-posterior direction. **b.** Signal homogeneity in the head-foot direction. **c.** Signal homogeneity in the left-right direction. Only limited data was collected for the linear birdcage coil based at the RCH.

In Figure 3-9a, for the surface coil, the signal measurement starts at the coil surface (where the signal is maximal) and extends 300 mm in the anterior direction. In Figures 3-9b and 3-9c, the x-axis scale marks the isocentre of the scanner bore, and the approximate centre point of the coil, as 0 mm.

The signal homogeneity, here defined as percentage signal drop-off across the centre 300 mm region of interest (chosen to approximate the linear dimensions of the thoracic cavity) in each of the three dimensions is displayed in Table 3.6. The values were calculated using:  $100 - \left( \frac{\text{minimum signal}}{\text{maximum signal}} \times 100 \right)$  where a high percentage represents a highly inhomogeneous signal.

	<b>Signal inhomogeneity within 300 mm imaging volume (%)</b>		
	<b>L-R</b>	<b>A-P</b>	<b>H-F</b>
<b>Surface coil</b>	92	98	97
<b>50 cm linear birdcage coil</b>	4	8	52
<b>40 cm quadrature birdcage coil</b>	67	43	43
<b>50 cm quadrature birdcage coil</b>	55	25	21

**Table 3.6:** Percentage signal drop-off measured along each dimension. The surface coil has notably poor signal homogeneity. The 50 cm quadrature birdcage coil offers the most homogeneous coverage along the length of the lungs.

### 3.4 Discussion

Perfluoropropane exhibits a very short  $^{19}\text{F}$ - $\text{CF}_3$   $T_2^*$  in vivo (Couch *et al.*, 2013), combined with a low signal density in the gaseous phase. Imaging pulmonary ventilation also requires acquisition of images covering the relatively large FOV of the full thoracic cavity within a short (ideally breath hold length) scan time. Due to these challenging imaging criteria, the ideal coil design for  $^{19}\text{F}$  imaging inhaled PFP would reflect these practical requirements, and exhibit a large and homogeneous sensitive volume covering the entire thoracic cavity, as well as efficient RF power handling required to obtain short TR and TE.

Acquiring human in vivo data on each of the coils was not feasible, and there are other coil designs that were not explored, but may be well suited to this application. Insight from research into hyperpolarised lung imaging research groups suggests that another suitable RF coil option would be a flexible design that conforms to the volunteers' torso (Rao and Wild, 2016). This would offer improved power efficiency compared to the birdcage design, as the sensitive volume of the coil is always close to the torso with minimal wasted volume. This coil design was not investigated here, but future research may benefit from improvements it can offer.

Comparing the sensitive volume of the coils investigated here, the surface coil has been immediately identified as unsuitable for this imaging purpose primarily due to it having a small sensitive volume, resulting in inadequate lung coverage. Comparison of the birdcage coils noted that the longer 50 cm quadrature coil geometry offered a noticeable homogeneity advantage over the 40 cm coil design. Where a shorter coil could be theoretically built to offer better power efficiency than a 50 cm coil, our data show that the homogeneity across the central 30 cm (approximate lung length) is likely to be diminished considerably, thus making it a costly trade-off. Additionally, the 40 cm coil length design would necessitate more restrictive positioning by removing the option of acquisitions with the volunteers arms by their sides for the acquisitions.

By increasing the maximum  $B_1$  amplitude, minimum echo time can be reduced. This is particularly valuable in maximising PFP signal due to its short  $T_2^*$  in vivo. Therefore, the efficiency of a coil at converting peak power (limited by what the RF amplifier can produce, and what the electrical components of the coils can handle) into a  $B_1$  field is particularly pertinent for large volume coils that require considerably more power than smaller surface coils to produce the same  $B_1$  amplitude. The  $B_1/\sqrt{P}$  values calculated in this chapter quantify

the inescapable poor relative power efficiency of the birdcage coils to the surface coil under heavy loading. Therefore, in order to improve image quality in a birdcage coil design, higher input power is required. It was seen that a significant proportion of the peak power is lost in the transmission chain between the multi-nuclear amplifier and the coil; implementing hardware that allows parts of the scanner RF chain circuitry (specifically long cables and lossy T/R switches) to be bypassed could reduce this attenuation. However, this would deliver a higher average power to the subject, requiring a longer TR to maintain SAR limits. This trade-off will be investigated in the following chapter.

The 50 cm quadrature birdcage coil was chosen for use in upcoming studies. This is primarily due to it offering a large homogeneous  $B_1$  field. As power efficiency is low in large heavily loaded volume coils, and there is scarce signal in perfluoropropane in vivo, it is valuable to optimise the imaging protocol used in human acquisitions to ensure maximum SNR is achieved without exceeding SAR limitations. Development of an optimised imaging protocol and an assessment of the potential benefits of implementing the highest achievable scan duty cycle is discussed in the following chapter.

Improved SNR could be achieved in the future by utilising this birdcage coil in conjunction with a receive-only array coil that will offer the enhanced receive sensitivity seen in surface coil designs. However, the implementation of such hardware falls outside the scope of this thesis.

### 3.5 Conclusions

A quadrature birdcage torso coil was constructed to operate at 120.12 MHz at 3.0 T with satisfactory results in phantoms. A larger commercial birdcage coil was then ordered for human studies and tested. This commercial coil presented improved power efficiency with low load;  $B_1/\sqrt{P}$  values measured on the in-house built coil were in the same region as those achieved on a commercially built birdcage coil, however upon loading with phantoms a large decrease in power performance was noted. Although ill-suited to human use because of this, it enabled  $^{19}\text{F}$ -MRI development work in phantoms.

This chapter has quantified the benefits of a birdcage coil design over a surface coil for lung imaging and quantified the corresponding trade-offs in coil RF power requirements. SNR and homogeneity measurements were made in gas phantoms containing PFP/O<sub>2</sub>. The results of these measurements confirmed that the geometry of the 50 cm long quadrature birdcage coil demonstrated good suitability for lung imaging using perfluorinated imaging agents, albeit with the expected disadvantages regarding RF power requirements. This coil was therefore used for subsequent human studies.

## **Chapter 4:**

# **Development of an Optimised Acquisition Sequence for Imaging Inhaled Perfluoropropane**

### **4.1 Overview**

As discussed in detail in Section 1.3, the low molarity and short  $^{19}\text{F}$   $T_2^*$  ( $\sim 2$  ms) of inhaled PFP contribute to a scarcity of detectable MR signal. This is further compounded by the necessarily short acquisition time available when restricted to a single breath hold. It is therefore highly valuable to verify that the imaging protocol used is being applied optimally; this requirement was the motivation for the work presented in this chapter. Here, we aim to develop an acquisition protocol that produces highest achievable image quality in short scan times. This will be achieved by two means, as follows.

In this chapter, the 3D spoiled gradient echo imaging sequence has been optimised for the scanner and hardware configuration used on-site, namely a Philips Achieva 3.0 T system, in conjunction with a 50 cm long  $^{19}\text{F}$  tuned elliptical birdcage torso coil (Rapid Biomedical). RF power limitations, due to SAR regulations and hardware capabilities were accounted for in the simulation. The imaging parameters required to attain the maximum SNR available in a specified scan length were determined by simulating the acquisition sequence, and verified in vitro.

A scan acceleration technique, compressed sensing, was then applied to the optimised acquisition sequence. Three compressed sensing protocols were then tested on a PFP-filled resolution phantom. The resultant images were compared and analysed for loss of image quality to identify the limitations of the compressed sensing technique. Finally, the optimised and accelerated acquisition protocol was tested in vivo by imaging inhaled PFP in a healthy volunteer.

## 4.2 Derivation of the relative SNR achieved in a 3D SPGR pulse sequence

The 3D spoiled gradient echo acquisition sequence was modelled in Matlab to facilitate optimisation of the imaging sequence. This section describes the theoretical derivation undertaken to model the key imaging parameters for a 3D SPGR imaging sequence for specific coil and hardware configurations. This derivation from the Bloch equations is well established and further detail can be found across the literature (Bernstein *et al.*, 2004; Atlas, 2009). This equation was then modified to describe the effect imaging parameters have upon the SNR achieved when limited to a pre-defined acquisition length.

The 3D SPGR sequence is discussed in Section 1.2.6, and the pulse sequence diagram is repeated here, Figure 4-1, for ease of reference.

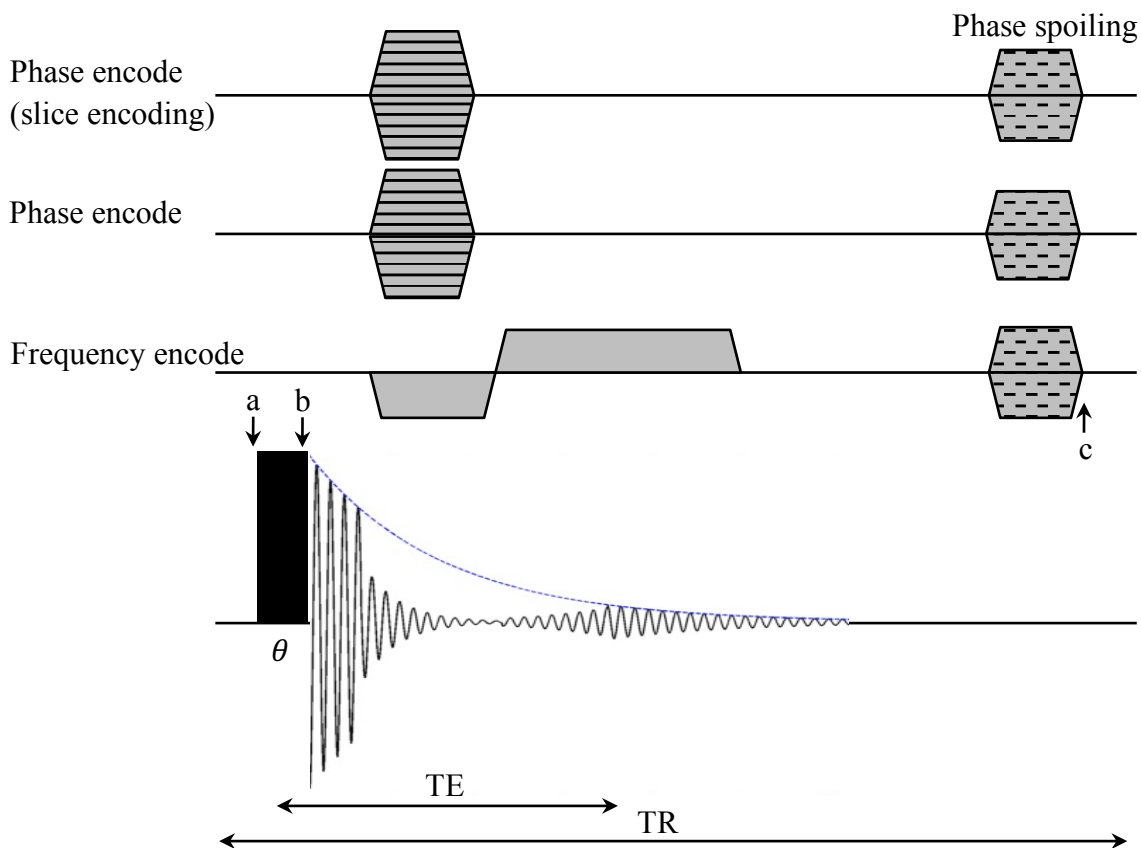


**Figure 4-1:** A 3D SPGR pulse sequence. This figure depicts a single repetition time, and the process must be repeated for multiple phase encode steps, and signal averages. The gradient spoiling results in a steady-state system, where the longitudinal magnetisation immediately before the pulse (labelled a) is equal to the longitudinal magnetisation after the gradient spoilers, c (immediately before the next pulse).

### 4.2.1 Sequence optimisation

The net magnetisation,  $M_{z,\text{before}}$ , begins in the longitudinal dimension,  $z$  (point a in Figure 4-1). After application of an RF pulse that imparts a flip angle,  $\theta$ , a proportion of that magnetisation is tipped into the transverse ( $x$ - $y$ ) plane, such that the amount of magnetisation remaining in the  $z$ -dimension,  $M_{z,\text{after}}$ , (point b in Figure 4-1) is:

$$M_{z,\text{after}} = M_{z,\text{before}} \cos\theta \quad 4.1$$

In a SPGR sequence where a train of RF pulses are used,  $M_{z,\text{after}}$  undergoes  $T_1$  relaxation in the time between the end of one excitation pulse and the start of the next (point c in Figure 4-1). The  $T_1$  relaxation process is described by the final term in the Bloch equation (Equation 1.8), as follows:

$$\frac{dM_z(t)}{dt} = \frac{1}{T_1} (M_0 - M_z(t)) \quad 4.2$$

Where  $M_0$  is the  $z$ -direction magnetisation at equilibrium after full relaxation, and  $M_z(t)$  is the time varying magnetisation caused by  $M_{z,\text{after}}$  undergoing  $T_1$  relaxation. This has the solution:

$$M_z(t) = M_0 + (M_{z,\text{after}} - M_0)e^{-TR/T_1} \quad 4.3$$

Substituting Equation 4.1 into this and rearranging yields:

$$M_z(t) = M_0(1 - e^{-TR/T_1}) + M_{z,\text{before}} e^{-TR/T_1} \cos\theta \quad 4.4$$

A spoiler gradient is applied to remove any transverse components of the steady state magnetisation.  $M_z(t) = M_{z,\text{before}}$  represents when the system has reached a steady state. In this case, Equation 4.4 is modified as follows:

$$M_{z,\text{before}}(1 - e^{-TR/T_1} \cos\theta) = M_0(1 - e^{-TR/T_1})$$

$$M_{z,\text{steady-state}} = \frac{M_0(1 - e^{-TR/T_1})}{1 - e^{-TR/T_1} \cos\theta} \quad 4.5$$

This is the  $z$ -direction steady-state magnetisation produced from a recurring pulse sequence with a specified flip angle and TR for a nucleus with known  $T_1$ .

Signal,  $S$ , which is measured in the x-y plane, and is proportional to the magnetisation in the z direction, decays according to  $T_2^*$ , labelled in Figure 4-1. This is described by the solution to the second Bloch equation, Equation 1.12, with the substitution:  $M_{x,y}(0) = M_{z,before} \sin \theta$ .

$$S = M_{x,y}(t) = M_{z,before} \sin(\theta) e^{-TE/T_2^*} = M_{x,y \text{ steady-state}} \quad 4.6$$

This is multiplied by the  $T_1$  decay, Equation 4.5, to yield:

$$S_{SPGR} = \frac{M_0 (1 - e^{-TR/T_1}) \sin \theta}{1 - e^{-TR/T_1} \cos \theta} e^{-TE/T_2^*} \quad 4.7$$

Equation 4.7 is the well-known equation for the spoiled gradient echo sequence. Where  $M_0$  is effectively a constant of proportionality describing the initial amount of magnetisation produced immediately after excitation. Its value depends on properties intrinsic to the scanner hardware as well as the  $^{19}\text{F}$  spin density of the perfluorinated gas.

This standard equation for a spoiled gradient echo sequence was then modified to represent signal to noise ratio achievable in a specified scan length using:

$$SNR \propto S V \sqrt{\frac{N_y N_z N_{ave}}{BW}} \quad 4.8$$

Where  $S$  is the signal from a single acquisition step and  $V$  is the voxel volume.  $N_x$ ,  $N_y$  and  $N_z$  are the number of frequency and phase encoding steps in each dimension,  $N_{ave}$  is the number of signal averages in a defined scan time, and  $BW$  is the receiver bandwidth measured in Hz/pixel. As each dimension in the voxel volume is calculated from:  $\text{length}_{x,y,z} = FOV_{x,y,z}/N_{x,y,z}$ , Equation 4.8 can be rewritten as:

$$SNR \propto S FOV_x FOV_y FOV_z \sqrt{\frac{N_{ave}}{N_x^2 N_y N_z BW}} \quad 4.9$$

The number of signal averages within a defined scan time is:

$$N_{ave} = \frac{\text{scan length}}{TR N_y N_z} (\times \text{partial k space factors}) \quad 4.10$$

In cases where acquisition options are used such that only a fraction of k-space is collected, such as an elliptical shutter, partial Fourier techniques, or compressed sensing, correction factors to account for the modified scan length are included here.

In order to maximise SNR and minimise scan length, TE and TR must be set to their minimum achievable values,  $TE_{\min}$  and  $TR_{\min}$ . These are both restricted by the rise times and amplitudes of the scanner gradients and RF pulse length.  $\theta$  denotes the flip angle achieved in the region of interest.

Equation 4.7 can therefore be modified to calculate the relative SNR achieved in a 3D SPGR acquisition in a defined acquisition time:

$$SNR_{SPGR} \propto FOV_x FOV_y FOV_z \sqrt{\frac{\text{scan length}}{N_x^2 N_y^2 N_z^2 TR_{\min} BW}} \times \frac{(1 - e^{-TR_{\min}/T_1}) \sin \theta}{1 - e^{-TR_{\min}/T_1} \cos \theta} e^{-TE_{\min}/T_2^*} \quad 4.11$$

#### 4.2.2 Defining input variables for the simulation

The input variables in Equation 4.11 were calculated as follows.

Firstly, the length of each of the components of the pulse sequence displayed in Figure 4-1 were determined: The length of the encoding gradient,  $T_{\text{encode}}$ , is dependent on the gradient strength, rise time, and BW. The spoiler gradient length,  $T_{\text{spoil}}$  was found to be constant in the Philips Achieva SPGR sequence. The excitation pulse length,  $T_{\text{excite}}$ , was defined as:

$$T_{\text{excite}} = \frac{\theta\pi/180}{\gamma B_1} \quad 4.12$$

The minimum achievable echo time,  $TE_{\min}$ , was then calculated as follows, by inspection of Figure 4-1:

$$TE_{\min} = \frac{T_{\text{excite}}}{2} + T_{\text{encode}} + \frac{1}{2 BW} \quad 4.13$$

The minimum achievable TR, without accounting for SAR restrictions, was calculated

similarly:

$$TR_{min} = T_{excite} + T_{encode} + \frac{1}{BW} + T_{spoil} \quad 4.14$$

SAR restrictions increase the minimum allowed TR to bring the maximum average power within pre-defined limits. This is such that:

$$SAR = C \times \frac{B_1^2 T_{excite}}{TR_{min}} \quad 4.15$$

Where C is a proportionality constant, which is coil specific and determined by the manufacturer. For this scanner hardware configuration C was equal to 5.3 based on SAR and safety information provided by the manufacturer. Therefore, in cases where the SAR calculated from Equation 4.15 exceeds the maximum SAR limit set, the  $TR_{min}$  defined above is expressed as:

$$TR_{min} = 5.3 \times \frac{B_1^2 T_{excite}}{SAR_{max}} \quad 4.16$$

In our calculations of sequence SNR, TR was limited to  $TR_{min}$ , such that SAR falls within the maximum SAR level. Relative SNR was calculated at each flip and bandwidth for minimum TR under the condition that SAR is less than or equal to the torso limit of 10 W/kg.

## 4.3 Methods

### 4.3.1 Simulation and optimisation of a 3D SPGR sequence

To establish how flip angle and receiver bandwidth impact the SNR, Equation 4.11 was simulated in Matlab over a range of flip angles from 1° to 180° in 1° intervals, and bandwidths from 1 Hz/pixel to 5000 Hz/pixel in 1 Hz/pixel intervals. Equations 4.12-4.16 were substituted in as appropriate. Both in vivo and in vitro acquisitions were simulated by using  $T_2^* = 2$  ms,  $T_1 = 12.4$  ms and a  $B_1$  of 4  $\mu$ T for in vivo simulation, and  $T_2^* = 9$  ms,  $T_1 = 13$  ms and  $B_1 = 8$   $\mu$ T for phantom simulation.

In the previous chapter, it was noted that less than half of the power produced by the multinuclear preamplifier reached the quadrature birdcage coil due to attenuation along components in the transmission line and so max  $B_1$  is limited by power delivered to the coil. The above simulation was modified to illustrate the effect of varying  $B_1$  on the SNR achieved in a fixed time, using:

$$B_{1,new} = \sqrt{\frac{P_{new}}{P_{known}}} B_{1,known} \quad 4.17$$

Where we know a power of 1.5 kW produced an in vivo  $B_1 = 4$   $\mu$ T in vivo (see Figure 3-8). This allowed investigation into what maximum  $B_1$  could be achieved by the RF amplifier if a simpler RF chain was utilised to reduce attenuation from the transmission line. RF power required for a desired  $B_1$  could also be calculated.

The peak power was arrayed, and the calculated new  $B_1$  values were substituted into the simulation accordingly. Applying this, the effect of changing  $B_1$  on SNR achieved in a fixed scan time was plotted.

### 4.3.2 Verification of optimised parameters in vitro

In vitro verification of the optimum parameters was performed on a 50 cm long quadrature birdcage coil (Rapid Biomedical) to test whether the simulations correctly predicted optimal acquisition parameters. A 2 L bottle of PFP/O<sub>2</sub> was positioned centrally in the coil. A 3D SPGR sequence with parameters mimicking those in the simulation was used, whilst receiver bandwidth and flip angle were varied independently, as shown in Table 4.1.

	Varying receiver bandwidth	Varying flip angle
<b>Acquisition sequence</b>	3D SPGR	
<b>Field of view (mm<sup>3</sup>)</b> H-F × L-R × A-P	400 × 400 × 250	
<b>Voxel size (mm<sup>3</sup>)</b>	10 × 10 × 10	
<b>Flip angle</b>	50°	10° - 180° in steps of 10°
<b>Bandwidth (Hz/pixel)</b>	500, 550, 600, 650, 700, 800, 1000, 2000	500
<b>Echo time (ms)</b>	Minimum: 1.01 to 1.63	Minimum: 1.37 to 2.90
<b>Repetition time (ms)</b>	Minimum: 7.5	Minimum: 4.0 to 27.0

**Table 4.1:** Parameters used to test the optimum bandwidth and flip angle. Minimum TE and TR were used in all acquisitions.

Each sequence was acquired for a total scan duration of as close to 30 s as possible by modifying the number of averages in the scan. SNR per unit time ( $SNR_{30\text{ s}}$ ) was calculated for each acquisition to account for these minor differences in scan duration. The SNR was measured from a 100 mm × 300 mm ROI from a slice central in the phantom corrected by Equation 4.18.

$$SNR_{30\text{ s}} = SNR \sqrt{\frac{30\text{ (s)}}{\text{scan length (s)}}} \quad 4.18$$

#### ***4.3.3 Application of compressed sensing techniques to the optimised imaging sequence: phantom based assessment of resultant image quality***

Numerous techniques exist to accelerate acquisitions, primarily by selective filling of k-space spatially or temporally. Compressed sensing is such a technique which uses a pseudo-random spatial sampling of k-space. Although the development of such a technique is beyond the scope of this thesis, a compressed sensing technique developed by Dr Kieren Hollingsworth (Newcastle University, UK) was applied to the optimised sequence developed above. As the sampling pattern was developed for in vivo human ventilation images, its application to phantoms cannot be considered a perfect reflection of the protocols utility in vivo, but provides a useful approximation of the comparable performance of different sequence accelerations. The utility of three accelerated imaging protocols were compared to that of the

full acquisition by assessing images of a resolution phantom using each of the acquisition sequences.

A resolution phantom was constructed from five cylindrical obstructions of diameters 5, 10, 15, 22, and 40 mm, positioned vertically and evenly spaced in a  $240 \times 170 \times 100 \text{ mm}^3$  container, and filled with PFP/O<sub>2</sub>, Figure 4-2. The phantom was used to test visibility of gas obstructions using the optimised imaging protocols under different accelerations.

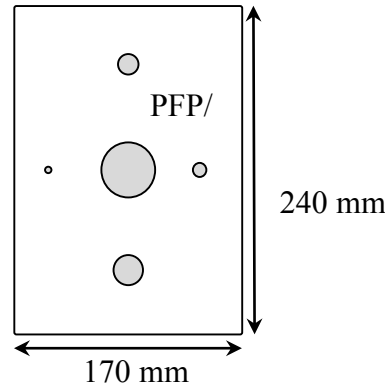


**Figure 4-2:** Schematic of the resolution phantom with 5 cylindrical obstructions of diameters: 5 mm, 10 mm, 15 mm, 22 mm, and 40 mm.

SPGR images were acquired by applying the imaging protocol specified in Table 4.2, using the optimal acquisition parameters found by the simulation. Three compressed sensing protocols, with accelerations of 1.8 $\times$ , 2.4 $\times$ , and 3.0 $\times$  the original fully sampled sequence, equivalent to 10.2 s, 7.5 s, and 6.0 s long acquisitions respectively were then applied.

Acquisition sequence	3D SPGR
Flip angle	50°
TE (ms)	1.7
TR (ms)	7.5
Bandwidth (Hz/pixel)	500
FOV: H-F $\times$ L-R $\times$ A-P (mm <sup>3</sup> )	400 $\times$ 320 $\times$ 250
Voxel size (mm <sup>3</sup> )	10 $\times$ 10 $\times$ 10
Dynamic duration (s) $\times$ number of dynamics	4.5 s $\times$ 4
Scan durations (s)	18

**Table 4.2:** Acquisition parameters for a 3D spoiled gradient echo sequence to assess the relative image quality in scans with compressed sensing applied.

A comparison of achievable image quality from the three compressed sensing regimes was carried out in a central slice of the 3D image. Firstly, SNR was measured from an ROI in an

unobstructed area of the phantom, and a noise measurement was taken from an ROI placed outside the phantom. SNR was calculated using  $\frac{\overline{\text{signal}} - \overline{\text{noise}}}{\sigma(\text{noise})}$ .

The visibility of the obstructions in the four resulting images was measured by comparing the signal minima within each of the obstructions with the average signal achieved in an unobstructed area of the image. The standard deviation of the mean signal in the unobstructed area was calculated and used as a threshold to reference which of the obstructions could be distinguished from the surrounding signal. Signal intensity profiles across the centre of the obstructed regions were plotted for the fully sampled acquisition, and the 3× accelerated acquisition in order to quantify and directly compare any change in image quality.

#### ***4.3.4 Application of the optimised protocol to imaging healthy volunteers***

After phantom based testing of the imaging protocol, a study was conducted to check its efficacy in healthy volunteers. Ethical approval was in place (assessed by the Newcastle and North Tyneside 1 ethics committee. REC reference number: 14/NE/0135, IRAS project ID: 69343), and the volunteer gave informed consent to participate. The volunteer had no history of smoking or current or historic pulmonary health diagnoses. A spirometric test was performed on the volunteer before participation to confirm normal lung function.

The study was carried out on a Philips Achieva 3.0 T MRI system. A 50 cm long quadrature birdcage coil (Rapid Biomedical, Germany) tuned to the  $^{19}\text{F}$  resonant frequency at 3.0 T, 120.15 MHz, was used.

The breathing protocol instructed three deep respiratory cycles inhaling from a supply of a 79:21 mixture of perfluoropropane and oxygen from a 25 L Douglas bag via a breathing rig (as used in Chapter 2, Figure 2-1) and a mouthpiece. This was followed by a 20-second breath hold period, during which the acquisition sequence detailed in Table 4.2 was performed. The volunteer was then switched to room air by means of a 3-way valve (Hans Rudolph Inc). Oxygen saturation levels were monitored throughout with a NONIN 7500FO pulse oximeter (NONIN Medical Inc). The above protocol was repeated on the same volunteer with compressed sensing applied, accelerating the acquisition time from 18 s to 6 s.

The resultant images were analysed by calculation of ventilated volume. This was done by masking the signal using a threshold value that was three standard deviations from the mean signal measured in a central ROI in the images. The number of voxels above this threshold were summed.

## 4.4 Results

### 4.4.1 Simulation and optimisation of a 3D SPGR sequence

The longitudinal relaxation time of the PFP/O<sub>2</sub> gas mixture in a 2 L bottle phantom was measured to be 13.0 ms at 3.0 T, with a T<sub>2</sub>\* of 9.0 ms. Using these values in the simulation, the optimum bandwidth was found to be 120 Hz/pixel, with an optimum flip angle of 62° (Figure 4-3). However, scanner hardware restrictions limit the achievable bandwidth to a minimum of 500 Hz/pixel, for which the optimum flip angle was found to be 50°.

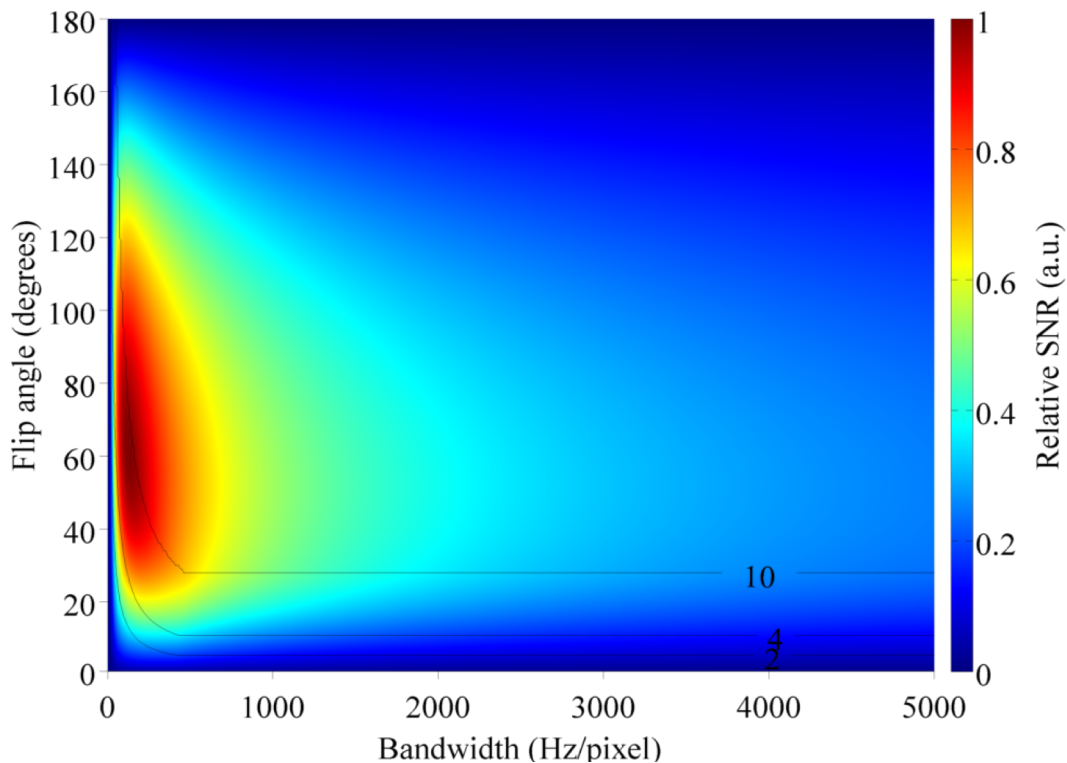


**Figure 4-3:** Relative SNR achievable (colour scale) in a fixed acquisition time over a range of flip angles and receiver bandwidths, using PFP T<sub>1</sub> and T<sub>2</sub>\* values measured in vivo. Isolines mark SAR values where 2, 4 and 10 W/kg are reached. Above these, TR values were increased in the simulation to limit the maximum SAR to the torso limit of 10 W/kg. Due to scanner hardware limitations, bandwidth values below 500 Hz/pixel were unachievable with the current scanner set-up.

The PFP/O<sub>2</sub> gas mixture was measured to have an in vivo T<sub>2</sub>\* of 2.0 ms. Previous studies have measured a value for T<sub>1</sub> of 12.4 ms in vivo at 3.0 T (Couch *et al.*, 2013). Simulations determined the optimum flip angle and bandwidth for the minimum allowed TR and TE for a fixed scan length, Figure 4-4. This predicted an optimum bandwidth of 500 Hz/pixel and a flip angle of 40°. However, SNR achieved drops dramatically at flip angles lower than this optimum value, and drops only gradually at flip angle values greater than this. Due to slight

$B_1$  inhomogeneities expected in the coil, as well as loading changing between volunteers, a slightly higher flip angle of  $50^\circ$  is favourable in order to mitigate the potential signal loss in cases of under tipping. This plot depicts the optimum achievable parameters for human studies and illustrates the impact of deviation from optimum SNR.

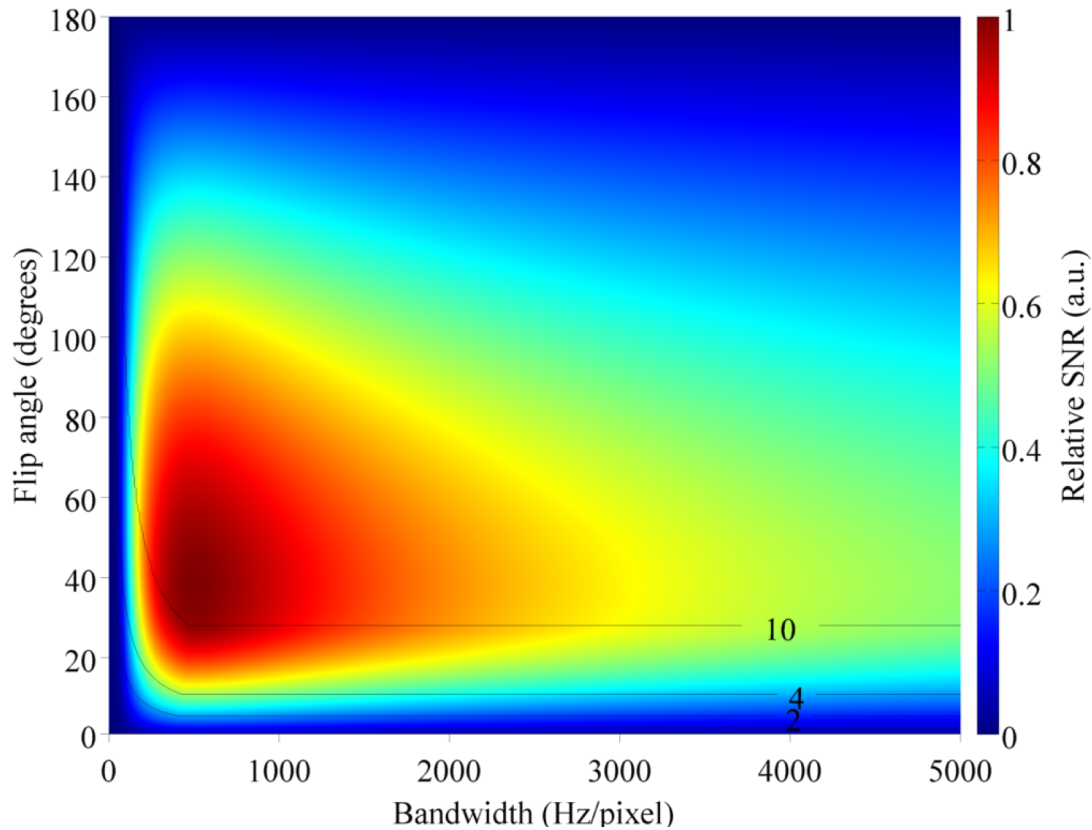


**Figure 4-4:** Relative SNR achievable in a fixed acquisition time over a range of flip angles and bandwidths, using  $T_1$  and  $T_2^*$  values representative of the human lung. Relative SNR was calculated at each flip and bandwidth for minimum TR under the condition of  $SAR \leq$  the torso limit of 10 W/kg. Isolines mark SAR values of 2, 4 and 10 W/kg.

Achievable  $B_1$  amplitude is limited by RF amplifier output and coil loading. It is therefore important to know the degree to which the scan is compromised by low  $B_1$ , and gauge the impact of potential hardware modifications to increase it. To investigate this, the simulation was utilised to map how the relative SNR changes across a range of  $B_1$  values, and in turn, how this affects the minimum allowed TR, Figure 4-5. This was calculated for three SAR limits up to 10 W/kg. The maximum SNR for a fixed length acquisition time at a SAR of 10 W/kg was found to occur at  $4 \mu T$ . Above this value, the longer TR required to maintain maximum average power limitations compromises any SNR gain from a higher peak power.

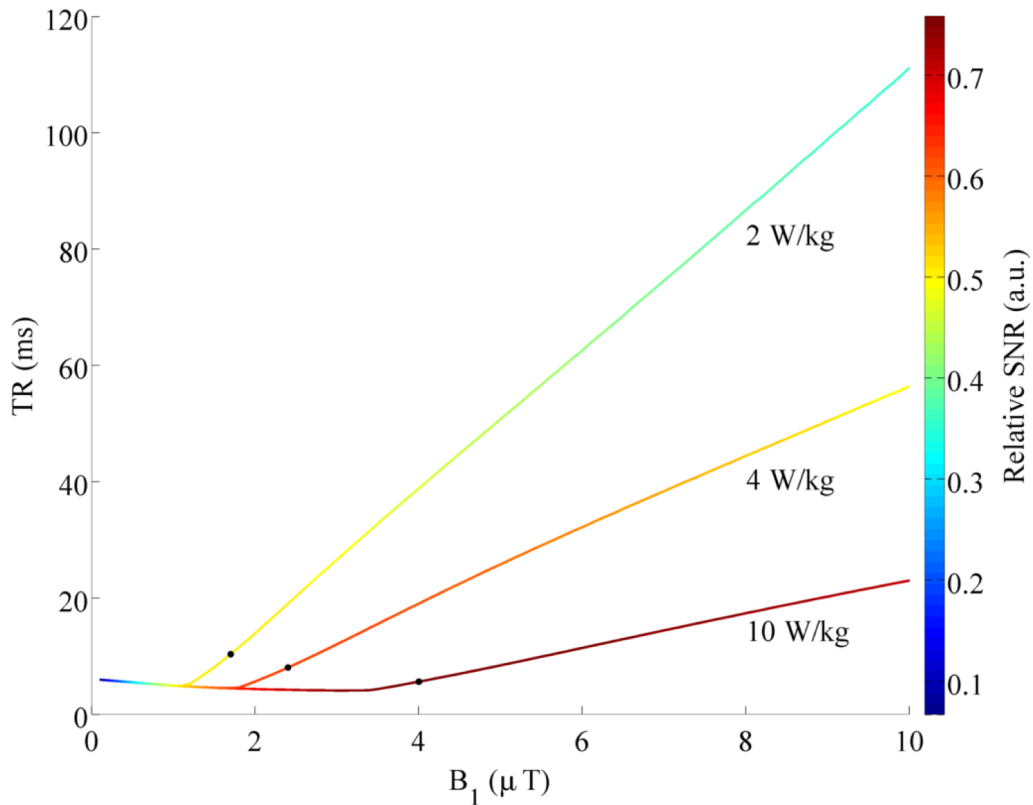


**Figure 4-5:** Relative SNR (colour scale) achievable over a range of maximum  $B_1$  values for SAR = 2, 4 and 10 W/kg, with the point at which maximum SNR is reached (circles) for each SAR level.

#### 4.4.2 Verification of optimised parameters *in vitro*

Figure 4-6a and 4-6b display the average SNR measured over a range of flip angles and bandwidths respectively. The grey line on each plot demonstrates the expected SNR as predicted by the simulations. Maximum SNR was seen at 500 Hz/pixel bandwidth (noting that values below this were unachievable with the current scanner configuration), and a flip angle of  $40^\circ - 50^\circ$ , in agreement with the pattern predicted in the simulations. The simulation calculated a minimum TR of 7.5 ms and a TE of 1.7 ms for these optimum values, which was verified on the scanner interface, confirming the accuracy of the equations used in the simulations.

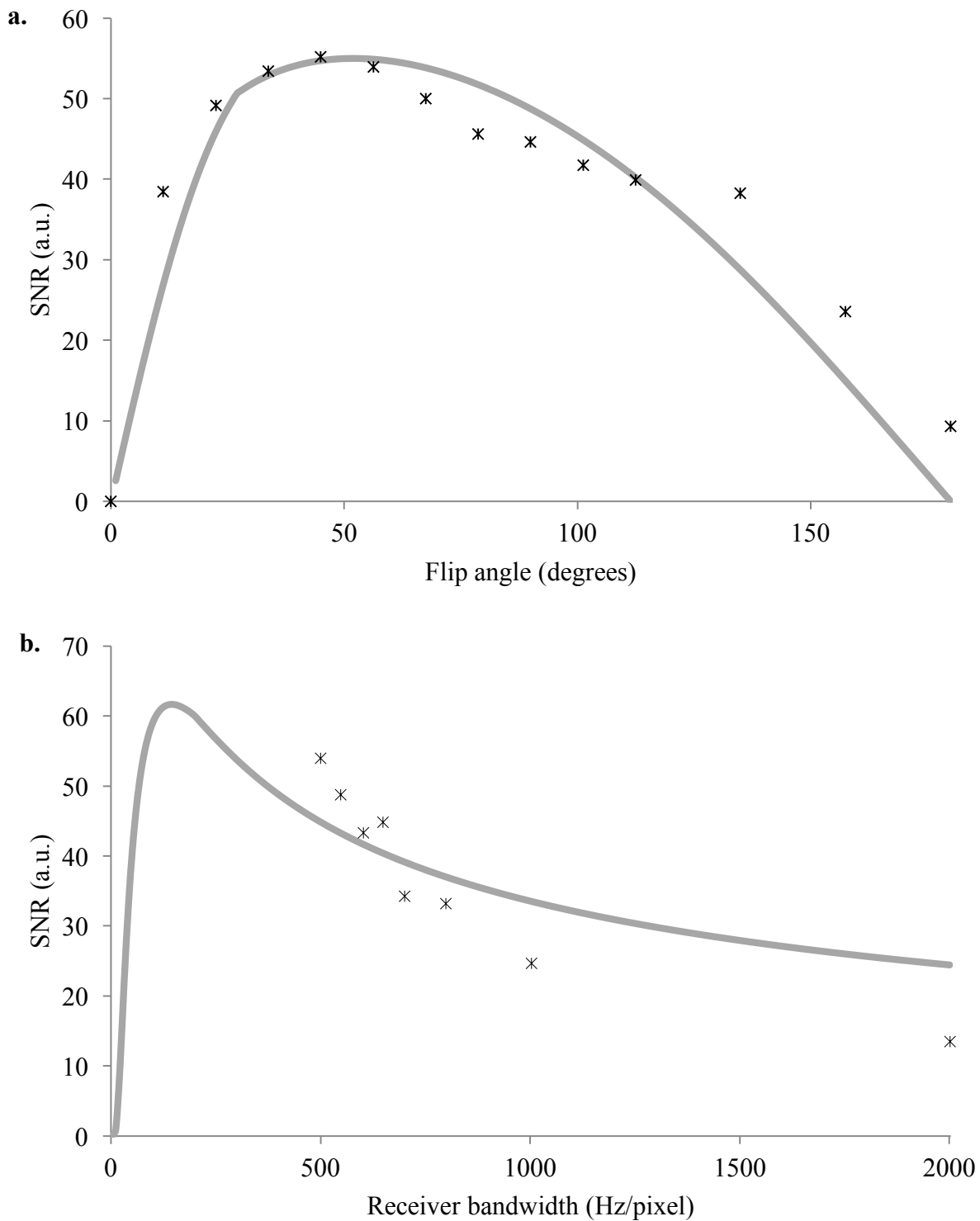


**Figure 4-6:** Measured SNR over a range of **a.**  $\theta$ , and **b.** BW. The predicted SNR (scaled to the SNR amplitude with least-squares fitting) is displayed as a grey line on both plots. Although plot b confirms the most suitable bandwidth in the 500-2000 Hz/pixel range, the simulated curve describes a different gradient to the collected data points. Further collection of data allowing the application of error bars and definition of the curve at bandwidths lower than 500 Hz/pixel would be required to fully investigate this finding.

#### 4.4.3 Phantom based assessment of scan resolution

Images of the resolution phantom filled with PFP/O<sub>2</sub> acquired at four different acquisition accelerations are shown in Figure 4-7. An ROI in an unobstructed area of the phantom had an average SNR of  $25 \pm 2$  in the four images, demonstrating minimal change between acquisitions.

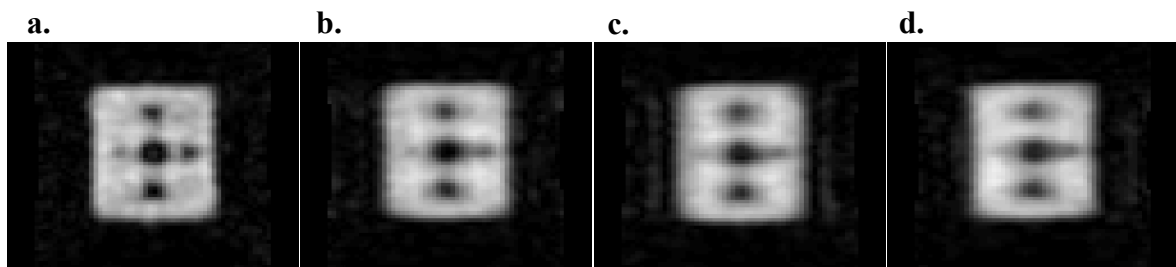


**Figure 4-7:** Images from four acquisitions with different compressed sensing regimes applied. **a.** 18 s fully sampled image. **b.** 10.2 s image (1.8× acceleration). **c.** 7.5 s image (2.4× acceleration). **d.** 6 s image (3.0× acceleration).

It was noted that loss of image detail and blurring artefacts were visible, particularly in the left-right phase encoding direction (in which compressed sensing was applied), becoming more pronounced in faster acquisitions. The obstructions were expected to produce a signal drop relative to the non-obstructed areas, with the reduction dependent upon the size of the obstruction, as some were smaller than the  $10 \times 10 \times 10 \text{ mm}^3$  imaging voxel size. Blurring from the accelerated acquisitions caused a less prominent signal change, correlated to the speed of the acceleration. This is visible in Figure 4-8, where for each size obstruction the change in signal is typically maximal for the fully sampled data set (diamond), and minimal for the most accelerated acquisition (cross).

The horizontal lines in Figure 4-8 mark the levels at which two and three standard deviations below the mean unobstructed signal occur, above which 95% and 99.7% of the signal values lie respectively. These therefore provide a threshold to which the signal achieved in the obstructed regions can be compared. Below these lines, the signal can be considered to be unlikely to be from a gas-filled region, and therefore can be identified as being a result of obstructions. Therefore, all obstructions apart from the 5 mm diameter cylinders could be identified as such, with the most accelerated acquisitions of the 10 mm diameter cylinder being visible to a lower certainty. As the image voxels have a 10 mm isotropic volume, this imaging protocol was not expected to detect the 5 mm and 10 mm circular cross-sections of the cylinders with clarity, but were included as a metric to test the cut-off point of

distinguishing obstructions close in size to that of a single voxel. A  $10 \times 10 \times 10 \text{ mm}^3$  voxel size represents the volume of three to ten pulmonary acini in humans, which, from these results, indicates the minimum volume of reduced ventilation that would be detectable in patients with obstructive lung disease using this technique (Schreider and Raabe, 1981;

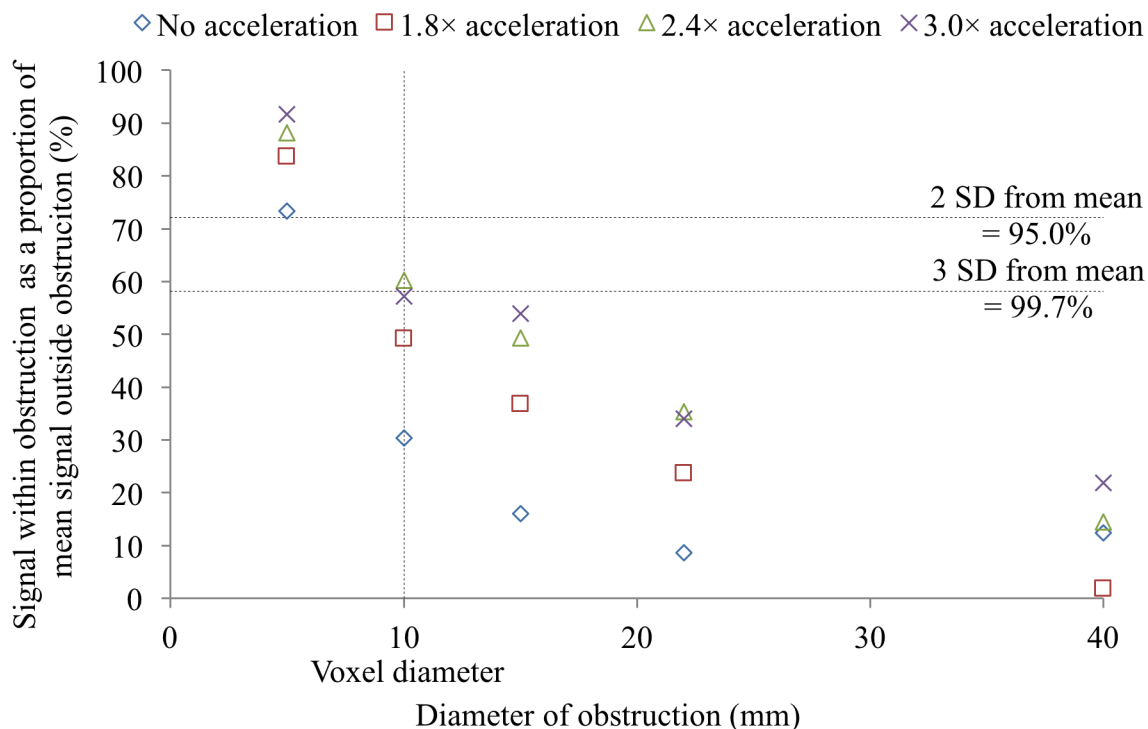


**Figure 4-8:** Visibility of obstructions plotted as a percentage decrease in signal measured within the ROI compared to the mean signal in the unobstructed regions of the phantom.

Osborne *et al.*, 1983; Haefelibleuer and Weibel, 1988).

The reduced edge definition associated with compressed sensing, results in loss of certainty of obstruction sizes. An example signal intensity profile drawn through the centre of the three largest obstructions for the fully acquired sequence and the  $3\times$  accelerated sequence is plotted in Figure 4-9. In both cases, all three obstructions are identifiable, but the sharpness of the signal gradient is reduced in the accelerated acquisition.

These in vitro results suggest that the three times accelerated acquisition sequence offers a good compromise between the improved speed and the loss of edge definition, although in vivo testing is necessary to verify this finding.

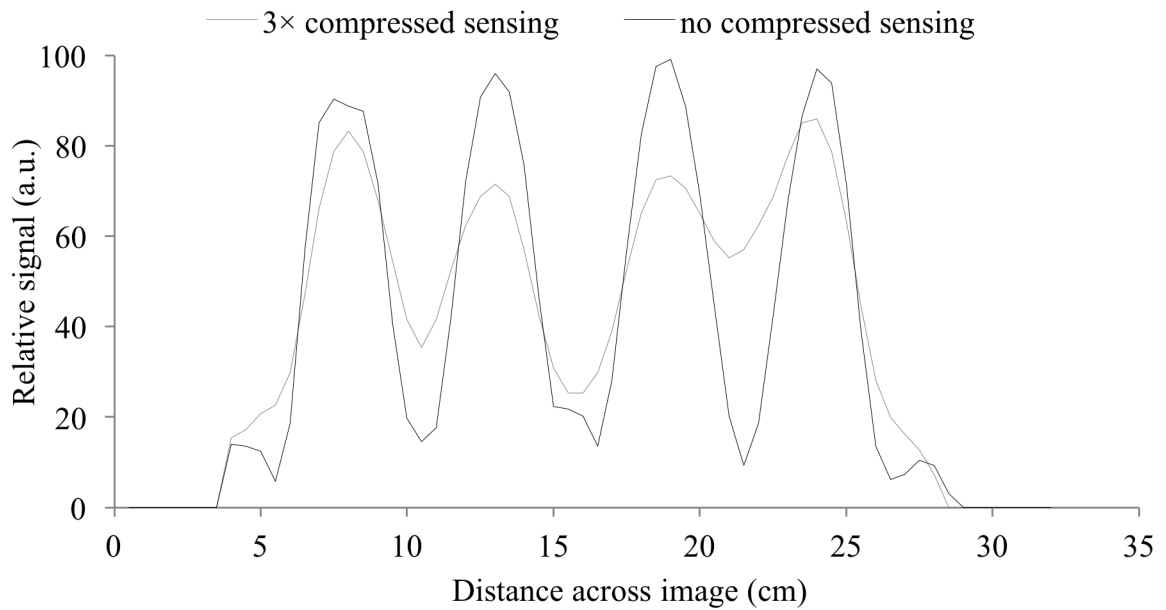


**Figure 4-9:** Signal intensity plot across the (left-right) 22 mm, 40 mm, and 15 mm diameter obstructions. The loss of edge definition is apparent.

#### 4.4.4 Application of the optimised protocol to imaging healthy volunteers

25 coronal slices through the centre of the 3D image acquired using the 18 s optimised acquisition protocol with no compressed sensing is shown in Figure 4-10a, with an image of the equivalent slice acquired using the acquisition protocol with 3× acceleration shown in 4-10b. The fully sampled acquisition achieved an SNR of 23:1, and the compressed sensing protocol achieved an SNR of 28:1.

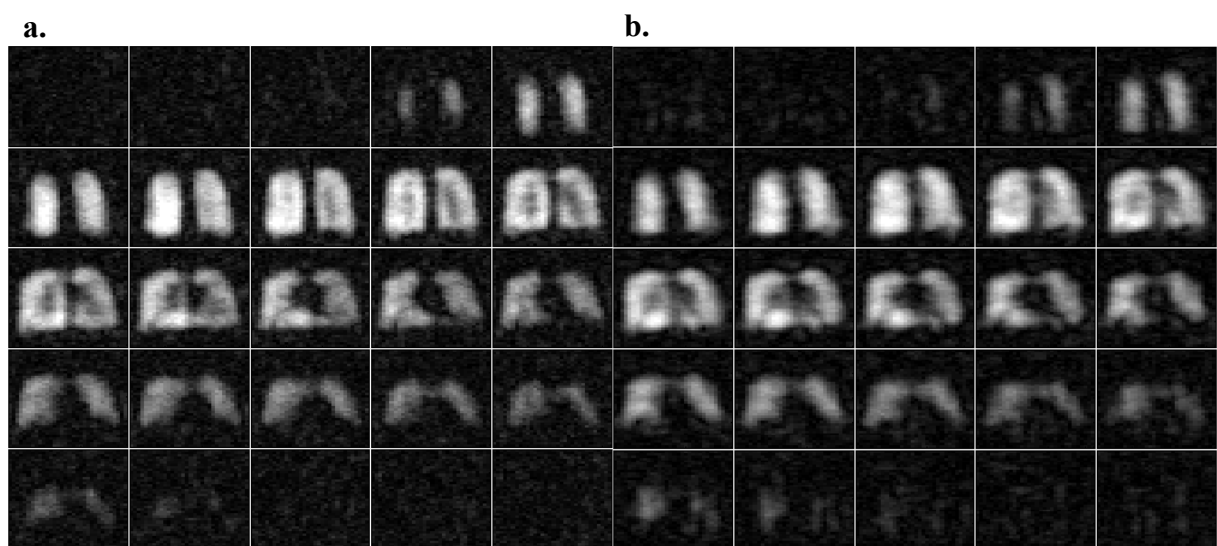


**Figure 4-10:** Slices through the two acquisition protocols: **a.** Fully sampled data, and **b.** 3×acceleration.

After applying a binary mask to the images using a threshold set to three standard deviations below the measured mean signal in the lung (Figure 4-11), the volume of the image acquired using the unaccelerated protocol was measured to be 5.18 L. The compressed sensing protocol resulted in a measured ventilated lung volume of 5.30 L. These are in broad agreement with the spirometric measurement of the volunteers forced vital capacity, which was 5.40 L. As these were acquired in different breath holds a small variation in lung volume is expected so cannot be considered directly comparable. However, they demonstrate that this preliminary testing of compressed sensing regime at  $3\times$  acceleration offers an acceptable image quality for quantitative image analysis of ventilated regions.

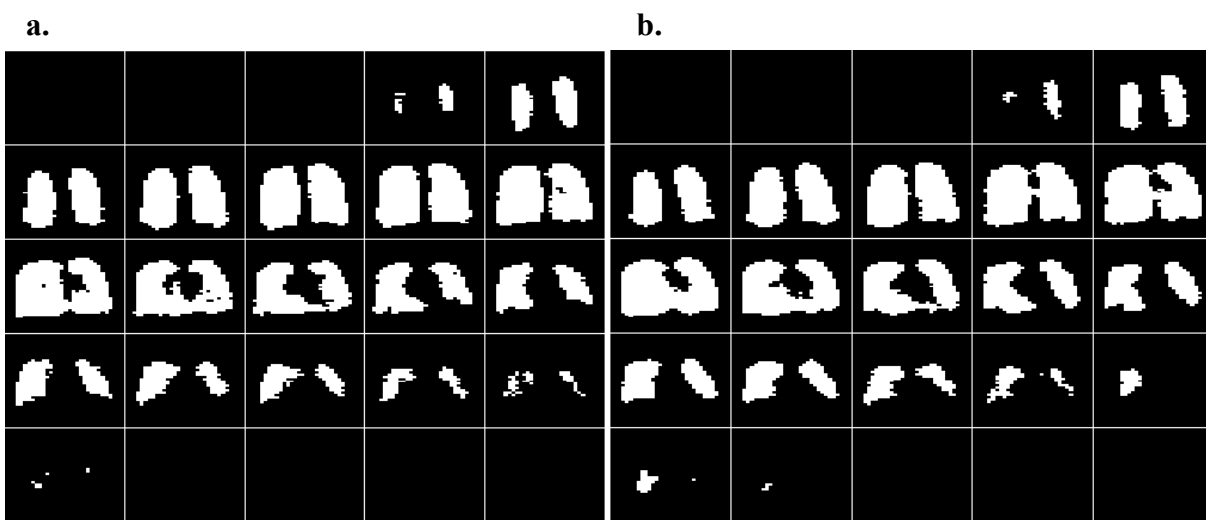


**Figure 4-11:** Lung images with a binary mask applied for **a.** The fully sampled acquisition, and **b.** The  $3\times$  accelerated acquisition. The threshold for masking was fixed at three standard deviations below the mean signal measured in an unobstructed area of the lung.

## 4.5 Discussion

The predicted optimal SPGR acquisition parameter values from the simulation were found to agree well with measured optimal acquisition parameters for the scanner hardware and software configuration used, under the limits imposed by SAR and maximum RF power restrictions. However, it was deemed unfeasible to verify the optimum in vivo values by arraying the acquisition parameters in vivo in human subjects due to being restricted to collecting data within a breath hold length acquisition time. Application of this simulation to other scanner configurations, such as different manufacturers or field strengths, would be possible with minimal modification of the simulation, and knowledge of the scanners RF power performance.

The simulation of the variation in SNR over a range of maximum  $B_1$  values demonstrated that the achievable SNR in the current coil and scanner combination is limited by the maximum allowed average power due to SAR restrictions, rather than the peak power, as elevated  $B_1$  has only a small impact on SNR. The result of this is that utilisation of a different transmit coil with a more permissive SAR limit will therefore have a potentially large impact on the SNR achieved and permit a higher maximum  $B_1$ , allowing shorted echo times to be achieved. For example, the body coil of the Philips Achieva 3.0 T system permits a TR of 5 ms is for a  $B_1$  of 4  $\mu$ T and a flip angle of  $50^\circ$  under standard SAR restrictions. Although not directly comparable due to different system hardware, the acquisitions utilised by previous studies imaging inhaled PFP/O<sub>2</sub> utilised some notably different parameters (Couch *et al.*, 2013; Halaweish *et al.*, 2013). In both cases, a lower bandwidth of 130-140 Hz/pixel was used. However, the primary limitation to these studies is likely being limited by a higher minimum TR of 13 ms and 20 ms respectively, necessitating a higher flip angle to approximate the Ernst angle.

Compressed sensing was found to offer a high degree of acceleration ( $3\times$ ) of the optimised acquisitions, but at a cost to image detail. However, due to the current sequence providing a  $10 \times 10 \times 10 \text{ mm}^3$  voxel size, image detail is already limited to these dimensions. All of the compressed sensing protocols tested offered acceptable visibility of 10 mm diameter obstructions and larger, on the scale of a single voxel, so can therefore be deemed a good trade-off for the acceleration they provide. The in vivo comparison of the fully sampled and the  $3\times$  accelerated acquisition protocols produced visually similar images in a healthy volunteer, with ventilated volume values within 3% using a simple thresholding technique. The primary limitation of the compressed sensing techniques is the associated loss of edge

definition (Lustig *et al.*, 2007), which in practice may lead to over- or underestimating the size of obstructions. Further *in vivo* sequence testing is needed to quantify the extent to which this may be a limitation, and the compressed sensing pattern adjusted appropriately to maintain acceptable image quality. Ideally, the accelerated imaging protocols would be tested and compared in a cohort of patients with ventilation defects.

Scan acceleration from an 18 s acquisition to a 6 s acquisition will be particularly valuable for future *in vivo* patient studies. The time saved can be used to acquire data at a finer resolution, or be used to collect more signal averages to improve the SNR. A further use of the faster imaging regime is the potential it has to allow more precise  $T_2^*$  mapping *in vivo*; a multi-echo sequence is inaccurate for this application as it has a relatively large minimum  $\Delta TE$ , limiting the number of useful data points for short  $T_2^*$ . Therefore, a faster acquisition would permit several SPGR images to be acquired within a signal breath hold with a range of echo times.

Non-Cartesian acquisition sequences such as ultra-short echo time imaging may offer further improvement in SNR, and has been utilised in a published study (Couch *et al.*, 2014). However, these radial acquisition regimes typically display artefacts caused by gridding the radial data onto a linear reconstruction, which reduces edge definition. They are also less suitable for combining with a compressed sensing acquisition scheme, which would further reduce the image quality. For this reason, we focussed on the optimised 3D SPGR with compressed sensing for our studies.

## 4.6 Conclusions

Simulation and practical validation of a 3D SPGR sequence found that the optimum acquisition parameters for  $^{19}\text{F}$  imaging of inhaled PFP/ $\text{O}_2$  are a flip angle of  $50^\circ$  and a receiver bandwidth of 500 Hz/pixel, with the minimum allowed TE and TR. Combined with a  $3\times$  acceleration from a compressed sensing acquisition scheme, a SNR of 28:1 was achieved in vivo in a 6 s breath hold acquisition. The compressed sensing technique provided a similar measure of ventilated volume to that measured by both spirometry and a fully sampled acquisition sequence.

It was also found that no potential improvement in SNR in a fixed scan time can be expected by increasing the input power from the RF amplifier to raise  $B_1$ , due to the longer TR required to stay within the SAR restrictions. This validated the suitability of the current RF chain configuration.

This acquisition protocol will be applied to acquire data for a large-scale study imaging healthy volunteers and patients with COPD and asthma.

## Chapter 5:

# The Effect of Susceptibility Gradients on the $T_2^*$ of Perfluoropropane: Studies in Lung-representative Phantoms

### 5.1 Overview

Local magnetic field gradients arise due to differences in magnetic susceptibility between the diamagnetic lung parenchyma and blood vessels, and the paramagnetic inhaled PFP/O<sub>2</sub> gas. This gradient markedly reduces the transverse relaxation time of the MR-sensitive nuclei (Wild *et al.*, 2012); the  $T_2^*$  of perfluoropropane –CF<sub>3</sub> is 9 ms in a magnetically homogeneous environment at 3.0 T, in contrast to 2 ms in the human lung at full inspiration, as measured in Chapter 2. In the same chapter, it was also observed that the  $T_2^*$  of inhaled PFP/O<sub>2</sub> varies over the respiratory cycle of healthy volunteers. This is caused by reduced influence of magnetic susceptibility gradients at inhalation. However, it is not known if the predominant mechanism for this is the changing surface area to volume ratio of the alveoli, or the bulk change in gas to tissue ratio seen during inhalation, or a combination of the two. This relationship is potentially valuable as a dependence of  $T_2^*$  on tissue microstructural properties could provide a biomarker sensitive to lung pathology and offer a novel utility for clinical identification of anatomical damage, such as that seen in early emphysema.

Expanding upon this concept suggests that altering the magnetic susceptibility of water, such as through intravenous administration of a paramagnetic contrast agent, could reduce the magnetic susceptibility gradient at the alveolar walls. This would result in the lengthening of the originally short *in vivo*  $T_2^*$  of the –CF<sub>3</sub> moieties of PFP, and in turn improve <sup>19</sup>F PFP signal amplitude in a SPGR acquisition, providing a potential mechanism to improve pulmonary ventilation mapping in a dynamic contrast-enhanced <sup>19</sup>F-MRI acquisition.

This chapter tests the hypothesis that perfluoropropane –CF<sub>3</sub>  $T_2^*$  is representative of its magnetic environment, and that by altering the magnetic susceptibility gradients experienced by the PFP, a change in  $T_2^*$  occurs. The objective of the following work is therefore to measure the magnetic properties of PFP/O<sub>2</sub> in a range of porous environments. This is achieved by the construction of two novel phantom models of PFP/O<sub>2</sub>-filled lung tissue, to allow assessment of the effect of changing pore size, gas to liquid ratio, and magnetic susceptibility gradients on the  $T_1$ ,  $T_2$ , and  $T_2^*$  of PFP –CF<sub>3</sub>.

## 5.2 Theoretical overview of magnetic susceptibility in pulmonary alveoli

Magnetic susceptibility,  $\chi$ , is a property intrinsic to every material, and is broadly related to the number of unpaired electrons within the molecule of interest (Schenck, 1996). It characterises the degree of magnetisation induced in a material in response to an external magnetic field. Variation of the magnetic susceptibility of materials within an external magnetic field alters the field strength, increasing it if paramagnetic ( $\chi > 0$ ) and decreasing it if diamagnetic ( $\chi < 0$ ) (Duyn, 2013). Regional differences in  $\chi$  cause regions of differing magnetisation. This results in magnetic field gradients as the field must be continuous between areas of different  $\chi$ . These magnetic field gradients on the macroscopic scale, between entire organs, can produce unwanted artefacts in MR images (Lüdeke *et al.*, 1985). However, on the mesoscopic scale – that including entire molecules and tissues, but smaller than the imaging voxel size – it is magnetic susceptibility-induced internal magnetic field gradients within a voxel at the gas-tissue boundaries which cause increased dephasing of spins, resulting in expedited decay of the transverse magnetisation (Chavhan *et al.*, 2009). When the nucleus is not exposed to magnetic field gradients, the primary determinant of the transverse magnetisation of a nucleus is the magnetic field inhomogeneities arising from molecular rotation of the nucleus of interest on the microscopic scale (Sukstanskii *et al.*, 2014). This results in the irreversible dephasing and magnetisation loss described by the  $T_1$  of the nucleus, which in turn limits  $T_2$  and  $T_2^*$ . The  $T_2^*$  of the  $-CF_3$  moieties of inhaled PFP is therefore principally related to both its molecular motion and its proximity to the magnetic field gradients produced by the air-tissue boundaries, thus its value reflects the surrounding alveolar structure.

The contraction of  $T_2^*$  in the lung caused by the presence of these susceptibility gradients is common across pulmonary MR imaging, including proton MRI and to a lesser extent, hyperpolarised noble gas MRI. Utilising these imaging techniques, the  $T_2^*$  of the nucleus of interest has been demonstrated to be sensitive to structural changes in the lung, both due to changing alveolar size after inspiration (Theilmann *et al.*, 2009), and alveolar enlargement in the emphysematous lung (Takahashi *et al.*, 2010; Ohno *et al.*, 2014). Chapter 2 demonstrated that the PFP  $-CF_3$   $T_2^*$  is affected by location in the respiratory cycle. However, to-date there is no published literature investigating the relationship between  $T_2^*$  and lung physiology using  $^{19}F$ -MRI of the lungs. A large body of literature exists studying the  $T_2^*$  of MR-sensitive nuclei in non-biological porous media (Watson and Chang, 1997; Valckenborg *et al.*, 2002; Veith *et al.*, 2004; Baete *et al.*, 2008; Smith *et al.*, 2016). These papers demonstrate the predominant contributor to  $T_2^*$  in a magnetically inhomogeneous microporous environment

as being the surface area to volume ratio (S/V) of the pore, such that  $\frac{1}{T_2^*} \propto \frac{S}{V}$ . This is in agreement with the  $T_2^*$  observations made in Chapter 2, where  $T_2^*$  increased with the average alveolar volume.

Applying this simple relationship to pulmonary structure, published theoretical models of the effect of lung anatomy on the  $T_2^*$  of inhalable imaging agents have identified the anatomical variables that influence  $T_2^*$ . These are: the dimensions of the alveoli, the volume fraction occupied by lung tissue and blood vessels, and the magnetic susceptibility gradient at the gas-tissue interface (Sukstanskii *et al.*, 2014; Yablonskiy *et al.*, 2015). Alveoli in the human lung are known to have a diameter of approximately 200  $\mu\text{m}$ , and although lung size varies significantly with subject height, alveolar size is considered largely invariant with lung size (Ochs *et al.*, 2004), and a gas volume fraction ranging between 50% and 80% at full expiration and inspiration respectively (Glauser and Wilson, 1977). Both PFP/O<sub>2</sub> and room air (predominantly composed of 21% oxygen and 79% nitrogen) are weakly paramagnetic with their magnetic susceptibility being predominantly determined by the molecular oxygen component. At a 21% partial pressure, PFP/O<sub>2</sub> has a volume magnetic susceptibility of  $\chi_{\text{PFP/O}_2} = +0.37 \times 10^{-6}$  (SI units, dimensionless, used throughout this chapter unless otherwise specified) (Schenck, 1996). This value is slightly reduced in alveolar gas, where oxygen content is typically reduced to 14%. However, this change is adequately small, and the magnetic susceptibility of PFP is sufficiently similar to that of oxygen compared to that of lung tissue, that spatially localised change in the transverse relaxation time of the gas mixture due to this variation in oxygen content can be considered negligible.

Water, and hence most biological tissues including lung tissue, are diamagnetic as a result of their constituent H<sub>2</sub>O molecules containing no unpaired electrons. The exact magnetic susceptibility of pulmonary tissue is determined by the summation of lung parenchyma, the blood content and, to a small degree, its oxygenation. The parenchyma has a magnetic susceptibility very close to that of water, with  $\chi_{\text{parenchyma}} = -9.0 \times 10^{-6}$  (Bergin *et al.*, 1991). The susceptibility of whole blood varies between  $\chi_{\text{blood,96\%ox}} = -9.1 \times 10^{-6}$  and  $\chi_{\text{blood,55\%ox}} = -8.8 \times 10^{-6}$ , this variability is minimal in practice as the percentage of oxygenated blood does not typically drop this low at rest, with blood oxygen saturation typically ranging between 75% and 97% (Thulborn *et al.*, 1982; Weisskoff and Kiihne, 1992; Albert *et al.*, 1993; Vignaud *et al.*, 2005).

Therefore, at the lung gas-tissue boundaries an average magnetic susceptibility gradient of

$\Delta\chi_{\text{air-lung}} = 9.4 \times 10^{-6}$  is present. Magnetic susceptibility gradients can be altered by intravenous administration of an appropriate agent. The use of an intravascular superparamagnetic iron oxide contrast agent, has been used to demonstrate air-tissue susceptibility matching in mice by measuring the increased transverse relaxation time of inhaled  $^3\text{He}$  after injection (Vignaud *et al.*, 2005). This study validated the potential of this technique, recording a 3-fold increase in the transverse relaxation time upon susceptibility matching. Due to restricted availability of clinically approved iron oxide contrast agents (Wang, 2011; Wang, 2015), translation of this technique to human studies would require a more suitable contrast agent.

Gadolinium based contrast agents are widely used with an extensive safety record for intravenous injection (Fok and Smith, 2017), and are highly paramagnetic due to having 7 unpaired electrons that remain unpaired when chelated. To date, just one publication has utilised these for susceptibility matching of the lung tissue to the alveolar gas (Dimitrov *et al.*, 2005). In this study, a change in inhaled hyperpolarised  $^3\text{He}$  signal pre- and post-administration of 30 mM Gadodiamide was noted in porcine lungs, however no  $T_2^*$  mapping was reported.

As hyperpolarised  $^3\text{He}$  has a large free diffusivity,  $D_0$ , due to its small atomic mass and small diameter, its transverse relaxation time is much longer than that of PFP. Due to  $^3\text{He}$  being in the motional narrowing regime it is influenced by the changing magnetic field gradient in the lung to a much smaller degree (Branca *et al.*, 2010). Similarly, the diffusivity of hyperpolarised  $^{129}\text{Xe}$  is much larger than that of PFP, therefore, the  $T_2^*$  of PFP - $\text{CF}_3$  is shorter and much more sensitive to susceptibility gradients. The free diffusivity, apparent diffusion coefficient (ADC), and  $T_2^*$  in the lung of hyperpolarised  $^3\text{He}$ ,  $^{129}\text{Xe}$ , and thermally polarised PFP is described in Table 5.1.

The comparably very slow  $D_0$  of PFP results in a root mean squared free displacement in one direction ( $\sqrt{2D_0t}$ ) in 2 ms of 170  $\mu\text{m}$ , smaller than a typical alveolar diameter. This is in contrast to  $^3\text{He}$ , which would travel 600  $\mu\text{m}$ , and can be considered to thoroughly explore the magnetic environment of the airspace. As the rapid atomic motion of  $^3\text{He}$  effectively averages the field distortions it experiences, the effect of a magnetic susceptibility gradient on its precessional frequency, and therefore  $T_2^*$ , is less than that experienced by PFP. Reduction of magnetic susceptibility differences in the lung is therefore expected to have a more apparent effect on the relative  $T_2^*$  of inhaled perfluoropropane - $\text{CF}_3$  compared to that of hyperpolarised  $^3\text{He}$  and  $^{129}\text{Xe}$ .

	<sup>3</sup> He diluted with N <sub>2</sub>	<sup>129</sup> Xe diluted with N <sub>2</sub>	PFP/O <sub>2</sub>
<b>D<sub>0</sub> at 300 K, 1 atm. (cm<sup>2</sup>/s)</b>	0.88 <sup>a</sup>	0.14 <sup>c</sup>	0.07 <sup>f</sup>
<b>ADC in healthy human lung (cm<sup>2</sup>/s)</b>	0.20 <sup>a</sup>	0.05 <sup>d</sup>	0.01 <sup>g</sup>
<b>T<sub>2</sub>* at 3.0 T in healthy human lungs at inspiration (ms)</b>	14.4 <sup>b</sup>	24.0 <sup>e</sup>	2.2 <sup>h</sup>

**Table 5.1:** D<sub>0</sub>, apparent diffusion coefficient and T<sub>2</sub>\* in the healthy human lung. Each has been measured at dilutions typically used in vivo. Values taken from: a. (Conradi *et al.*, 2006), b. (Deppe *et al.*, 2009), c. (Chen *et al.*, 1999), d. (Kirby *et al.*, 2012), e. (Xu *et al.*, 2012), f. (Albert and Hane, 2016), g. (Albert and Hane, 2016), h. (Couch *et al.*, 2013).

Investigating the behaviour of T<sub>2</sub>\* with changing susceptibility in the lung is challenging due to any acquisition being time-limited to a single breath hold and the limitation of inter-volunteer variation in physiology and breathing compliance. Having a highly controlled in vitro model of the alveoli therefore presents an opportunity to investigate and explain the in vivo observations. The requirements for such a phantom were that its gas filled pores represented alveolar structure and dimensions, and that the surrounding medium had a magnetic susceptibility equal to that of lung parenchyma such that the model reflected the gas to tissue ratio and magnetic susceptibility gradients found in the lung. It was also required to be stable over time, allowing MR acquisitions to be made. In order to investigate the hypothesis, control over pore size and the ability to add gadolinium chelates to the tissue-representative medium in order to assess the effect of the magnetic susceptibility gradient on T<sub>2</sub>\* was also required.

A foam phantom made from a standardised liquid and PFP/O<sub>2</sub> allowed control of both model physical and magnetic properties. Foam fabrication methods described in previously published literature (Xu *et al.*, 2009; Parhizkar *et al.*, 2015) were attempted, but proved to be unsuitable, primarily due to their instability in the quantities required for MR measurements, so will not be discussed further here. Two novel foam models of lung tissue were developed and detailed in the following section. The first produced monodisperse (uniform bubble diameter) foam, which allowed investigation into the effect of pore size on T<sub>2</sub>\*. The second model was formed from a polydisperse foam, but offered a fabrication method better suited to investigation into the effect of changing magnetic susceptibility gradients on T<sub>2</sub>\* by addition of varying quantities of a gadolinium based contrast agent, allowing comprehensive testing of the hypotheses.

## 5.3 Methods

### 5.3.1 Construction of a lung representative phantom: monodisperse foam

Polyethyleneglycol-40 stearate (PEG-40s, CAS number 9004-99-3, Sigma-Aldrich LLC), with the chemical structure  $\text{CH}_3-(\text{CH}_2)_{17}-(\text{C}_2\text{H}_4\text{O})_{40}-\text{OH}$  was used as a neutral surfactant to facilitate the formation of foam. Agarose (melting point of  $90^\circ\text{C}$  and gelling temperature of  $33^\circ\text{C} - 38^\circ\text{C}$ , CAS: 9012-36-6, Sigma-Aldrich LLC), was added to aqueous solutions of PEG-40s to improve foam stability. The same PFP/O<sub>2</sub> gas mixture utilised in earlier chapters was used to form the gas phase of the foam.

2 wt% PEG-40s was added to 1 wt% agarose in water. The concentration of PEG-40s was chosen such that it was in excess of its critical micelle concentration, 0.01 wt% (Parhizkar *et al.*, 2015), to ensure sufficient quantities were available to avoid inhibiting the yield of microbubbles. This solution was transferred to a sealed syringe and heated to  $95^\circ\text{C}$  in a water bath to melt the agarose. The syringe was then repeatedly inverted for one minute to ensure adequate mixing to produce a clear homogeneous solution, and then maintained at  $95^\circ\text{C}$  until immediately prior to use. A magnetic susceptibility balance (MK1, Sherwood Scientific Ltd, UK) was used to measure the magnetic susceptibility of this solution.

Monodisperse PFP/O<sub>2</sub>-filled foam was formed by feeding the detergent solution and gas mixture through a 200  $\mu\text{m}$  diameter T-junction microfluidic chip (Dolomite, UK) using a syringe pump. The PFP/O<sub>2</sub> was fed to the T-junction directly from a cylinder via a pressure regulator equipped with a pressure gauge. The T-junction was warmed to  $40^\circ\text{C}$  in a water bath to ensure the solution did not gel within the chip. The resulting monodisperse foam left the microfluidic chip via 1 mm internal diameter tubing which passed through an ice bath and into a chilled 6 ml vial. This configuration allowed the foam to set rapidly, before bubble coalescence, producing stable foam. Figure 5-1 presents a schematic diagram of the apparatus configuration.

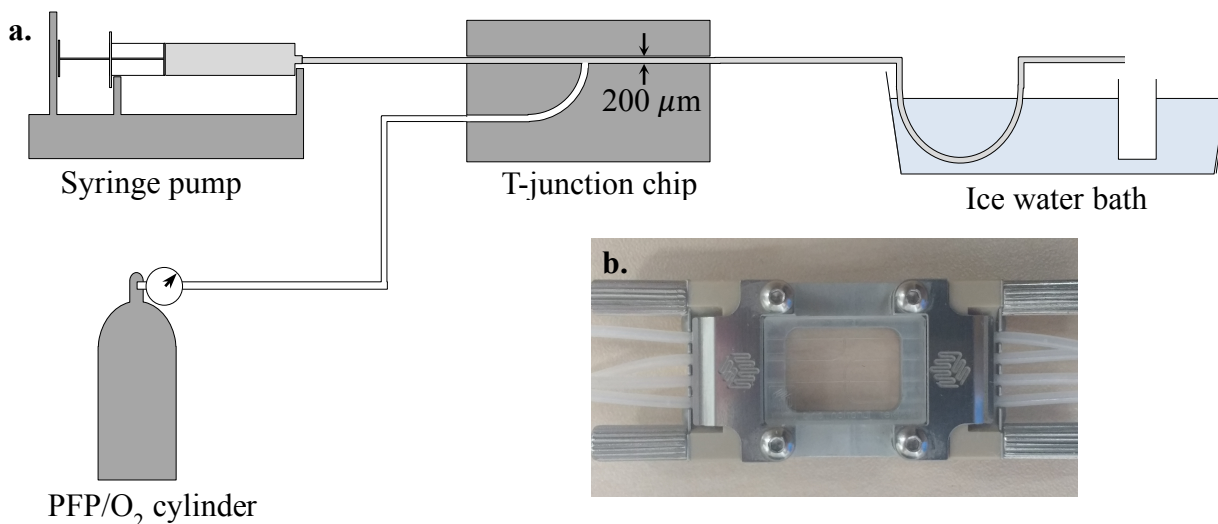


**Figure 5-1:** **a.** The apparatus used to produce monodisperse PFP/O<sub>2</sub>-filled foam, using an aqueous detergent and agarose solution. **b.** The microfluidic chip used. The liquid and gas entered the chip via the top two tubes on the left, and the foam exited via the upper right tube.

The foam bubble diameter was dependent on the relative flow rate of the detergent mixture and the PFP/O<sub>2</sub> pressure. A gas pressure of 12-16 psi allowed a small variation in the foam gas to liquid ratio, and liquid flow rates of 25 and 45 ml/hour produced foams with two distinct bubble diameters. These flow rates were chosen as they most robustly produced stable bubble sizes with the described hardware setup. Seven 6 ml samples of each bubble size were made and equilibrated to room temperature for 30 minutes prior to MR acquisitions.

Following the same procedure, a single 6 ml sample of foam was made with 30 mM Gadodiamide (Omniscan, GE Healthcare) added to the aqueous solution, changing the magnetic susceptibility gradient at the gas/water boundary at the pore surface.

### 5.3.2 *In vitro* measurements: monodisperse foam

Photomicrographs of foam from each vial were taken using a digital microscope (Celestron, LLC) immediately prior to MR acquisitions. Mean bubble diameter was measured from 100 bubbles per sample, and intra- and inter-sample size variability was assessed.

Four <sup>19</sup>F-MR protocols were then performed as described below to assess the MR properties of the PFP utilising a small (3 cm long, 2 cm diameter) <sup>19</sup>F-tuned coil built in-house, Figure 5-2, interfaced to a Philips Achieva 3.0 T system.

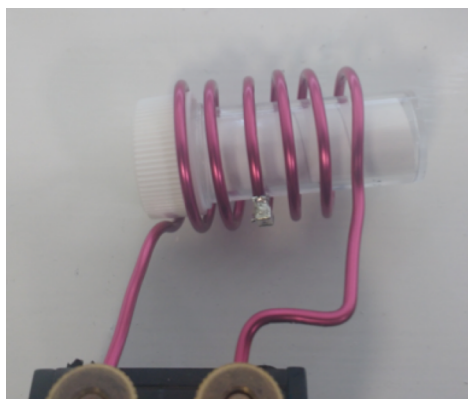


**Figure 5-2:** RF coil with 6 ml vial of foam.

A pulse-acquire sequence was used to determine the average  $T_2^*$  of each foam sample by fitting a decaying exponential to the amplitude of the FID. The acquisition parameters used are listed in Table 5.2.

Acquisition sequence	Unlocalised pulse-acquire
Flip angle	90° hard pulse
Number of FID samples	256
Sample frequency (Hz)	8000
TR (ms)	34

**Table 5.2:** The acquisition parameters for measurement of the average  $T_2^*$  in the foam phantoms.

A  $T_2^*$  map of each sample was produced by means of an SPGR sequence with varying TE. Image resolution was  $3 \times 3 \times 5 \text{ mm}^3$ . Table 5.3 shows scan acquisition parameters.

Acquisition sequence	3D SPGR
Flip angle	90°
TE (ms)	Array: 2.0, 4.0, 6.0, 8.0, 15.0
TR (ms)	250
Bandwidth (Hz/pixel)	500
FOV: H-F $\times$ L-R $\times$ A-P ( $\text{mm}^3$ )	60 $\times$ 60 $\times$ 60
Voxel size ( $\text{mm}^3$ )	3 $\times$ 3 $\times$ 5
Scan duration	55 s per TE

**Table 5.3:** The acquisition parameters for an echo time array of a 3D spoiled gradient echo sequence, allowing mapping of  $T_2^*$  in the sample.

An inversion recovery spectroscopy sequence with a hard pulse was used to measure the  $T_1$  of each sample by arraying inversion time (the time between the  $180^\circ$  and  $90^\circ$  pulse) and measuring the  $^{19}\text{F}$  peak amplitude, Table 5.4. From this the longitudinal relaxation recovery curve could be plotted from the signal measurements, and a recovering exponential equation fitted to the data.

Acquisition sequence	Unlocalised inversion recovery
Flip angle	$180^\circ - \text{TI} - 90^\circ$
TI (ms)	Array: 1.0, 2.0, 3.0, 4.0, 10.0, 15.0, 20.0, 30.0
TR (ms)	250
Sample frequency (Hz)	8000
Number of samples	256

**Table 5.4:** The acquisition parameters for an inversion recovery sequence with an inversion time array, allowing measurement of average  $T_1$  in each of the foam samples.

A 1D spin echo sequence was used to measure the  $T_2$  by arraying the echo time, Table 5.5. A chemical shift imaging (CSI) sequence was utilised to offer spatially localised signal measurements at short echo times. The average  $T_2$  of the sample was then calculated by fitting the exponential  $T_2$  decay curve to the signal measurements from each TE. Equation 1.12 was fitted to the data to calculate  $T_2$ .

Acquisition sequence	1D CSI spin echo
Flip angle	$90^\circ - \text{TE} - 180^\circ$
TE (ms)	Array: 1.7, 3.0, 5.0, 10.0, 20.0
TR (ms)	250
Sample frequency (Hz)	8000
Number of samples	256

**Table 5.5:** The acquisition parameters for a spin echo sequence, allowing measurement of the average  $T_2$  in the foam samples.

The ratio of gas to liquid in the foam samples was determined by measuring foam density, with comparison to density of PFP/ $\text{O}_2$  gas and water/agarose/surfactant solution.

### 5.3.3 Construction of a lung representative phantom: polydisperse foam

Pasteurised egg white powder (Dr Oetker Ltd., UK) was mixed in a 1:6 weight ratio with water to form a viscous solution capable of forming a stable foam. The magnetic

susceptibility of this solution was then modified by addition of the paramagnetic gadolinium based contrast agent Gadobutrol (Gadovist, Bayer Schering Pharma, UK). 1.0 M Gadobutrol was added to produce concentrations of 0, 15, 30, 45, and 60 mM in 3 ml volumes of egg white solution. Three samples were made at each concentration of Gadobutrol.

A further twelve samples were made following the same process using the contrast agent Gadodiamide (Omniscan, GE Healthcare) with concentrations ranging from 0 to 70 mM to verify the results using a different contrast agent.

Each 3 ml solution was mixed with 12 ml of PFP/O<sub>2</sub> gas by passing the mixture between two syringes via a 2-way valve twenty times, as depicted in Figure 5-3. This process frothed the mixture to produce homogenous polydisperse foam, with a gas to liquid ratio similar to the gas to tissue ratio found in the human lung.

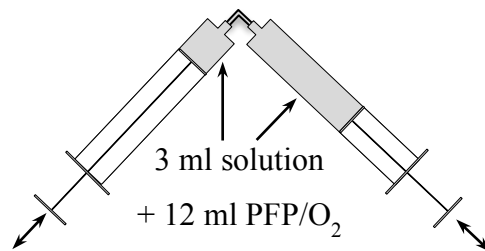


**Figure 5-3:** Schematic depicting the method for frothing the egg white based foam. A sample of the foam was decanted into a 6 ml vial for MR acquisitions.

#### **5.3.4 *In vitro* measurements: polydisperse foam**

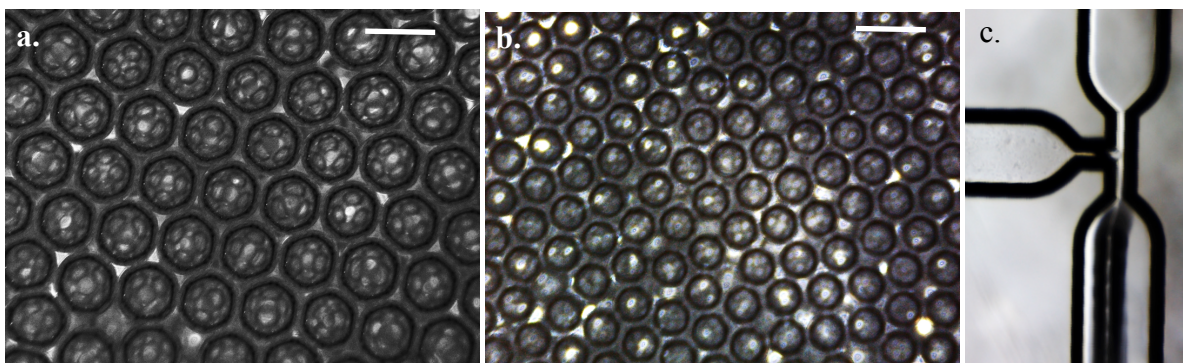
Photomicrographs were taken of each egg white foam sample immediately before MR acquisitions. The mean bubble diameter and standard deviation of the mean was determined from diameter measurements of 100 bubbles in each sample image. The protocols described in Tables 5.2-5.5 were repeated using the same scanner hardware configurations as for the detergent phantoms to make  $T_1$ ,  $T_2$ , and  $T_2^*$  measurements of PFP in the egg white foam.

A magnetic susceptibility balance (MK1, Sherwood Scientific Ltd, UK) was used to measure the magnetic susceptibility of 1.0 M Gadobutrol.

## 5.4 Results

### 5.4.1 *In vitro* measurements: monodisperse foam

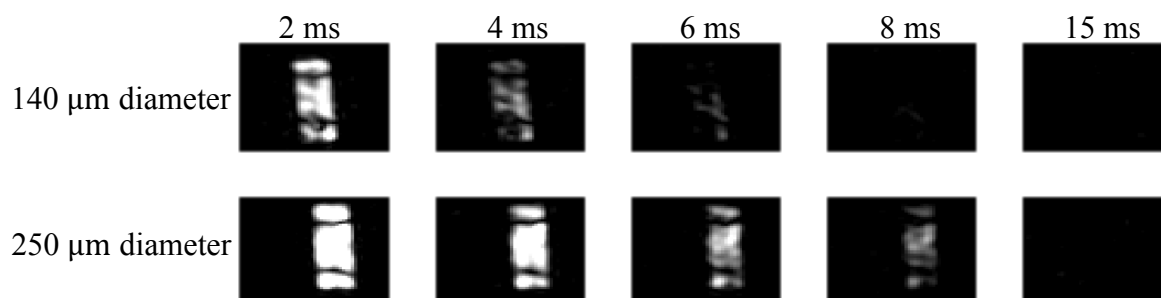
This foam fabrication technique was found to produce monodisperse bubbles with the liquid having a magnetic susceptibility equivalent to that of water. Photomicrographs of the two distinct sizes produced are shown in Figure 5-4, along with a photomicrograph of the bubble sample being formed at the T-junction.



**Figure 5-4:** Microscopy images of: **a.** bubbles produced using a liquid flow rate of 25 ml/hour, and **b.** bubbles produced using a liquid flow rate of 45 ml/hour. The scale bar in both images defines a length of 250  $\mu\text{m}$ . **c.** Microbubbles leaving the T-junction during foam formation, where PFP/O<sub>2</sub> was fed from the left into the stream of liquid.

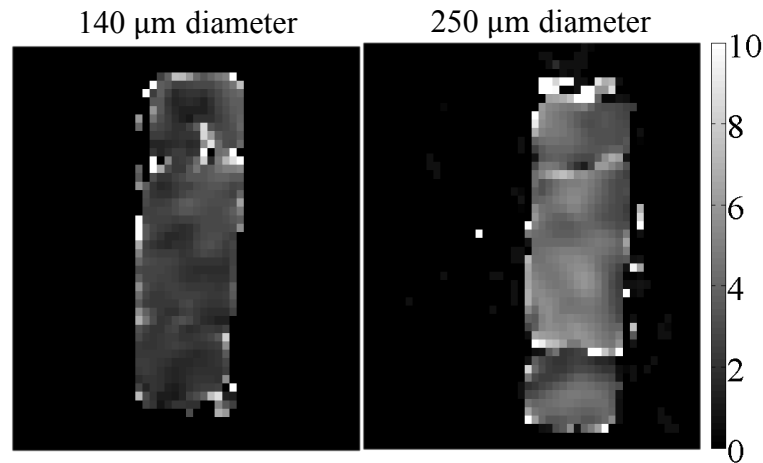
The average diameter of 100 large bubbles from a sample was measured to be  $246 \pm 20 \mu\text{m}$ . The standard deviation of mean bubble size between three samples was found to be 13.4  $\mu\text{m}$ . The average diameter of 100 bubbles from a sample of small bubble was  $138 \pm 22 \mu\text{m}$ , with a standard deviation of 21  $\mu\text{m}$  between average diameter measured in three samples.

Figure 5-5 shows images from an SPGR echo time array experiment for two samples: the  $\sim 140 \mu\text{m}$  bubble diameter foam and the  $\sim 250 \mu\text{m}$  diameter foam.



**Figure 5-5:** Relative signal amplitude over varying TE for two foam samples.

$T_2^*$  maps for the two bubble sizes is shown in Figure 5-6.



**Figure 5-6:**  $T_2^*$  maps of: **a.**  $\sim 140 \mu\text{m}$  diameter bubble foam and **b.**  $\sim 250 \mu\text{m}$  diameter bubble foam.

The relaxation properties for the two bubble sizes with the standard deviation between samples are shown in Table 5.6.

	<b>250 <math>\mu\text{m}</math> diameter bubble foam</b>	<b>140 <math>\mu\text{m}</math> diameter bubble foam</b>
<b>Surface area/volume (<math>\text{cm}^{-1}</math>)</b>	12.2	22.7
<b><math>T_2^*</math> (ms)</b>	$3.3 \pm 0.5$	$2.0 \pm 0.1$
<b><math>T_2</math> (ms)</b>	$8.7 \pm 1.3$	$10.6 \pm 1.3$
<b><math>T_1</math> (ms)</b>	$12.5 \pm 1.3$	$13.1 \pm 1.5$

**Table 5.6:** Average ( $\pm$ SD) relaxation properties of the foam samples with two bubble diameters.

A plot of foam percentage liquid content against  $T_2^*$  is shown in Figure 5-7.

A physiologically representative gas:liquid ratio of 80:20 at inspiration could not be reached. This is due to the densest possible positioning of spheres (for example, when arranged in a hexagonal close packed structure, as seen in Figure 5-4) being limited filling approximately 74% of the total volume. This density of packing is only achieved with the larger bubble samples. Although liquid content could be controlled to some extent, homogeneity of the gas:liquid ratio in a large sample could not be accurately guaranteed using this fabrication method, due to it requiring precise gas and liquid pressure control, and immediate stabilisation of the foam by adequate cooling. This fabrication method was however well suited to producing highly monodisperse bubble sizes in two distinct sizes on a physiologically representative scale.

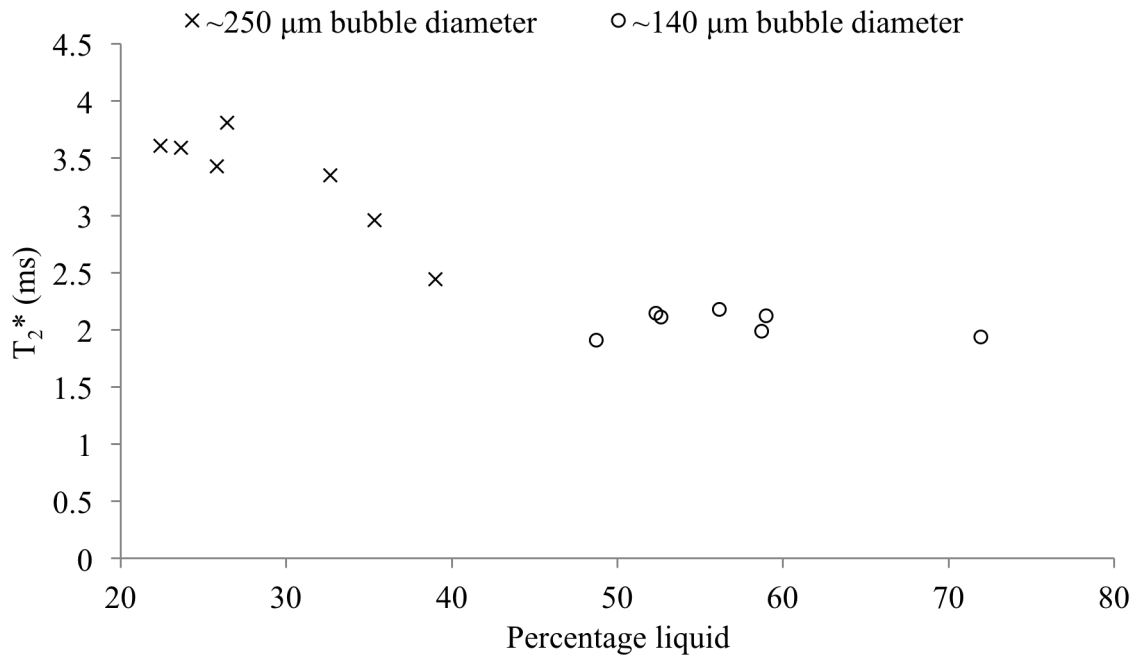


**Figure 5-7:** Percentage liquid measured in the surfactant and agarose phantoms plotted against the  $T_2^*$  measured from a spectroscopic FID. The markers differentiate the two distinct bubble sizes.

A sample of the  $250 \mu\text{m}$  diameter bubbles made with the same solution containing 30 mM Gadodiamide produced a PFP- $\text{CF}_3$   $T_2$  of 12.3 ms and  $T_2^*$  of 9.8 ms, a three-fold increase compared to the comparable foam without Gadodiamide.

The relative signal achieved in the  $\sim 250 \mu\text{m}$  diameter bubble foam and the  $\sim 250 \mu\text{m}$  diameter bubble foam with 30 mM Gadodiamide is depicted in Figure 5-8.

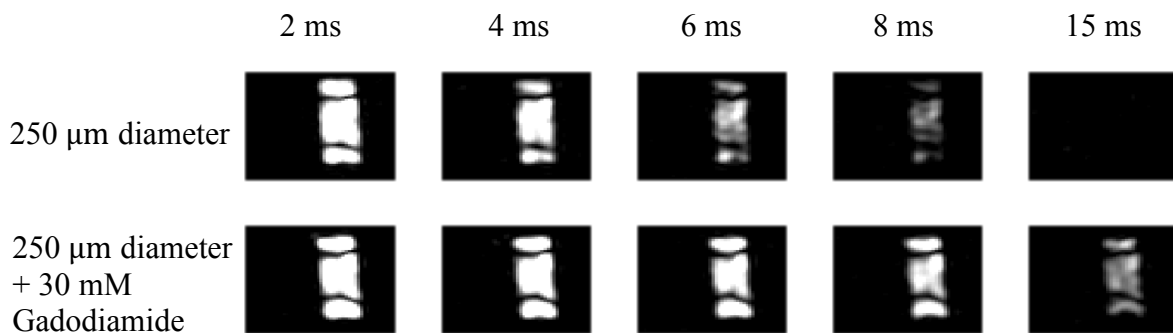


**Figure 5-8:** Relative signal amplitude over varying TE for foam samples with and without Gadodiamide.

$T_2^*$  maps of the foam samples are depicted in Figure 5-9.

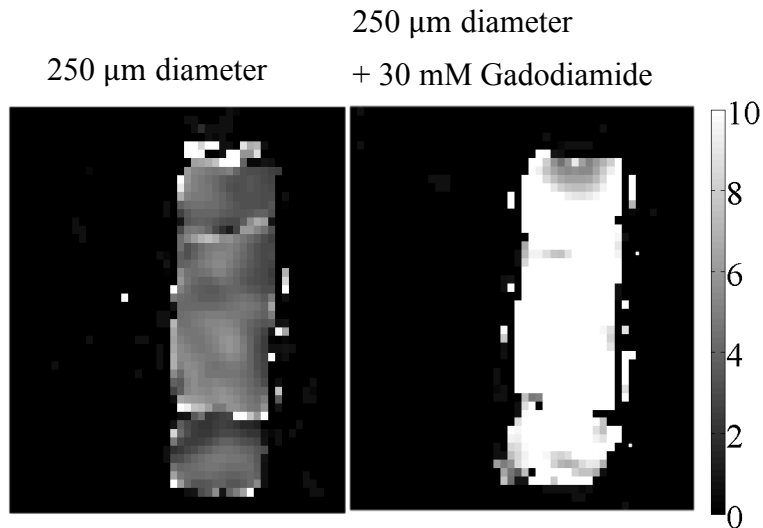


**Figure 5-9:**  $T_2^*$  maps of: **a.**  $\sim 250$   $\mu\text{m}$  diameter bubble foam, and **b.**  $\sim 250$   $\mu\text{m}$  diameter bubble foam with 30 mM Gadodiamide.

#### 5.4.2 *In vitro* measurements: polydisperse foam

The bubble sizes produced using this technique were polydisperse; a sample was found to have a mean diameter of  $29 \pm 12$   $\mu\text{m}$ . A representative photomicrograph of a sample of the bubbles is shown in Figure 5-10 next to an image of the bulk foam.

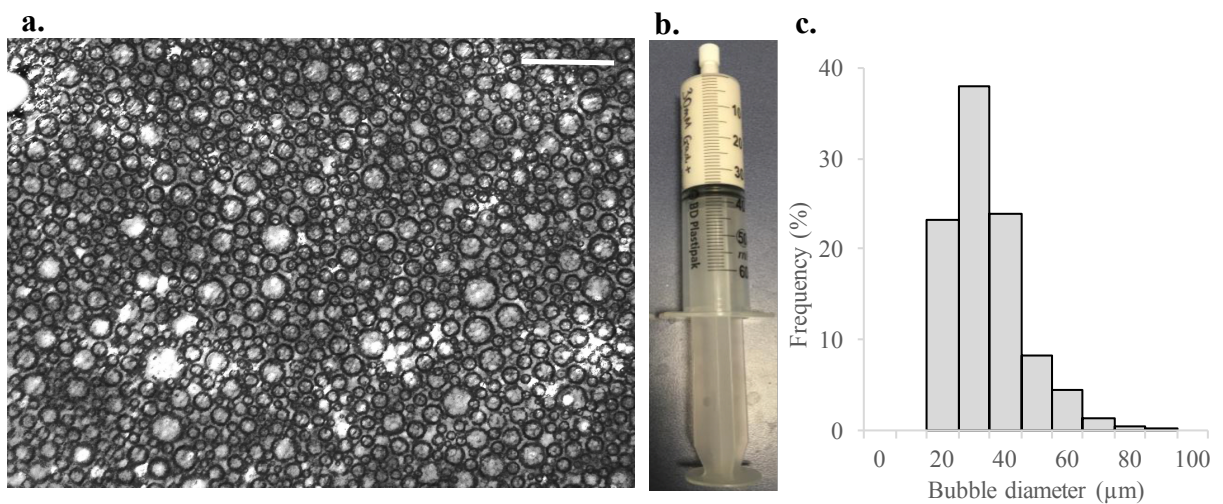


**Figure 5-10:** **a.** A microscope image from a sample of PFP/ $\text{O}_2$  bubbles in an egg white solution. The scale bar represents a length of 250  $\mu\text{m}$ . **b.** An image of the bulk foam. **c.** A histogram depicting the spread of bubble sizes in the polydisperse bubble sample.

The average  $T_2^*$  ( $\pm\text{SD}$ ),  $T_2$ , and  $T_1$  relaxation times for three samples of the polydisperse foam is displayed in Table 5.7.

<b>Polydisperse foam</b>	
<b>T<sub>2</sub><sup>*</sup> (ms)</b>	4.0 ± 0.2
<b>T<sub>2</sub> (ms)</b>	11.6 ± 0.3
<b>T<sub>1</sub> (ms)</b>	14.3 ± 0.5

**Table 5.7:** Average (±SD) relaxation properties for the polydisperse foam.

This foam fabrication method allowed precise knowledge of the gas to liquid ratio, and a physiologically representative ratio was achieved in all samples. However, the bubble size could not be controlled, and the resultant foam produced polydisperse bubbles significantly smaller than the human alveolar size. There was however a macroscopically homogeneous dispersion of bubbles in the liquid medium. The T<sub>2</sub><sup>\*</sup> of PFP –CF<sub>3</sub> in this foam was measured to be much lower than that in a magnetically homogeneous environment. Monodisperse bubbles were therefore not necessary to study the effect of varying the susceptibility gradient on T<sub>2</sub><sup>\*</sup>.

#### 5.4.3 Altering magnetic susceptibility of the foam liquid component

Table 5.8 displays the magnetic susceptibility of the components of the foam. Four samples of Gadobutrol were measured to have an average molar magnetic susceptibility of 322 ± 14 cm<sup>3</sup>/mol.

<b>Foam component</b>	<b>Magnetic susceptibility, <math>\chi</math></b>
Water	-9.0 × 10 <sup>-6</sup>
PFP/O <sub>2</sub>	+0.37 × 10 <sup>-6</sup>
Gadobutrol	+322 ± 14 cm <sup>3</sup> /mol

**Table 5.8:** Magnetic susceptibility of the polydisperse foam components.

Using these values, the concentration of Gadobutrol required to susceptibility match the solution to the PFP/O<sub>2</sub> gas can be approximated using:

$$[C_{\text{gad}}] = \frac{\Delta\chi_{\text{gas-tissue}}}{\chi_{\text{gad}}} = \frac{(0.4 - -9)}{322} = 29 \text{ mM} \quad 5.1$$

$T_2^*$  maps of these five samples of polydisperse foam with varying Gadobutrol concentrations are depicted in Figure 5-11.

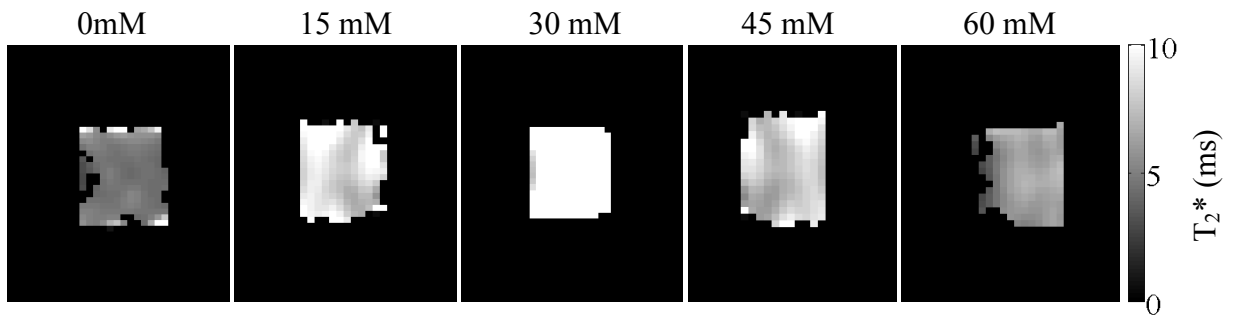


**Figure 5-11:**  $T_2^*$  maps of the polydisperse foam containing Gadobutrol concentrations of 0 mM to 60 mM.

The  $T_2^*$  of PFP in egg white foam samples with five different Gadobutrol concentrations (crosses) and eleven Gadodiamide samples (circles) are marked in Figure 5-12.

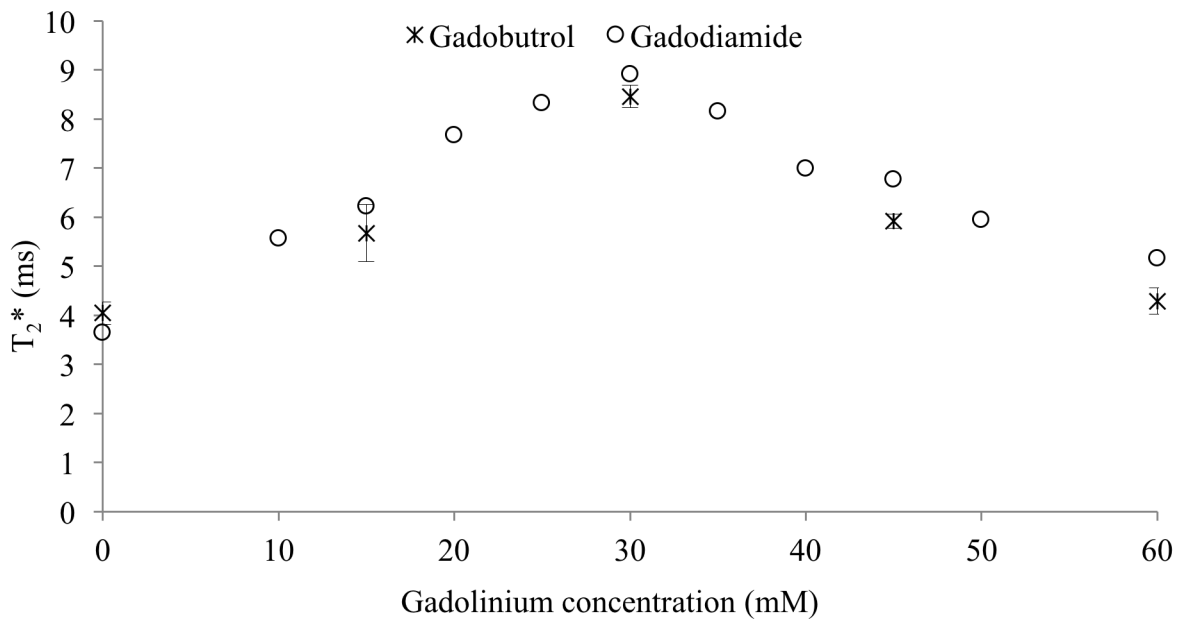


**Figure 5-12:** The effect of gadolinium based contrast agent concentration on the  $T_2^*$  of PFP in polydisperse foam phantoms. The crosses represent measurements from foam containing Gadobutrol, with the error bars displaying the standard deviation of three samples made at each concentration. The circle data points display results from varying the concentration of Gadodiamide in smaller intervals. In this case, only one sample was made for each concentration. Both demonstrate good agreement with Equation 5.1.

The error bars represent the standard deviation from measurements made in three samples at each concentration. Repeated measurements using Gadodiamide in 5 mM concentration intervals showed the same pattern (circles in Figure 5-12), both reaching a maximum  $T_2^*$

when a 30 mM gadolinium concentration is utilised, in agreement with the calculated value.

Minimal change in  $T_1$  with gadolinium concentration was noted (Figure 5-13a); with an average value of 15.5 ms. A change in  $T_2$  was measured (Figure 5-13b). In both cases the error bars depict the standard deviation of measurements made in three samples at each concentration.

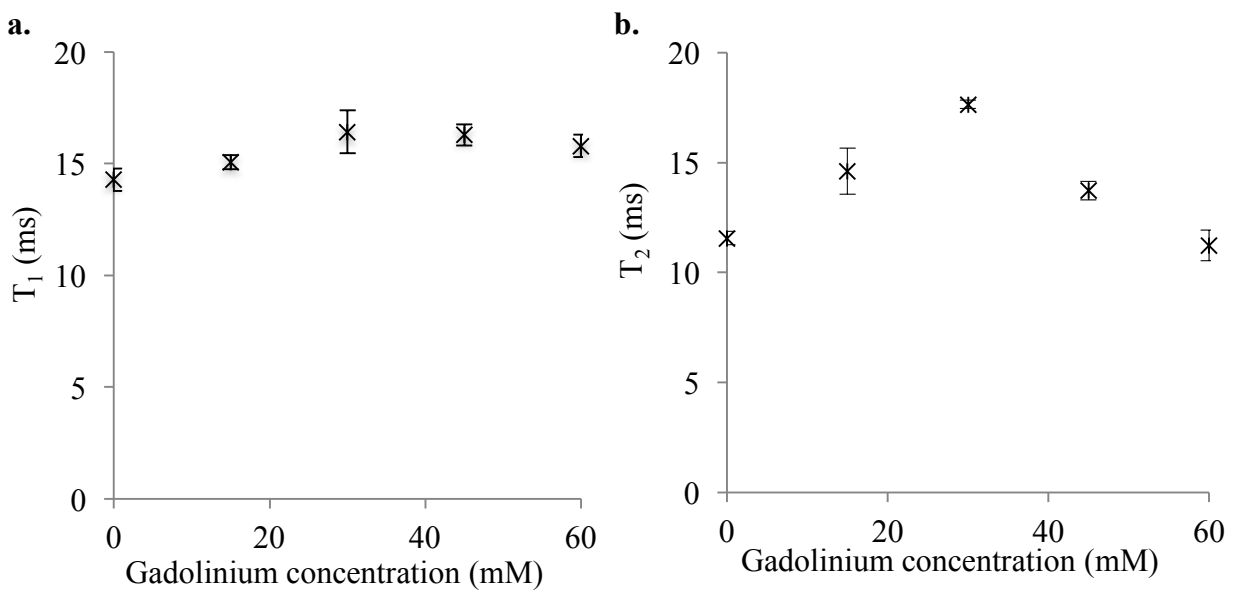


**Figure 5-13:**  $T_1$  and  $T_2$  measurements for the polydisperse foam at a range of Gadobutrol concentrations. The error bars represent the SD from three samples.

## 5.5 Discussion

### 5.5.1 Assessment of the efficacy of the lung representative phantoms

An ideal lung-representative phantom for this research would have monodisperse bubbles that could be fabricated to have known varying diameters around 200  $\mu\text{m}$  and an 80% gas content to represent the gas to tissue ratio conditions seen at maximal inspiration. The material used to represent the lung should have a magnetic susceptibility similar to that of lung parenchymal tissue, with ease of addition of paramagnetic contrast agents to allow susceptibility-matching studies. Neither of the foam fabrication methods met the criteria in full, but both achieved different aspects. The polydisperse foam phantom had a much smaller average bubble size than the alveoli of the human lung. However, the fabrication process allowed accurate control over the achieved gas to liquid ratio and capacity to efficiently alter the magnetic susceptibility of the liquid component. The agarose and PEG-40s phantom allowed production of highly monodisperse bubbles that more closely resembled alveolar size; the size of these monodisperse bubbles could be easily varied. Although only two bubble sizes were fabricated and compared in this work, further variation of the relative gas and liquid pressures, or utilisation of a different microfluidic chip, would allow more bubble sizes to be investigated. However, an unavoidable change in gas to liquid ratio occurred with changing diameter, with the 80% gas volume being unachievable; the achievable proportional gas volume ranged from 30% to 75%. A further drawback is that the slow batch fabrication method restricted the ability to make many samples, making it an inefficient procedure to test susceptibility matching.

Detailed reference to the composition of lung-representative phantoms used for MR investigations in the literature is scarce. Glass beads (Hopkins and Prisk, 2010), sponge (Minard *et al.*, 2005; Menke *et al.*, 2010; Molinari *et al.*, 2014), and porous polyethylene (Pavlovskaya *et al.*, 2005) have all been utilised. These designs highlight a key limitation of the lung models fabricated in this chapter in that it could not be translated to hyperpolarised gas imaging research due to the stable conditions the gas must be kept in until immediately before use. Sponge and glass bead phantoms are also better suited to making phantoms on a larger scale than those achieved in this work. However, the phantoms developed here were designed with the specific aim of testing the relationship between magnetic susceptibility gradients and  $T_2^*$ , something that would have been challenging to investigate using other media due to limitations with sourcing standardised materials, and modifying the susceptibility of the materials in a controlled and quantifiable means.

### 5.5.2 Determinants of PFP -CF<sub>3</sub> T<sub>2</sub>\*

The monodisperse and polydisperse foam produced different PFP -CF<sub>3</sub> T<sub>2</sub>\* values. The T<sub>2</sub>\* measured in the smaller (~140 μm diameter, 50-70% liquid) monodisperse bubble samples were comparable that measured in healthy volunteers in Chapter 2 and literature values of in vivo measures of PFP T<sub>2</sub>\* at 2.0 - 2.2 ms (Couch *et al.*, 2013). This demonstrates the efficacy of this fabrication technique to produce an alveolar-representative magnetic environment for MR imaging, although the gas:liquid ratio unrepresentative.

The average T<sub>2</sub>\* measured in the polydisperse foam samples was around 4 ms, greater than that measured in healthy volunteers. The reason for this was not determined, but may be due to the few larger bubbles distorting the average T<sub>2</sub>\* measured from the polyexponential decay curve, or the magnetic susceptibility of the liquid component of the foam being less diamagnetic than lung tissue in practice. Alternatively, as a result of motional averaging in the very small pores, the PFP molecules may have experienced a more homogeneous magnetic field than is present, resulting in the longer T<sub>2</sub>\* measured. Further investigation into T<sub>2</sub>\* at very small pore sizes in different materials will be required to confirm the cause. The fabrication method used to make the polydisperse foam allowed gadolinium based contrast agents to be easily added in varying concentrations, and clearly identified the optimal molar concentration of Gadobutrol to produce susceptibility matching in the phantom, 30 mM. At this value, the T<sub>2</sub>\* of PFP -CF<sub>3</sub> was maximised, in good agreement with theoretical calculations. At higher contrast agent concentrations, the magnetic susceptibility gradient increased due to the foam being more paramagnetic than the PFP/O<sub>2</sub>. The single measurement in the surfactant and agarose phantom supported these findings, with a similar T<sub>2</sub>\* being achieved after introduction of the 30 mM Gadodiamide. Additionally, this concentration of gadolinium based contrast agent was utilised in a susceptibility matching study imaging inhaled <sup>3</sup>He and an injected gadolinium based contrast agent reviewed at the beginning of this chapter (Dimitrov *et al.*, 2005).

Due to the larger effect of the magnetic susceptibility gradients in the lung on the T<sub>2</sub>\* of PFP -CF<sub>3</sub> than on hyperpolarised <sup>3</sup>He and <sup>129</sup>Xe, techniques to alter the magnetic susceptibility gradient can be expected to produce a more pronounced effect on the T<sub>2</sub>\* with <sup>19</sup>F MR techniques than hyperpolarised gas imaging alternatives.

The impact of temperature on the PFP -CF<sub>3</sub> relaxation times was not investigated, so repetition of the study at 37°C to represent body temperature may further alter the T<sub>1</sub> and T<sub>2</sub>\*

of the gas.

Despite the limitations of each fabrication technique, both produced results that demonstrate shortened  $T_2^*$  behaviour seen in the lung, and satisfactorily confirmed the potential gain in  $T_2^*$  by susceptibility matching using Gadobutrol.

### ***5.5.3 Translation of findings to in vivo measurements***

In Chapter 2, a relationship between position in the respiratory cycle and average  $T_2^*$  of inhaled PFP/O<sub>2</sub> was observed in healthy volunteers. Localised measurement of  $T_2^*$  in the human lung is predominantly limited by the breath hold duration of the subject. This is because multiple 3D SPGR sequences must be acquired at varying TE within a single breath hold to allow a  $T_2^*$  signal decay to be plotted at each voxel. A fast and optimised acquisition would be required, as developed in previous chapters. Even so, the accuracy of the  $T_2^*$  map is likely to be limited due scan duration constraints strictly limiting the number of echo time points collected. Collection of this data at expiration, or in patients with obstructive lung disease would be further limited due to the reduced comfortable breath hold duration.

The translation of the magnetic susceptibility matching findings to in vivo studies is unlikely to be direct as the pulmonary vasculature provides inhomogeneous coverage of the lung tissue making complete susceptibility matching unattainable. It is also clearly unfeasible to significantly change the magnetic susceptibility of the total blood volume in human subjects. Therefore, an adequately fast imaging technique would be required to image a bolus of gadolinium move through the lung vasculature immediately after injection into venous blood when intravascular Gadobutrol is at its highest concentration. After the first pass through the lungs, the dose would be sufficiently diluted by the total blood volume that there would be minimal effect on the magnetic susceptibility of the blood.

### ***5.5.4 Potential clinical applications***

These in vitro measurements detected a change in  $T_2^*$  associated with pore size, reflecting the in vivo results seen between inspiration and expiration in Chapter 2. The pathophysiology of emphysema, with microstructural changes in parenchymal tissue resulting in enlarged and less elastic alveoli present a clear clinical application of this finding.

Reduction of the magnetic susceptibility gradient at the alveolar walls by introduction of an intravenous gadolinium based contrast agent would result in a longer  $T_2^*$  of inhaled PFP, permitting acquisitions with higher SNR. Application to patient cohorts would present

another capability of this technique; as only well-perfused lung tissue would be susceptibility matched, a single acquisition could display pulmonary ventilation and perfusion information simultaneously, with signal related to both  $^{19}\text{F}$  spin density, and proximity of PFP molecules to gadolinium imbued blood. This therefore presents a potential ventilation and perfusion sensitive imaging modality.

## 5.6 Conclusions

This chapter has demonstrated the utility of two novel lung-representative phantoms for investigating the behaviour of the MR properties of inhaled PFP. The use of a microfluidic chip with a detergent and agarose solution and PFP/O<sub>2</sub> gas allowed fabrication of stable monodisperse foam with bubble sizes and T<sub>2</sub>\* measurements representative of that seen in human alveoli. It was also utilised to investigate the effect of varying pore size on PFP T<sub>2</sub>\*, with both the bubble size and the percentage gas identified as contributory factors.

The polydisperse foam, although structurally less representative of alveolar dimensions, allowed susceptibility matching to be investigated and presented a two to three-fold increase in T<sub>2</sub>\* by addition of 30 mM of Gadobutrol or Gadodiamide. This result was in good agreement to the preliminary measurement made in the surfactant and agarose phantom.

This work has presented a foundation for a novel approach for visualising pulmonary structure using T<sub>2</sub>\* mapping of inhaled perfluoropropane. Development of a T<sub>2</sub>\* mapping protocol that can be performed ideally within a short breath hold length acquisition time (which patients would be capable of performing) is required, before verification of the technique in both healthy volunteers and patient cohorts with emphysema. It also highlights the potential value of introduction of an intravenously administered gadolinium based contrast agent to increase the T<sub>2</sub>\* of inhaled PFP in the lung to achieve higher SNR images. This has potential to be utilised for simultaneous identification of both poorly perfused and poorly ventilated regions of the lung.

## **Chapter 6:**

# **Dynamic Contrast-enhanced $^{19}\text{F}$ MRI of Inhaled Perfluoropropane in Rodents and Healthy Volunteers**

### **6.1 Overview**

Chapter 5 defined the concentrations of Gadobutrol and Gadodiamide required to susceptibility match a homogeneous diamagnetic aqueous solution to the paramagnetic PFP/O<sub>2</sub> gas microbubbles suspended in it. When fully susceptibility-matched, a three-fold increase in PFP T<sub>2</sub>\* was achieved in the lung-representative phantoms. This in vitro model demonstrated potential utility for in vivo combined ventilation and perfusion mapping.

The motivation for this chapter was therefore the development and translation of this gadolinium enhanced imaging technique to  $^{19}\text{F}$ -MR imaging of inhaled PFP/O<sub>2</sub> in rodents and healthy volunteers. We tested the hypothesis that the local magnetic susceptibility gradients at the alveolar walls can be reduced by intravenous injection of a paramagnetic contrast agent, resulting in an increased T<sub>2</sub>\* of PFP -CF<sub>3</sub>. This chapter therefore aimed to achieve full susceptibility matching in rodent lungs by cumulative injections of a gadolinium based contrast agent (GBCA) and to detect a change in magnetic properties via both T<sub>2</sub>\* and SNR measurements before and after injection of a GBCA in both rodents and healthy volunteers. Translation of this susceptibility-matching concept to in vivo environments is challenging due to the complex structure of the lung parenchyma; the macroscopically irregular distribution of pulmonary vasculature proximal to the alveolar walls requires the intravenously injected GBCA to exchange between the intravascular and extracellular regions of the parenchyma. It was unfeasible to produce a phantom model to accurately replicate this biological environment. Therefore, although the optimum concentration of Gadobutrol for susceptibility matching was calculated within the phantom model to be 30 mM, a higher concentration in the blood would be needed to account for the extravascular tissue volume.

Initial development studies were carried out in mouse models on a preclinical MR system. This allowed testing of the susceptibility-matching theory and assessment of the concentration of Gadobutrol required for maximal elevation of PFP T<sub>2</sub>\* in an in vivo environment.

The promising preclinical results were then translated to human studies. In healthy volunteers, adherence to maximum dose regulations required a single bolus of Gadobutrol to be measured

on its first pass through the pulmonary vasculature, after which it would be diluted across the full blood volume to an undetectable concentration. This necessitated fast  $T_2^*$ -weighted imaging protocols to detect change in PFP -CF<sub>3</sub> signal before, during, and after intravenous administration of the contrast agent. A dynamic contrast-enhanced <sup>19</sup>F-MRI and dynamic <sup>19</sup>F unlocalised spectroscopy acquisition were performed on two healthy volunteers to observe the impact of a bolus of intravenous GBCA on inhaled PFP -CF<sub>3</sub>  $T_2^*$  during its first pass through the pulmonary vasculature.

## 6.2 Susceptibility matching in the lung for mapping pulmonary perfusion: background

### 6.2.1 Existing modalities for imaging pulmonary perfusion

CT pulmonary angiography and ventilation/perfusion (V/Q) scintigraphy are well-established techniques for mapping pulmonary perfusion in current clinical practice (Stein *et al.*, 2004; Freeman and Haramati, 2009). Both provide similar diagnostic capabilities (Freeman and Haramati, 2009) and are economical and readily available (Johns *et al.*, 2017). However, both utilise ionising radiation which is associated with increased risk of cancer, particularly for repeated acquisitions during long-term patient monitoring. CT pulmonary angiography alone offers no information about ventilation, and uses an intravenous iodinated contrast agent, which is associated with a 3 – 15% risk of adverse reactions, dependent on iodinated contrast-agent type (Iyer *et al.*, 2013).

Innovations in MRI have presented options for perfusion imaging without using ionising radiation. Fourier decomposition MRI has been used to simultaneously assess ventilation and perfusion during free-breathing, without requiring contrast agents (Bauman *et al.*, 2013). The parenchymal  $^1\text{H}$  signal varies with position in respiratory cycle, and the change in blood velocity in the parenchymal vasculature varies throughout the cardiac cycle, with the higher blood velocity associated with faster dephasing of the MR signal. Fourier decomposition analysis of dynamic images can separate these two signal-varying effects and produce separate images weighted to depict ventilation or perfusion. However, as ventilation and perfusion are both measured by indirect means using this technique, a highly robust methodology for quantitative analysis is required to be clinically valuable (Johns *et al.*, 2017).

$^1\text{H}$  DCE-MRI has been extensively studied on clinical cohorts as a perfusion mapping method (Amundsen *et al.*, 2000; Ley and Ley-Zaporozhan, 2012; Zhang *et al.*, 2016). It utilises  $T_1$ -weighted imaging protocols to detect a transient increase in parenchymal  $^1\text{H}$  signal during passage of an intravenously injected GBCA bolus. This imaging technique uses a typical GBCA injection dose of 0.05 - 0.1 mmol/kg body weight and acquisition sequences with 0.5 - 1 s long dynamics.

Comparatively, the technique developed in this chapter utilises intravenously administered GBCA in combination with inhaled perfluoropropane. The signal intensity of the inhaled imaging agent provides a direct measure of ventilation, and the GBCA provides a means for indirect measurement of perfusion by its  $T_2^*$  lengthening effect on inhaled PFP proximal to the GBCA, as described in the previous chapter. This technique therefore avoids ionising

radiation and has the potential to provide simultaneous ventilation and perfusion measurements.

### **6.2.2 Susceptibility matching in the mouse lung**

Due to the small circulating blood volume, measured to be approximately 72 ml/kg, equating to ~2 ml for a 30g mouse (Diehl *et al.*, 2001), it is possible to significantly alter the magnetic susceptibility of the entire blood volume by intravenous injection of Gadobutrol, something that would be unfeasible to do in humans. A 30 mM Gadobutrol concentration can be achieved in a 2 ml blood volume with a 60  $\mu$ L dose of 1.0 M Gadobutrol. However, equilibration of the Gadobutrol with organs, as well as filtration out of the vasculature by the kidneys, will impede susceptibility matching, therefore a larger volume of Gadobutrol was used in the following in vivo study.

A further consideration in the preclinical mouse model is the small alveolar diameter, measured in a number of studies to range from 34 to 68  $\mu$ m depending on mouse strain, lung region, and whether measured at inspiration or expiration (Soutiere *et al.*, 2004; Knust *et al.*, 2009; Osmanagic *et al.*, 2010; Chang *et al.*, 2015). Following the discussion of the relationship between local magnetic susceptibility gradients and  $T_2^*$  in previous chapters, and the higher field strength of the 7.0 T preclinical MR system, the  $T_2^*$  of inhaled perfluoropropane would be expected to be shorter than the 2.0 ms  $T_2^*$  measured in humans at 3.0 T (Couch *et al.*, 2013).

### **6.2.3 Safety review of gadolinium based contrast agents**

Intravenously administered GBCAs have been associated with nephrogenic systemic fibrosis (NSF) in patients with renal impairment (Agarwal *et al.*, 2009). More recently, evidence of deposition of gadolinium in the brain after injection has been published, however the clinical and biological significance of this is currently unknown (Gulani *et al.*, 2017). Although rare, GBCAs are also known to cause allergic and adverse reactions in subjects. Recent large-scale studies have investigated the safety of macrocyclic GBCAs. A study of 24,308 injections of gadoterate maglumine at 61 institutions in Germany found a 0.4% rate of adverse events, most rated as minor, with just one serious adverse event reported (Herborn *et al.*, 2007). 38,580 injections in a single institution in Seoul recorded 31 incidences of hypersensitivity. Four of which were described as severe meeting the criteria for anaphylaxis (Jung *et al.*, 2012). Intravenously administered Gadobutrol has been the subject of a recent large multi-centre study investigating 23,708 patients in 272 institutions across four continents, which

demonstrated a high tolerability by subjects and a good safety record, with a 0.7% incidence rate of adverse reactions and 0.02% rate of serious adverse events (Prince *et al.*, 2017). The risk to healthy volunteers is therefore regarded as low when used within manufacturer guidelines, which permit a dose up to 0.3 mmol/kg (Bayer, 2016). This is reflected in the over 300 million doses administered since the introduction of GBCAs 30 years ago (Runge, 2015).

Dynamic susceptibility weighted MRI (DSC-MRI) detects areas of damage to the blood-brain barrier by mapping locations of decreased signal intensity caused by GBCA leakage following bolus injection. It has been the subject of a large number of studies which typically utilise GBCAs in 0.5 – 1.0 mmol/ml concentrations, at a dose of 0.1 – 0.2 mmol/kg and a high delivery rate of 4 – 6 ml/s (Weber *et al.*, 2005; Jarnum *et al.*, 2010; Korfiatis and Erickson, 2014). The dose and delivery rate of GBCAs used in the following healthy volunteer study were chosen in-part to not exceed these values.

#### **6.2.4 Susceptibility matching in healthy volunteers**

Unlike the mouse model, alteration of the magnetic susceptibility of the full circulating blood volume is unfeasible in human subjects. However, a bolus of Gadobutrol can be delivered to the pulmonary vasculature by intravenous injection into a large vein in the forearm. Upon entering the right atrium, it will progress through to the right ventricle and out of the pulmonary artery, providing a direct route to the pulmonary vasculature with minimal opportunity for dilution. The concentration of the bolus delivered to the pulmonary vasculature would therefore be dependent upon the rate of injection and the heart rate and stroke volume of the subject. This method requires fast measurement of the transient change in susceptibility as the bolus passes through the pulmonary vasculature.

The dose of Gadobutrol required to achieve a local bolus concentration of 30 mM in the blood can be calculated for a known cardiac output:

$$\text{dose rate}(\text{mmol/s}) = \text{cardiac output}(\text{ml/s}) \times 0.03(\text{mmol/ml}) \quad 6.1$$

Where cardiac output is calculated from stroke volume  $\times$  heart rate. Stroke volume has been measured to be an average of 94 ml (Maceira *et al.*, 2006), resulting in a typical cardiac output of 100 to 150 ml/s for a healthy volunteer at rest. With a dose of 0.2 mmol/kg, a 30 mM Gadobutrol concentration can therefore typically be achieved for a period of 3-5 s bolus injection length.

The lung is known to have a density of 0.29 g lung tissue/ml thoracic volume, with an approximate fractional blood volume of 0.15 ml blood/ml thoracic volume (Wollmer *et al.*, 1984; Brudin *et al.*, 1987). Therefore, the gadolinium imbued blood only changes the magnetic susceptibility of about half the parenchymal volume, with the tissue magnetic susceptibility remaining unchanged. Perfect susceptibility matching is therefore unachievable in humans as, unlike the mouse model, the transient bolus will not equilibrate with the extravascular space. Furthermore, although the path to the lung from a major vein is relatively direct, a small amount of unavoidable dilution is expected. Anticipating this effect, a concentration of Gadobutrol greater than 30 mM is likely to be required for maximal susceptibility matching of tissue and gas components of the lung.

## 6.3 Methods

### 6.3.1 Mouse study: $^{19}\text{F}$ MRI preparation

Preclinical studies were performed under a project licence granted by the Home Office in accordance with the Animals (Scientific Procedures) Act of 1986. The study used four 14 week old male mice of strain C57BL/6, with an average weight of  $30 \pm 2$  g. An anaesthetic (a Hypnorm/midazolam/water mixture in a 1:1:2 volume ratio, at a dose of 10 ml/kg body weight) was administered by intraperitoneal injection approximately 10 minutes prior to MR acquisitions. The dose used permitted approximately one hour of anaesthesia. A tail vein cannula was placed and used to inject Gadobutrol as required.

Once anaesthetised, the mouse was placed in a 10 cm long birdcage RF coil, tuned to the  $^{19}\text{F}$  resonant frequency at 7.0 T (280 MHz). This was positioned at the isocentre of a 7.0 T Varian DirectDrive horizontal bore preclinical MR scanner (Varian Medical Systems, Inc. USA). A diagram illustrating the layout of the primary components of the hardware used is displayed in Figure 6-1.

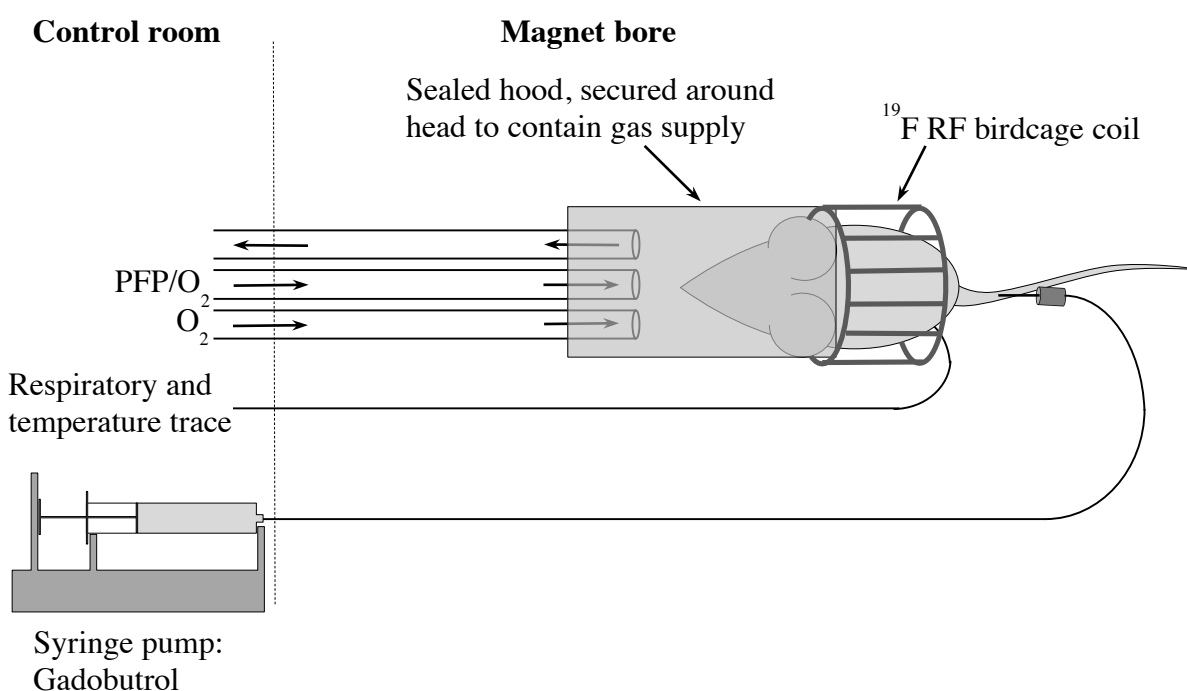


**Figure 6-1:** Schematic of the hardware configuration for imaging inhaled PFP/O<sub>2</sub> after Gadobutrol injections in a 7.0 T preclinical MR system.

Two tubes provided a supply of oxygen (used between MR acquisitions) or 79% PFP/ 21% O<sub>2</sub> (during MR acquisitions) both at a flow rate of 0.2 L/min. A third tube carried the flow of gas away from the scanner suite. A sealed container with a close-fitting latex neck collar was placed around the mouse's head to ensure PFP was delivered to the head, minimising extraneous PFP/O<sub>2</sub> gas in the imaging FOV around the animal. Microbore tubing connected to the cannula from a syringe pump located in the control room allowed remote injection of Gadobutrol.

Respiratory bellows and a rectal thermometer were used to monitor the mouse from the control room. A fan and heater positioned at the end of the magnet bore were used to maintain mouse body temperature at 37°C.

### 6.3.2 *Mouse study: acquisition protocol*

Each mouse inhaled the PFP/O<sub>2</sub> gas for a minimum of 1 minute prior to commencing the MR acquisitions to ensure complete equilibrated PFP wash-in over the full lung volume for the duration of the scan. A non-slice selective 2D spoiled gradient echo imaging sequence with arrayed TE was acquired, allowing calculation of PFP T<sub>2</sub>\*. The principal acquisition parameters used are listed in Table 6.1.

Acquisition sequence	2D SPGR
Flip angle	90°
TE (ms)	Array: 1.0, 1.2, 1.4, 1.6, 1.8
TR (ms)	4.0
Bandwidth (Hz)	50000
FOV: H-F × L-R (mm)	50 × 50
Acquisition matrix	64 × 64
Number of averages	200
Scan durations (s)	256

**Table 6.1:** Acquisition parameters for a 2D spoiled gradient echo sequence with an TE array. This acquisition protocol was repeated after intravenous administration of five cumulative 0.2 mmol doses of Gadobutrol.

1.0 mmol/ml Gadobutrol was then injected at a rate of 600 µL/min for 20 s, resulting in an injection volume of 200 µL, equivalent to 0.2 mmol. A period of 40 seconds was then allowed to elapse to ensure equilibration of the Gadobutrol throughout the circularity system. The acquisition sequence described in Table 6.1 was then repeated. This injection and imaging

protocol was repeated a further four times, resulting in a total injected volume of 1.0 ml of Gadobutrol. This protocol was replicated on a further three mice. All mice remained in the MR scanner for less than 1 hour and were euthanised by cervical dislocation whilst still sedated immediately after removal from the scanner.

Mean signal achieved was calculated from a  $4 \times 4$  pixel ROI in the centre of the left lung. PFP  $T_2^*$  was then calculated by fitting a decaying exponential to the mean signal measured over the TE array.

### ***6.3.3 Healthy volunteer study: effect of intravenous gadolinium-based contrast agent on PFP $T_2^*$ and signal magnitude***

Translation of the technique from an animal model to a human model required a GBCA to be detected via its impact on PFP -CF<sub>3</sub>  $T_2^*$  as the bolus passes through the pulmonary vasculature.

The healthy volunteer study received ethical approval (assessed by the Newcastle and North Tyneside 1 Research Ethics Committee of the NHS National Research Ethics Service. Reference: 14/NE/0135). Two healthy volunteers were recruited and gave informed consent to participate. Both were non-smokers and in good health with no history of respiratory, cardiac, or cerebrovascular disease. A spirometric test was carried out on each participant to confirm normal lung function. A respiratory clinician and MR radiographers were present throughout the scan sessions.

Each volunteer was cannulated in a large superficial vein in the right forearm, which was connected to an MR-safe power injector loaded with 1.0 mmol/ml Gadobutrol and saline (0.9% NaCl). Each volunteer was then positioned supine on the scanner bed with a 20 cm diameter <sup>19</sup>F surface coil (PulseTeq Ltd. – as used in Chapter 2) positioned on their upper back, with the top of the coil aligned with the subject's clavicle. Whilst in the magnet bore, volunteers breathed through an inhalation rig as depicted in Figure 2-1, allowing control over the supply of room air and PFP/O<sub>2</sub> to the subject. Participant oxygen saturation and heart rate were continually monitored from the MR control room via a MR-compatible pulse oximeter sensor on their index finger (Model 7500FO, Nonin Medical).

An unlocalised FID spectroscopy sequence was utilised to dynamically measure change in in vivo signal amplitude and  $T_2^*$  of the PFP -CF<sub>3</sub> resonance on volunteer 1. The principal acquisition parameters are listed in Table 6.2. The acquisitions had a temporal resolution of

0.25 s.

Acquisition sequence	Unlocalised spectroscopy
Flip angle	90° block pulse
TE (ms)	0.49
TR (ms)	250
Bandwidth (Hz)	8000
Number of samples per FID	256
Number of dynamics	350
Scan durations (s)	88

**Table 6.2:** Acquisition parameters for a dynamic unlocalised FID sequence. The Gadobutrol bolus was injected 20 s into the acquisition.

Concurrent with the start of the acquisition, the volunteer was instructed to perform three deep respiratory cycles of PFP/O<sub>2</sub> through the inhalation rig, ensuring wash-in of the PFP/O<sub>2</sub>, as deemed adequate in Chapter 3. After the third inspiration, the volunteer performed a 30 s breath hold. Simultaneously with the start of the breath hold, 17 ml of 1.0 mmol/ml Gadobutrol (0.2 mmol/kg) was injected at a rate of 4 ml/s, immediately followed by 20 ml of saline at the same rate.

After a period of 5 minutes had elapsed, allowing time for complete wash-out of PFP/O<sub>2</sub> and equilibration of the Gadobutrol in the body, the dynamic <sup>19</sup>F spectroscopy acquisition protocol was repeated without further administration of Gadobutrol. This allowed comparison of relative dynamic signal and T<sub>2</sub>\* patterns with and without a paramagnetic bolus. Fitting an exponential decay curve to the FID at each dynamic allowed calculation of the average <sup>19</sup>F T<sub>2</sub>\* of PFP –CF<sub>3</sub>.

The acquisition protocol applied to volunteer 2 utilised the same hardware setup in conjunction with a  $^{19}\text{F}$  2D spoiled gradient echo sequence. The volunteer performed three deep respiratory cycles of PFP/ $\text{O}_2$  followed by a 30 s breath hold at maximal inspiration. Upon commencing the breath hold, the imaging acquisition was started and a Gadobutrol bolus and saline flush were delivered following the same injection protocol as for volunteer 1. The principal acquisition parameters are listed in Table 6.3.

Acquisition sequence	2D SPGR
Flip angle	$50^\circ$
TE (ms)	1.7
TR (ms)	4.2
Bandwidth (Hz/pixel)	500
FOV: H-F $\times$ L-R $\times$ A-P (mm)	$300 \times 300 \times 200$
Acquisition matrix	$24 \times 24$
Number of dynamics	600
Scan durations (s)	60

**Table 6.3:** Acquisition parameters for a 2D spoiled gradient echo sequence to dynamically detect PFP - $\text{CF}_3$  signal.

This sequence allowed spatially resolved change in signal to be mapped across the lung volume within the sensitive volume of the RF coil with a 0.1 s temporal resolution. After acquisition, averaging was applied producing images showing 4 s dynamics.

## 6.4 Results

### 6.4.1 Mouse study: effect of intravenous Gadobutrol on $T_2^*$ and signal amplitude

The  $T_2^*$  of the  $-\text{CF}_3$  groups of inhaled PFP/ $\text{O}_2$  was found to vary from an average of  $0.75 \pm 0.11$  ms without Gadobutrol to  $2.6 \pm 0.4$  ms after injection of 400  $\mu\text{L}$  of Gadobutrol, corresponding to a  $\Delta R_2^*$  of  $-950 \text{ s}^{-1}$ . The relative signal detected in TE-array SPGR acquisitions prior to, and following Gadobutrol administration in a representative mouse is displayed in Figure 6-2.

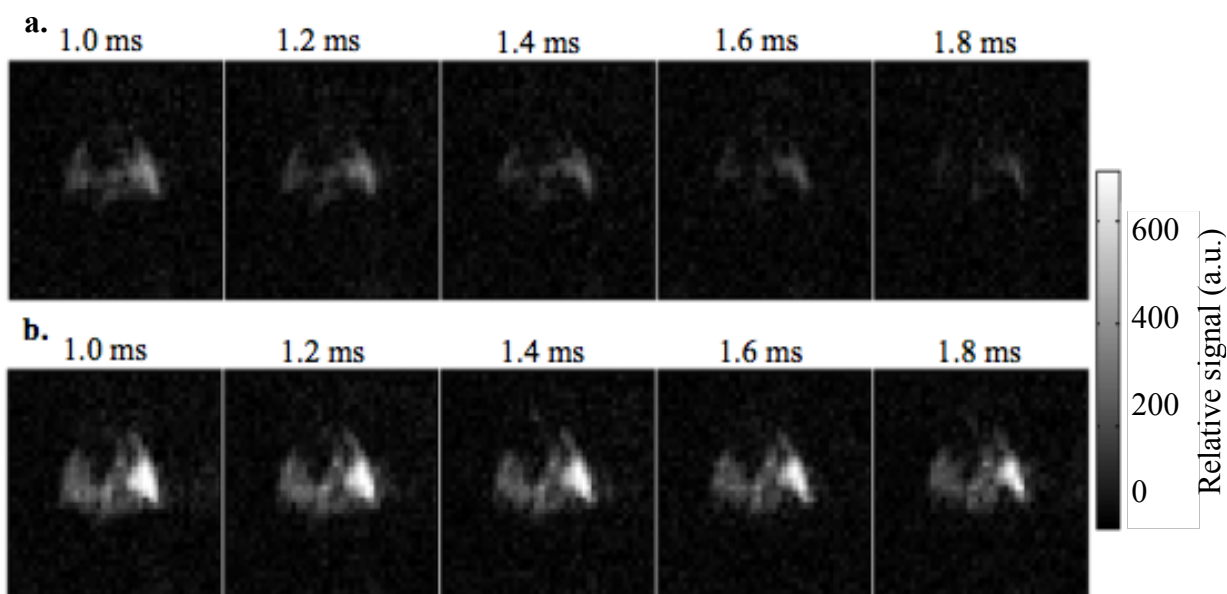


**Figure 6-2:** Relative signal intensity over a range of echo times from **a.** inhaled PFP/ $\text{O}_2$  before injection of Gadobutrol, and **b.** inhaled PFP/ $\text{O}_2$  after injection of a total volume of 400  $\mu\text{L}$  of Gadobutrol.

At injected Gadobutrol concentrations above 400  $\mu\text{L}$ , the  $T_2^*$  of PFP was found to decrease, representing the lung parenchyma becoming more paramagnetic than the inhaled PFP/ $\text{O}_2$ , creating an increasing magnetic susceptibility gradient between tissue and gas compartments. The average  $^{19}\text{F}$   $-\text{CF}_3$   $T_2^*$  measured in the four mice over changing Gadobutrol volumes is plotted in Figure 6-3. The standard deviation of  $T_2^*$  measured between the mice is represented by the error bars.

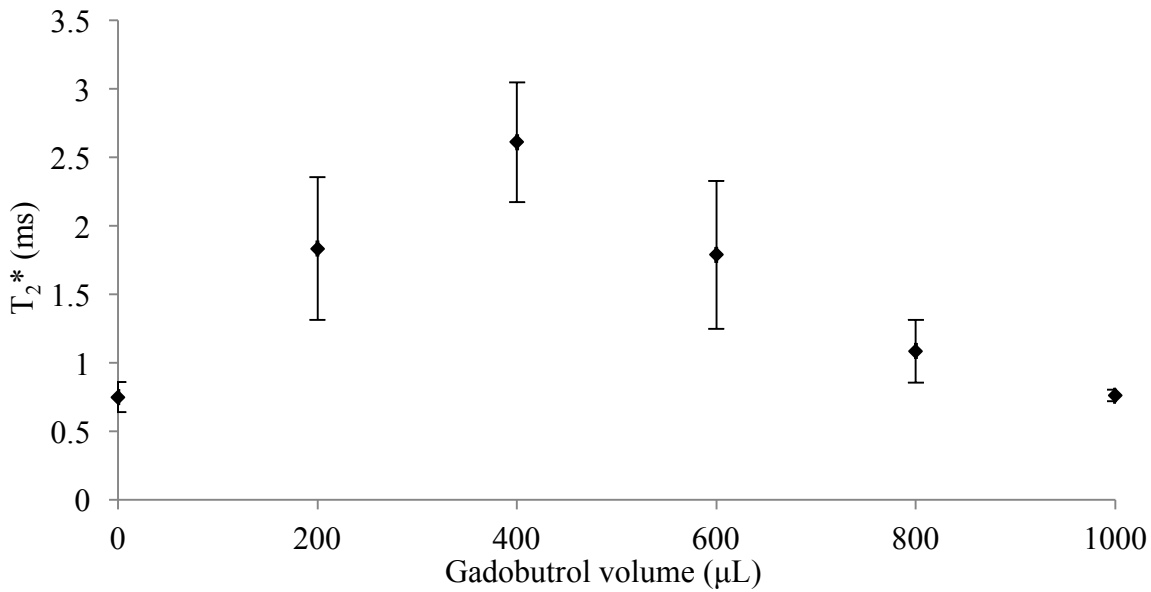


**Figure 6-4:** Average  $T_2^*$  ( $\pm$ SD) after cumulative intravenous injections of 200  $\mu$ L volumes of 1.0 mmol/ml Gadobutrol for four mice.

The associated relative signal change over the imaging protocol due to changing  $T_2^*$  in a representative mouse at a 1.0 ms TE is depicted in Figure 6-4. In the four mice, the average increase in signal amplitude ( $\pm$ SD) between 0  $\mu$ L and 400  $\mu$ L Gadobutrol calculated from an ROI in the left (brightest) lung was 198%  $\pm$  29%. The left lung is larger in the through-plane direction than the right lung in this non-slice selective acquisition, resulting in it being brighter.

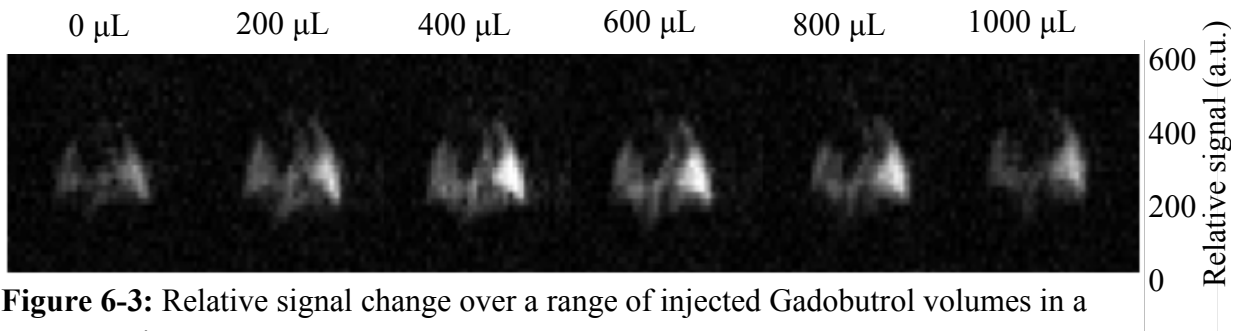


**Figure 6-3:** Relative signal change over a range of injected Gadobutrol volumes in a representative mouse.

#### 6.4.2 Healthy volunteer study: effect of intravenous gadolinium on average $T_2^*$

The average  $T_2^*$  and relative signal amplitude from the unlocalised spectroscopy sequences acquired on volunteer 1 are displayed in Figures 6-5 and 6-6. Figure 6-5 displays the acquisition sequence that utilised the Gadobutrol injection during the breath hold. The results show a  $\sim 5$  s delay after commencement of the injection at the start of the breath hold for the Gadobutrol to enter the pulmonary vasculature. At this point, the  $T_2^*$  of the PFP  $-\text{CF}_3$  increases from an average of 1.50 ms during the breath hold prior to the effect of Gadobutrol to a peak of 1.67 ms, representing an increase of 11% and  $\Delta R_2^*$  of  $-68 \text{ s}^{-1}$ . The elevation in  $T_2^*$  lasts for 10 s, demonstrating a spread from the initial 4 s bolus injection time.

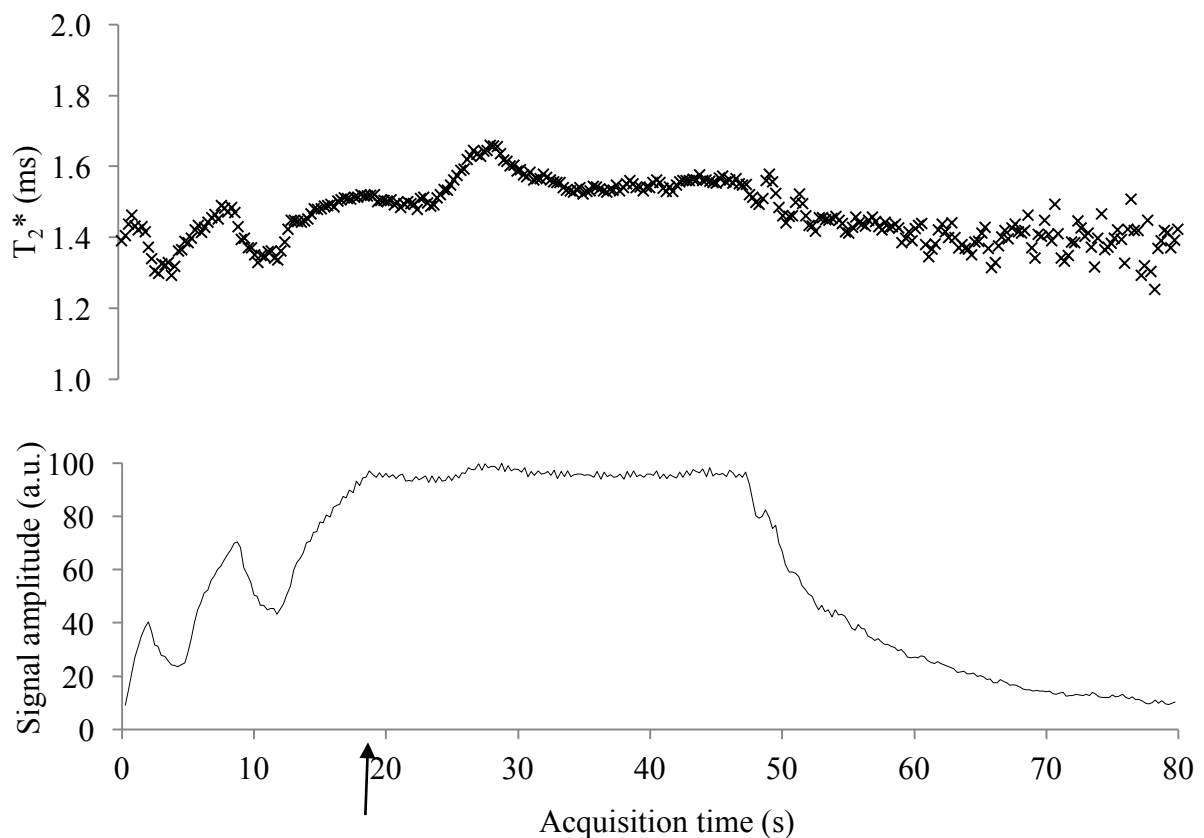


**Figure 6-5:** Unlocalised spectroscopy data displayed as average  $T_2^*$ , and signal amplitude. The arrow denotes the time-point at which Gadobutrol was injected, coinciding with the commencement of a 30 s breath hold. It is seen to transiently alter the  $T_2^*$  of inhaled PFP shortly after.

Figure 6-6 displays the dynamic spectroscopy acquisition repeated without injection of a bolus of Gadobutrol. Notably, a stable  $T_2^*$  is present throughout the breath hold.

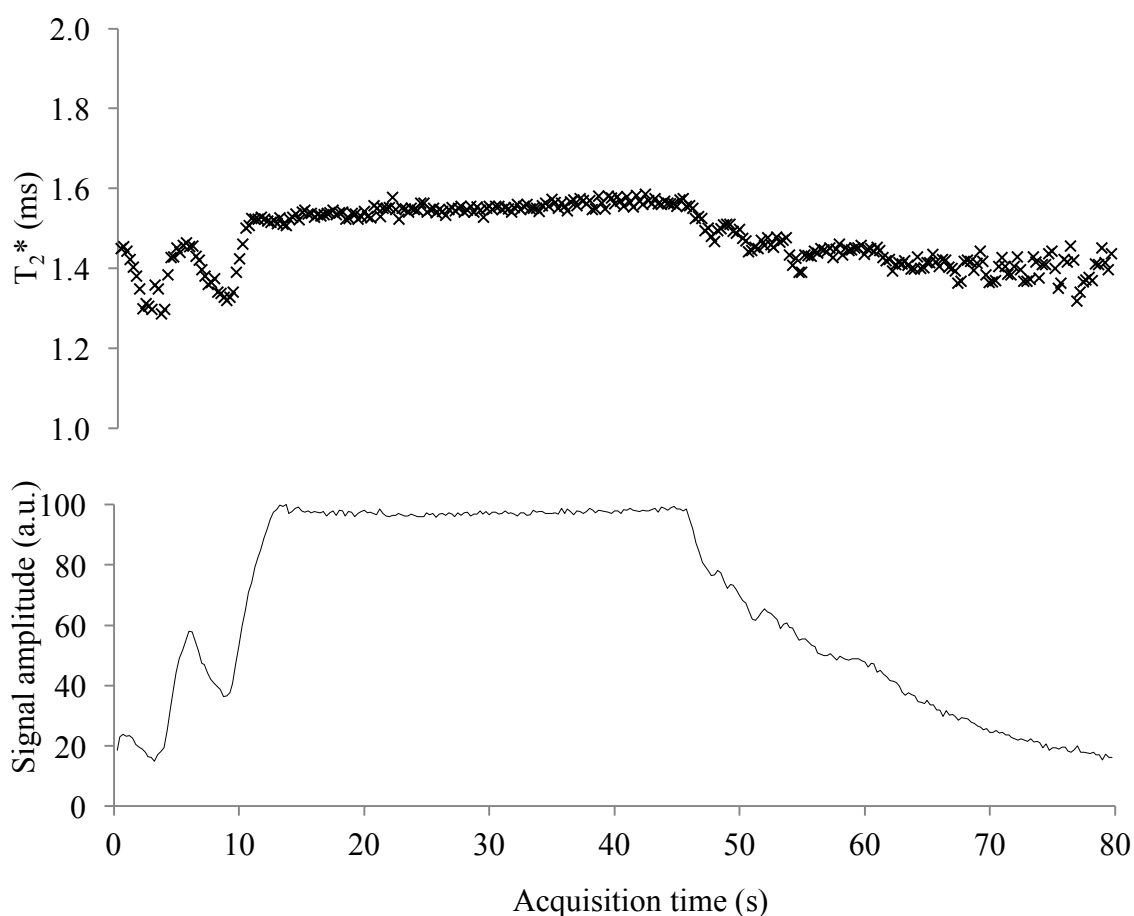


**Figure 6-6:** Unlocalised spectroscopy data displayed as average  $T_2^*$  and signal amplitude. This acquisition was performed without administration of intravenous Gadobutrol.

#### 6.4.3 Healthy volunteer study: effect of intravenous GBCA on $^{19}\text{F}$ -MRI signal amplitude

The 2D SPGR imaging sequence allowed dynamic images to be acquired with a 0.1 s temporal resolution. Only partial lung coverage was achieved as these were acquired due to the small sensitive volume of the surface coil used. 3 second averages produced by summing the dynamics, and scaled to depict change in signal intensity are depicted in Figure 6-7.

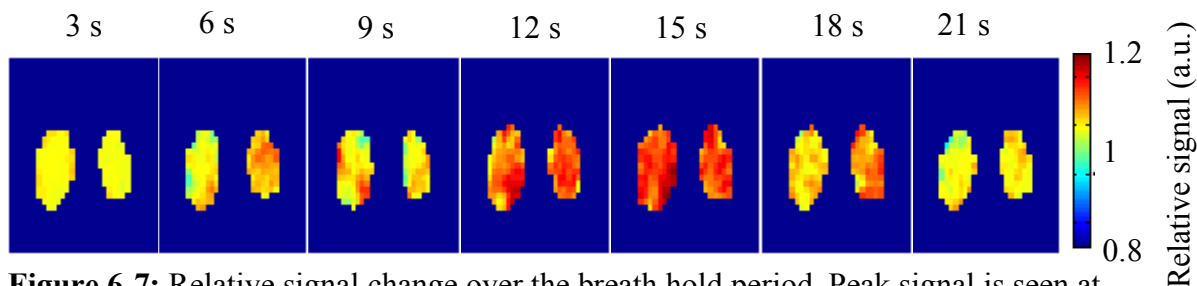


**Figure 6-7:** Relative signal change over the breath hold period. Peak signal is seen at 12-15s.

Figure 6-8 displays the relative signal amplitude over time from each dynamic.

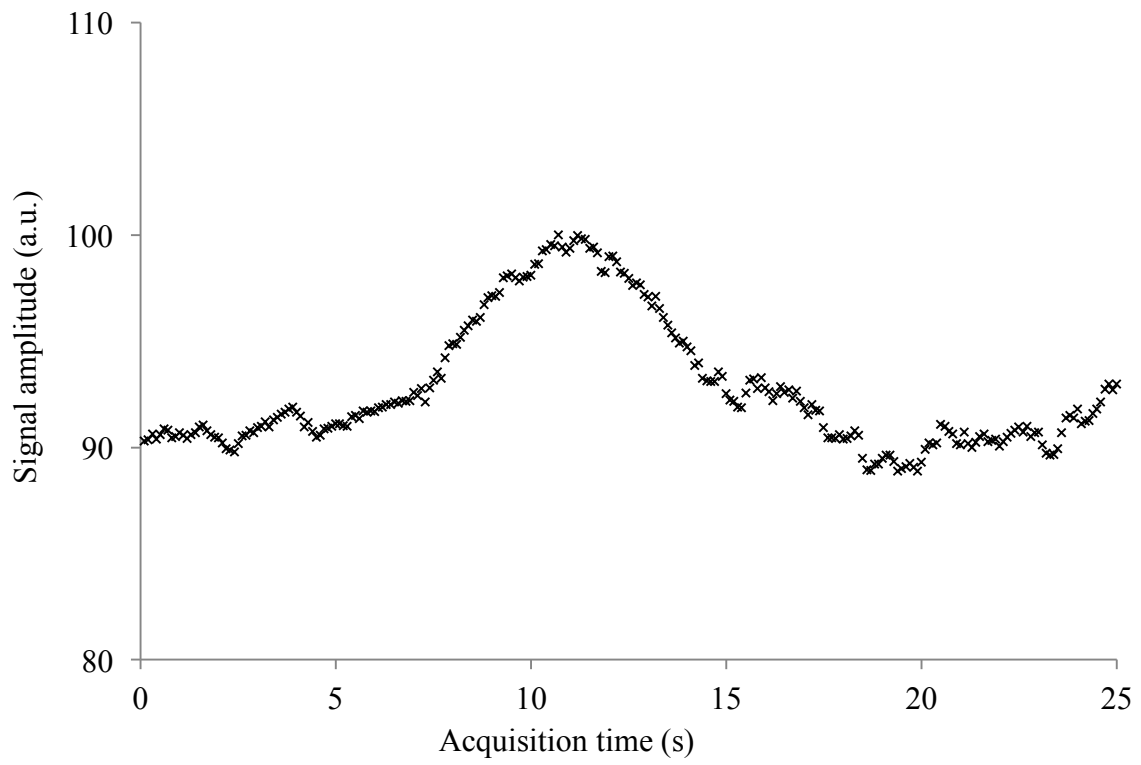


**Figure 6-8:** Relative signal amplitude across the 25 second breath hold. Gadobutrol is injected at  $t = 0$  s.

## 6.5 Discussion

### 6.5.1 Mouse study

The 3.5 fold increase in PFP  $T_2^*$  achieved in the mouse models with introduction of intravenous Gadobutrol is analogous to the increase in PFP  $T_2^*$  measured in the foam models reported in the previous chapter, and in a publication on susceptibility matching in rodents measuring hyperpolarised  $^3\text{He}$  (Vignaud *et al.*, 2005). However, the volume of Gadobutrol required to achieve 30 mM in the lung parenchyma was greatly increased, despite the mouse blood being similar in volume to the liquid component in the foam samples produced. This is likely to be primarily due to equilibration of the gadolinium into extravascular extracellular space resulting in reduced blood concentrations, with smaller contributory factors including filtration of the gadolinium from the mouse through the kidneys during the relatively long acquisitions, and a bigger range of magnetic susceptibility gradients in the lung than those seen in the homogeneously distributed gadolinium in the phantom models. Further investigation, such as taking blood samples during the study for measurement of magnetic susceptibility and GBCA concentration would be required to more precisely define the predominant contributory factors.

The  $T_2^*$  of inhaled PFP in the mouse lung was found to be much lower than that measured in the human lung, 1.5 – 2.0 ms (our measurements and Couch *et al.* (2013)). This is partly due to the stronger magnetic field at 7.0 T causing lower  $T_2^*$ , but is also in part likely due to the alveolar diameter of the mouse being a quarter of the human alveolar diameter (Ochs *et al.*, 2004; Soutiere *et al.*, 2004; Knust *et al.*, 2009; Osmanagic *et al.*, 2010; Chang *et al.*, 2015). This results in the mouse alveoli having a larger surface area to volume ratio, consequently causing the inhaled PFP to be on average in closer proximity to the magnetic field gradients at the alveolar surface. This effect was seen in the monodisperse foam samples of differing sizes fabricated in Chapter 5.

The mouse model provided an opportunity to verify the efficacy of intravenously administering Gadobutrol to modify the  $-\text{CF}_3$   $T_2^*$  of inhaled PFP/ $\text{O}_2$  with markedly positive results. However, the unrepresentative alveolar diameter and the high doses of Gadobutrol required prevented direct translation of these results to human studies. The results however are invaluable at demonstrating the potential capabilities of this technique in humans with further development.

### **6.5.2 *Healthy volunteer study***

The 10% change in both average PFP  $T_2^*$  and PFP signal amplitude observed in both volunteers after injection of Gadobutrol supported the hypothesis. Unlike in the mouse studies, the change was transient, requiring a fast imaging sequence and sensitive RF coil to be detected. Although challenging to image, the transient nature of the signal change is however necessary to utilise this technique for V/Q measurements.

The mouse model has demonstrated that higher concentrations than those used in humans are needed to minimise the in vivo susceptibility gradient and further increase the PFP  $T_2^*$ . The difference in  $\Delta R_2^*$  measured between the rodent and human studies suggests that a ~14-fold increase in Gadobutrol concentration at the parenchyma would be required for full susceptibility matching in humans.

The Gadobutrol injection periods were shorter than the ~10 s long elevated  $T_2^*$  observed. This spreading of the signal peak seen reflects dilution of the Gadobutrol with blood either side of the bolus. A longer injection duration combined with a higher Gadobutrol concentration would allow greater potential for utilisation of the signal produced, but would necessitate a larger dose than the 0.2 mmol/kg Gadobutrol used in this study. Manufacturer guidelines currently allow up to 0.3 mmol/kg of Gadobutrol, which offers some flexibility in increasing the dose in future studies if this can be justified from an ethical standpoint. Use of a more paramagnetic contrast agent could potentially offer susceptibility matching with a smaller dose, however commercially available substitutes such as superparamagnetic iron oxide are not currently marketed for human use (Wang, 2011; Wang, 2015).

Other approaches to increase the SNR would allow utilisation of a coil with a larger field of view, allowing images from the full lung volume to be acquired. This will be necessary for the technique to have clinical utility.

### **6.5.3 *Application to clinical practice***

Altering the magnetic susceptibility gradient present at the air-tissue boundary in the mouse and human alveoli resulted in a demonstrable increase in  $T_2^*$  of inhaled PFP. In a healthy lung, it is expected that this signal change would be relatively homogeneous over the full lung volume, assuming that the pulmonary capillaries are relatively uniformly distributed across the alveoli. This would allow higher SNR images of inhaled PFP/O<sub>2</sub> to be acquired than can currently be achieved. In patients where the ventilation/perfusion ratio is typically spatially variable, such as that seen in pulmonary embolism, a  $T_2^*$ -weighted <sup>19</sup>F MRI of inhaled PFP

with an injected Gadobutrol contrast agent would display information related to both ventilation and perfusion in a single acquisition.

## 6.6 Conclusions

Mouse studies have demonstrated a 3.5-fold increase in average PFP –CF<sub>3</sub> T<sub>2</sub>\* in the alveoli from 0.76 to 2.61 ( $\Delta R_2^* = -950 \text{ s}^{-1}$ ) with intravenous injection of 0.4 ml of 1.0 mmol/ml Gadobutrol, equivalent to 13.3 mmol/kg. This result was in good agreement with similar measurements seen in vitro in lung-representative phantoms in the previous chapter. This novel method for lengthening the in vivo T<sub>2</sub>\* by reduction of the local magnetic field gradients resulted in a two-fold increase in signal intensity for acquisitions at a TE of 1 ms.

Translation to healthy volunteer studies resulted in a transient T<sub>2</sub>\* increase of 10% ( $\Delta R_2^* = -68 \text{ s}^{-1}$ ) when administering a 0.2 mmol/kg bolus of Gadobutrol at a rate of 4 ml/s. This study has demonstrated the first use of susceptibility matching in the human lung to enhance <sup>19</sup>F-MRI of inhaled PFP, allowing improved visualisation of pulmonary structure in locations immediately adjacent to well-perfused pulmonary parenchyma. Therefore, this technique has scope to be a valuable biomarker of compromised ventilation-perfusion ratio.

## **Chapter 7:**

### **Conclusions and Future Work**

This thesis details  $^{19}\text{F}$ -MR acquisition techniques developed to image inhaled perfluoropropane to provide quantitative assessment of pulmonary function. The resultant techniques described in this work were demonstrated in healthy volunteer studies after initial validation in phantom and preclinical models. The outcomes of these studies demonstrate the utility of MRI for imaging inhaled perfluoropropane and provide a number of opportunities for further development of the novel imaging techniques described.

In Chapter 2, a preliminary  $^{19}\text{F}$ -MRI study of inhaled PFP/ $\text{O}_2$  in healthy volunteers demonstrated the capabilities of the technique; 3D images with a SNR of 40:1 proximal to the RF coil were produced with  $1.0\text{ cm}^3$  spatial resolution within a 15 s acquisition time. Assessment of PFP wash-in and wash-out rates confirmed near-complete wash-in was achieved after three deep inhalations of PFP/ $\text{O}_2$ . This finding guided the number of inspirations used in healthy volunteer studies in the subsequent chapters. A change in average PFP - $\text{CF}_3$   $T_2^*$  with position in the respiratory cycle was also observed, with the mean  $T_2^*$  varying between 1.3 and 1.7 ms. It was postulated that this was related to alveolar size, an idea further researched in phantom models in a later chapter.

The results of the study described in this chapter also identified primary areas of focus to aid improvement of the imaging technique, namely the requirement of an RF coil with a larger sensitive volume, and an acquisition sequence optimised to achieve maximal SNR in a fixed acquisition time. These were addressed directly in the two following chapters.

In Chapter 3, a quadrature birdcage torso coil was constructed to operate at 120.12 MHz at 3.0 T with satisfactory results in phantoms, however poor power performance was noted under heavy loading. A larger commercial quadrature transmit/receive birdcage coil was assessed for suitability, and compared with three alternative RF coils. This commercial coil presented adequate power efficiency with loading and offered the most homogeneous signal amplitude within its sensitive volume compared to alternative birdcage coil configurations. The results of these measurements confirmed good suitability of this coil for lung imaging using inhaled perfluoropropane. This coil was therefore used in subsequent human studies.

In Chapter 4, the 3D SPGR sequence was simulated to define the parameter values required to

achieve the highest SNR in a defined acquisition period for  $^{19}\text{F}$ -MRI of inhaled PFP/ $\text{O}_2$ . These were a flip angle of  $50^\circ$  and a receiver bandwidth of 500 Hz/pixel, with the minimum allowed TE and TR, where the minimum TR was SAR-limited. It was also found that no potential improvement in SNR in a fixed scan time can be expected by increasing the input power from the RF amplifier to raise the maximum  $B_1$  amplitude, due to the longer TR required to stay within the SAR restrictions. This validated the suitability of the current RF chain configuration. A compressed sensing technique was applied to allow an up to three-fold acceleration of the sequence. Once implemented, 3D full-lung images with a 1 cm isotropic resolution were acquired. A SNR of 28:1 was achieved in a 6 s breath hold acquisition consisting of four averages. With this technique, improvement of the spatial resolution or further signal averaging could be investigated whilst maintaining breath hold length acquisition times. The acceleration that this technique offers also presents the opportunity to develop dynamic ventilation imaging techniques. This could also permit imaging during steady-state breathing with retrospective respiratory gating to achieve static ventilation images removing any necessity for the subject to conform to breathing protocols. Dynamic MRI of inhaled perfluoropropane therefore has potential to offer additional utility to hyperpolarised noble gas MRI which is ill-suited to dynamic imaging due to the non-renewable nature of its hyperpolarisation and the expense of using large gas volumes.

This optimised ventilation imaging protocol was primarily developed for application to a large-scale study to test the utility of the technique in patients and healthy volunteers. This study will continue over the following 3 years, during which, 40 healthy volunteers, 40 patients with asthma and 40 patients with COPD will participate to test the utility of this imaging technique for quantitative assessment of pulmonary ventilation defects. This will involve testing the reproducibility of the inhalation protocol and the optimised and accelerated imaging technique in healthy volunteers before they are applied to patient cohorts. The degree of airway disease measured will be tested against established inhaled hyperpolarised gas MRI methods. This study, if successful, will be a stepping stone towards the ultimate goal of implementation in clinical practice.

Chapter 5 introduced susceptibility matching as a tool to offer a modality for assessment of pulmonary function. Two novel lung-representative phantoms were fabricated and used to investigate the behaviour of the MR properties of inhaled PFP with changing structural and magnetic environments, with both the bubble size and the percentage gas identified as contributory factors to the length of the PFP- $\text{CF}_3$   $T_2^*$ . Susceptibility matching the liquid media with the gas-phase PFP/ $\text{O}_2$  bubble suspension by addition of 30 mM Gadobutrol or

Gadodiamide demonstrated an up to three-fold increase in PFP -CF<sub>3</sub> T<sub>2</sub>\*. This work highlighted the potential value of introduction of an intravenously administered gadolinium based contrast agent to increase the T<sub>2</sub>\* of inhaled PFP in the lung. The novel monodisperse microbubble phantoms developed in this chapter would benefit from further studies to quantitatively assess their stability over time. If determined to be highly stable, they may present valuable tools in microporous media research beyond the application described in this thesis.

Chapter 6 described the translation of the susceptibility matching results of Chapter 5 to in vivo rodent and human subjects. Intravenous injection of 0.4 ml of 1.0 mmol/ml Gadobutrol resulted in a 3.5-fold increase in average PFP -CF<sub>3</sub> T<sub>2</sub>\* from 0.76 to 2.61 ms in four mice. This result was in good agreement with similar measurements seen in vitro in lung-representative phantoms in the previous chapter. Further in vivo studies in mouse models would be valuable to determine the extent of susceptibility changes in the lung tissue as well as in the blood. This could be achieved by taking blood or tissue samples after injection of a GBCA and measuring their magnetic susceptibility, thus identifying the proportion of susceptibility matching caused by the changing circulating blood susceptibility, and the extent of extravascular diffusion of the GBCA. This would inform the potential extent of susceptibility matching we can expect to achieve in human subjects where the injected GBCA bolus has minimal extravascular diffusion in the lung.

Translation to healthy volunteer studies demonstrated a transient increase in the T<sub>2</sub>\* of inhaled PFP of 10% after intravascular injection of a 17 ml bolus of 1.0 mmol/ml Gadobutrol at a rate of 4 ml/s. Using this technique, susceptibility matching of the parenchyma to the inhaled PFP/O<sub>2</sub> can only occur in ventilated alveoli proximal to well-perfused regions of lung tissue. Therefore, this technique offers the potential to concurrently acquire images reflecting both pulmonary ventilation and perfusion. The novel work described in this chapter is in its infancy, with significant potential for future development. In order to develop this further, the next steps would be to make the technique viable for full lung acquisitions, requiring use of a larger coil. In order to maintain adequate SNR and acquisition speed, the optimised imaging protocol combined with the compressed sensing acceleration technique developed in Chapter 4 could be applied. Further development would necessitate investigation into the most suitable paramagnetic contrast agent type, volume, and injection rate to produce the most pronounced transient change, before reproducibility testing the protocol in healthy volunteers.

## References

- Agarwal, R., Brunelli, S.M., Williams, K., Mitchell, M.D., Feldman, H.I. and Umscheid, C.A. (2009) 'Gadolinium-based contrast agents and nephrogenic systemic fibrosis: a systematic review and meta-analysis', *Nephrology Dialysis Transplantation*, 24(3), pp. 856-863.
- Albert, M.S., Cates, G.D., Driehuys, B., Happer, W., Saam, B., Springer, C.S. and Wishnia, A. (1994) 'Biological magnetic resonance imaging using laser polarized Xe-129', *Nature*, 370(6486), pp. 199-201.
- Albert, M.S. and Hane, F.T. (2016) *Hyperpolarized and Inert Gas MRI: From Technology to Application in Research and Medicine*. Elsevier Science.
- Albert, M.S., Huang, W., Lee, J.H., Balschi, J.A. and Springer, C.S. (1993) 'Aqueous shift-reagents for high-resolution cation NMR. Titration curves for in vivo Na-23 and (H2O)-H-1 MRS obtained from rat blood', *NMR in Biomedicine*, 6(1), pp. 7-20.
- Amis, T.C., Jones, H.A. and Hughes, J.M.B. (1984) 'Effect of posture on inter-regional distribution of pulmonary ventilation', *Respiration Physiology*, 56(2), pp. 145-167.
- Amundsen, T., Torheim, G., Waage, A., Bjermer, L., Steen, P.A. and Haraldseth, O. (2000) 'Perfusion magnetic resonance imaging of the lung: characterization of pneumonia and chronic obstructive pulmonary disease. A feasibility study', *Journal of magnetic resonance imaging : JMRI*, 12(2), pp. 224-31.
- Atlas, S.W. (2009) *Magnetic Resonance Imaging of the Brain and Spine*. Wolters Kluwer Health/Lippincott Williams & Wilkins.
- Baete, S.H., De Deene, Y., Masschaele, B. and De Neve, W. (2008) 'Microstructural analysis of foam by use of NMR R-2 dispersion', *Journal of Magnetic Resonance*, 193(2), pp. 286-296.
- Ball, W.C., Jr., Stewart, P.B., Newsham, L.G. and Bates, D.V. (1962) 'Regional pulmonary function studied with xenon 133', *The Journal of clinical investigation*, 41, pp. 519-31.
- Bauman, G., Scholz, A., Rivoire, J., Terekhov, M., Friedrich, J., de Oliveira, A., Semmler, W., Schreiber, L.M. and Puderbach, M. (2013) 'Lung ventilation- and perfusion-weighted Fourier decomposition magnetic resonance imaging: In vivo validation with hyperpolarized <sup>3</sup>He and dynamic contrast-enhanced MRI', *Magnetic Resonance in Medicine*, 69(1), pp. 229-237.
- Bayer (2016) 'Summary of product characteristics', [www.mhra.gov.uk/home/groups/spcpil/documents/spcpil/con1498197990792.pdf](http://www.mhra.gov.uk/home/groups/spcpil/documents/spcpil/con1498197990792.pdf) [Online].

(Accessed: 20th August 2017).

Bergin, C.J., Glover, G.H. and Pauly, J.M. (1991) 'Lung parenchyma - Magnetic-susceptibility in MR imaging', *Radiology*, 180(3), pp. 845-848.

Bernstein, M.A., King, K.F. and Zhou, X.J. (2004) *Handbook of MRI pulse sequences*. 1 edn. Elsevier Inc.

Bhatti, U., Rani, K. and Memon, M.Q. (2014) 'Variation in lung volumes and capacities among young males in relation to height', *Journal of Ayub Medical College, Abbottabad : JAMC*, 26(2), pp. 200-2.

Bloch, F. (1946) 'Nuclear induction', *Physical Review*, 70(7-8), pp. 460-474.

Bloch, F., Hansen, W.W. and Packard, M. (1946) 'Nuclear induction', *Physical Review*, 69(3-4), pp. 127-127.

Bloembergen, N., Purcell, E.M. and Pound, R.V. (1948) 'Relaxation effects in nuclear magnetic resonance absorption', *Physical Review*, 73(7), pp. 679-712.

Bodduluri, S., Bhatt, S.P., Hoffman, E.A., Newell, J.D., Martinez, C.H., Dransfield, M.T., Han, M.K., Reinhardt, J.M. and Investigators, C.O. (2017) 'Biomechanical CT metrics are associated with patient outcomes in COPD', *Thorax*, 72(5), pp. 409-414.

Boissoles, P. and Caloz, G. (2006) 'Magnetic field properties in a birdcage coil ', *HAL*, 13(06).

Branca, R.T., Cleveland, Z.I., Fubara, B., Kumar, C., Maronpot, R.R., Leuschner, C., Warren, W.S. and Driehuys, B. (2010) 'Molecular MRI for sensitive and specific detection of lung metastases', *Proceedings of the National Academy of Sciences of the United States of America*, 107(8), pp. 3693-3697.

Brown, K.C. (2016) *Essential Mathematics for NMR and MRI Spectroscopists*. Royal Society of Chemistry.

Brown, R.W., Cheng, Y.C.N., Haacke, E.M., Thompson, M.R. and Venkatesan, R. (2014) *Magnetic Resonance Imaging: Physical Principles and Sequence Design*. Wiley.

Brudin, L.H., Rhodes, C.G., Valind, S.O., Wollmer, P. and Hughes, J.M.B. (1987) 'Regional lung density and blood-volume in nonsmoking and smoking subjects measured by PET', *Journal of Applied Physiology*, 63(4), pp. 1324-1334.

Bruno, T.J. and Svoronos, P.D.N. (2010) *CRC Handbook of Basic Tables for Chemical Analysis, Third Edition*. CRC Press.

Bryan, A.C., Bentivoglio, L.G., Beerel, F., Macleish, H., Zidulka, A. and Bates, D.V. (1964) 'Factors affecting regional distribution of ventilation and perfusion in the lung', *Journal of applied physiology*, 19, pp. 395-402.

Carr, H.Y. and Purcell, E.M. (1954) 'Effects of diffusion on free precession in nuclear magnetic resonance experiments', *Physical Review*, 94(3), pp. 630-638.

Carrero-Gonzalez, L., Kaulisch, T. and Stiller, D. (2013) 'In vivo diffusion-weighted MRI using perfluorinated gases: ADC comparison between healthy and elastase-treated rat lungs', *Magnetic Resonance in Medicine*, 70(6), pp. 1761-4.

Celli, B.R., MacNee, W., Agusti, A., Anzueto, A., Berg, B., Buist, A.S., Calverley, P.M.A., Chavannes, N., Dillard, T., Fahy, B., Fein, A., Heffner, J., Lareau, S., Meek, P., Martinez, F., McNicholas, W., Muris, J., Austegard, E., Pauwels, R., Rennard, S., Rossi, A., Siafakas, N., Tieg, B., Vestbo, J., Wouters, E. and ZuWallack, R. (2004) 'Standards for the diagnosis and treatment of patients with COPD: a summary of the ATS/ERS position paper', *European Respiratory Journal*, 23(6), pp. 932-946.

Chae, E.J., Seo, J.B., Goo, H.W., Kim, N., Song, K.S., Lee, S.D., Hong, S.J. and Krauss, B. (2008) 'Xenon ventilation CT with a dual-energy technique of dual-source CT: Initial experience', *Radiology*, 248(2), pp. 615-624.

Chang, S., Kwon, N., Kim, J., Kohmura, Y., Ishikawa, T., Rhee, C.K., Je, J.H. and Tsuda, A. (2015) 'Synchrotron x-ray imaging of pulmonary alveoli in respiration in live intact mice', *Scientific Reports*, 5, p. 6.

Chang, Y.L.V. and Conradi, M.S. (2006) 'Relaxation and diffusion of perfluorocarbon gas mixtures with oxygen for lung MRI', *Journal of Magnetic Resonance*, 181(2), pp. 191-198.

Charles, H.C., MacIntyre, N.R., Moon, R., Foster, W.M., McAdams, H.P. and Ainslie, M. (2014) 'In-vivo visualization of slow to fast filling compartments in human lungs using 19F MRI of perfluorinated gases mixed with oxygen', *American Journal of Respiratory and Critical Care Medicine*, 189, p. 1.

Chavhan, G.B., Babyn, P.S., Thomas, B., Shroff, M.M. and Haacke, E.M. (2009) 'Principles, techniques, and applications of T2\*-based MR imaging and its special applications', *Radiographics*, 29(5), pp. 1433-U272.

Chen, C.N., Hoult, D.I. and Sank, V.J. (1983) 'Quadrature detection coils - a further square-root 2 improvement in sensitivity', *Journal of Magnetic Resonance*, 54(2), pp. 324-327.

Chen, D.L., Cheriyan, J., Chilvers, E.R., Choudhury, G., Coello, C., Connell, M., Fisk, M., Groves, A.M., Gunn, R.N., Holman, B.F., Hutton, B.F., Lee, S., MacNee, W., Mohan, D.,

- Parr, D., Subramanian, D., Tal-Singer, R., Thielemans, K., van Beek, E.J.R., Vass, L., Wellen, J.W., Wilkinson, I. and Wilson, F.J. (2017) 'Quantification of lung PET images: Challenges and opportunities', *Journal of Nuclear Medicine*, 58(2), pp. 201-207.
- Chen, Q., Jakob, P.M., Griswold, M.A., Levin, D.L., Hatabu, H. and Edelman, R.R. (1998) 'Oxygen enhanced MR ventilation imaging of the lung', *Magnetic Resonance Materials in Physics Biology and Medicine*, 7(3), pp. 153-161.
- Chen, X.J., Moller, H.E., Chawla, M.S., Cofer, G.P., Driehuys, B., Hedlund, L.W. and Johnson, G.A. (1999) 'Spatially resolved measurements of hyperpolarized gas properties in the lung in vivo. Part I: Diffusion coefficient', *Magnetic Resonance in Medicine*, 42(4), pp. 721-728.
- Chin, C.L., Collins, C.M., Li, S.H., Dardzinski, B.J. and Smith, M.B. (2002) 'BirdcageBuilder: Design of specified-geometry birdcage coils with desired current pattern and resonant frequency', *Concepts in Magnetic Resonance*, 15(2), pp. 156-163.
- Conradi, M.S., Saam, B.T., Yablonskiy, D.A. and Woods, J.C. (2006) 'Hyperpolarized He-3 and perfluorocarbon gas diffusion MRI of lungs', *Progress in Nuclear Magnetic Resonance Spectroscopy*, 48(1), pp. 63-83.
- Conway, J. (2012) 'Lung imaging - Two dimensional gamma scintigraphy, SPECT, CT and PET', *Advanced Drug Delivery Reviews*, 64(4), pp. 357-368.
- Couch, M., Ball, I., Li, T. and Fox, M. (2014) 'Optimized strategies for <sup>19</sup>F MRI of human lungs and comparison of UTE and gradient echo imaging', *Int. Soc. Mag. Reson. Med.* p. 0777.
- Couch, M.J., Ball, I.K., Li, T., Fox, M.S., Littlefield, S.L., Biman, B. and Albert, M.S. (2013) 'Pulmonary ultrashort echo time F-19 MR imaging with inhaled fluorinated gas mixtures in healthy volunteers: Feasibility', *Radiology*, 269(3), pp. 903-909.
- Couch, M.J., Fox, M.S., Viel, C., Gajawada, G., Li, T., Ouriadov, A.V. and Albert, M.S. (2016) 'Fractional ventilation mapping using inert fluorinated gas MRI in rat models of inflammation and fibrosis', *Nmr in Biomedicine*, 29(5), pp. 545-552.
- Dale, B.M., Brown, M.A. and Semelka, R.C. (2015) *MRI: basic principles and applications*. Wiley.
- Damadian, R., Goldsmith, M. and Minkoff, L. (1977) 'NMR in cancer: XVI. FONAR image of the live human body', *Physiol Chem Phys*, 9(1), pp. 97-100, 108.
- de Prost, N., Sasanelli, M., Deux, J.F., Habibi, A., Razazi, K., Galacteros, F., Meignan, M.,

Maitre, B., Brun-Buisson, C., Itti, E. and Dessap, A.M. (2015) 'Positron emission tomography with F-18-fluorodeoxyglucose in patients with sickle cell acute chest syndrome', *Medicine*, 94(18), p. 10.

Deninger, A.J., Eberle, B., Ebert, M., Grossmann, T., Heil, W., Kauczor, H.U., Lauer, L., Markstaller, K., Otten, E., Schmiedeskamp, J., Schreiber, W., Surkau, R., Thelen, M. and Weiler, N. (1999) 'Quantification of regional intrapulmonary oxygen partial pressure evolution during apnea by He-3 MRI', *Journal of Magnetic Resonance*, 141(2), pp. 207-216.

Deppe, M.H., Parra-Robles, J., Ajraoui, S., Parnell, S.R., Clemence, M., Schulte, R.F. and Wild, J.M. (2009) 'Susceptibility effects in hyperpolarized <sup>3</sup>He lung MRI at 1.5T and 3T', *Journal of Magnetic Resonance Imaging*, 30(2), pp. 418-423.

Diehl, K.H., Hull, R., Morton, D., Pfister, R., Rabemampianina, Y., Smith, D., Vidal, J.M. and van de Vorstenbosch, C. (2001) 'A good practice guide to the administration of substances and removal of blood, including routes and volumes', *Journal of Applied Toxicology*, 21(1), pp. 15-23.

Dimitrov, I.E., Insko, E., Rizi, R. and Leigh, J.S. (2005) 'Indirect detection of lung perfusion using susceptibility-based hyperpolarized gas imaging', *Journal of Magnetic Resonance Imaging*, 21(2), pp. 149-155.

Duyn, J. (2013) 'MR susceptibility imaging', *Journal of magnetic resonance (San Diego, Calif. : 1997)*, 229, pp. 198-207.

Ebner, L., He, M., Virgincar, R.S., Heacock, T., Kaushik, S.S., Freemann, M.S., McAdams, H.P., Kraft, M. and Driehuys, B. (2017) 'Hyperpolarized (<sup>129</sup>)xenon magnetic resonance imaging to quantify regional ventilation differences in mild to moderate asthma a prospective comparison between semiautomated ventilation defect percentage calculation and pulmonary function tests', *Investigative Radiology*, 52(2), pp. 120-127.

Elster, A.D. (1993) 'Gradient-echo MR imaging - techniques and acronyms', *Radiology*, 186(1), pp. 1-8.

Emsley, J. (1998) *The elements*. 3rd ed.. edn. Oxford : New York: Oxford : Clarendon Press ; New York : Oxford University Press.

Felmlee, J.P., Morin, R.L., Salutz, J.R. and Lund, G.B. (1989) 'Magnetic resonance imaging phase encoding: a pictorial essay', *RadioGraphics*, 9(4), pp. 717-722.

Fok, J.S. and Smith, W.B. (2017) 'Hypersensitivity reactions to gadolinium-based contrast agents', *Current Opinion in Allergy and Clinical Immunology*, 17(4), pp. 241-246.

- Freeman, L.M. and Haramati, L.B. (2009) 'V/Q scintigraphy: alive, well and equal to the challenge of CT angiography', *European Journal of Nuclear Medicine and Molecular Imaging*, 36(3), pp. 499-504.
- Frerichs, I., Dudykevych, T., Hinz, J., Bodenstein, M., Hahn, G. and Hellige, G. (2001) 'Gravity effects on regional lung ventilation determined by functional EIT during parabolic flights', *Journal of Applied Physiology*, 91(1), pp. 39-50.
- Galvin, I., Drummond, G.B. and Nirmalan, M. (2007) 'Distribution of blood flow and ventilation in the lung: gravity is not the only factor', *British Journal of Anaesthesia*, 98(4), pp. 420-428.
- Gast, K.K., Viallon, M., Eberle, B., Lill, J., Puderbach, M.U., Hanke, A.T., Schmiedeskamp, J. and Kauczor, H.U. (2002) 'MRI in lung transplant recipients using hyperpolarized He-3: Comparison with CT', *Journal of Magnetic Resonance Imaging*, 15(3), pp. 268-274.
- Giovannetti, G. (2014) 'Birdcage coils: equivalent capacitance and equivalent inductance', *Concepts in Magnetic Resonance Part B-Magnetic Resonance Engineering*, 44(2), pp. 32-38.
- Glauser, F.L. and Wilson, A.F. (1977) 'Pulmonary parenchymal tissue volume in normal subjects - effect of age and sex', *Chest*, 72(2), pp. 207-212.
- Goto, T., Nakata, Y., Ishiguro, Y., Niimi, Y., Suwa, K. and Morita, S. (2000) 'Minimum alveolar concentration-awake of xenon alone and in combination with isoflurane or sevoflurane', *Anesthesiology*, 93(5), pp. 1188-1193.
- Gulani, V., Calamante, F., Shellock, F.G., Kanal, E., Reeder, S.B. and Int Soc Magnetic Resonance, M. (2017) 'Gadolinium deposition in the brain: summary of evidence and recommendations', *Lancet Neurology*, 16(7), pp. 564-570.
- Gurler, N. and Ider, Y. (2012) 'FEM based design and simulation tool for MRI birdcage coils including eigenfrequency analysis', *COMSOL*. Milan. Available at: <Go to WoS>://WOS:A1988N096600009.
- Haase, A., Frahm, J., Matthaei, D., Hancic, W. and Merboldt, K.D. (1986) 'Flash imaging - rapid NMR imaging using low flip-angle pulses', *Journal of Magnetic Resonance*, 67(2), pp. 258-266.
- Haefelibleuer, B. and Weibel, E.R. (1988) 'Morphometry of the human pulmonary acinus', *Anatomical Record*, 220(4), pp. 401-414.
- Hahn, A.D., Cadman, R.V., Sorkness, R.L., Jarjour, N.N., Nagle, S.K. and Fain, S.B. (2016) 'Redistribution of inhaled hyperpolarized He-3 gas during breath-hold differs by asthma

severity', *Journal of Applied Physiology*, 120(5), pp. 526-536.

Hahn, E. (1953) 'Free nuclear induction', *Physics Today*, 6(11), pp. 4-9.

Halaweish, A.F. and Charles, H.C. (2014) 'Physiorack: An integrated MRI safe/conditional, Gas delivery, respiratory gating, and subject monitoring solution for structural and functional assessments of pulmonary function', *Journal of Magnetic Resonance Imaging*, 39(3), pp. 735-741.

Halaweish, A.F., Moon, R.E., Foster, W.M., Soher, B.J., McAdams, H.P., MacFall, J.R., Ainslie, M.D., MacIntyre, N.R. and Charles, H.C. (2013) 'Perfluoropropane gas as a magnetic resonance lung imaging contrast agent in humans', *Chest*, 144(4), pp. 1300-1310.

Hamedani, H., Clapp, J.T., Kadlecsek, S.J., Emami, K., Ishii, M., Geftter, W.B., Xin, Y., Cereda, M., Shaghghi, H., Siddiqui, S., Rossman, M.D. and Rizi, R.R. (2016) 'Regional fractional ventilation by using multibreath wash-in He-3 MR imaging', *Radiology*, 279(3), pp. 917-924.

Hatabu, H., Alsop, D.C., Listerud, J., Bonnet, M. and Geftter, W.B. (1999a) 'T2\* and proton density measurement of normal human lung parenchyma using submillisecond echo time gradient echo magnetic resonance imaging', *European Journal of Radiology*, 29(3), pp. 245-252.

Hatabu, H., Gaa, J., Tadamura, E., Edinburgh, K.J., Stock, K.W., Garpestad, E. and Edelman, R.R. (1999b) 'MR imaging of pulmonary parenchyma with a half-Fourier single-shot turbo spin-echo (HASTE) sequence', *European Journal of Radiology*, 29(2), pp. 152-159.

Hayes, C.E. and Axel, L. (1985) 'Noise performance of surface coils for magnetic resonance imaging and 1.5-T', *Medical Physics*, 12(5), pp. 604-607.

Hayes, C.E., Edelstein, W.A., Schenck, J.F., Mueller, O.M. and Eash, M. (1985) 'An efficient, highly homogeneous radiofrequency coil for whole-body NMR imaging at 1.5-T', *Journal of Magnetic Resonance*, 63(3), pp. 622-628.

Herborn, C.U., Honold, E., Wolf, M., Kemper, J., Kinner, S., Adam, G. and Barkhausen, J. (2007) 'Clinical safety and diagnostic value of the gadolinium chelate gadoterate meglumine (Gd-DOTA)', *Investigative Radiology*, 42(1), pp. 58-62.

Hernández - Flores, R., Rodríguez - González, A.O., Salgado - Lujambio, P. and Barrios - Alvarez, F.A. (2002) 'Concentric loop surface coil', *AIP Conference Proceedings*, 630(1), pp. 134-140.

Hersman, F.W., Ruset, I.C., Ketel, S., Muradian, I., Covrig, S.D., Distelbrink, J., Porter, W.,

Watt, D., Ketel, J., Brackett, J., Hope, A. and Patz, S. (2008) 'Large production system for hyperpolarized Xe-129 for human lung imaging studies', *Academic Radiology*, 15(6), pp. 683-692.

Hinshaw, W.S. and H, L.A. (1983) 'An introduction to NMR imaging: from the Bloch equation to the imaging equation', *Proceedings of the IEEE*, 71(3), pp. 338-350.

Holland, G.N., Bottomley, P.A. and Hinshaw, W.S. (1977) 'F-19 magnetic-resonance imaging', *Journal of Magnetic Resonance*, 28(1), pp. 133-136.

Holland, J., Milic-Emili, J., Macklem, P.T. and Bates, D.V. (1968) 'Regional distribution of pulmonary ventilation and perfusion in elderly subjects', *The Journal of clinical investigation*, 47(1), pp. 81-92.

Hopkins, S.R. and Prisk, G.K. (2010) 'Lung perfusion measured using magnetic resonance imaging: new tools for physiological insights into the pulmonary circulation', *Journal of Magnetic Resonance Imaging*, 32(6), pp. 1287-1301.

Hoult, D.I. and Richards, R.E. (1976) 'The signal-to-noise ratio of the nuclear magnetic resonance experiment', *Journal of Magnetic Resonance*, 24(1), pp. 71-85.

Irvin, C.G. (2011) 'Will the small airways rise again?', *American Journal of Respiratory and Critical Care Medicine*, 184(5), pp. 499-501.

Iyer, R.S., Schopp, J.G., Swanson, J.O., Thapa, M.M. and Phillips, G.S. (2013) 'Safety essentials: acute reactions to iodinated contrast media', *Canadian Association of Radiologists Journal-Journal De L Association Canadienne Des Radiologistes*, 64(3), pp. 193-199.

Jacob, R.E., Chang, Y.V., Choong, C.K., Bierhals, A., Hu, D.Z., Zheng, J., Yablonskiy, D.A., Woods, J.C., Gierada, D.S. and Conradi, M.S. (2005) 'F-19 MR imaging of ventilation and diffusion in excised lungs', *Magnetic Resonance in Medicine*, 54(3), pp. 577-585.

Jakob, P.M., Hillenbrand, C.M., Wang, T.T., Schultz, G., Hahn, D. and Haase, A. (2001) 'Rapid quantitative lung H-1 T-1 mapping', *Journal of Magnetic Resonance Imaging*, 14(6), pp. 795-799.

Jarnum, H., Steffensen, E.G., Knutsson, L., Frund, E.T., Simonsen, C.W., Lundbye-Christensen, S., Shankaranarayanan, A., Alsop, D.C., Jensen, F.T. and Larsson, E.M. (2010) 'Perfusion MRI of brain tumours: a comparative study of pseudo-continuous arterial spin labelling and dynamic susceptibility contrast imaging', *Neuroradiology*, 52(4), pp. 307-317.

Johns, C.S., Swift, A.J., Hughes, P.J.C., Ohno, Y., Schiebler, M. and Wild, J.M. (2017) 'Pulmonary MR angiography and perfusion imaging-A review of methods and applications',

*European Journal of Radiology*, 86, pp. 361-370.

Jung, J.-W., Kang, H.-R., Kim, M.-H., Lee, W., Min, K.-U., Han, M.-H. and Cho, S.-H. (2012) 'Immediate hypersensitivity reaction to gadolinium-based MR contrast media', *Radiology*, 264(2), pp. 414-422.

Kakinuma, R., Moriyama, N., Muramatsu, Y., Gomi, S., Suzuki, M., Nagasawa, H., Kusumoto, M., Aso, T., Tsuchida, T., Tsuta, K., Maeshima, A.M., Tochigi, N., Watanabe, S., Sugihara, N., Tsukagoshi, S., Saito, Y., Kazama, M., Ashizawa, K., Awai, K., Honda, O., Ishikawa, H., Koizumi, N., Komoto, D., Moriya, H., Oda, S., Oshiro, Y., Yanagawa, M., Tomiyama, N. and Asamura, H. (2015) 'Ultra-high-resolution computed tomography of the lung: image quality of a prototype scanner', *Plos One*, 10(9), p. 16.

Kauczor, H.U., Surkau, R. and Roberts, T. (1998) 'MRI using hyperpolarized noble gases', *European Radiology*, 8(5), pp. 820-827.

Kirby, M., Eddy, R.L., Pike, D., Svenningsen, S., Coxson, H.O., Sin, D.D., McCormack, D.G. and Parraga, G. (2017) 'MRI ventilation abnormalities predict quality-of-life and lung function changes in mild-to-moderate COPD: longitudinal TINCan study', *Thorax*, 72(5), p. 475.

Kirby, M., Pike, D., Coxson, H.O., McCormack, D.G. and Parraga, G. (2014) 'Hyperpolarized <sup>3</sup>He ventilation defects used to predict pulmonary exacerbations in mild to moderate chronic obstructive pulmonary disease', *Radiology*, 273(3), pp. 887-896.

Kirby, M., Svenningsen, S., Kanhere, N., Owrangi, A., Wheatley, A., Coxson, H.O., Santyr, G.E., Paterson, N.A.M., McCormack, D.G. and Parraga, G. (2013) 'Pulmonary ventilation visualized using hyperpolarized helium-3 and xenon-129 magnetic resonance imaging: differences in COPD and relationship to emphysema', *Journal of Applied Physiology*, 114(6), pp. 707-715.

Kirby, M., Svenningsen, S., Owrangi, A., Wheatley, A., Farag, A. and Ouriadov, A. (2012) 'Hyperpolarized <sup>3</sup>He and <sup>129</sup>Xe MR imaging in healthy volunteers and patients with chronic obstructive pulmonary disease', *Radiology*, 265.

Kirby, M., Tan, W.C., Hague, C., Leipsic, J., Bourbeau, J., Hogg, J.C. and Coxson, H. (2016) 'CT total airway count explains airflow limitation in COPD patients without emphysema', *American Journal of Respiratory and Critical Care Medicine*, 193, p. 2.

Knust, J., Ochs, M., Gundersen, H.J.G. and Nyengaard, J.R. (2009) 'Stereological estimates of alveolar number and size and capillary length and surface area in mice lungs', *Anatomical Record-Advances in Integrative Anatomy and Evolutionary Biology*, 292(1), pp. 113-122.

- Kołodziej, M., de Veer, M.J., Cholewa, M., Egan, G.F. and Thompson, B.R. (2017) 'Lung function imaging methods in Cystic Fibrosis pulmonary disease', *Respiratory Research*, 18(1), p. 96.
- Korfiatis, P. and Erickson, B. (2014) 'The basics of diffusion and perfusion imaging in brain tumors', *Applied radiology*, 43(7), pp. 22-29.
- Kramer, D. (2011) 'For some, helium-3 supply picture is brightening', *Physics Today*, 64(5), pp. 20-23.
- Kudo, M., Ishigatsubo, Y. and Aoki, I. (2013) 'Pathology of asthma', *Frontiers in Microbiology*, 4, p. 263.
- Kueth, D.O., Behr, V.C. and Begay, S. (2002) 'Volume of rat lungs measured throughout the respiratory cycle using F-19 NMR of the inert gas SF<sub>6</sub>', *Magnetic Resonance in Medicine*, 48(3), pp. 547-549.
- Kueth, D.O., Caprihan, A., Fukushima, E. and Waggoner, R.A. (1998) 'Imaging lungs using inert fluorinated gases', *Magnetic Resonance in Medicine*, 39(1), pp. 85-88.
- Lai, C.M. and Lauterbur, P.C. (1981) 'True 3-dimensional image-reconstruction by nuclear magnetic-resonance zeugmatography', *Physics in Medicine and Biology*, 26(5), pp. 851-856.
- Lange, E.E.d., Altes, T.A., Patrie, J.T., Battiston, J.J., Juersivich, A.P., John P. Mugler, I. and Platts-Mills, T.A. (2009) 'Changes in regional airflow obstruction over time in the lungs of patients with asthma: evaluation with 3He MR imaging', *Radiology*, 250(2), pp. 567-575.
- Lauterbur, P.C. (1973) 'Image formation by induced local interactions: examples employing nuclear magnetic resonance', *Nature*, 242(5394), pp. 190-191.
- Lederlin, M. and Cremillieux, Y. (2014) 'Three-dimensional assessment of lung tissue density using a clinical ultrashort echo time at 3 tesla: A feasibility study in healthy subjects', *Journal of Magnetic Resonance Imaging*, 40(4), pp. 839-847.
- Ley, S. and Ley-Zaporozhan, J. (2012) 'Pulmonary perfusion imaging using MRI: clinical application', *Insights into Imaging*, 3(1), pp. 61-71.
- Lilburn, D.M.L., Pavlovskaya, G.E. and Meersmann, T. (2013) 'Perspectives of hyperpolarized noble gas MRI beyond He-3', *Journal of Magnetic Resonance*, 229, pp. 173-186.
- Lizak, M.J., Conradi, M.S. and Fry, C.G. (1991) 'NMR imaging of gas imbibed into porous ceramic', *Journal of Magnetic Resonance*, 95(3), pp. 548-557.

- Loffler, R., Muller, C.J., Peller, M., Penzkofer, H., Deimling, M., Schwaiblmair, M., Scheidler, J. and Reiser, M. (2000) 'Optimization and evaluation of the signal intensity change in multisection oxygen-enhanced MR lung imaging', *Magnetic Resonance in Medicine*, 43(6), pp. 860-866.
- Lüdeke, K.M., Röschmann, P. and Tischler, R. (1985) 'Susceptibility artefacts in NMR imaging', *Magnetic Resonance Imaging*, 3(4), pp. 329-343.
- Lustig, M., Donoho, D. and Pauly, J.M. (2007) 'Sparse MRI: The application of compressed sensing for rapid MR imaging', *Magnetic Resonance in Medicine*, 58(6), pp. 1182-1195.
- Lutfi, M.F. (2017) 'The physiological basis and clinical significance of lung volume measurements', *Multidisciplinary Respiratory Medicine*, 12, p. 12.
- Lynch, D.A., Austin, J.H.M., Hogg, J.C., Grenier, P.A., Kauczor, H.U., Bankier, A.A., Barr, R.G., Colby, T.V., Galvin, J.R., Gevenois, P.A., Coxson, H.O., Hoffman, E.A., Newell, J.D., Pistolesi, M., Silverman, E.K. and Crapo, J.D. (2015) 'CT-definable subtypes of chronic obstructive pulmonary disease: A statement of the Fleischner Society', *Radiology*, 277(1), pp. 192-205.
- Maceira, A.M., Prasad, S.K., Khan, M. and Pennell, D.J. (2006) 'Reference right ventricular systolic and diastolic function normalized to age, gender and body surface area from steady-state free precession cardiovascular magnetic resonance', *European Heart Journal*, 27(23), pp. 2879-2888.
- Maclaughlin, D.E. (1989) 'Coaxial-cable attenuation in NMR sample coil circuits', *Review of Scientific Instruments*, 60(10), pp. 3242-3248.
- Mai, V.M., Liu, B., Li, W., Polzin, J., Kurucay, S., Chen, Q. and Edelman, R.R. (2002) 'Influence of oxygen flow rate on signal and T-1 changes in oxygen-enhanced ventilation imaging', *Journal of Magnetic Resonance Imaging*, 16(1), pp. 37-41.
- Mansfield, P. and Grannell, P.K. (1975) '"Diffraction" and microscopy in solids and liquids by NMR', *Physical Review B*, 12(9), pp. 3618-3634.
- McDowell, S.A.C. (1999) 'A simple derivation of the Boltzmann distribution', *Journal of Chemical Education*, 76(10), pp. 1393-1394.
- Menke, J., Helms, G. and Larsen, J. (2010) 'Viewing the effective k-space coverage of MR images: phantom experiments with fast Fourier transform', *Magnetic Resonance Imaging*, 28(1), pp. 87-94.
- Milic-Emili, J., Henderson, J.A., Dolovich, M.B., Trop, D. and Kaneko, K. (1966) 'Regional

- distribution of inspired gas in the lung', *Journal of applied physiology*, 21(3), pp. 749-59.
- Miller, K.W., Smith, R.A., Smith, E.B. and Paton, W.D.M. (1972) 'Physicochemical approaches to mode of action of general anaesthetics', *Anesthesiology*, 36(4), p. 339.
- Minard, K.R., Timchalk, C. and Corley, R.A. (2005) 'T2-shortening of <sup>3</sup>He gas by magnetic microspheres', *Journal of Magnetic Resonance*, 173(1), pp. 90-96.
- Mohanty, S. and Bernstein, H. (1970) 'Fluorine relaxation by NMR absorption in gaseous CF<sub>4</sub>, SIF<sub>4</sub>, and SF<sub>6</sub>', *Journal of Chemical Physics*, 53(1), p. 461.
- Molinari, F., Madhuranthakam, A.J., Lenkinski, R. and Bankier, A.A. (2014) 'Ultrashort echo time MRI of pulmonary water content: assessment in a sponge phantom at 1.5 and 3.0 Tesla', *Diagnostic and Interventional Radiology*, 20(1), pp. 34-41.
- Mosbah, K., Ruiz-Cabello, J., Berthezene, Y. and Cremillieux, Y. (2008) 'Aerosols and gaseous contrast agents for magnetic resonance imaging of the lung', *Contrast Media & Molecular Imaging*, 3(5), pp. 173-190.
- Mugler, J.P. and Altes, T.A. (2013) 'Hyperpolarized <sup>129</sup>Xe MRI of the human lung', *Journal of Magnetic Resonance Imaging*, 37(2), pp. 313-331.
- Mukherjee, M., Stoddart, A., Gupta, R.P., Nwaru, B.I., Farr, A., Heaven, M., Fitzsimmons, D., Bandyopadhyay, A., Aftab, C., Simpson, C.R., Lyons, R.A., Fischbacher, C., Dibben, C., Shields, M.D., Phillips, C.J., Strachan, D.P., Davies, G.A., McKinstry, B. and Sheikh, A. (2016) 'The epidemiology, healthcare and societal burden and costs of asthma in the UK and its member nations: analyses of standalone and linked national databases', *BMC Medicine*, 14(1), p. 113.
- Murphy, D.M.F., Nicewicz, J.T., Zabbatino, S.M. and Moore, R.A. (1989) 'Local pulmonary ventilation using nonradioactive xenon-enhanced ultrafast computed-tomography', *Chest*, 96(4), pp. 799-804.
- Musch, G., Layfield, J.D.H., Harris, R.S., Melo, M.F.V., Winkler, T., Callahan, R.J., Fischman, A.J. and Venegas, J.G. (2002) 'Topographical distribution of pulmonary perfusion and ventilation, assessed by PET in supine and prone humans', *Journal of Applied Physiology*, 93(5), pp. 1841-1851.
- Nagao, M., Murase, K., Ichiki, T., Sakai, S., Yasuhara, Y. and Ikezoe, J. (2000) 'Quantitative analysis of technegas SPECT: Evaluation of regional severity of emphysema', *Journal of Nuclear Medicine*, 41(4), pp. 590-595.
- Nakagawa, T., Sakuma, H., Murashima, S., Ishida, N., Matsumura, K. and Takeda, K. (2001)

'Pulmonary ventilation-perfusion MR Imaging in clinical patients', *Journal of Magnetic Resonance Imaging*, 14(4), pp. 419-424.

Nakawah, M.O., Hawkins, C. and Barbandi, F. (2013) 'Asthma, chronic obstructive pulmonary disease (COPD), and the overlap syndrome', *Journal of the American Board of Family Medicine*, 26(4), pp. 470-477.

Nitz, W.R. and Reimer, P. (1999) 'Contrast mechanisms in MR imaging', *European Radiology*, 9(6), pp. 1032-1046.

Ochs, M., Nyengaard, L.R., Lung, A., Knudsen, L., Voigt, M., Wahlers, T., Richter, J. and Gundersen, H.J.G. (2004) 'The number of alveoli in the human lung', *American Journal of Respiratory and Critical Care Medicine*, 169(1), pp. 120-124.

Ogrady, K., Doyle, D.J., Irish, J. and Gullane, P. (1997) 'Biophysics of airflow within the airway: A review', *Journal of Otolaryngology*, 26(2), pp. 123-128.

Ohno, Y., Koyama, H., Nogami, M., Takenaka, D., Matsumoto, S., Obara, M. and Sugimura, K. (2008) 'Dynamic oxygen-enhanced MRI versus quantitative CT: Pulmonary functional loss assessment and clinical stage classification of smoking-related COPD', *American Journal of Roentgenology*, 190(2), pp. W93-W99.

Ohno, Y., Koyama, H., Yoshikawa, T., Matsumoto, K., Takahashi, M., Van Cauteren, M. and Sugimura, K. (2011) 'T2\* measurements of 3-T MRI with ultrashort TEs: Capabilities of pulmonary function assessment and clinical stage classification in smokers', *American Journal of Roentgenology*, 197(2), pp. W279-W285.

Ohno, Y., Nishio, M., Koyama, H., Yoshikawa, T., Matsumoto, S., Seki, S., Obara, M., van Cauteren, M., Takahashi, M. and Sugimura, K. (2014) 'Pulmonary 3 T MRI with ultrashort TEs: influence of ultrashort echo time interval on pulmonary functional and clinical stage assessments of smokers', *Journal of Magnetic Resonance Imaging*, 39(4), pp. 988-997.

Orphanidou, D., Hughes, J.M.B., Myers, M.J., Alsuhal, A.R. and Henderson, B. (1986) 'Tomography of regional ventilation and perfusion using krypton 81m in normal subjects and asthmatic patients', *Thorax*, 41(7), pp. 542-551.

Osborne, D.R.S., Effmann, E.L. and Hedlund, L.W. (1983) 'Postnatal growth and size of the pulmonary acinus and secondary lobule in man', *American Journal of Roentgenology*, 140(3), pp. 449-454.

Osmanagic, E., Sukstanskii, A.L., Quirk, J.D., Woods, J.C., Pierce, R.A., Conradi, M.S., Weibel, E.R. and Yablonskiy, D.A. (2010) 'Quantitative assessment of lung microstructure in healthy mice using an MR-based He-3 lung morphometry technique', *Journal of Applied*

*Physiology*, 109(6), pp. 1592-1599.

Ouriadov, A.V., Fox, M.S., Couch, M.J., Li, T., Ball, I.K. and Albert, M.S. (2015) 'In vivo regional ventilation mapping using fluorinated gas MRI with an x-centric FGRE method', *Magnetic Resonance in Medicine*, 74(2), pp. 550-557.

Parhizkar, M., Edirisinghe, M. and Stride, E. (2015) 'The effect of surfactant type and concentration on the size and stability of microbubbles produced in a capillary embedded T-junction device', *Rsc Advances*, 5(14), pp. 10751-10762.

Park, E.A., Goo, J.M., Park, S.J., Lee, H.J., Lee, C.H., Park, C.M., Yoo, C.G. and Kim, J.H. (2010) 'Chronic obstructive pulmonary disease: quantitative and visual ventilation pattern analysis at xenon ventilation CT performed by using a dual-energy technique', *Radiology*, 256(3), pp. 985-997.

Pauli, W. (1924) 'Zur Frage der theoretischen Deutung der Satelliten einiger Spektrallinien und ihrer Beeinflussung durch magnetische Felder', *Naturwissenschaften*, 12(37), pp. 741-743.

Pavlovskaya, G.E., Cleveland, Z.I., Stupic, K.F., Basaraba, R.J. and Meersmann, T. (2005) 'Hyperpolarized krypton-83 as a contrast agent for magnetic resonance imaging', *Proceedings of the National Academy of Sciences of the United States of America*, 102(51), pp. 18275-18279.

Perez-Sanchez, J.M., de Alejo, R.P., Rodriguez, I., Cortijo, M., Peces-Barba, G. and Ruiz-Cabello, J. (2005) 'In vivo diffusion weighted F-19 MRI using SF6', *Magnetic Resonance in Medicine*, 54(2), pp. 460-463.

Petersson, J., Sanchez-Crespo, A., Larsson, S.A. and Mure, M. (2007) 'Physiological imaging of the lung: single-photon-emission computed tomography (SPECT)', *Journal of Applied Physiology*, 102(1), pp. 468-476.

Prince, M.R., Lee, H.G., Lee, C.H., Youn, S.W., Lee, I.H., Yoon, W., Yang, B.Q., Wang, H.P., Wang, J., Shih, T.T.F., Huang, G.S., Lirng, J.F., Palkowitsch, P. and Grp, G.S. (2017) 'Safety of gadobutrol in over 23,000 patients: the GARDIAN study, a global multicentre, prospective, non-interventional study', *European Radiology*, 27(1), pp. 286-295.

Purcell, E.M., Torrey, H.C. and Pound, R.V. (1946) 'Resonance absorption by nuclear magnetic moments in a solid', *Physical Review*, 69(1-2), pp. 37-38.

Rao, M. and Wild, J.M. (2016) 'RF instrumentation for same-breath triple nuclear lung MR imaging of H-1 and hyperpolarized 3 He and Xe-129 at 1.5T', *Magnetic Resonance in Medicine*, 75(4), pp. 1841-1848.

- Rath, A.R. (1990) 'Design and performance of a double-tuned birdcage coil', *Journal of Magnetic Resonance*, 86(3), pp. 488-495.
- Redpath, T.W. (1998) 'Signal-to-noise ratio in MRI', *The British Journal of Radiology*, 71(847), pp. 704-707.
- Rhodes, C.G. and Hughes, J.M.B. (1995) 'Pulmonary studies using positron emission tomography', *European Respiratory Journal*, 8(6), pp. 1001-1017.
- Rinck, P.A., Petersen, S.B. and Lauterbur, P.C. (1984) 'NMR imaging of fluorine-containing substances. 19-fluorine ventilation and perfusion studies', *Fortschritte Auf Dem Gebiete Der Rontgenstrahlen Und Der Nuklearmedizin*, 140(3), pp. 239-243.
- Roach, P.J., Schembri, G.P. and Bailey, D.L. (2013) 'V/Q scanning using SPECT and SPECT/CT', *Journal of Nuclear Medicine*, 54(9), pp. 1588-1596.
- Ruiz-Cabello, J., Barnett, B.P., Bottomley, P.A. and Bulte, J.W.M. (2011) 'Fluorine (F-19) MRS and MRI in biomedicine', *NMR in Biomedicine*, 24(2), pp. 114-129.
- Ruiz-Cabello, J., Perez-Sanchez, J.M., de Alejo, R.P., Rodriguez, I., Gonzalez-Mangado, N., Peces-Barbas, G. and Cortijo, M. (2005) 'Diffusion-weighted F-19-MRI of lung periphery: Influence of pressure and air-SF6 composition on apparent diffusion coefficients', *Respiratory Physiology & Neurobiology*, 148(1-2), pp. 43-56.
- Runge, V.M. (2015) 'Commentary on T1-weighted hypersignal in the deep cerebellar nuclei Aafter repeated administrations of gadolinium-based contrast agents in healthy rats difference between linear and macrocyclic agents', *Investigative Radiology*, 50(8), pp. 481-482.
- Saam, B., Happer, W. and Middleton, H. (1995) 'Nuclear-relaxation of He-3 in the presence of O-2', *Physical Review A*, 52(1), pp. 862-865.
- Saam, B.T., Yablonskiy, D.A., Kodibagkar, V.D., Leawoods, J.C., Gierada, D.S., Cooper, J.D., Lefrak, S.S. and Conradi, M.S. (2000) 'MR imaging of diffusion of He-3 gas in healthy and diseased lungs', *Magnetic Resonance in Medicine*, 44(2), pp. 174-179.
- Salerno, M., de Lange, E.E., Altes, T.A., Truwit, J.D., Brookeman, J.R. and Mugler, J.P. (2002) 'Emphysema: Hyperpolarized helium 3 diffusion MR imaging of the lungs compared with spirometric indexes - Initial experience', *Radiology*, 222(1), pp. 252-260.
- Schenck, J.F. (1996) 'The role of magnetic susceptibility in magnetic resonance imaging: MRI magnetic compatibility of the first and second kinds', *Medical Physics*, 23(6), pp. 815-850.
- Scholz, A.W., Wolf, U., Fabel, M., Weiler, N., Heussel, C.P., Eberle, B., David, M. and Schreiber, W.G. (2009) 'Comparison of magnetic resonance imaging of inhaled SF6 with

respiratory gas analysis', *Magnetic Resonance Imaging*, 27(4), pp. 549-556.

Schreiber, W.G., Eberle, B., Laukemper-Ostendorf, S., Markstaller, K., Weiler, N., Scholz, A., Heussel, C.P., Thelen, M. and Kauczor, H.U. (2001) 'Dynamic F-19-MRI of pulmonary ventilation using sulfur hexafluoride (SF6) gas', *Magnetic Resonance in Medicine*, 45(4), pp. 605-613.

Schreiber, W.G., Markstaller, K., Weiler, N., Eberle, B., Laukemper-Ostendorf, S., Scholz, A., Burger, K., Thelen, M. and Kauczor, H.U. (2000) 'Breathhold F-19-magnetic resonance imaging of lung ventilation using SF6 gas', *Rofo-Fortschritte Auf Dem Gebiet Der Rontgenstrahlen Und Der Bildgebenden Verfahren*, 172(6), pp. 500-503.

Schreider, J.P. and Raabe, O.G. (1981) 'Structure of the human respiratory acinus', *American Journal of Anatomy*, 162(3), pp. 221-232.

Senda, M., Murata, K., Itoh, H., Yonekura, Y. and Torizuka, K. (1986) 'Quantitative-evaluation of regional pulmonary ventilation using PET and N-13 gas', *Journal of Nuclear Medicine*, 27(2), pp. 268-273.

Sheikh, K., Guo, F., Capaldi, D.P.I., Ouriadov, A., Eddy, R.L., Svenningsen, S., Parraga, G. and Canadian Resp Res, N. (2017) 'Ultrashort echo time MRI biomarkers of asthma', *Journal of Magnetic Resonance Imaging*, 45(4), pp. 1204-1215.

Smith, F.W., Hutchison, J.M.S., Johnson, G., Mallard, J.R., Reid, A., Redpath, T.W. and Selbie, R.D. (1981) 'Clinical application of nuclear magnetic resonance', *The Lancet*, 317(8211), pp. 78-79.

Smith, K., Burbidge, A., Apperley, D., Hodgkinson, P., Markwell, F.A., Topgaard, D. and Hughes, E. (2016) 'Stray-field NMR diffusion q-space diffraction imaging of monodisperse coarsening foams', *Journal of Colloid and Interface Science*, 476, pp. 20-28.

Snell, N., Strachan, D., Hubbard, R., Gibson, J., Gruffydd-Jones, K. and Jarrold, I. (2016) 'S32 Epidemiology of chronic obstructive pulmonary disease (COPD) in the uk: findings from the british lung foundation's 'respiratory health of the nation' project', *Thorax*, 71(Suppl 3), p. A20.

Soher, B., Ainslie, M., MacFall, J., Hashoian, R. and Charles, H. (2010) 'Lung imaging in humans at 3T using perfluorinated gases as MR contrast agents', *ISMRM*. Sweden.

Soutiere, S.E., Tankersley, C.G. and Mitzner, W. (2004) 'Differences in alveolar size in inbred mouse strains', *Respiratory Physiology & Neurobiology*, 140(3), pp. 283-291.

Stein, P.D., Kayali, F. and Olson, R.E. (2004) 'Trends in the use of diagnostic imaging in

patients hospitalized with acute pulmonary embolism', *American Journal of Cardiology*, 93(10), pp. 1316-1317.

Suga, K. (2002) 'Technical and analytical advances in pulmonary ventilation SPECT with xenon-133 gas and Tc-99m-Technegas', *Annals of Nuclear Medicine*, 16(5), pp. 303-310.

Sukstanskii, A.L., Quirk, J.D. and Yablonskiy, D.A. (2014) 'Probing lung microstructure with hyperpolarized He-3 gradient echo MRI', *Nmr in Biomedicine*, 27(12), pp. 1451-1460.

Sun, Y.P., O'Sullivan, B.P., Roche, J.P., Walvick, R., Reno, A., Baker, D., Mansour, J.K. and Albert, M.S. (2011) 'Using hyperpolarized He-3 MRI to evaluate treatment efficacy in cystic fibrosis patients', *Journal of Magnetic Resonance Imaging*, 34(5), pp. 1206-1211.

Takahashi, M., Togao, O., Obara, M., van Cauteren, M., Ohno, Y., Doi, S., Kuro-o, M., Malloy, C., Hsia, C.C. and Dimitrov, I. (2010) 'Ultra-short echo time (UTE) MR imaging of the lung: comparison between normal and emphysematous lungs in mutant mice', *Journal of Magnetic Resonance Imaging*, 32(2), pp. 326-333.

Theilmann, R.J., Arai, T.J., Samiee, A., Dubowitz, D.J., Hopkins, S.R., Buxton, R.B. and Prisk, K. (2009) 'Quantitative MRI measurement of lung density must account for the change in T(2)\* with lung inflation', *Journal of Magnetic Resonance Imaging*, 30(3), pp. 527-534.

Thulborn, K.R., Waterton, J.C., Matthews, P.M. and Radda, G.K. (1982) 'oxygen dependence of the transverse relaxation time of water protons in whole blood at high field', *Biochimica Et Biophysica Acta*, 714(2), pp. 265-270.

Thurlbeck, W.M. (1982) 'Postnatal human lung growth', *Thorax*, 37(8), pp. 564-571.

Triphan, S.M.F., Jobst, B.J., Anjorin, A., Sedlaczek, O., Wolf, U., Terekhov, M., Hoffmann, C., Ley, S., Duber, C., Biederer, J., Kauczor, H.U., Jakob, P.M. and Wielputz, M.O. (2017) 'Reproducibility and comparison of oxygen-enhanced T-1 quantification in COPD and asthma patients', *Plos One*, 12(2), p. 10.

Tyler, D.J., Robson, M.D., Henkelman, R.M., Young, I.R. and Bydder, G.M. (2007) 'Magnetic resonance imaging with ultrashort TE (UTE) PULSE sequences: Technical considerations', *Journal of Magnetic Resonance Imaging*, 25(2), pp. 279-289.

Valckenborg, R.M.E., Huinink, H.P., Sande, J. and Kopinga, K. (2002) 'Random-walk simulations of NMR dephasing effects due to uniform magnetic-field gradients in a pore', *Physical Review E*, 65(2), p. 8.

Veith, S.R., Hughes, E., Vuataz, G. and Pratsinis, S.E. (2004) 'Restricted diffusion in silica particles measured by pulsed field gradient NMR', *Journal of Colloid and Interface Science*,

274(1), pp. 216-228.

Venegas, J., Winkler, T. and Harris, R.S. (2013) 'Lung physiology and aerosol deposition imaged with positron emission tomography', *Journal of Aerosol Medicine and Pulmonary Drug Delivery*, 26(1), pp. 1-8.

Vestbo, J., Hurd, S.S., Agusti, A.G., Jones, P.W., Vogelmeier, C., Anzueto, A., Barnes, P.J., Fabbri, L.M., Martinez, F.J., Nishimura, M., Stockley, R.A., Sin, D.D. and Rodriguez-Roisin, R. (2013) 'Global strategy for the diagnosis, management, and prevention of chronic obstructive pulmonary disease GOLD executive summary', *American Journal of Respiratory and Critical Care Medicine*, 187(4), pp. 347-365.

Vignaud, A., Maitre, X., Guillot, G., Durand, E., de Rochefort, L., Robert, P., Vives, V., Santus, R. and Darrasse, L. (2005) 'Magnetic susceptibility matching at the air-tissue interface in rat lung by using a superparamagnetic intravascular contrast agent: Influence on transverse relaxation time of hyperpolarized helium-3', *Magnetic Resonance in Medicine*, 54(1), pp. 28-33.

Vogelmeier, C.F., Criner, G.J., Martinez, F.J., Anzueto, A., Barnes, P.J., Bourbeau, J., Celli, B.R., Chen, R.C., Decramer, M., Fabbri, L.M., Frith, P., Halpin, D.M.G., Varela, M.V.L., Nishimura, M., Roche, N., Rodriguez-Roisin, R., Sin, D.D., Singh, D., Stockley, R., Vestbo, J., Wedzicha, J.A. and Agusti, A. (2017) 'Global strategy for the diagnosis, management, and prevention of chronic obstructive lung disease 2017 report', *American Journal of Respiratory and Critical Care Medicine*, 195(5), pp. 557-582.

Vullo, T., Zipagan, R.T., Pascone, R., Whalen, J.P. and Cahill, P.T. (1992) 'Experimental design and fabrication of birdcage resonators for magnetic resonance imaging', *Magnetic Resonance in Medicine*, 24(2), pp. 243-252.

Walkup, L.L. and Woods, J.C. (2014) 'Translational applications of hyperpolarized He-3 and Xe-129', *Nmr in Biomedicine*, 27(12), pp. 1429-1438.

Wang, C.B., Mugler, J.P., de Lange, E.E., Patrie, J.T., Mata, J.F. and Altes, T.A. (2014) 'Lung injury induced by secondhand smoke exposure detected with hyperpolarized helium-3 diffusion MR', *Journal of Magnetic Resonance Imaging*, 39(1), pp. 77-84.

Wang, Y.-X.J. (2011) 'Superparamagnetic iron oxide based MRI contrast agents: Current status of clinical application', *Quantitative Imaging in Medicine and Surgery*, 1(1), pp. 35-40.

Wang, Y.X.J. (2015) 'Current status of superparamagnetic iron oxide contrast agents for liver magnetic resonance imaging', *World Journal of Gastroenterology*, 21(47), pp. 13400-13402.

Watson, A.T. and Chang, C.T.P. (1997) 'Characterizing porous media with NMR methods',

*Progress in Nuclear Magnetic Resonance Spectroscopy*, 31, pp. 343-386.

Weatherley, N., Chan, F., Stewart, N., Saunders, L., Collier, G., Norquay, G., Rao, M., Austin, M., Bianchi, S. and Wild, J. (2016) 'Late-breaking abstract: Diffusion-weighted hyperpolarised gas MRI in idiopathic pulmonary fibrosis: Reproducibility and clinical significance', *European Respiratory Journal*, 48(suppl 60).

Webb, S. (1988) *The Physics of Medical Imaging*. Surrey: CSC Publishing.

Weber, M.A., Risse, F., Giesel, F.L., Schad, L.R., Kauczor, H.U. and Essig, M. (2005) 'Measurement of perfusion using the first-pass dynamic susceptibility-weighted contrast-enhanced (DSC) MRI in neurooncology. Physical basics and clinical applications', *Radiologe*, 45(7), pp. 618-632.

Weisskoff, R.M. and Kiihne, S. (1992) 'MRI susceptometry - image based measurement of absolute susceptibility of MR contrast agents and human blood', *Magnetic Resonance in Medicine*, 24(2), pp. 375-383.

West, J.B. (2008) *Pulmonary Pathophysiology: The Essentials*. Lippincott Williams & Wilkins.

West, J.B. (2012) *Respiratory Physiology: The Essentials*. Wolters Kluwer Health/Lippincott Williams & Wilkins.

Wild, J. (2009) *MRI of Pulmonary Ventilation*. Berlin: Springer.

Wild, J., Smith, L., Horn, F., Collier, G., Swift, A., Stewart, N., Rao, M., Norquay, G., Hughes, D., Ugonna, K. and Marshall, H. (2015) 'Hyperpolarised gas MR lung imaging – Breaks through to clinical practice', *European Respiratory Journal*, 46(suppl 59).

Wild, J.M., Marshall, H., Bock, M., Schad, L.R., Jakob, P.M., Puderbach, M., Molinari, F., Van Beek, E.J.R. and Biederer, J. (2012) 'MRI of the lung (1/3): methods', *Insights into Imaging*, 3(4), pp. 345-353.

Wolf, U., Scholz, A., Heussel, C.P., Markstaller, K. and Schreiber, W.G. (2006) 'Subsecond fluorine-19 MRI of the lung', *Magnetic Resonance in Medicine*, 55(4), pp. 948-951.

Wolf, U., Scholz, A., Terekhov, M., Muennemann, K. and Kreitner, K. (2008) 'Fluorine-19 MRI of the lung: first human experiment', *Proc. Intl. Soc. Mag. Reson. Med.*, 16, p. 3207.

Wollmer, P., Rhodes, C.G. and Hughes, J.M.B. (1984) 'Regional extravascular density and fractional blood volume of the lung in interstitial disease', *Thorax*, 39(4), pp. 286-293.

Woodhouse, N., Wild, J.M., Beek, E.J., Hoggard, N., Barker, N. and Taylor, C.J. (2009)

- 'Assessment of hyperpolarized  $^3\text{He}$  lung MRI for regional evaluation of interventional therapy: a pilot study in pediatric cystic fibrosis', *J Magn Reson Imaging*, 30.
- Xu, J.H., Moonen, M., Johansson, A., Gustafsson, A. and Bake, B. (2001) 'Quantitative analysis of inhomogeneity in ventilation SPET', *European Journal of Nuclear Medicine*, 28(12), pp. 1795-1800.
- Xu, Q., Nakajima, M., Ichikawa, S., Nakamura, N., Roy, P., Okadome, H. and Shiina, T. (2009) 'Effects of surfactant and electrolyte concentrations on bubble formation and stabilization', *Journal of Colloid and Interface Science*, 332(1), pp. 208-214.
- Xu, X.J., Norquay, G., Parnell, S.R., Deppe, M.H., Ajraoui, S., Hashoian, R., Marshall, H., Griffiths, P.D., Parra-Robles, J. and Wild, J.M. (2012) 'Hyperpolarized  $^{129}\text{Xe}$  gas lung MRI-SNR and  $T_2^*$  comparisons at 1.5 T and 3 T', *Magnetic Resonance in Medicine*, 68(6), pp. 1900-1904.
- Yablonskiy, D., Sukstanskii, A. and Quirk, J. (2015) 'Diffusion lung imaging with hyperpolarized gas MRI', *NMR in Biomedicine*, 30(3), pp. 1-24.
- Yokoe, K., Satoh, K., Yamamoto, Y., Nishiyama, Y., Asakura, H., Haba, R. and Ohkawa, M. (2006) 'Usefulness of Tc-99m-Technegas and Xe-133 dynamic SPECT in ventilatory impairment', *Nuclear Medicine Communications*, 27(11), pp. 887-892.
- Zhang, W.J., Niven, R.M., Young, S.S., Liu, Y.Z., Parker, G.J.M. and Naish, J.H. (2015) 'Dynamic oxygen-enhanced magnetic resonance imaging of the lung in asthma-Initial experience', *European Journal of Radiology*, 84(2), pp. 318-326.
- Zhang, W.J., Niven, R.M., Young, S.S., Liu, Y.Z., Parker, G.J.M. and Naish, J.H. (2016) 'T1-weighted dynamic contrast-enhanced MR imaging of the lung in asthma: semiquantitative analysis for the assessment of contrast agent kinetic characteristics', *Radiology*, 278(3), pp. 906-916.